Western Australian School of Mines: Minerals, Energy and Chemical Engineering

Synthesis and Evaluation of Novel Photocatalysts for Photocatalytic Reactions

Huayang Zhang

This thesis is presented for the Degree of
Doctor of Philosophy
of
Curtin University

May 2018

Declaration

To the best of my knowledge and belief this thesis contains no material previously published by any other person except where due acknowledgment has been made. This thesis contains no material which has been accepted for the award of any other degree or diploma in any university.

Signature: Huayang Zhang (Huayang Zhang)

Date: 15/05/2018

Acknowledgement

My sincerest gratitude goes first and foremost to my principal supervisor, Prof. Shaobin Wang, for his patient, inspiring and professional guidance during my research work. Thanks for all his guidance devoted to my research project, including helping me choose the topic, deciding on the thesis outline, polishing my manuscripts via email and face-to-face instructions. His scholarly demeanour and dedication to the research and academia not only motivate me to pay more enthusiasm on the scientific research, but also lead me to be more patient and calm to deal with the problems during the study.

In the same way, I would also like to express my great thanks towards my co-supervisor, Prof. Hongqi Sun, whom I always regarded as my role model. His recognition and encouragement before and during my PhD career not only supported my research but also provided me with a turning point in my study career. He always offers me valuable suggestions in my academic studies and guided me to improve the quality of my manuscripts. Many thanks go to Prof. Sun for his patience and effort to my manuscript revision and submission. His unwavering support has sustained me through frustration and depression.

No matter what I plan to do for my research, both Profs. Wang and Sun always provide me with adequate guidance and support and encourage me to make attempts to the experiments. Grateful acknowledgement is made to them once again. I am lucky and proud to be one of their students.

Also, many thanks to Prof. Shaomin Liu, who is the chairperson of this thesis committee for his kind encouragement and instructive suggestions on my work.

I would also like to extend my thanks to the lab technician groups of Curtin University for their assistance in preparing chemicals and training equipment. Special thanks are given to Roshanak and Anja for their constant help and understanding during the process of conducting experiments in the lab. I am also greatly indebted to the technical teams in Centre for Microscopy, Characterization and Analysis of University of Western Australia and Microscopy and Microanalysis Facility of Curtin University. My special thanks go to Prof. Martin Saunders and Dr. Alexandra Suvorova for their considerate training.

Again, I would like to express my warm thanks to my friends and fellow students, Xiaoguang, Li, Xiaochen, KJ, Yuxian, Chi, Ping, Chen, Qi, Yazi, Heng, Xiaojie, Qiaoran, Ruofei, Zhengxin, Guanliang, Stacey, Zana, Hussein, Jun, Jinqiang, Hong, Lei, Lihong, Spark, Sharon, Wei, and Yi. They are always willing to share their experiences and give me kind suggestions about the experiment and life. Thanks for their support, assistance and joy, which have enriched my life and encouraged me to continue my study. Meanwhile, I would like to express my thanks to Prof. Degang Li, Dr. Zhenyu Chu, Dr Guohua Jia and Dr. Jian Pan, the communications with them can not only broaden my horizon but also enrich my knowledge.

The deepest love is given to my family for their love and unconditional care all the time. You are my motivation to carry on. Thank you, my beloved Wenjie, for understanding, helping and encouraging me so much throughout this period. Thank you for accompanying me through every memorable moment, no matter sour or sweet. I love you all.

Abstract

Growing energy demands and environmental problems have caused extensive research on the development of efficient technologies for clean energy and green environment. Inspired by natural photosynthesis, photocatalytic or photoelectrochemical (PEC) water splitting to convert solar energy into electrical or chemical energy has been considered as one of the most promising approaches and attracted enormous attention. Specifically, half-reaction of water oxidation is generally viewed as the primary barrier of this renewable-energy technology, due to its process requirement of multiple protons and electrons. Furthermore, the critical challenge of water oxidation is the design of efficient, low-cost water oxidation catalysts (WOCs) with excellent stability. Along with the rapid advancement of nanoscience, low-dimensional (LD) nanostructures have shown decent performances and thus presented themselves as a promising WOCs candidate, because of their tunable electronic, optoelectronic properties and large specific surface areas.

In our studies, we investigated the morphology, structure and photocatalytic water oxidation performances of a series of low-dimensional materials. On the basis of single-component LD semiconductors such as graphitic carbon nitride (g-C_3N_4) nanosheet, zinc oxide (ZnO) nanorods, we made further modifications to enhance their photocatalytic performances by coupling or in-situ depositing other LD cocatalysts or electrocatalysts such as Co_3O_4 quantum dots, $CoWO_4$ layers and Mn-Bi complex layers. The selection of materials was based on earth-abundant elements and the synthesis followed the principle of low-cost, feasibility and simplicity. Benefiting from the interaction between them, the modified LD hybrids can exhibit multifarious morphological and structural changes. Through photochemical and electrochemical measurements, the synthesized LD hybrids showed increased charge separation and transfer rates, enhanced oxygen evolution rates and higher photoelectric conversion efficiencies. Both experimental and theoretical studies revealed the significant roles of the heterostructure, surface defects and cocatalysts for enhancing photoconversion efficiency and reducing the water oxidation energy barriers. This thesis demonstrates a possibility in exploring the functional LD materials with earth-abundant elements for better photo-related performance of the materials.

Publications

1. H. Zhang, W. Tian, Y. Li, H. Sun*, M. Tadé, S. Wang*, Heterostructured WO_3@$CoWO_4$ bilayer nanosheets for enhanced visible-light photo, electro and photoelectro-chemical oxidation of water. *J. Mater. Chem. A* 2018, 6: 6265-6272.

2. H. Zhang, W. Tian, L. Zhou, H. Sun*, M. Tadé, S. Wang*, Monodisperse Co_3O_4 quantum dots on porous carbon nitride nanosheets for enhanced visible-light-driven water oxidation. *Appl. Catal. B: Environ.* 2018, 223: 2–9.

3. **H. Zhang**, W. Tian, Z. Qian, T. Ouyang, M. Saunders, J. Qin, S. Wang*, M. Tadé, H. Sun*, Co@C/CoO_x coupled with N-doped layer-structured carbons for excellent CO_2 capture and oxygen reduction reaction. *Carbon* 2018, 133: 306–315.

4. H. Zhang, W. Tian, X. Guo, L. Zhou, H. Sun*, M. Tadé, S. Wang*, Flower-like cobalt hydroxide/oxide on graphitic carbon nitride for visible-light-driven water oxidation. *ACS Appl. Mater. Inter.* 2016, 8 (51), 35203–35212.

5. W. Tian, **H. Zhang**, H. Sun*, A. Suvorova, M. Saunders, M. Tadé, S.B. Wang*. Heteroatom (N or N-S)-doping induced layered and honeycomb microstructures of porous carbons for CO_2 capture and energy applications. *Adv. Funct. Mater.* 2016, 26 (47): 8651–8661.

6. D. Chen, **H. Zhang**, Y. Li, Y. Pang, Z. Yin, H. Sun, L.-C. Zhang, S. Wang, M. Saunders, E. Barker and G. Jia*, Spontaneous formation of noble- and heavy-metal-free alloyed semiconductor quantum rods for efficient photocatalysis. *Adv. Mater.* 2018, 1803351.

7. W. Tian, **H. Zhang**, Z. Qian, T. Ouyang, H. Sun*, J. Qin, M. Tadé, S. Wang*, Bread-making synthesis of hierarchically Co@C nanoarchitecture in heteroatom doped porous carbons for oxidative degradation of emerging contaminants. *Appl. Catal. B: Environ.* 2018, 225: 76–83.

8. W. Tian, **H. Zhang**, H. Sun*, M. Tadé, S. Wang*, One-step synthesis of flour-derived functional nanocarbons with hierarchical pores for versatile environmental applications. *Chem. Eng. J.* 2018, 347: 432–439.

9. W. Tian, **H. Zhang**, X. Duan, H. Sun*, M. Tadé, H. Ang, S. Wang*, Nitrogen-and sulfur-codoped hierarchically porous carbon for adsorptive and oxidative removal of pharmaceutical contaminants. *ACS Appl. Mater. Inter.* 2016, 8: 7184–7193.

10. W. Tian, **H. Zhang**, H. Sun*, M. Tadé, S. Wang*, Template-free synthesis of N-doped carbon with pillared-layered pores as bifunctional materials for supercapacitor and environmental applications. *Carbon* 2017, 118: 98–105.

11. Y. Liu, **H. Zhang**, J. Ke, J. Zhang, W. Tian, X. Xu, X. Duan, H. Sun, M. Tadé and S. Wang, 0D(MoS_2)/2D (g-C_3N_4) heterojunctions in Z-scheme for enhanced photocatalytic and electrochemical hydrogen evolution. *Appl. Catal. B Environ.* 2018, 228, 64–74.

12. F. Song, **H. Zhang**, S. Wang*, L. Liu*, X, Tan and S. Liu, Atomic-level design of $CoOH^+$–hydroxyapatite@C catalysts for superfast degradation of organics via peroxymonosulfate activation. *Chem. Commun.* 2018, **54**, 4919–4922.

13. L. Zhou, **H. Zhang**, H. Sun*, S. Liu, M. Tadé, S. Wang* and W. Jin, Recent advances in non-metal modification of graphitic carbon nitride for photocatalysis: a historic review. *Catal. Sci. Technol.* 2016, 6, 7002–7023.

14. S. Zhang, **H. Zhang**, S. Wang*, L. Liu* and S. Liu, Singlet oxygen formation in bio-inspired synthesis of a hollow Ag@AgBr photocatalyst for microbial and chemical decontamination. *Catal. Sci. Technol.* 2017, 7, 4355–4360.

15. E. Saputra, **H. Zhang**, Q. Liu, H. Sun* and S. Wang*, Egg-shaped core/shell α-Mn_2O_3@α-MnO_2 as heterogeneous catalysts for decomposition of phenolics in aqueous solutions. Chemosphere 2016, 159, 351–358.

16. L. Zhou, **H. Zhang**, X. Guo, H. Sun*, S. Liu, M. Tadéand S. Wang*, Metal-free hybrids of graphitic carbon nitride and nanodiamonds for photoelectrochemical and photocatalytic applications. *J. Colloid Interf. Sci*. 2017, 493, 275–280.

17. X. Guo, **H. Zhang**, H. Sun, M. Tadé and S. Wang, Green Synthesis of Carbon Quantum Dots for Sensitized Solar Cells. *ChemPhotoChem* 2017, 1, 116–119.

18. X. Duan, Z. Ao, **H. Zhang**, M. Saunders, H. Sun*, Z. Shao and S. Wang*, Nanodiamonds in sp2/sp3 configuration for radical to nonradical oxidation: Core-shell layer dependence. *Appl. Catal. B Environ.* 2018, 222, 176–181.

19. C. Wang, J. Kang, P. Liang, **H. Zhang**, H. Sun*, M. Tadé and S. Wang*, Ferric carbide nanocrystals encapsulated in nitrogen-doped carbon nanotubes as an outstanding environmental catalyst. *Environ. Sci. Nano* 2017, 4, 170–179.

20. J. Ke, J. Liu, H. Sun*, **H. Zhang**, X. Duan, P. Liang, X. Li, M. , S. Liu and S. Wang*, Facile assembly of Bi_2O_3/Bi_2S_3/MoS_2 n-p heterojunction with layered n-Bi_2O_3 and p-MoS_2

for enhanced photocatalytic water oxidation and pollutant degradation. *Appl. Catal. B Environ.* 2017, 200, 47–55.

Manuscripts in Preparation

H. Zhang, W. Tian, Y. Li, H. Sun*, S. Wang*, Photochemical deposition of M-Bi (M = Ni, Co, Mn) layers onto rGO/ZnO nanorod arrays for enhanced solar water splitting. *Submitted*.

H. Zhang, W. Tian, H. Sun, S. Wang, Low-Dimensional materials for photocatalytic water oxidation application: A selection of 0D, 1D and 2D cases.

International Academic Conference

10th-13th July 2016 9th International Conference on Environmental Catalysis (ICEC2016), Newcastle, Australia (Oral Presentation).

Contents

Declaration .... **I**

Acknowledgement .... **II**

Abstract .... **IV**

Publications .... **V**

Contents .... **VIII**

Chapter 1. Introduction **1**

  1.1 Background **1**

  1.2 Research Objectives **3**

  1.3 Thesis Organizations **3**

Chapter 2. Literature Review **8**

  2.1 Introduction **8**

  2.2 Pros and Cons of Low-Dimensional System **11**

    2.2.1 Advantages of LD Photocatalysts for Water Oxidation 12

    2.2.2 Disadvantages of LD Photocatalysts for Water Oxidation 15

  2.3 0D Semiconductor Materials for Photo-Related Water Oxidation **17**

    2.3.1 0D Metal Complexes and Nanoclusters 18

    2.3.2 Metal Oxides Quantum Dots and Nanocrystals 20

  2.4 1D Semiconductor Materials for Photo-Related Water Oxidation **23**

    2.4.1 Application of 1D Semiconductors in Wireless Systems 24

    2.4.2 Application of 1D Semiconductors in Wired Systems 24

  2.5 2D Semiconductor Materials for Photo-Related Water Oxidation **27**

    2.5.1 2D Metal Oxide Nanosheets for Photocatalytic Water Oxidation 27

    2.5.2 Layered Double Hydroxides (LDHs) Nanosheets for Photocatalytic Water Oxidation 30

    2.5.3 Metal-Based Chalcogenides (Sulfides and Selenides) and Oxyhalide Semiconductors for Photocatalytic Water Oxidation 31

  2.6 LD Semiconductor-Based Hybrids for Photo-Related Water Oxidation **33**

    2.6.1 1D-Based (0D/1D, 1D/1D and 2D/1D) Semiconductor Hybrids for Enhanced Photo Water Oxidation 34

    2.6.2 2D-Based (0D/2D, 2D/2D) Semiconductor Hybrids for Enhanced Photo Water Oxidation 37

  2.7 Metal-Free Based Semiconductors for Water Oxidation **37**

  2.8 Catalytic Active Sites-Catalysis Correlation in LD Semiconductors **38**

2.9 Conclusions and Perspectives 39
References 39
Chapter 3. Flower-Like Cobalt Hydroxide/Oxide on Graphitic Carbon Nitride for Visible-Light-Driven Water Oxidation 51
Abstract 51
3.1 Introduction 52
3.2 Experimental Section 53
3.2.1 Chemical Reagents 53
3.2.2 Materials Preparation 53
3.2.3 Characterization Techniques 54
3.2.4 Photoelectrochemical Measurements 55
3.2.5 Oxygen Evolution Reaction 56
3.3 Results and Discussion 57
3.4 Conclusions 73
References 73
Chapter 4. Monodisperse Co_3O_4 Quantum Dots on Porous Carbon Nitride Nanosheets for Enhanced Visible-Light-Driven Water Oxidation 81
Abstract 81
4.1 Introduction 81
4.2 Experimental Section 83
4.2.1 Chemical Reagents 83
4.2.2 Preparation of g-C_3N_4 84
4.2.3 Synthesis of Co_3O_4 QDs/g-C_3N_4 Samples 84
4.2.4 Photoelectrochemical and Oxygen Evolution Reaction 84
4.2.5 Characterizations 85
4.3 Results and Discussion 86
4.4 Conclusions 94
References 95
Chapter 5. Heterostructured WO_3@$CoWO_4$ Bilayer Nanosheets for Enhanced Visible-Light Photo, Electro and Photoelectrochemical Oxidation of Water 100
Abstract 100
5.1 Introduction 101
5.2 Experimental Section 102
5.2.1 Synthesis of WO_3 Nanosheets 102
5.2.2 Synthesis of WO_3@$CoWO_4$ Nanosheet Composites 102

5.2.3. Electrochemical Measurements 103
5.2.4 Photocatalytic Oxygen Evolution Reaction Tests 104
5.2.5 Photoelectrochemical Measurement 104
5.2.6 Materials Characterizations 105
5.2.7 Density Functional Theory (DFT) calculations 105
5.3 Results and Discussion 107
5.3.1 Synthesis and Structure Analysis 107
5.3.2 Evaluation of the Electrochemical OER Performance 113
5.3.3 Visible-Light Photocatalytic OER Performance 115
5.3.4 Photoelectrochemical (PEC) OER Performance 121
5.3.5 DFT Calculations for OER 123
5.4 Conclusions 127
References 127
Chapter 6. Photochemical Deposition of M-Bi (M = Ni, Co, Mn) Layers onto rGO/ZnO Nanorod Arrays for Solar Water Splitting 134
Abstract 134
6.1 Introduction 135
6.2 Experimental Section 137
6.2.1 Chemical Reagents 137
6.2.2 Preparation of ZnO and rGO/ZnO 137
6.2.3 Preparation of M-Bi/rGO/ZnO 138
6.2.4 PEC Measurement 138
6.2.5 Materials Characterizations 139
6.2.6 Simulation Details 140
6.3 Results and Discussion 141
6.3.1 DFT Calculations 141
6.3.2 Material Characterization 143
6.3.3 PEC Tests 148
6.4 Conclusions 154
References 155
Chapter 7. Conclusions and Perspectives 161
7.1 Conclusions 161
7.1.1 Flower-Like Cobalt Hydroxide/Oxide on Graphitic Carbon Nitride for Visible-Light-Driven Water Oxidation 161
7.1.2 Monodisperse Co_3O_4 Quantum Dots on Porous Carbon Nitride Nanosheets for Enhanced Visible-Light-Driven Water Oxidation 162

7.1.3 Heterostructured WO_3@$CoWO_4$ Bilayer Nanosheets for Enhanced Visible-Light Photo, Electro and Photoelectrochemical Oxidation of Water 162

7.1.4 Photochemical Deposition of M-Bi (M = Ni, Co, Mn) Layers onto rGO/ZnO Nanorod Arrays for Solar Water Splitting 163

7.2 Perspectives and Suggestions for Future Research 163

Appendix........ 165

Copyright Permissions........ 165

Chapter 1. Introduction

1.1 Background

Nowadays, our energy sources heavily rely on fossil fuels (coal, oil or natural gas), which unfortunately are projected to be steadily exhausted in near future.[1] The combustion of the fossil fuels also has led to various environmental issues, for instance, the increasing serious greenhouse effect (mainly caused by carbon dioxide and methane emissions) and air contamination due to the fine dust. Considering the goal of sustainability for the benefit of all humankind, energy resources must come from renewable and environmentally friendly sources to fulfil the increasing demands.[2,3] Fortunately, we have explored a series of renewable sources such as wind, solar energy, geothermal heat, and ocean energy, etc., among them solar energy is considered as the most attractive and abundant renewable energy source.[4] It is estimated that one-hour energy output from the Sun to the Earth can provide even more power than the annual energy consumption by the human society.[1]

The conversion of renewable solar energy is a principal challenge in terms of both scientific and technological aspects to match the future energy requirement. Inspired by nature, efficient solar-light-driven water splitting to produce the hydrogen energy is one of the major objectives in solar power conversion.[5] Commonly, overall water splitting is composed by two half-reactions, e.g. water oxidation and reduction. Since the water oxidation reaction requires a four-electron transfer process coupled with the removal of four protons from water molecules to form one dissociative oxygen molecule, this half-reaction is recognized as the rate-limiting step to complete the overall water splitting.[6,7] In general, the efficiency of the photocatalytic water oxidation is largely related to the optical absorption, electronic structure, band structure of the semiconductor based photocatalysts.[5,8–10] Therefore, the most challenging task in photocatalytic water oxidation is to explore efficient photocatalysts that are able to absorb sunlight and oxidize water. In the earlier studies of photocatalytic water oxidation catalysts (WOCs), the most active homogeneous and heterogeneous catalysts are found to be noble metals (e.g. iridium, ruthenium, or rhodium), which would largely raise the final cost of practical applications.[11–13] Inspired by the natural photosynthesis that utilizes manganese (Mn) as one of the essential metal ions to construct the Mn_4CaO_4 water oxidation catalyst, recent attention has been focused on various earth abundant complexes to mimic the water oxidation process in Photosystem II.[14]

Nanoscaled photocatalysts represent the most promising materials in the research area of WOCs, while among different types of nanostructures, low-dimensional (LD) nanoscaled photocatalysts have been described as the ideal high-performance candidates for water oxidation because of their unique optical and structural properties.[15,16] LD structured materials mainly refer to zero-dimensional (0D), one dimensional (1D), and two dimensional (2D) materials, whose sizes are below 100 nm at least in one dimension. 0D materials contain nanoparticles, nanoclusters and quantum dots; 1D materials include nanowires, nanorods and nanotubes; and 2D materials refer to the nanosheet and layer-structured materials. Generally, LD WOCs can show improved photocatalytic performance than bulk materials. The reasons can be either regulating the size and thickness, or exposing high-index facets and active sites/defect, or doping engineering for a faster charge transport/transfer.[17–19] For instance, pore-rich WO_3 ultrathin nanosheets with nearly fully exposed active crystal facets, and nitrogen-doped TiO_2 nanowire both showed higher water oxidation performances than that of the bulk or pristine counterpart.[20] Besides, the LD WOCs can extend from metal to non-metal based catalysts such as graphitic carbon nitride (g-C_3N_4) nanosheet[10] or carbon quantum dots.[21] In addition, strong van der Waals (vdW) forces allow single-component LD to assemble into vdW heterostructures,[22] which can be further divided into several groups such as 0D–1D, 0D–2D, 1D–2D and 2D–2D systems. Coupling different LD WOCs with matched band structures can not only improve the charge separation and transfer, but also provide high-quality heterojunctions between the materials with ideally aligned band offsets for improved light absorption.

Although low-dimensional WOCs offer more opportunities to improve the photocatalytic efficiency, they also have vital disadvantages such as the decreased thermo-dynamic stability which can lead to a reduced quantum efficiency.[23,24] Hence, the current research emphasis of LD WOCs has been concentrated on balancing all the aspects of factors including crystallite size, morphology and composition.

1.2 Research Objectives

This work aims to synthesize various low-dimensional, from 0D to 2D semiconductor photocatalysts and optimize the structural properties and water oxidation performance by rationally incorporating different single-component to form heterojunctions or applying them as water oxidation cocatalysts. The approaches of material selection and synthesis followed the principle of low-cost and simplicity. The LD hybrids were used in the form of photocatalysts or photoanodes to test their optical properties, structural changes and photocatalytic performances by a series of characterization methods and photo- and photoelectrochemical measurements.

The specific objectives are as follows:

1) Rationally select suitable materials and design novel methods to synthesize the low-dimensional semiconductors.

2) Based on the unique characteristics of the pristine LD materials, optimize their light absorption, band structures and morphologies by impregnating or in-situ depositing other LD cocatalysts.

3) Investigate and verify the optimized morphologies, optical properties and electronic structure of the synthesized LD hybrids by advanced characterization techniques.

4) Examine and compare the electroconductivity, stability and oxygen evolution rates of the designed photocatalysts through photo- or photoelectrochemical systems.

5) Illustrate the mechanism of the enhanced water oxidation performance via the experimental and theoretical calculation methods.

1.3 Thesis Organizations

This thesis is composed of seven chapters, including introduction, literature review, results and discussions (four chapters), main conclusions with outlooks and perspectives for future studies.

Chapter 1: Introduction

This chapter summarizes the current issues with photo-related water oxidation. In addition, research objectives and thesis organization are provided in this chapter.

Chapter 2: Literature Review

This chapter makes a survey and investigation over the recent progress on the development and modification of low-dimensional semiconductor materials for photochemical water oxidation applications.

Chapter 3: Flower-Like Cobalt Hydroxide/Oxide on Graphitic Carbon Nitride for Visible-Light-Driven Water Oxidation (*Adapted from Appl. Mater. Inter.* 2016, 8 (51), 35203–35212 and reuse permission has been achieved)

In this chapter, we reported the facile coating of 2D-nanosheet-built, flower-like cobalt hydroxide/oxide (Fw-$Co(OH)_2$/Fw-Co_3O_4) onto 2D g-C_3N_4 nanosheet for enhanced visible-light-driven water oxidation process.

Chapter 4: Monodisperse Co_3O_4 Quantum Dots on Porous Carbon Nitride Nanosheets for Enhanced Visible-Light-Driven Water Oxidation (*Adapted from Appl. Catal. B: Environ.* 2018, 223: 2–9 and reuse permission has been achieved)

In this chapter, 0D Co_3O_4 quantum dots were uniformly deposited onto 2D porous g-C_3N_4 nanosheets by a facile annealing process to construct surface heterojunctions for visible-light-driven water oxidation.

Chapter 5: Heterostructured WO_3@$CoWO_4$ Bilayer Nanosheets for Enhanced Visible-Light Photo, Electro and Photoelectrochemical Oxidation of Water (*Adapted from J. Mater. Chem. A* 2018, 6: 6265–6272 and reuse permission has been achieved)

In this chapter, an interface-induced synthesis method was newly established to fabricate 2D bilayer nanosheets of WO_3@$CoWO_4$ as highly efficient catalysts for enhanced photo, electro and photoelectron-chemical OERs, as revealed by experimental and density functional theory (DFT) studies.

Chapter 6: Photochemical Deposition of M-Bi (M = Ni, Co, Mn) Layers onto rGO/ZnO Nanorod Arrays for Solar Water Splitting

In this chapter, the OER activity of M-Bi (M = Ni, Co, Mn) catalysts were compared in a combined computational and experimental investigation, in which M-Bi thin layers were self-assembled onto ZnO nanorod arrays and reduced graphene oxide (rGO/ZnO) as a ternary electrocatalyst/light-harvester PEC system.

Chapter 7: **Conclusions and Perspectives**

This chapter summarized the above research results and presented perspectives for future research.

References

1) Nocera, D. G.; Nash, M. P. Powering the Planet: Chemical Challenges in Solar Energy Utilization. PNAS **2007**, *104*, 15729.

2) Du, P.; Eisenberg, Catalysts Made of Earth-Abundant Elements (Co, Ni, Fe) for Water Splitting: Recent Progress and Future Challenges. *Energy & Environmental Science* **2012**, *5*, 6012.

3) Kang, D.; Kim, T. W.; Kubota, S. R.; Cardiel, A. C.; Cha, H. G.; Choi, K. S. Electrochemical Synthesis of Photoelectrodes and Catalysts for Use in Solar Water Splitting. *Chemical Reviews* **2015**, *115*, 12839.

4) Tachibana, Y.; Vayssieres, L.; Durrant, J. R. Artificial Photosynthesis for Solar Water-Splitting. *Nature Photonics* **2012**, *6*, 511.

5) Osterloh, F. E. Frank E Inorganic Materials as Catalysts for Photochemical Splitting of Water. *Chemistry of Materials* **2008**, *20*, 35.

6) Kärkäs, M. D.; Verho, O.; Johnston, E. V.; Åkermark, B. Artificial Photosynthesis: Molecular Systems for Catalytic Water Oxidation. *Chemical Reviews* **2014**, *114*, 11863.

7) Park, Y.; McDonald, K. J.; Choi, K.-S. Progress in Bismuth Vanadate Photoanodes for Use in Solar Water Oxidation. *Chemical Society Reviews* **2013**, *42*, 2321.

8) Walter, M. G.; Warren, E. L.; McKone, J. R.; Boettcher, S. W.; Mi, Q.; Santori, E. A.; Lewis, N. S. Solar Water Splitting Cells. *Chemical Reviews* **2010**, *110*, 6446.

9) Hisatomi, T.; Kubota, J.; Domen, K. Recent Advances in Semiconductors for Photocatalytic and Photoelectrochemical Water Splitting. *Chemical Society Reviews* **2014**, *43*, 7520.

10) Di, J.; Xiong, J.; Li, H.; Liu, Z. Ultrathin 2D Photocatalysts: Electronic-Structure Tailoring, Hybridization, and Applications. *Advanced Materials* **2017**, *30*,1704548.

11) Li, J.; Zheng, G. One-Dimensional Earth-Abundant Nanomaterials for Water-Splitting Electrocatalysts. *Advanced Science* **2017**, *4*, 1600380.

12) Puntoriero, F.; La Ganga, G.; Sartorel, A.; Carraro, M.; Scorrano, G.; Bonchio, M.; Campagna, S. Photo-Induced Water Oxidation with Tetra-Nuclear Ruthenium Sensitizer and Catalyst: A Unique 4 x 4 Ruthenium Interplay Triggering High Efficiency with Low-Energy Visible Light. *Chemical Communications* **2010**, *46*, 4725.

13) Bledowski, M.; Wang, L.; Neubert, S.; Mitoraj, D.; Beranek, R. Improving the Performance of Hybrid Photoanodes for Water Splitting by Photodeposition of Iridium Oxide Nanoparticles. *The Journal of Physical Chemistry C* **2014**, *118*, 18951.

14) Hocking, R. K.; Brimblecombe, R.; Chang, L. Y.; Singh, A.; Cheah, M. H.; Glover, C.; Casey, W. H.; Spiccia, L. Water-Oxidation Catalysis by Manganese in a Geochemical-like Cycle. *Nature Chemistry* **2011**, *3*, 461.

15) Zhao, Y. S.; Fu, H.; Peng, A.; Ma, Y.; Xiao, D.; Yao, J. Low-Dimensional Nanomaterials Based on Small Organic Molecules: Preparation and Optoelectronic Properties. *Advanced Materials* **2008**, *20*, 2859.

16) Voiry, D.; Shin, H. S.; Loh, K. P.; Chhowalla, M. Low-Dimensional Catalysts for Hydrogen Evolution and CO_2 Reduction. *Nature Review* **2018**, *2*, 1.

17) Zhang, J.; Zhang, P.; Wang, T.; Gong, J. Monoclinic WO_3 nanomultilayers with Preferentially Exposed (002) Facets for Photoelectrochemical Water Splitting. *Nano Energy* **2015**, *11*, 189.

18) Huang, Z.-F.; Pan, L.; Zou, J.-J.; Zhang, X.; Wang, L. Nanostructured Bismuth Vanadate-Based Materials for Solar-Energy-Driven Water Oxidation: A Review on Recent Progress. *Nanoscale* **2014**, *6*, 14044.

19) Zhou, M.; Lou, X. W.; Xie, Y. Two-Dimensional Nanosheets for Photoelectrochemical

Water Splitting: Possibilities and Opportunities. *Nano Today* **2013**, *8*, 598.

20) Liu, Y.; Liang, L.; Xiao, C.; Hua, X.; Li, Z.; Pan, B.; Xie, Y. Promoting Photogenerated Holes Utilization in Pore-Rich WO_3 Ultrathin Nanosheets for Efficient Oxygen-Evolving Photoanode. *Advanced Energy Materials* **2016**, *6*, 1600437.

21) Liu, J.; Liu, Y.; Liu, N.; Han, Y.; Zhang, X.; Huang, H.; Lifshitz, Y.; Lee, S. T.; Zhong, J.; Kang, Z. Metal-Free Efficient Photocatalyst for Stable Visible Water Splitting via a Two-Electron Pathway. *Science* **2015**, *347*, 970.

22) Jariwala, D.; Marks, T. J.; Hersam, M. C. Mixed-Dimensional van Der Waals Heterostructures. *Nature Materials* **2017**, *16*, 170.

23) Sun, Y.; Cheng, H.; Gao, S.; Sun, Z.; Liu, Q.; Leu, Q.; Lei, F.; Yao, T.; He, J.; Wei, S.; Xie, Y. Freestanding Tin Disulfide Single-Layers Realizing Efficient Visible-Light Water Splitting. *Angewandte Chemie - International Edition* **2012**, *51*, 8727.

24) Osterloh, F. E. Inorganic Nanostructures for Photoelectrochemical and Photocatalytic Water Splitting. *Chemical Society Reviews* **2013**, *42*, 2294.

Every reasonable effort has been made to acknowledge the owners of copyright material. I would be pleased to hear from any copyright owner who has been omitted or incorrectly acknowledged.

Chapter 2. Literature Review

Low-dimensional (LD) semiconductor materials and their hybrids have arisen as attractive candidates for photocatalytic water oxidation. There has been extensive progress for the rational design of photocatalytic nanomaterials in the artificial photosynthesis system. In this chapter, we attempt to outline the state-of-the-art development of earth-abundant LD semiconductor based nanomaterials for photo-induced water oxidation. Particular attention was given to the mechanisms of water oxidation and the different strategies to select suitable LD catalysts to optimize the activity and efficiency.

2.1 Introduction

The establishment of novel technologies to engender sustainable energy sources that can take over fossil fuels is a hot research subject. Since the discovery of the Honda-Fujishima effect,[1] tremendous attention has been centered on solar-light-driven water splitting, by adopting various inorganic semiconductors that possess strong photoinduced redox abilities. Researches have extended from TiO_2 to ZnO,[2] WO_3,[3] Fe_2O_3[4] and others. Since the oxidative half-reaction, namely water oxidation, is a four-electron transfer and four-proton removal process to form oxygen from water molecules, it is generally considered as the rate-limiting step to achieve overall water splitting. Therefore, much attention has been given to water oxidation.

Photocatalytic water oxidation is usually divided into two kinds of configurations, i.e. wired and wireless photochemical systems as shown in Figure 2.1.[5,6] To be specific, single wired, also known as photoelectrochemical (PEC) system (Figure 2.1a) is composed of a photoanode for water oxidation and a counter electrode for water reduction (a photocathode or reference electrode is also connected in some cases).[5] Under light illumination, the photogenerated electron-hole pairs in photoanode are separated inside the semiconductors by an electric field. Subsequently, the photoinduced holes migrate to the semiconductor surface to oxidize water molecules and evolve O_2. On the other side, the separated photogenerated electrons transfer to the counter electrode via an external electrical circuit, where they reduce H^+ to H_2. An additional bias voltage is generally imposed as an external potential driving-force for electron transport.[1] In contrast, as shown in Figure 2.1b, wireless, also known as autonomous photocatalytic system contains a suspension of photocatalyst particles dispersed in a solvent.[7,8] Each photocatalyst particle serves as an independent "short-circuited" PEC cell, implementing oxidation or reduction of water on the surface.[8] The wireless configuration has the merits of being simpler, cheaper and more universal to be developed and used than wired PEC system. Due to the high electrical resistivity or the difficulty to be deposited onto photoelectrodes, many semiconductor materials are unable to be used as PEC anodes, but they can be employed in a wireless system. In addition, the light absorption efficiency of the wireless system tends to be higher due to the larger exposed semiconductor surface area. For instance, if the particle diameters are around 100 nm, 100 mg photocatalyst dispersed in water may consist of more than 10^{11} mobile and independent particles, and thus the exposed surface area is much larger than PEC anode.[8] However, the wireless photocatalytic system has its drawbacks because the charge carrier separation efficiency is much lower than that in the PEC system. Besides, there are difficulties to separate the stoichiometric mixture of O_2 and H_2 effectively and to avoid backward reactions. The water oxidation efficiency in a wireless photocatalytic system remains far below that in wired PEC system powered by photovoltaic cells. It was reported that PEC system can afford high solar-to-hydrogen efficiencies up to 30% in a three-junction solar cell, approaching the Shockley-Queisser limit.[7]

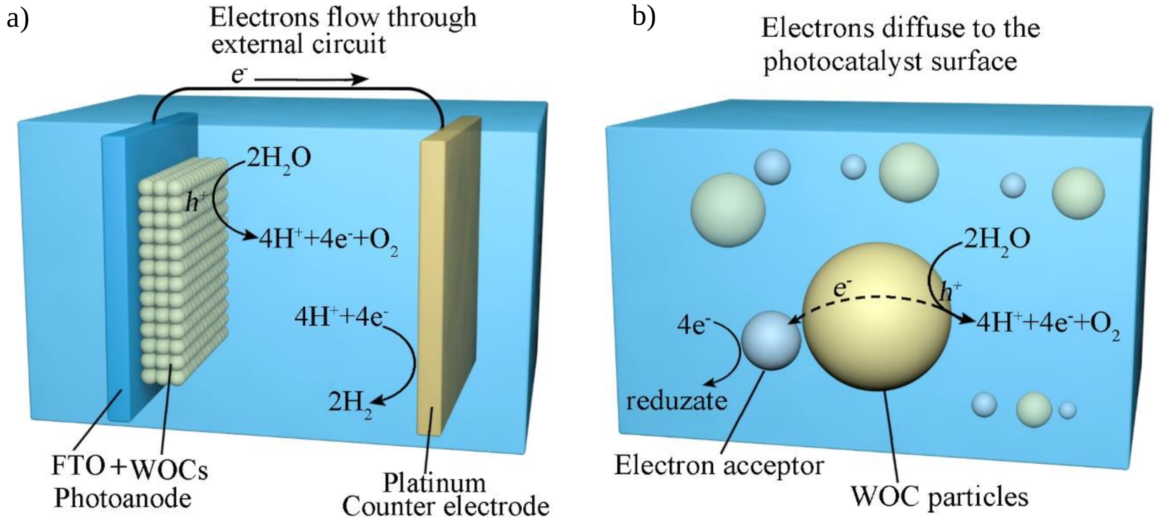

Figure 2.1 Schematic illustration of photocatalytic water oxidation systems: a) wired and b) wireless configuration (Original pictures).

In spite of the different configurations of the two systems, there are some similar criteria on the semiconductors. Firstly, to proceed the solar water splitting reaction successfully, the band gap energies of semiconductors should be larger than 1.23 eV to straddle the HER and OER potentials (0 and 1.23 V vs. normal hydrogen electrode, NHE, respectively, at pH 0).[9,10] However, a larger band gap will result in the inadequate light absorption. For instance, corresponding to the band gap energies of 1.23 eV, the semiconductor material needs to absorb an equivalent light wavelength of 1100 nm, which is in the near-infrared region of the sunlight spectrum.[11] In general, the band gap energies of most semiconductors are larger than 2 eV, meaning that they can only adsorb light wavelengths of $\leq$ 620 nm.[11] Therefore, the high requirement of appropriate band gap energy highly limits the selection of semiconductors for water oxidation.[9,11] In that case, suitable modifications such as doping, hybriding, size-control will be required to adjust the band structure of these semiconductors for a successful application in water oxidation reaction. Secondly, the energies of the photogenerated holes should be high enough to overcome the overpotentials related with this oxidative reaction, namely η_{ox}.[7] Apart from structural modifications on semiconductors, it is worth noting that a bias voltage imposed on semiconductors in a wired PEC system or external electron acceptors (sacrificial reagents such as $Na_2S_2O_8$ or $AgNO_3$) added in the wireless system can work effectively to overcome η_{ox} and actuate water oxidation.[12] Thirdly, an appropriate structural control on semiconductors will also be demanded to deal with the issues of high electron-hole recombination and slow hole diffusion kinetics. It is known that the photoinduced holes within the semiconductors must travel through long distances to the surface and react with water. Unless separated effectively, the holes can recombine with electrons trapped on the surface or in the bulk of semiconductor materials, leading to deficient oxygen evolution reaction (OER).

Based on the above discussion, we can derive that a special research emphasis should be put on searching highly efficient semiconductor-based water oxidation catalysts (WOCs) for practical photocatalytic water oxidation. Recently, LD structured semiconductors have been proposed as promising candidates, because of their attractive attributes including short carrier-transfer distance, readily tunable band gap structure, large surface area, unique electronic and optical properties that can be adjusted by doping or dimensional modification.[7,13,14]

Generally, LD materials should have at least one dimension of ≤ 100 nm and typical LD examples include zero-dimensional (0D) nanoparticles (NPs), nanoclusters and quantum dots (QDs); one-dimensional (1D) nanotubes (NTs), and nanowires (NWs)/or nanorods; and two-dimensional (2D) nanosheets and layers. Further, there are various types of 0D/1D/2D based hybrid materials in natural or artificial systems, which could be inorganic, organic, metallic-organic or inorganic-organic matters.

Since Mn_4CaO_4 was identified as the oxygen-evolving center of photosystem II in the leaves of plants,[15] most recent studies have been pointed to exploit various earth-abundant elements based photocatalysts to mimic this function.[15–17] From the perspective of a practical application that desires a low cost of production, we will concentrate on LD semiconductors based on low cost and earth-abundant elements, which have been exploited to promote the water oxidation efficiency in wireless and wired photocatalytic systems. The basic properties of LD semiconductor materials including the extraordinary advantages and inherent disadvantages will be outlined. Subsequently, through referencing some classic examples, we tried to present some fundamental insights into how the photocatalytic water oxidation performance is enhanced on LD materials and their hybrids. Besides, we also explore the different water oxidation mechanism regarding 0D, 1D and 2D semiconductors. Finally, conclusive remarks will be summarized and the key challenges and the future strategies for the management of LD photocatalysts for water oxidation will be discussed.

2.2 Pros and Cons of Low-Dimensional System

Without any doubt, the unique properties endow LD semiconductor materials with superior advantages in improving the photocatalytic capability. Meanwhile, they also possess their inherent disadvantages. Hence, it is necessary to make clear both the merits and drawbacks of LD materials so as to control and exploit their properties for better catalysis.

2.2.1 Advantages of LD Photocatalysts for Water Oxidation

Quantum Confinement. An essential feature of LD materials is the quantum confinement effect, which endows the materials with unique electronic, optical, and structural properties compared with their bulk counterparts.[18–20] Quantum confinement effects can be achieved when the nanoparticle size is close to the exciton Bohr radius. In that case, the energy level spacing of the particle will exceed kT (k is Boltzmann's constant and T is temperature), and the corresponding energy differences (> kT) will restrict the electron/hole mobility.[13] In 1974, Dingle et al. first confirmed the carriers confinement in 2D materials, where numerous restricted-electron and -hole states of rectangular potential wells were observed.[21] Compared to bulk materials, the quantum confinement effect will bring about modified properties in LD materials, two of which are of particular importance. The first one is the energy states changing from quasi-continuous states to discrete and well-separated states due to the reduced atom number in the LD direction. Figure 2.2a-d show the density of states (DOS) as a function of energy in 3D to 0D semiconductor materials, which provide novel opportunities to control charge diffusion directions and pathways. Another valuable property is described in Figure 2.2e. Depending on the characteristics of a semiconductor, once the LD diameter decreases to a particular value, an increase (blue shift) in band-gap energy is observed. To be specific, the conduction band edge shifts towards a lower potential, while the valence band moves to more oxidizing position. According to Marcus-Gerischer theory, this change is expected to increase thermodynamic driving force which can accelerate interfacial charge transfer and enhance the water splitting rate.[22,23] For example, since their conduction band edges are more positive than the hydrogen evolution potential, bulk WO_3, $BiVO_4$, and Fe_2O_3 are inefficient to produce hydrogen despite of their strong visible-light absorption.[10] However, by reducing at least one dimension of these bulk materials to a certain level, the band gap position will shift to cover the reduction potential, allowing for efficient water splitting on these semiconductors.

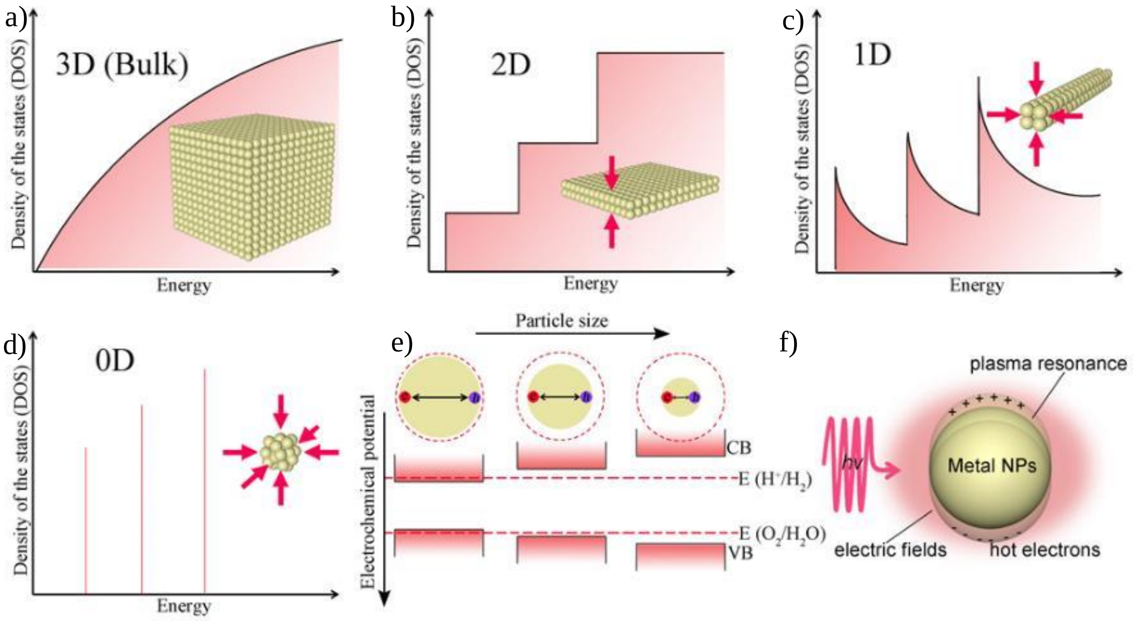

Figure 2.2 Comparison of electronic DOS of a) 3D bulk semiconductor materials and LD semiconductor materials including b) 2D, (c) 1D and d) 0D. The inset arrows on related models indicate the quantum confinement direction and dimensionalities; (e) quantum size effect on band structure; (f) Schematic illustration of surface plasmon resonance excitation on metallic NPs (Adapted based on ref. [13] and ref. [22]).

Although the quantum confinement is common in the LD system, the upper limit of dimensionality or size to trigger this effect will exactly depend on the individual electronic structure of each semiconductor.[24] For example, Li's group found that even though the thickness was as thin as 1.0 nm for 2D TiO_2 nanosheets, the quantum confinement was not apparent as no obvious changes are observed in the band gap structure and electronic property. As such, they inferred that the quantum effects of some specific LD semiconductors should only occur on some specific dimensionality.[25] Nevertheless, since the diffusion distance of minority charge carriers in most semiconductors is below several nanometers, it is still challenging to control the quantum confinement within this range.[26] We will discuss in detail the quantum confinement in water oxidation in below sections where applicable.

Localized Surface Plasmon Resonance (LSPR). Apart from quantum confinement effect, another beneficial feature of LD metal-based semiconductors is the (localized) surface plasmon resonance (SPR/LSPR). Plasmon resonance can be defined as the collective resonant oscillation of free conduction electrons restricted in metallic nanomaterials under light irradiation, while surface plasmon resonances are oscillations restricted to the surfaces of nanomaterials and interact actively with light.[27] As shown in Figure 2.2f, irradiating metal nanoparticles with light at their plasmon frequency can produce energy ('hot') electrons or intense electric fields on the surface of the particles, which can be extracted and applied in catalytic reactions.[28] In the past decade, SPR has been widely employed on specific 0D noble metals, e.g., Au, Ag, Pt in photocatalysis.[29] Besides, plasmonic semiconductors usually possess excellent light absorption due to stronger light trapping. However, the SPR effect of these costly noble-metal 0D materials is only beneficial to visible-light harvesting. Further studies discovered that, LSPR can be also found in transition metal-based catalysts.[27,30] It was reported that the LSPR effect can be employed to optimize the optical absorption maximum in the NIR and mid-infrared regions of non-noble metal oxide based semiconductors.[27,31] As shown in Figure 2.3A-E, through the formation of cations or oxygen vacancies, some non-stoichiometric self-doped semiconductors (e.g. $Cu_{2-x}Se$, $Cu_{2-x}Te$, WO_{3-x}) are identified as attractive LSPR hosts[32–34] and were applied for improving the photocatalytic water oxidation.[35,36] It is also indicated that the plasma resonance frequency can be controlled by modifying the sizes (Figure 2.3D-E) or shapes (Figure 2.3F-H) of LD materials.

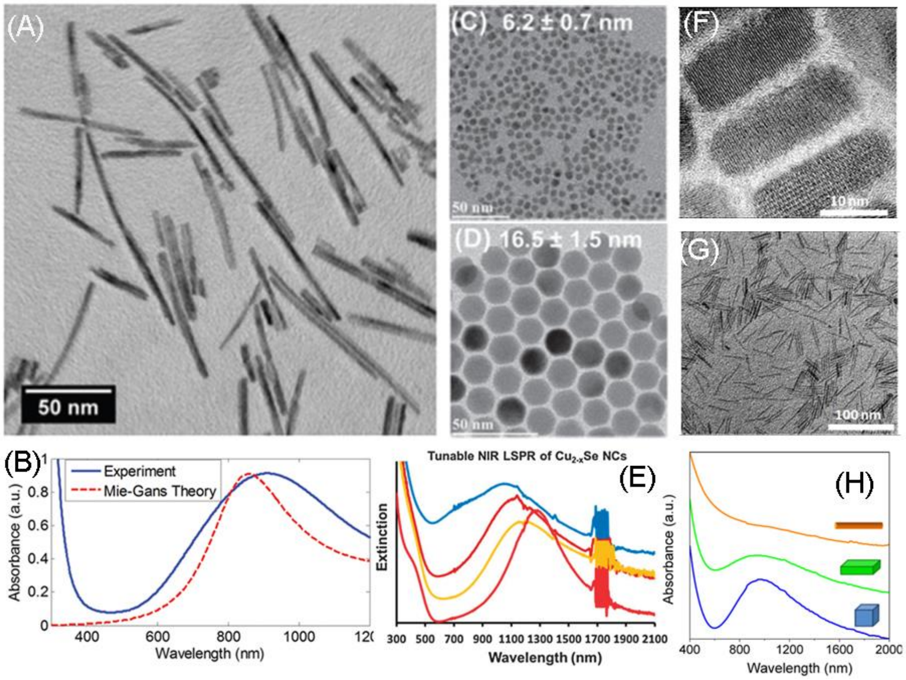

Figure 2.3 A) TEM image of $WO_{2.83}$ nanorods. B) Experimental measurement and theoretical

simulation of LSPR in 1D $WO_{2.83}$ nanorods. Adapted from Manthiram et al.[32] Copyright © 2012 ACS Publications. C, D) representative TEM images and (E) Tunable LSPR of $Cu_{2-x}Se$ NCs with uniform size of 6.2 nm and 16.5 nm. Adapted from Liu et al.[34] Copyright © 2013 Wiley VCH. F) HRTEM of $Cu_{2-x}Te$ nanoplates, G) TEM images of $Cu_{2-x}Te$ nanorods and H) UV/Vis spectra nanoplate and nanorod. Adapted from Li et al.[33] Copyright © 2013 ACS Publications

Surface-Area and Exposed-Facet Enhanced Charge Transfer. As the catalytic reaction occurs on the surface atoms, the surface area to volume ratio of catalysts plays a significant role in heterogeneous catalysis.[17] The large surface area to volume ratio of LD materials is another promising feature of LD semiconductor materials, which makes the most of the catalyst surface atoms where reactions occur. For instance, a catalyst with the size of 100 nm has only around 1% atoms distributed on the surface, whereas this value increases to 10% and 90% for a catalyst of 10 and 1 nm size, respectively.[17] Furthermore, the larger specific surface area can promote the activity, selectivity and faradic efficiency of the catalytic reactions by improving the formation of edges and defects or by preferentially exposing highly active crystal facets. Besides, the more exposed surface atoms also make it easier to regulate LD material properties through elemental doping, surface modification, and defect engineering, and so on.[37] Taking doping as an example, most of the dopants are trapped inside the structure of bulk materials, however, in LD materials, dopants are located close to the surface, acting as active catalytic sites. More importantly, doping can be adopted to adjust the electron density and enhance the light absorption of LD semiconductor materials.

In addition to the above three main superiorities, LD materials also own some other features which can be employed in photochemical energy conversions such as the reduced carrier collection pathways,[22] enhanced light distribution[38] and multiple exciton generations.[39] All these advantages have been intensively studied for water oxidation system. This will be discussed in below sections.

2.2.2 Disadvantages of LD Photocatalysts for Water Oxidation

Although LD materials possess superior photochemical advantages in terms of fast charge transport, excellent light harvesting ability, improved reaction kinetics, and vigorous photocatalytic activity, they have some inherent restrictions that may result in poor durability and diminished power conversion efficiency. This will be described in the following discussion regarding increased surface recombination and decreased thermo-dynamic stability.

For single-component LD materials with sizes lower than certain values, carrier separation is even more difficult than in bulk materials.[22,40] Taking n-type semiconductor as an example, as shown in Figure 2.4, when the diameter of LD materials is lower than twice the value of surface space charge layer width (L_d) of bulk materials, it might be difficult to relax the bands completely to the bulk level. In that case, small LD materials tend to possess a lower potential drop and electric field across the space charge layer, which can elevate the recombination rate of photogenerated charge carriers. Therefore, a suitable size balance needs to be established to maximize the exposured surface active sites while optimize charge separations at the same time. It was suggested that the size should approach twice the value of L_d.[41]

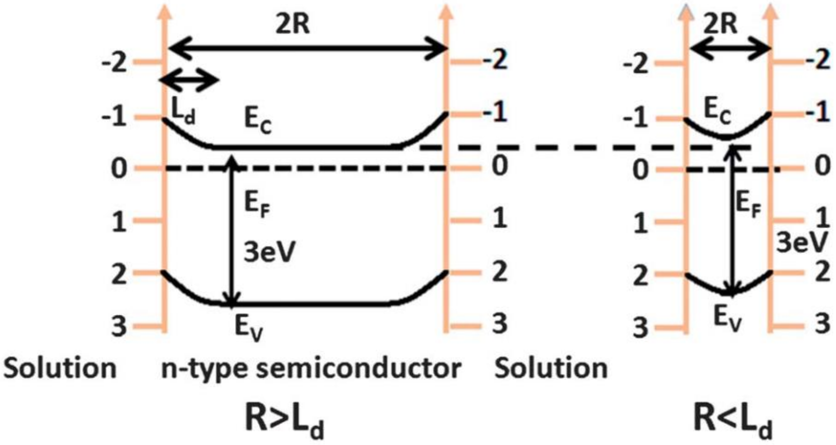

Figure 2.4 Band structure of an n-type semiconductor in solution with different LD sizes. a) R is larger than the space charge width and b) R is smaller than the space charge width. E_V is the valence band edge, E_F is the Fermi level, E_C is the conduction band edge and L_d represents the space charge width. Adapted from Li et al.[41] Copyright © The Royal Society of Chemistry 2014.

Another drawback of LD materials is the declined thermo-dynamic stability along with the increased surface energy. Hopefully, this could be overcome by some tactics such as the rational establishment of heterostructures to protect photoabsorber by facilitating efficient separation of charge carriers and migration of holes to a more stable component. This will be discussed where applicable in the following discussion regarding LD based hybrid materials.

Considering the above advantages and disadvantages of LD materials comprehensively, a series of modification approaches for water oxidation enhancement have been summarized in this chapter, including defect/doping engineering, LSPR, active facet exposure, size control or constructing LD hybrid materials, as described in Figure 2.5. The following sections are divided into 0D, 1D, 2D and LD hybrid semiconductor materials for photocatalytic water oxidation. At last, the mechanism about the unique catalytic properties of 0D, 1D and 2D materials are compared and LD metal-free semiconductors are also described briefly.

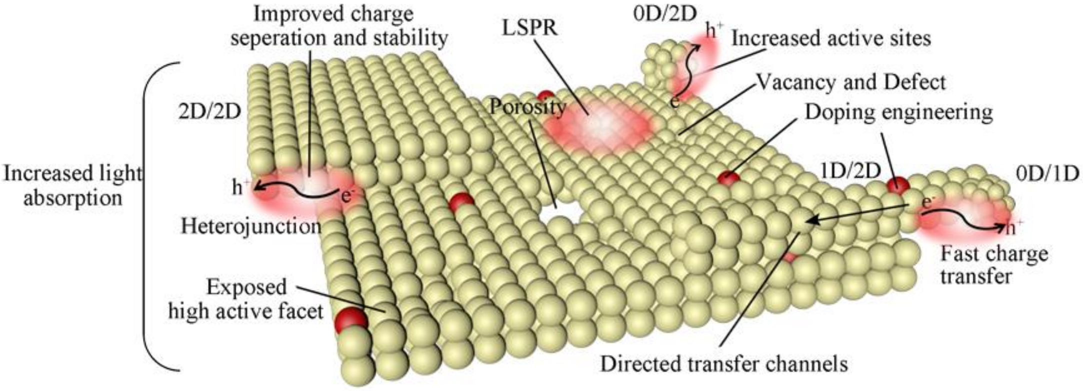

Figure 2.5 The photocatalytic properties of LD materials including light absorption, charge transfer can be improved by doping engineering, active facet exposure, defect or vacancy creation, and LSPR etc. Hybrid LD materials with heterojunction can also be constructed in the form of 0D/1D, 1D/2D, 0D/2D, 2D/2D configurations.

2.3 0D Semiconductor Materials for Photo-Related Water Oxidation

In general, 0D photocatalysts including metal complexes or nanoparticles and metal oxide quantum dots have been intensively investigated. In this part, we summarize common 0D non-noble metal based semiconductors for photocatalytic water oxidation.

2.3.1 0D Metal Complexes and Nanoclusters

In natural photosynthetic systems, water oxidation is catalyzed by a 0D Mn_4CaO_4 cluster, which has stimulated the construction of transition metal clusters and complexes as effective catalysts for solar water oxidation at the 0D molecular level.[42] Spiccia and co-workers had reported that a PEC device prepared by impregnating synthetic tetranuclear-manganese clusters into Nafion matrix, could achieve efficient water oxidation catalysis.[42] Through in situ X-ray absorption spectroscopy and TEM methods, they elucidated that the tetranuclear-manganese cluster could dissociate into Mn (II) compounds in Nafion, which are then reoxidized to form dispersed 0D nanoparticles with a diameter of 1 - 2 nm. The in situ cycling between the photoreduced Mn (II) product and oxidized Mn (III/IV) oxide phase proceeds during water oxidation catalysis, while the original metal clusters serve only as the precursors. The observations of this manganese redox cycling on the electrode bear a striking resemblance to the biogeochemical cycling of manganese in nature and provide us with an understanding of the essence of PEC water oxidation based on metal complexes. Thus, it is conceivable that the catalytic activities observed for many of the molecular metal complexes in homogeneous solutions are based on a similar mechanism. When incorporating these metal complex into various solid supports (such as zeolites, membranes and metal oxide surfaces) for heterogeneous catalysis, metal-oxide particles could be formed and deposited on these supports by metal complex dissociation.

Inspired by this, Nocera’s group reported the electrodeposition of 0D cobalt-phosphonate (Co-Pi) photocatalyst onto a graphite substrate in methyl phosphonate (MePi) electrolyte.[43] In the work, they investigated the nucleation, growth and repair mechanism of the catalyst. The nucleation process of the catalyst was analyzed through chronoamperometry and AFM imaging (Figure 2.6). As shown, the catalyst island was formed, and the surface density can be controlled by adjusting the electrodeposition potential and time. The particle sizes ranged from 35 to 70 nm, accompanied by the catalyst covers increasing from 9% to a saturated 65% on the surface. Through making clear the relationship between catalyst formation and pH values, a mechanistic foundation was also presented on regulation of the 0D nanoparticle-based photoanodes for water oxidation. Some other nanosized catalysts like nickel oxide (NiO_x)[44], and iron(III) oxide[45] were also deposited from molecular complexes, which exhibited promising opportunities as effective photoanodes for wired water oxidation.

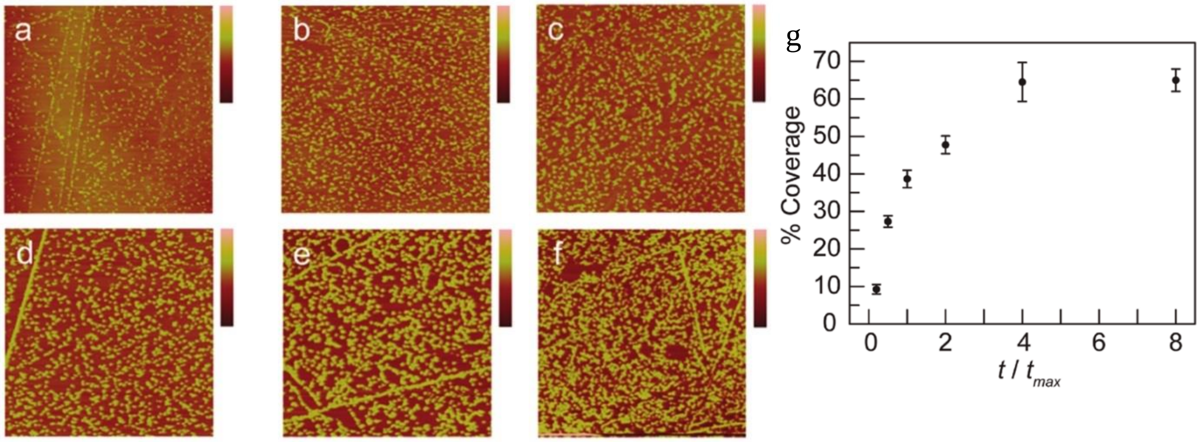

Figure 2.6 AFM images of a highly oriented pyrolytic graphite electrode after being subjected to potential step polarization from 0.75 to 0.97 V for a-f) different deposition time. Bars to the right of each image indicate the depth with full scale values of (a) 20, (b) 30, (c) 50, (d) 75, (e) 75, and (f) 50 nm. g) Coverage percentage of catalyst versus the normalized duration of potential step polarization, t/t_{max}. Adapted from Nocera's group.[43] Copyright © 2012 ACS Publications.

Another model of 0D photocatalysts that have been intensively employed is nanoclusters. In a rather interesting study, Frei and Jiao reported that cobalt or manganese oxide nanoclusters loaded on mesoporous silica (SBA-15) can exhibit effective water oxidation under mild pH conditions.[46,47] The Co_3O_4 and MnO_x nanoclusters on SBA-15 provided large quantities of surface metal sites per projected area, while the mesoporous silica frameworks offered the nanoclusters with high dispersion stability and prevented destruction of surface active sites. Wireless photocatalytic OER by these nanoclusters was performed using $Na_2S_2O_8$ as the electron acceptor. Due to the large geometrical surface area provided by such a nanostructure, increased TOF were obtained, which were over a thousand times higher than that of the bulk-sized counterparts. In the following work, Jiao's group employed various substances, including mesoporous silica KIT-6, SBA-15 and γ-Al_2O_3 nanoparticles to support Co_3O_4 nanoclusters for fabricating a series of WOCs.[48] The results confirmed that a smaller Co_3O_4 cluster size resulted in a higher water oxidation activity. Compared with SBA-15, KIT-6 was found to be a better support, due to its 3D porous structure that offers a more accessible system. More importantly, they concluded that the principal function of these mesoporous skeletons in photocatalytic water oxidation reaction is to physically disperse the Co_3O_4 nanoclusters rather than to participate in the reaction.

2.3.2 Metal Oxides Quantum Dots and Nanocrystals

Comparing with the above in situ formed 0D metal complexes or clusters, the ex situ synthesis allows for better control over surface accessibility and dimensionality of the catalysts such as QDs.[49] Because of the unique optical property, quantum effect and relatively high photostability, semiconductor QDs have emerged as extraordinary 0D photocatalysts. Over the past decades, transition metal-based QDs such as Co_3O_4, Fe_2O_3 had been developed,[50,51] while studies over the applications of these QDs for water splitting just started in recent years. Guo's group first tried to synthesize the Co_3O_4 QDs through a reverse micelle technique and applied them for wireless water oxidation.[52] The QDs exhibited the stable oxygen evolution (0.40 μmol h^{-1}) even in the absence of a sacrificial agent or cocatalyst. Mechanistic studies revealed that the band gap of Co_3O_4 QDs was increased by the quantum confinement effect, and the shifted conduction band minimum was lower than the hydrogen reduction potential. In this case, the QDs were able to realize overall water splitting under visible-light irradiation. Following this success, Wang et al. synthesized α-Fe_2O_3 QDs (3 nm) using the same method and investigated them for wireless visible-light-driven water oxidation.[51] Also, by adding ammonium hydroxide into the benzyl alcohol route, Niederpberger and co-workers successfully synthesized monodisperse Co_3O_4 QDs with sizes of 4.5 nm for excellent visible-light-driven OER performance.[53]

Although some QDs present considerable water oxidation performances, the presence of stabilizing agent, an organic ligand, attached on the surface of QDs during synthesis could inevitably block the accessibility of surface-active centers, and then limit their extensive applications. In addition, the annealing or drying process for removing this ligand, in turn, would affect the dispersion of quantum dots. Fortunately, approaches to increase the dispersibility and to synthesize the ligand-free nanoparticles have been achieved successfully.[49,54,55] Grzelczak, et al.[49] reported the first example of ligand-free Co_3O_4 nanoparticles with tunable sizes for water oxidation (Figure 2.7 a-d). As shown in Figure 2.7

e, at Co_3O_4 particle size of 3 nm, the surface area was elevated seven times higher than that of 40 nm size particles. With the reduced particle sizes, the absorption band edge displayed gradual blue-shift toward lower wavelengths, further revealing the apparent quantum size effect. The Co_3O_4 nanoparticles with an excellent colloidal stability were examined in the wireless photocatalytic system with $Na_2S_2O_8$ as the sacrificial agent and $Ru[bpy]_3^{2+}$ as the photosensitizer. The calculated turnover number (TON) per mole of cobalt gradually raised with reduced particles sizes; from 0.1 (bulk Co_3O_4) to 2.3 (3 nm Co_3O_4). The researchers also anchored the 3 nm Co_3O_4 onto SBA-15 and found that the OER rate was improved evidently, compared with the homogeneous dispersed 3 nm Co_3O_4.

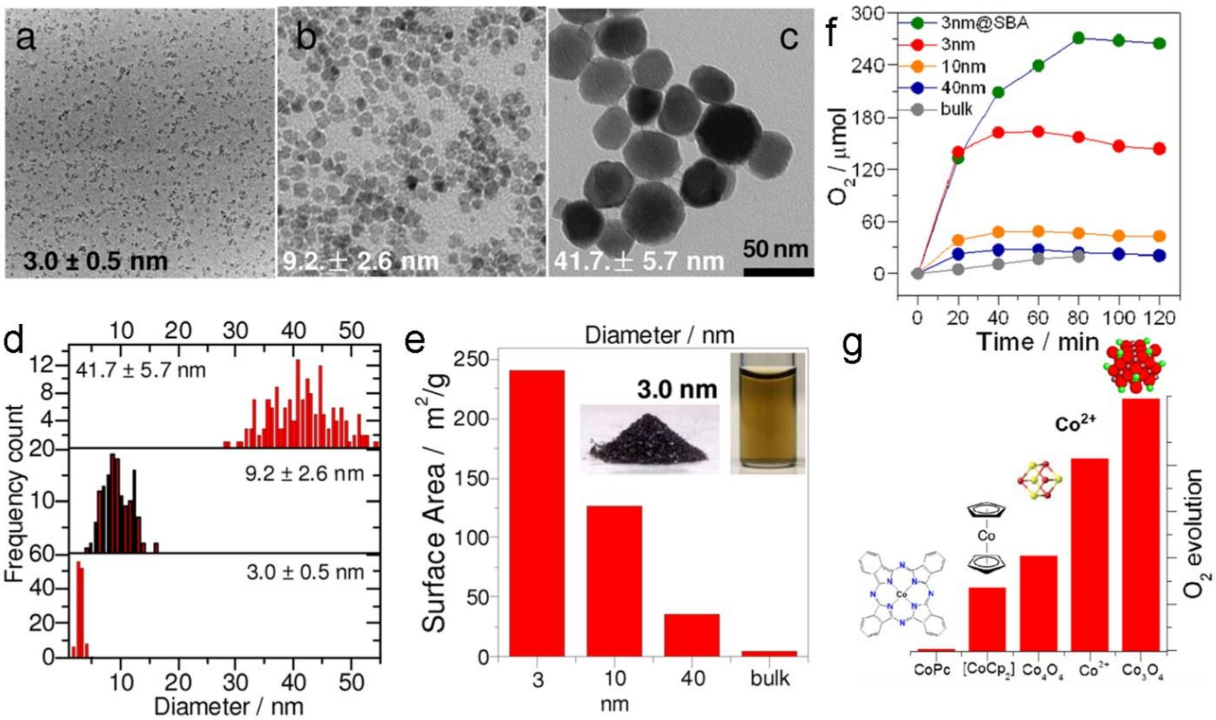

Figure 2.7 Size evolution of the Co_3O_4 nanoparticles. a-c) TEM images of Co_3O_4 with diameters of 3, 10, and 40 nm, respectively and d) corresponding size distributions. e) Plot of particle diameter versus surface area. Inset: NPs in the form of powder or dispersed in water. f) Size-dependent oxygen evolution in aqueous suspension of Co_3O_4 NPs using a $Ru(bpy)_3^{2+}$ visible light sensitization system (λ>450 nm). g) Visible light-induced oxygen evolution from a variety of cobalt compounds deposited on SBA-15.[49] Copyright © 2013 ACS Publications.

Later, Blakemore et al.[56] reported a pulsed laser ablation method to obtain surfactant-free, quantum-confined Co_3O_4 nanoparticles (< 5 nm) with an excellent wired water oxidation activity. The nanoparticles produced by this technique can also be instantly deposited onto the photoanodes for PEC water oxidation. Interestingly, the Co_3O_4 nanoparticle suspensions prepared in this work showed yellow color, which is completely different from that of bulk Co_3O_4 (black). This optical spectroscopic property adds evidence for quantum confinement. Judging from the increase in direct and indirect band gaps as a function of the reciprocal squared particle diameter, this work precisely deduced that the maximum diameter to achieve quantum confinement effects of Co_3O_4 would be 5 nm. This work gives us an idea to rigorously control the experimental condition to employ the quantum confinement effects for water oxidation.

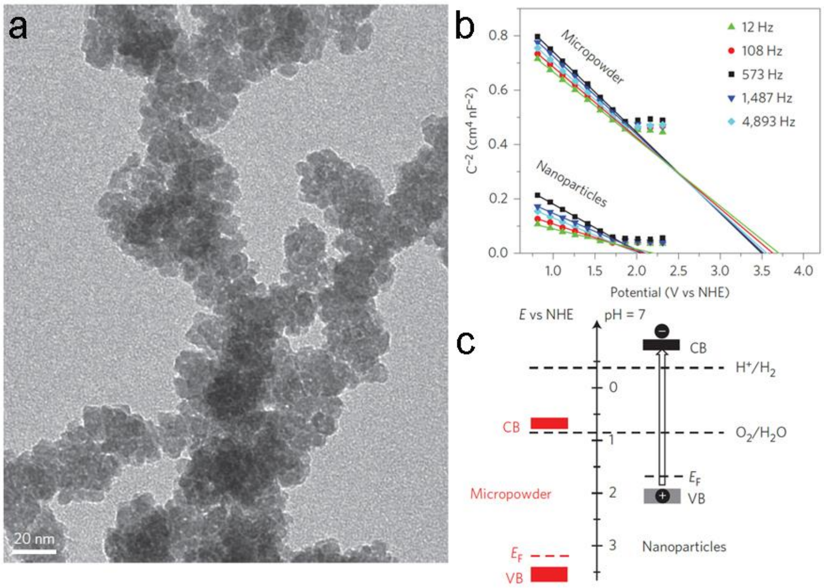

Figure 2.8 (a) TEM image of CoO nanoparticles; b) Mott-Schottky plots for CoO nanocrystals and micropowders according to impedance measurements. The flat-band potentials are obtained from the intercepts of the extrapolated lines. c) Band positions of CoO nanocrystals and micropowders according to the bandgaps and flat-band potentials.[57] Copyright © 2014 Macmillan Publishers Limited.

The above prediction about the quantum confinement of cobalt oxides can be partly supported by a recent work from Liao et al..[57] In this work, CoO nanocrystals were employed as a photocatalyst to split water into oxygen and hydrogen under visible-light irradiations in the absence of sacrificial reagents. Through diffuse reflectance spectroscopy, they determined that the band gaps of both CoO nanocrystals and bulk counterpart were very close to 2.6 eV. They further concluded that the comparatively large size of CoO nanoparticles (5 - 8 nm, as shown in Figure 2.8 a) led to the loss of the quantum-confinement effect. However, Mott-Schottky plots confirmed that the nanoscale morphology could considerably alter the band-edge positions of a semiconductor, in spite of the absence of quantum-confinement effect (Figure 2.8 b and c). In this case, the researchers assumed that it is the band-edge position rather than the band gap resulted in the more excellent wireless photocatalytic performance of CoO than their bulk counterparts.

Some other semiconductor nanoparticles like CoSe,[58] α-Fe_2O_3[59], and $BiVO_4$,[60] were also employed as photocatalytic water oxidation catalysts. For example, Osterloh's group first investigated the photocatalytic water oxidation using freely dispersed α-Fe_2O_3 nanocrystals.[59] In this work, hematite with different sizes including 5.4 nm α-Fe_2O_3 nanoparticles, 44 nm ultrasonicated bulk-α-Fe_2O_3 and 120 nm bulk-type-α-Fe_2O_3 were achieved by hydrolysis of $FeCl_3 \cdot 6H_2O$. Beneficial to the decreased diffusion path of photogenerated holes, the suspended crystals of α-Fe_2O_3 showed a robust photocatalytic performance under irradiations with initial O_2 evolution rates of up to 1072 μmol $h^{-1}g^{-1}$ in the presence of $AgNO_3$.

2.4 1D Semiconductor Materials for Photo-Related Water Oxidation

Since carbon nanotubes (CNTs) were discovered by Lijima et al. in 1991,[61] extensive interests have been activated in studying 1D nanomaterials including nanowires, nanorods and nanotubes. Substantial breakthroughs have been achieved in applying 1D materials in various fields of modern techniques, for example, photocatalytic water splitting system. By preferential exposure of selected facets, 1D photocatalysts possess several advantages, for example, high accessible surface area and directed transfer channels,[7] endowing them with a better ability for transfer of (photo)generated charges away from potential recombination sites. Attributed to their linear morphologies, 1D semiconductors are more widely applied in wired water oxidation than wireless one. Therefore, in this section, we mainly investigate the implementation of 1D nanomaterials for PEC water oxidation.

2.4.1 Application of 1D Semiconductors in Wireless Systems

1D nanostructured semiconductors in the form of nanowires, nanorods or nanotubes have been broadly reported. Xie's group first fabricated novel quantum tubes of $BiVO_4$, which had ultra-narrow diameters (of about 5 nm) and ultrathin wall thicknesses (down to 1 nm). A well-defined visible-light response was observed on the resulting high-quality $BiVO_4$, revealing the evident superiority of quantum-sized nanotubes compared with bulk materials.[62] Inspired by this study, $BiVO_4$ quantum tubes were utilized as excellent photocatalysts for solar-light water oxidation.[62–64] Interestingly, Sun et al.[64] reported that the quantum-sized $BiVO_4$ can simultaneously split pure water into O_2 and H_2 under simulated solar light irradiations without loading any cocatalysts or adding any sacrificial reagents. Electrochemical tests indicated that quantum confinement effect results in the negative shift of conduction band edge (E_{cb}) and reduces water oxidation overpotentials, resulting in a significant photocatalytic activity. These findings provided new insights to enhancing water splitting performance by controlling the sizes of photocatalysts.

2.4.2 Application of 1D Semiconductors in Wired Systems

Electrons tend to migrate randomly and interact with scattering sites easily on 0D, 2D or 3D semiconductor materials, bringing about a high possibility of charge recombination.[22] Distinctly, the confined conductive channels of 1D semiconductors[24] can direct electrons to transfer along the 1D diffusion channel to external circuit, and thus reduce electron-hole recombination to a great extent. Taking advantage of this attribute, 1D nanowires/nanorods/or nanotubes were usually in-situ grown onto the conductive substrate for facile electron collection and potentially enhanced PEC application. Among all the semiconductors, 1D TiO_2 nanostructures are most thoroughly studied.[65,66] For example, Zheng's group found that the photocurrent density in PEC test increased steadily when the morphologies were changed from particles to rods and to branched rods, mainly because of the facilitated electron transfer to the back-contact and promoted transport of holes to the semiconductor-electrolyte interface.[67] Grimes et al. conducted a systematic study on developing 1D TiO_2 nanotubes for photocleavage of water.[65] Through a facile anodization process, ordered TiO_2 nanotubes arrays were grown on Ti foils, which exhibited power conversion efficiencies up to 6.8%

under UV-light illumination (k = 320 ~ 400 nm),[66] and the efficiency was further enhanced to 16.25% in their later work.[68]

As mentioned above, once the sizes of LD semiconductors are below certain nanometer scale, the band gap will begin to increase, known as the quantum-size effects. To meet this demand, Serpone et al. reported that the exciton radius (r_{ex}) of TiO_2 should be in the range of 0.35 - 1.9 nm.[69] In a density functional theory (DFT) study by Iacomino et al., r_{ex} was calculated to be at least 1.5 nm.[70] Specifically, compared to the bulk value, the blue shift of nanowires grown along the [001] direction can vary from 0.18 to 0.67 eV, depending on the size variations. Therefore, the quantum confinement can be adopted as an effective approach to improve the photocatalytic water oxidation capability and many studies have been performed on TiO_2 inspired by this. Recently, John et al. prepared single-crystal-like TiO_2 nanotubes with the [001] orientation direction with a better electronic transport property.[71]

Although TiO_2 performs well in UV region, it hardly has absorption for visible-light that represents the most abundant part of the solar light energy, making it a poor choice for applications. Some attempts have been made to modify the band gap of TiO_2 including nitrogen incorporation, which can upshift the valence band edge of TiO_2 by hybridizing substitutional N 2p with O 2p states, while the conduction band edge can be almost remaind unchanged.[72] By a nitridation treatment, Hoang et al. presented N-modified TiO_2 nanowire arrays with a narrowed band gap as visible-light-active PEC anodes with typical dimension of ~5 nm and a length up to 4.4 μm, as displayed in Figures 2.9a and b.[73] It was noted that the N-modified TiO_2 nanowires exhibited higher absorption under visible-light irradiations (Figure 2.9c), but they had a lower incident photon to current conversion efficiency (IPCE) under full-spectrum illumination than unmodified TiO_2 samples (Figure 2.9d). Notably, by loading a cobalt cocatalyst onto the N-modified TiO_2, the efficiencies increased evidently with a higher substitutional N concentration, which were higher than unmodified TiO_2 in both visible-light and UV regions.

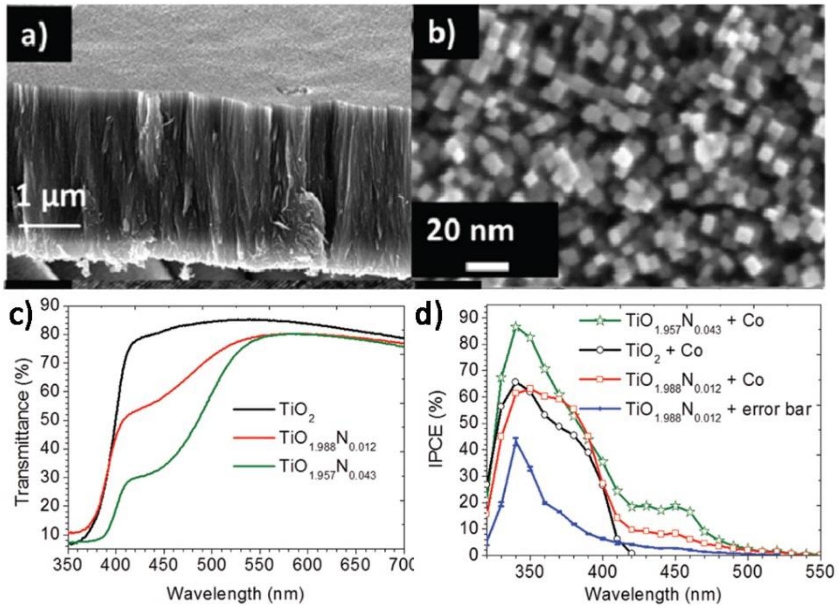

Figure 2.9 a, b) SEM images of TiO_2 nanowire arrays on FTO glass. c) UV-vis transmittance spectra of unmodified and N-modified TiO_2 nanowire samples, and an as-synthesized sample (black curve) was included as a reference; d) IPCE spectra of N-modified TiO_2 films at 1.4 V RHE.[73] Copyright © 2012 ACS publications.

For stronger visible-light absorption, semiconductors with intrinsic narrow band gaps (E_g) like hematite (α-Fe_2O_3, E_g = 2.0 - 2.2 eV), WO_3 (E_g = 2.5 - 2.8 eV) or $BiVO_4$ (2.4 eV) are especially attractive in spite of their respective challenges. Additionally, ZnO with an electron mobility rate of 10-100 times higher than that of TiO_2 is another common 1D nanostructured candidate. Through resonant inelastic X-ray scattering (RIXS) analysis, Vayssieres et al. discovered a substantial band gap (and mostly the conduction band edge) increase (0.3 - 0.6 eV) on oriented ultrafine α-Fe_2O_3 nanowire arrays because of the 1D quantum confinement effect.[68] The upward increase of the conduction band edge makes α-Fe_2O_3 an ideal PEC water oxidation anode material. By an anodization route, Mohapatra et al.[26] prepared ultrathin and self-standing Fe_2O_3 nanotube arrays (with nanowall thicknesses of 5 - 6 nm) on Fe foil, which obtained a much higher oxidation photocurrent density (1.4 mA/cm^2) than Fe_2O_3 nanoparticles (0.004 mA/cm^2). Interestingly, once Fe_2O_3 nanotubes were shaved off from the Fe foil and recoated by dipping, the activity decreased drastically (145 μA/cm^2). This means that the vertically oriented 1D nanotubes possess the optimum geometrical channel arrangement for more excellent light absorption and charge transport. Zheng's group synthesized a $WO_3/BiVO_4$ core/shell nanowire photoanode where $BiVO_4$ served as the principal light-harvester while WO_3 was an electron conductor.[74] This photoanode finally created an astonishing oxidation photocurrent of 3.1 mA/cm^2 at 1.23 V (vs RHE) upon simulated solar light illumination, accompanied by a photon-to-current conversion efficiency of ~60% at 300-450 nm.

2.5 2D Semiconductor Materials for Photo-Related Water Oxidation

2D nanosheets or nanolayered materials have been explored in a wider range of photocatalysis than 0D or 1D materials, because of their ultrahigh specific surface area, unique physical, optical and chemical properties.[75–77] However, as mentioned above, a main drawback of 2D semiconductors is the high recombination rate caused by randomly migrated electrons and larger specific interfacial areas. This can be mitigated by suitable control over the morphology, thickness, surface defects and the vacancies. In this section, representative 2D materials including metal oxide nanosheets, layered double hydroxide nanosheets (LDH), metal-based chalcogenides and oxyhalides, for photocatalytic water oxidation are summarized to better explore key approaches to enhance the photocatalytic performance of 2D materials.

2.5.1 2D Metal Oxide Nanosheets for Photocatalytic Water Oxidation

Discoveries on the optoelectronic properties of 2D metal oxide nanosheets can be traced back to 1990s.[77,78] In an earlier example, Sasaki and co-workers conducted the exfoliation of layered titanates and acquired $Ti_{0.91}O_2$ nanosheets at 0.93 nm thickness, which astonishingly showed a semiconducting activity similar to bulk TiO_2 anatase. Specifically, $Ti_{0.91}O_2$ nanosheets exhibited a sharp photoabsorption peak at 265 nm (4.77 eV), revealing their larger band gap energy than bulk TiO_2.[79] Since then, the photoelectrochemical properties of various 2D metal oxides have been extensively studied. Here we focus on recent advances on modification and application of these 2D materials for photocatalytic water oxidation.

Tailoring exposed crystal facets is a conventional strategy for optimizing the heterogeneous reactivity of 2D materials, which is closely related to the bonding environment and surface atomic configuration. Recent studies revealed that nanosheets exposed with the (001) facets show better catalytic activities than that with the other facet exposures due to the highest oxygen atom density.[3] Taking TiO_2 as an example, it was reported that the formation energies were 0.90, 0.53 and 0.44 J m^{-2} for the (001), (100) and (101) facets, respectively.[80] The super high Ti–O–Ti bond angles and coordinatively unsaturated O, Ti atoms on the (001) endow the facets with the highest surface energy. Using a modified hydrothermal strategy, Li and co-workers reported anatase TiO_2 nanosheets with ultrathin thicknesses (1.6-2.7 nm) and a high percentage of reactive (001) facet exposure (82%).[25] Attributed to these features, the resulting products showed a high UV-vis light-driven water splitting performance. Another typical 2D semiconductor whose catalytic activity is relevant to exposed facets is WO_3. Waller et al. investigated WO_3 nanosheets (0.75 nm thick) with the exposed {001} facets obtained by $Bi_2W_2O_9$ exfoliation for wireless photochemical water oxidation.[81] It is worth noting that this work also discovered the extended band gap of nano-WO_3 by quantum confinement, providing the designing opportunities of thickness-dependent 2D semiconductors for adjustable band edge positions and band gap energies.

Defect and vacancy engineering also play a vital role in enhancing the water oxidation performance of 2D materials.[35] On one hand, grain boundaries, surface defects, and bulk defects in the 2D materials are generally considered as the electron/hole trapping sites and recombination centers. On the other hand, proper introduction of defects to semiconductors such as by doping with foreign elements or via creating oxygen vacancies, can improve the electrical conductivity significantly. It is worth noting that oxygen vacancies have more important implications on 2D nanosheets than on bulk materials, due to the localized surface plasmon resonance (LSPR). In 2015, Gong and co-workers synthesized WO_3 nanosheets rich of surface oxygen vacancies for solar-driven water oxidation.[35] In this study, layered tungstic acid was first exfoliated to WO_3 nanosheets, followed by a vacuum or hydrogen treatment to introduce oxygen vacancies and surface disorder of oxides (Figure 2.10 a-c). As obtained from UV-vis-NIR spectra, the LSPR absorption peaks were observed at the near-infrared region for WO_{3-x}-VT (≈1520 nm) and WO_{3-x}–HT (≈ 1450 nm). As demonstrated in Figure 2.10 d, three different channels were theoretically proposed for solar light harvesting: (1) electrons activated from the valence band maximum to the conduction band minimum; (2)

electrons generated from the valence band maximum to oxygen vacancies under conduction band; and (3) electrons activated by LSPR. The created oxygen vacancies caused surface plasmon resonance of WO_3, which not only resulted in enhanced photocatalytic activity in the ultraviolet and visible region, but also induced light harvesting in the near-infrared region through LSPR. Consequently, the as-prepared substoichiometric WO_3 nanosheets exhibited a drastically enhanced photocurrent response in wired photocatalytic water oxidation under full-spectrum (300 - 2000 nm) light irradiations.

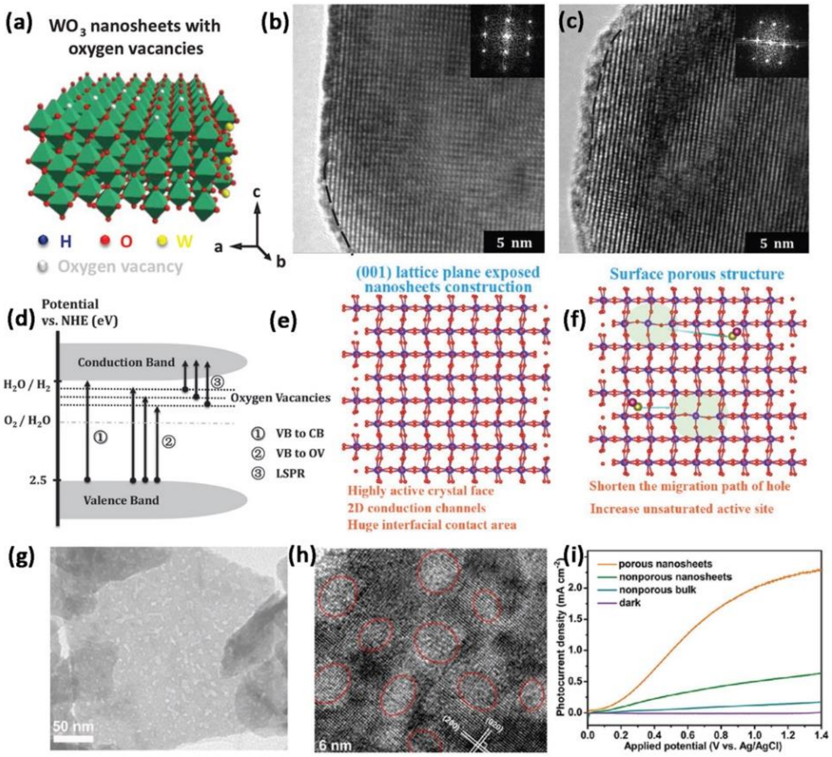

Figure 2.10 a) Tungsten oxide single crystal nanosheets; b, c) HRTEM images of WO_3, WO_{3-x}-VT, and WO_{3-x}-HT nanosheets; d) band level arrangements of tungsten oxide nanosheets with oxygen vacancies.[35] Copyright © 2015 WILEY-VCH. e, f) Schematic illustration of (001) facet structure and g) TEM and h) HRTEM images of pore-rich WO_3 ultrathin nanosheets; (i) The photocurrent versus applied potential curves of pore-rich WO_3 ultrathin nanosheets and the counterparts.[3] Copyright © 2016 WILEY-VCH.

Another noteworthy example is the pore-rich ultrathin WO_3 nanosheets exposed with active (001) crystal facets for wired PEC measurement, derived from the high-temperature topological transformation of $WO_3 \cdot 2H_2O$ (Figure 2.10 e-i)[3] The longish migration of photogenerated holes along the W–O–W chains in the x-direction of the (001) facets makes it inevitable for numerous carriers recombination. Notably, the abundant pores on the nanosheet surfaces can effectively shorten the migration distance of holes, making it conducive to form O_2 on the WO_3 surface. The synergy effect of peculiar atomic arrangement and electron configuration on the pore-rich WO_3 ultrathin nanosheets was verified, realizing the optimization of multilimiting factors during water oxidation including charge carrier generation and migration. Finally, a high photocurrent density of 2.14 mA cm^{-2} was observed on pore-rich WO_3 nanosheets, which was 18 times higher than that of the bulk counterpart. There are also tremendous reports on other metal-oxide-based photocatalysts (e.g. Fe_2O_3,[4,82] Cu_2O[83]) with ultrathin 2D structure for outstanding photocatalytic water oxidation applications.

2.5.2 Layered Double Hydroxides (LDHs) Nanosheets for Photocatalytic Water Oxidation

LDHs refer to a class of 2D ionic compounds composed of balanced anions and solvation molecules intercalated inside the positively brucite-like layers. Since Garcia et al. first proposed that LDHs can act as band-gap-controllable semiconductors for splitting water into oxygen,[84] a series of Zn/Ti, Zn/Ce, and Zn/Cr LDHs have been synthesized and applied for the visible-light-driven wireless photocatalytic OER. The most active Zn/Cr LDH nanosheets showed an impressive quantum yield up to 60.9% at 410 nm for O_2 generation, which was one of the highest values ever reported for the visible light water oxidation at that time. Kim et al.[85] synthesized Co–Fe LDH photocatalysts with different Co–Fe ratios, and the sample with the highest Fe content exhibited the highest efficiency for visible light water oxidation. It was indicated that Co–O–Fe bridges existed in the LDH structure can effectively suppress the electron-hole recombination, which was responsible for the high photocatalytic efficiency.

The catalytic activity of LDHs can be readily tuned by adjusting the interlayer distance through the balanced anions of different ionic diameters. It has been proven that a larger interlayer spacing will lead to a higher OER activity, possibly attributable to the increased active sites exposure and the enhanced exchange of the intercalated reactive anions.

Exfoliating LDHs to several layers and even to monolayer is an attractive approach to shorten the charge diffusion path and increase the active electrical surface area (ECSA). As such, nanosized LDHs have received much attention. Lee et al.[86,87] prepared a series of nanosized Ti-embedded LDHs for excellent wireless water oxidation. The abundant surface Ti^{3+}−O defects served as the trapping sites to improve charge separation, while TiO_6 octahedra confined within the 2D matrix can suppress the charge carrier recombination under visible light irradiations. Distinctly, the high-surface-area Ni/Ti-LDH with absorption bands in blue and red light regions, exhibited a higher O_2 evolution rate than that of the Cu/Ti-LDH by the visible light wireless reaction.

During the synthesis process of ultrathin LDHs, a certain amount of surface atoms tend to be easily removed or lost, creating local structural distortions and vacancy defects, which will exert important impacts on the photochemical activity of LDH nanomaterials. To gain a deeper understanding into the types of defects and corresponding effect, extensive works have been conducted.[86] In an earlier example, Zhao et al.[88,89] synthesized ultrathin Ti^{3+}-containing LDH layers (thickness of about 2.0 nm) incorporated with M^{2+} cations (e.g. Ni^{2+} or Zn^{2+}) through a reverse microemulsion method. The detection of Ti^{3+} species in NiTi-LDH nanosheets indicated the presence of oxygen defects, which affected the electronic properties and facilitated efficient separation of electron-hole pairs. DFT calculations revealed that the electronic structure was modified and the band gap energy was reduced to boost stronger light absorption. As a result, the NiTi-LDH displayed a super high photocatalytic oxygen evolution activity (2148 μmol g^{-1} h^{-1}) with a quantum yield of 65.0% at 400 nm, which is one of the most effective OER efficiencies to date.

2.5.3 Metal-Based Chalcogenides (Sulfides and Selenides) and Oxyhalide Semiconductors for Photocatalytic Water Oxidation

2D chalcogenides (sulfides and selenides, like $CoSe_2$, SnS) have also been widely investigated as promising alternatives for OER.[90,91] Transition-metal-based selenides generally display excellent water oxidation performances, but they suffer from the photo-instability as they can be oxidized easily under harsh condition. Some studies pointed that both stability and activity can be improved by control of thickness which induces changes of atomic arrangement within 2D nanosheets. For instance, single freestanding layer of ZnSe was controllably synthesized by ultrasonic exfoliation of a lamellar hybrid intermediate (Zn_2Se_2)(n-propylamine), as shown in Figures 2.11 a and b.[92] Through X-ray absorption fine structure spectroscopy (XAFS) measurements, the electronic structures and local atomic arrangements of the derived ZnSe can be precisely probed (Figure 2.11 c). Remarkably, the four-atomic thicknesses of ZnSe nanosheets enabled more than 50% atoms to be exposed on the surface. It was indicated that a remarkable variation in local atomic arrangement was observed as the thickness of ZnSe layers was reduced to the atomic level. Surface distortion occurred within the single layer, which would undoubtedly decrease the surface energy and improve the stability of ZnSe. Benefited from the unique chemical and electronic structures, four-atomic-thick ZnSe single layer exhibited enhanced light absorption, reduced charge transfer resistance, elevated charge separation efficiency, increased photostability and solar water splitting efficiency in wired PEC tests.

As a new class of 2D materials, it is facile to obtain single or few-layer structures in bismuth oxyhalide (BiOX, X = Cl, Br, I). BiOCl nanolayer with atomically thin thickness and the (001) exposed facets was firstly developed by Liu and co-workers.[93] DFT calculations revealed that the (001) facets showed lower valence band (VB) and conduction band (CB) positions than the (110) facets in BiOCl. This means that, under light irradiations, photogenerated electrons tend to accumulate on the (001) facets while holes are inclined to migrate along the (110) facets, as depicted in Figure 2.11 d. It was also discovered that defects created in basal planes of 2D BiOCl lowered CB edge while VB edge remained unchanged. As shown in Figures 2.11 e and f, the defects in BiOCl nanosheet could promote more efficient charge separations while they had little effect on the oxidizing ability of photo-induced holes. Under the synergetic function of quantum-size effect and defect-triggered properties, defect-rich BiOCl exhibited dramatically enhanced wireless photocatalytic OER activity (with OER rate of 56.85 mmol g^{-1} h^{-1} in $AgNO_3$ solution (Figure 2.11 g), which was approximately 3 and 8 times higher than that of 2D BiOCl and bulk BiOCl, respectively.

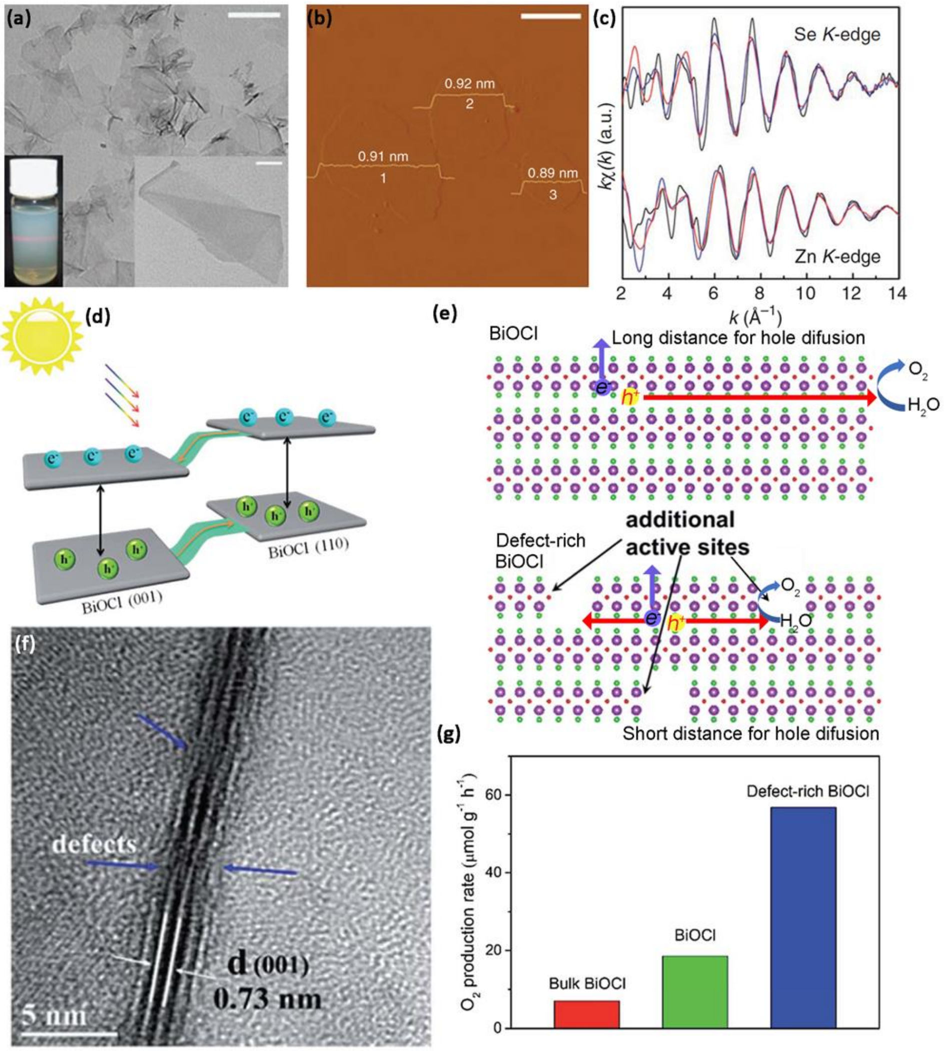

Figure 2.11 a) TEM images and the corresponding colloidal ethanol dispersion displaying Tyndall effect; b) Atomic force microscopic image with an average thickness of 0.91 nm, scale bar, 500 nm; c) Zn and Se K-edge extended XAFS oscillation function kχ(k).[92] Copyright © 2012 Macmillan Publishers Limited. d) TEM images of the defect-rich BiOCl ultrathin nanosheets; e) schematic description of the separation and transfer of photogenerated charges in the BiOCl and defect-rich BiOCl material; f) a schematic diagram illustrating the charge migration between (001) and (110) facets; g) photocatalytic OER for BiOCl and defect-rich BiOCl.[93] Copyright © The Royal Society of Chemistry 2017.

2.6 LD Semiconductor-Based Hybrids for Photo-Related Water Oxidation

As mentioned above, due to fast recombination rate of photogenerated holes, pristine photocatalysts generally show limited photocatalytic activities. [94,95] Here we summarized possible modification methods to tackle this problem. Apart from structural adjustment, synthesizing low-dimensional hybrid materials is another appealing approach, which allows the construction of cascading heterojunctions with atomically sharp interfaces to promote charge dissociation. The sensible screening of LD materials with various dimensionalities for building p–n junctions in the hybrids can further accelerate charge-carrier transport. In this section, we will focus on the synergistic effect caused by the LD hybrids for photochemical water oxidation.

2.6.1 1D-Based (0D/1D, 1D/1D and 2D/1D) Semiconductor Hybrids for Enhanced Photo Water Oxidation

As mentioned above, 1D nanoarray structure is mostly applied in a wired PEC system, as it offers a vectorial and confined channel for transmit of photogenerated electrons to the conductive substrate and external circuit, thereby separating the electron and hole efficiently. In contrast, the electron transport on 0D or 1D nanostructures is relatively slow since the electrons are scattered or trapped at grain boundaries. However, the variety of 1D semiconductors are limited and their photocatalytic activities are sometimes low with a smaller number of active sites. A suitable hybridization of 1D with 0D or 2D nanostructures can solve their respective drawbacks and realize material optimization. On one hand, 1D channels can serve as excellent supports for 0D and 2D semiconductors. Furthermore, appropriate 0D or 2D nanostructure can act as OER cocatalysts to reduce reaction barriers for 1D photocatalysts. Heterojunctions can be built among 1D/0D or 1D/2D photocatalysts, which further enhance the separation and transport of charge carriers.

Taking 1D TiO_2 for instance, several groups have prepared TiO_2-based 0D/1D hybrids that exhibited higher wired OER efficiencies in visible light.[94,96,97] For instance, Maeda et al.[96] discovered that rutile TiO_2 nanorods decorated with 0D $Co(OH)_2$ nanoclusters (about 2 nm) were able to oxidize water into O_2 under visible-light with wavelengths up to 850 nm (Figure 2.12 a-c), which is the longest wavelength ever reported for heterogeneous photo water oxidation. It is worth noting that $Co(OH)_2$ nanoclusters could not only function as a catalyst for water oxidation, but also as visible-light absorbers, as presented in Figure 2.12 d.

Pioneering work related to coupling of 0D CdX (X = S, Se, Te) QDs with 1D semiconductor nanoarrays like TiO_2,[2,98] ZnO[99,100] have been presented recently. As a typical example, Chen et al.[2] proved a well-built photodevice on the basis of ZnO nanowire photosensitization with CdTe QDs through a simple impregnation approach. The achievement of significantly enhanced anodic photocurrent and stability confirmed the positive impact of such a structure in elevating the performance of overall water-splitting reaction. The resulting photoconversion efficiency (1.83%) of the hybrid was over 200% higher than that of unmodified ZnO nanowires. In another study, a series of QDs including FeOOH, ZnO and WO_3 were synthesized and loaded onto ZnO nanorods for an excellent PEC application.[101] Apart from the binary system, other 0D/1D hybrid materials containing ternary LD semiconductors were reported. Cao et al.[102] tested ZnO nanoarrays sensitized with $ZnFe_2O_4$ and CdS QDs. With the extra loading of $ZnFe_2O_4$ QDs on CdS/ZnO photoanode, improved PEC performances with a high stability were achieved. This can be attributed to the stair-like type-II band alignment and the heterojunction construction among the ZnO, $ZnFe_2O_4$ and CdS in the derived photoanode. Furthermore, $ZnFe_2O_4$ served as a hole receptor for CdS and the stability of the photoanode was improved, due to the reduced photocorrosion of CdS by photoinduced holes.

Regarding the design of 2D/1D and 1D/1D photocatalyst hybrids, 2D nanosheets or 1D nanorods can either grow vertically or wrap around the surface of 1D materials. Various 2D LDH nanosheets have been directly grown on semiconductor supports (e.g. 1D TiO_2 or ZnO nanoarrays) for PEC applications. For instance, using an electrodeposition method, NiFe LDH nanosheet were grown on rGO modified TiO_2 nanorod arrays by Ning et al.[103] Ni-Fe LDH nanosheets can accelerate the transport of photogenerated holes and improve water oxidation kinetics of TiO_2 because of its high electrocatalytic activity. In another example, Shao et al. reported a well-aligned 1D ZnO nanoarray core wrapped by 2D CoNi-LDH shells, which displayed a significantly improved photocurrent density and stability in wired water splitting (Figure 2.12 e, f).[103] This configuration can be readily extended to core-shell TiO_2 @LDH or Co_3O_4@LDH arrays with attractive physiochemical properties.

Representative structures for 1D/1D hybrids mainly include a combination of nanobundles or branched nanorods. For example, Wang et al. fabricated WO_2-WO_3 hybrid nanorods to show a highly active visible-light-driven photocatalytic water oxidation activity.[30] The platinum-like property of metallic WO_2 caused LSPR, which extended the visible-light absorption to near infrared region (NIR) and facilitated the charge-carrier separation on WO_3. As a result, the photocatalytic oxygen evolution rates reached approximately 220 ($\lambda = 700$ nm) and 200 ($\lambda = 800$ nm) mmol g^{-1} h^{-1}.

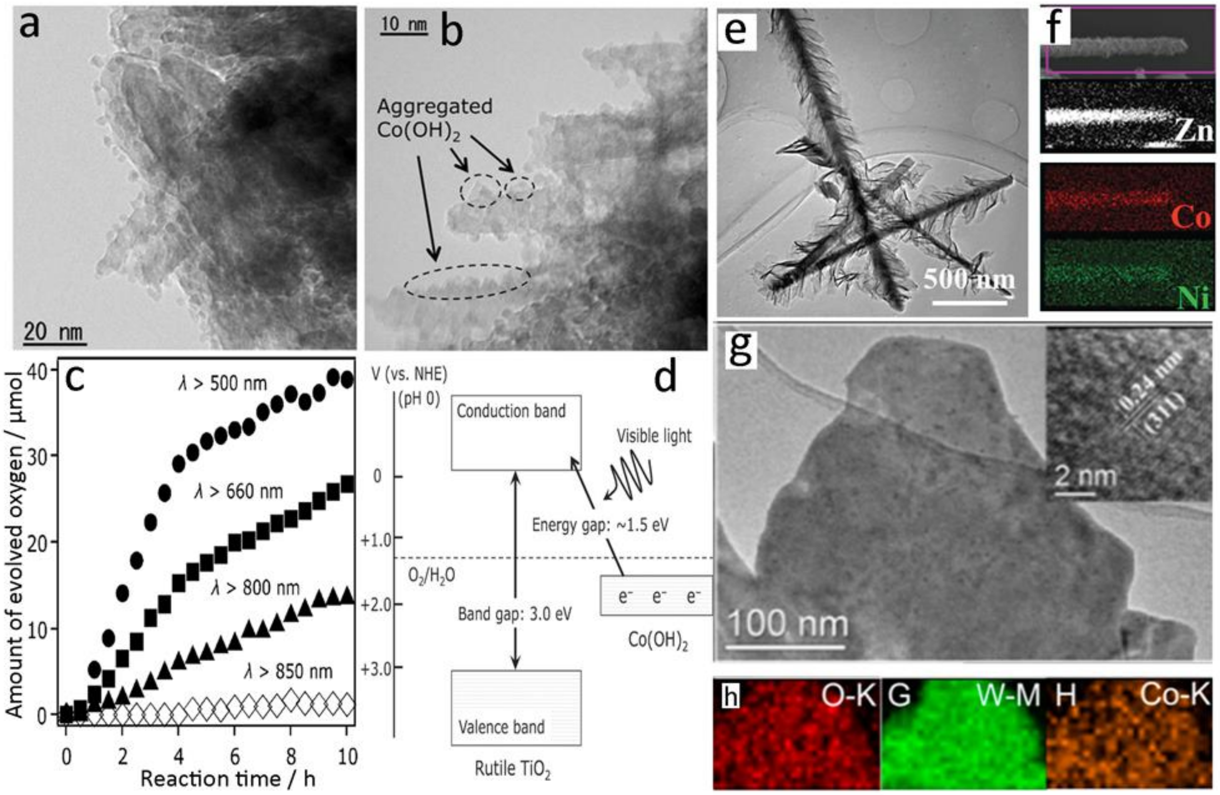

Figure 2.12 a, b) TEM images, c) Time dependence of the O_2 evolution and d) Proposed energy diagram for $Co(OH)_2/TiO_2$.[96] Copyright © 2016 Wiley-VCH. e, f) TEM image and EDS mapping of ZnO@LDH core-shell NWs.[103] Copyright © 2013 WILEY-VCH. g, h) TEM image and EDS mapping of CoO_x/WO_3 (Inset photomicrograph shows a HRTEM of CoO_x).[104] Copyright © 2017 ACS Publications.

2.6.2 2D-Based (0D/2D, 2D/2D) Semiconductor Hybrids for Enhanced Photo Water Oxidation

Similar to QDs sensitized 1D nanoarrays, QDs can also be combined with 2D nanosheets for excellent photo water oxidation, where the electron conductivity is enhanced and the interfacial charge transfer is boosted. Tang et al.[105] reported the in-situ growth of 0D CdTe QDs onto 2D Co-based LDH nanosheets, which were adopted to improve the PEC performance of $BiVO_4$ photoanode. It was claimed that the energy levels of this 0D/2D hybrid corresponded to Type-II band alignment, which could efficiently boost photoinduced charge separation under illumination. 0D/2D structure, loading 0D CoO_x nanoparticles onto WO_3 nanoflake arrays were also reported,[104] using a hydrothermal method, as shown in Figures 2.12 g, h. Consequently, the efficiency of charge separation and charge injection, as well as the PEC water oxidation selectivity of WO_3 were elevated simultaneously by building CoO_x/WO_3 p-n heterojunctions.

Compared to heterostructures of 0D/2D and 1D/2D hybrids, it is generally accepted that 2D/2D heterostructures have relatively better-built hetero-interfaces for transfer and separation of electron-hole pairs. Recently, our group synthesized novel 2D/2D WO_3@$CoWO_4$ bilayer nanosheets as efficient wired and wireless water oxidation catalysts.[106] The constructed WO_3@$CoWO_4$ p-n heterostructure and created interfacial oxygen vacancies reduced the energy barriers for OER. DFT calculations indicated that the p-n heterojunction vested the 2D/2D composite with a narrowed band gap for better visible-light absorption, rapid interface charge transfer and separation. Note that the stability of WO_3 that is sensitive to photocorrosion was improved by promoting the migration of holes to $CoWO_4$.

2.7 Metal-Free Based Semiconductors for Water Oxidation

Although we mainly illustrated the applications of earth-abundant metal-based LD semiconductors for water oxidation, a series of LD metal-free conductors like 0D carbon quantum dots,[63] 2D g-C_3N_4,[107,108] and their hybridizations with other metal- or metal-free based materials like WO_3,[109] α-Fe_2O_3[110] were also used for the application. Due to the limited space, it is difficult to illustrate both metal-free and metal-based semiconductors for water oxidation. However, apart from the metal-based photocatalysts, we also adopted 2D g-C_3N_4 as a research object in our following chapters because of its excellent visible-light absorption and great potential in visible-light photocatalysis.[111–113] Besides, the metal-free nature and simple synthesis method endow g-C_3N_4 with the merits of environmental friendliness and sustainability. However, water oxidation performance of pristine g-C_3N_4 nanosheets is unsatisfactory because of the poor charge separation capability.[114] To some extents, some strategies summarized in this chapter for modifying photocatalytic properties of metal-based semiconductors such as building suitable heterojunctions, morphology control, doping, synthesizing thin films or dots to generate quantum effect, can also apply for 2D g-C_3N_4 modifications.

2.8 Catalytic Active Sites-Catalysis Correlation in LD Semiconductors

The differences in dimensionality define the various catalytic attributes of 0D, 1D and 2D semiconductor materials and we tried to point out their most unique properties, respectively.

As discussed in this review, 0D semiconductors, which are easier to be dispersed in solution, are more favored in wireless water oxidation. They are also commonly applied to fabricate hybrid materials because of the small size, easy dispersion and deposition on other materials. Without a doubt, quantum size effect exists mostly on 0D materials to trigger changes in the band structure and enable more active OER, due to the low dimensions in all directions. Owing to the explicit growing orientation, 1D nanowires or nanotubes can be easily assembled into ordered vertical arrays that are more suitable for wired PEC applications, mainly thanks to the directed electron transfer channels. In addition, 1D nanowire/or nanotube arrays can serve as ideal supports for other catalysts. 2D materials have the highest photoconversion efficiency due to the short travel distance of the photoexcited carriers in the 2D nanosheet, and with the large section area, enormous photons can be absorbed in transient time under a low photon flux density. 2D materials are widely used in both wired and wireless systems. The more exposed surface atoms bring out more possibilities in adjusting the active facets, porosities and creating surface defects or oxygen vacancies, which can induce unique LSPR and active sites on 2D materials.

2.9 Conclusions and Perspectives

Semiconductors with low dimensions have provided us fundamental insights and new possibilities into the burgeoning photocatalytic field, showing well-defined technological promises. By means of regulating the nanostructures and/or electronic properties of LD semiconductors, the photocatalytic performances can be readily enhanced, allowing for the well establishment of superior photocatalysts for water oxidation. Specifically, we have outlined some prominent strategies for better LD semiconductors in this chapter including quantum size effect, LSPR, active facet exposure, defect engineering, heterojunction construction in LD hybrids. As a result, inspiring progress including enhanced efficiencies, improved activities and prolonged stabilities have been achieved in LD photocatalysts.

For future research in selecting suitable LD semiconductors for water oxidation, several factors such as band-edge position, charge-carrier diffusion length, charge separation and stability, need to be considered. In addition, it is vital to identify the optimal operation conditions (e.g. light, and optimum pH values in aqueous solution) of specific LD semiconductors to ensure that they are both active and stable. Because of the sustainable energy requirements in society, further efforts are needed to be given in reducing the cost of earth-abundant LD semiconductors, because the projected expenditure of artificial photosynthesis systems is principally determined by light-harvesters. At last, the mechanism of water oxidation has not been fully unveilled, and will still be a challenging subject in the foreseeable future research. It is expected that photocatalytic and photoelectrochemical water oxidation will play a significant role in the future sustainability.

References

1) Akira Fujishima, K. H. Electrochemical Photolysis of Water at a Semiconductor Electrode. *Nature* **1972**, *238*, 37.

2) Chen, H. M.; Chen, C. K.; Chang, Y. C.; Tsai, C. W.; Liu, R. S.; Hu, S. F.; Chang, W. S.; Chen, K. H. Quantum Dot Monolayer Sensitized ZnO Nanowire-Array Photoelectrodes: True Efficiency for Water Splitting. *Angewandte Chemie*

International Edition **2010**, *122*, 6102.

3) Liu, Y.; Liang, L.; Xiao, C.; Hua, X.; Li, Z.; Pan, B.; Xie, Y. Promoting Photogenerated Holes Utilization in Pore-Rich WO_3 Ultrathin Nanosheets for Efficient Oxygen-Evolving Photoanode. *Advanced Energy Materials* **2016**, *6*, 1600437.

4) Zhu, J.; Yin, Z.; Yang, D.; Sun, T.; Yu, H.; Hoster, H. E.; Hng, H. H.; Zhang, H.; Yan, Q. Hierarchical Hollow Spheres Composed of Ultrathin Fe_2O_3 Nanosheets for Lithium Storage and Photocatalytic Water Oxidation. *Energy & Environmental Science* **2013**, *6*, 987.

5) Bard, A. J. Photoelectrochemistry and Heterogeneous Photo-Catalysis at Semiconductors. *Journal of Photochemistry* **1979**, *10*, 59.

6) Bard, A. J. Photoelectrochemisi. Science **1980**, *207*, 139.

7) Voiry, D.; Shin, H. S.; Loh, K. P.; Chhowalla, M. Low-Dimensional Catalysts for Hydrogen Evolution and CO_2 Reduction. *Nature Reviews* **2018**, *2*, 1.

8) Navarro, R. M.; del Valle, F.; Villoria de la Mano, J. A.; Álvarez-Galván, M. C.; Fierro, J. L. G. Photocatalytic Water Splitting Under Visible Light. Concept and Catalysts Development. *Advances in Chemical Engineering* **2009**, *36*, 111.

9) Wang, T.; Gong, J. Single-Crystal Semiconductors with Narrow Band Gaps for Solar Water Splitting. *Angewandte Chemie - International Edition* **2015**, *54*, 10718.

10) Hisatomi, T.; Kubota, J.; Domen, K. Recent Advances in Semiconductors for Photocatalytic and Photoelectrochemical Water Splitting. *Chemical Society Reviews* **2014**, *43*, 7520.

11) Reza Gholipour, M.; Dinh, C.-T.; Béland, F.; Do, T.-O. Nanocomposite Heterojunctions as Sunlight-Driven Photocatalysts for Hydrogen Production from Water Splitting. *Nanoscale* **2015**, *7*, 8187.

12) Kärkäs, M. D.; Verho, O.; Johnston, E. V.; Åkermark, B. Artificial Photosynthesis: Molecular Systems for Catalytic Water Oxidation. *Chemical Reviews* **2014**, *114*, 11863.

13) Yoffe, A. D. Low-Dimensional Systems: Quantum Size Effects and Electronic Properties of Semiconductor Microcrystallites (Zero-Dimensional Systems) and Some Quasi-Two-Dimensional Systems. *Advances in Physics* **1993**, *42*, 173.

14) Zhao, Y. S.; Fu, H.; Peng, A.; Ma, Y.; Xiao, D.; Yao, J. Low-Dimensional

Nanomaterials Based on Small Organic Molecules: Preparation and Optoelectronic Properties. *Advanced Materials* **2008**, *20*, 2859.

15) Du, P.; Eisenberg, R. Catalysts Made of Earth-Abundant Elements (Co, Ni, Fe) for Water Splitting: Recent Progress and Future Challenges. *Energy & Environmental Science* **2012**, *5*, 6012.

16) Ran, J.; Zhang, J.; Yu, J.; Zhang, S. Earth-Abundant Cocatalysts for Semiconductor-Based Photocatalytic Water Splitting. *Chemical Society Reviews* **2014**, *43*, 7787.

17) Deng, X.; Tüysüz, H. Cobalt-Oxide-Based Materials as Water Oxidation Catalyst: Recent Progress and Challenges. *ACS Catalysis* **2014**, *4*, 3701.

18) Mino, L.; Agostini, G.; Borfecchia, E.; Gianolio, D.; Piovano, A.; Gallo, E.; Lamberti, C. Low-Dimensional Systems Investigated by X-Ray Absorption Spectroscopy: A Selection of 2D, 1D and 0D Cases. *Journal of Physics D: Applied Physics* **2013**, *46*, 680.

19) Rossetti, R.; Ellison, J. L.; Gibson, J. M.; Brus, L. E. Size Effects in the Excited Electronic States of Small Colloidal CdS Crystallites. *The Journal of Chemical Physics* **1984**, *80*, 4464.

20) Gerischer, H.; Lübke, M. A Particle Size Effect in the Sensitization of TiO_2 Electrodes by a CdS Deposit. *Journal of Electroanalytical Chemistry* **1986**, *204*, 225.

21) Dingle, R.; Wiegmann, W.; Henry, C. H. Quantum States of Confined Carriers in Very Thin Al_xGa_{1-x} As-GaAs-$Al_xGa_{1-x}As$ Heterostructures. *Physical Review Letters* **1974**, *33*, 827.

22) Osterloh, F. E. Inorganic Nanostructures for Photoelectrochemical and Photocatalytic Water Splitting. *Chemical Soiety Reviews* **2013**, *42*, 2294.

23) Robel, I.; Kuno, M.; Kamat, P. V. Size-Dependent Electron Injection from Excited CdSe Quantum Dots into TiO_2 Nanoparticles. *Journal of the American Chemical Society* **2007**, *129*, 4136.

24) Wang, X.; Li, Z.; Shi, J.; Yu, Y. One-Dimensional Titanium Dioxide Nanomaterials: Nanowires, Nanorods, and Nanobelts. *Chemical Reviews* **2014**, *114*, 9346.

25) Yang, X. H.; Li, Z.; Liu, G.; Xing, J.; Sun, C.; Yang, H. G.; Li, C. Ultra-Thin Anatase TiO_2 Nanosheets Dominated with {001} Facets: Thickness-Controlled Synthesis, Growth Mechanism and Water-Splitting Properties. *CrystEngComm* **2011**, *13*, 1378.

26) Mohapatra, S. K.; John, S. E.; Banerjee, S.; Misra, M. Water Photooxidation by Smooth and Ultrathin γ-Fe_2O_3 Nanotube Arrays. *Chemistry of Materials* **2009**, *21*, 3048.

27) Liu, X.; Swihart, M. T. Heavily-Doped Colloidal Semiconductor and Metal Oxide Nanocrystals: An Emerging New Class of Plasmonic Nanomaterials. *Chemical Society Reviews* **2014**, *43*, 3908.

28) Lee, J.; Mubeen, S.; Ji, X.; Stucky, G. D.; Moskovits, M. Plasmonic Photoanodes for Solar Water Splitting with Visible Light. *Nano Letters* **2012**, *12*, 5014.

29) Hou, W.; Cronin, S. B. A Review of Surface Plasmon Resonance-Enhanced Photocatalysis. *Advanced Functional Materials* **2013**, *23*, 1612.

30) Wang, S. L.; Mak, Y. L.; Wang, S.; Chai, J.; Pan, F.; Foo, M. L.; Chen, W.; Wu, K.; Xu, G. Q. Visible-Near-Infrared-Light-Driven Oxygen Evolution Reaction with Noble-Metal-Free WO_2 –WO_3 Hybrid Nanorods. *Langmuir* **2016**, *32*, 13046.

31) Zhou, S.; Pi, X.; Ni, Z.; Ding, Y.; Jiang, Y.; Jin, C.; Delerue, C.; Yang, D.; Nozaki, T. Comparative Study on the Localized Surface Plasmon Resonance of Boron- and Phosphorus-Doped Silicon Nanocrystals. *ACS Nano* **2015**, *9*, 378.

32) Manthiram, K.; Alivisatos, A. P. Tunable Localized Surface Plasmon Resonances in Tungsten Oxide Nanocrystals. *Journal of the American Chemical Society* **2012**, *134*, 3995.

33) Li, W.; Zamani, R.; Rivera Gil, P.; Pelaz, B.; Ibáñez, M.; Cadavid, D.; Shavel, A.; Alvarez-Puebla, R. A.; Parak, W. J.; Arbiol, J.; Cabot, A. CuTe Nanocrystals: Shape and Size Control, Plasmonic Properties, and Use as SERS Probes and Photothermal Agents. *Journal of the American Chemical Society* **2013**, *135*, 7098.

34) Liu, X.; Wang, X.; Zhou, B.; Law, W. C.; Cartwright, A. N.; Swihart, M. T. Size-Controlled Synthesis of Cu_2-XE (E = S, Se) Nanocrystals with Strong Tunable near-Infrared Localized Surface Plasmon Resonance and High Conductivity in Thin Films. *Advanced Functional Materials* **2013**, *23*, 1256.

35) Yan, J.; Wang, T.; Wu, G.; Dai, W.; Guan, N.; Li, L.; Gong, J. Tungsten Oxide Single Crystal Nanosheets for Enhanced Multichannel Solar Light Harvesting. *Advanced Materials* **2015**, *27*, 1580.

36) Wang, Z.; Yang, C.; Lin, T.; Yin, H.; Chen, P.; Wan, D.; Xu, F.; Huang, F.; Lin, J.;

Xie, X.; Jiang, M. H-Doped Black Titania with Very High Solar Absorption and Excellent Photocatalysis Enhanced by Localized Surface Plasmon Resonance. *Advanced Functional Materials* **2013**, *23*, 5444.

37) Liu, Y.; Xiao, C.; Huang, P.; Cheng, M.; Xie, Y. Regulating the Charge and Spin Ordering of Two-Dimensional Ultrathin Solids for Electrocatalytic Water Splitting. *Chem* **2018**, **DOI**: org/10.1016/j.chempr.2018.02.006.

38) Polman, A.; Atwater, H. A. Photonic Design Principles for Ultrahigh-Efficiency Photovoltaics. *Nature Materials* **2012**, *11*, 174.

39) Semonin, O. E.; Luther, J. M.; Choi, S.; Chen, H.; Gao, J.; Nozik, A. J.; Beard, M. C. In a Quantum Dot Solar *Cell*. **2011**, *334*, 1530.

40) Tian, J.; Zhao, Z.; Kumar, A.; Boughton, R. I.; Liu, H. Recent Progress in Design, Synthesis, and Applications of One-Dimensional TiO_2 Nanostructured Surface Heterostructures: A Review. *Chemical Society Reviews* **2014**, *43*, 6920.

41) Li, L.; Salvador, P. A.; Rohrer, G. S. Photocatalysts with Internal Electric Fields. *Nanoscale* **2014**, *6*, 24.

42) Hocking, R. K.; Brimblecombe, R.; Chang, L. Y.; Singh, A.; Cheah, M. H.; Glover, C.; Casey, W. H.; Spiccia, L. Water-Oxidation Catalysis by Manganese in a Geochemical-like Cycle. *Nature Chemistry* **2011**, *3*, 461.

43) Surendranath, Y.; Lutterman, D. A.; Liu, Y.; Nocera, D. G. Nucleation, Growth, and Repair of a Cobalt-Based Oxygen Evolving Catalyst. *Journal of the American Chemical Society* **2012**, *134*, 6326.

44) Singh, A.; Chang, S. L. Y.; Hocking, R. K.; Bach, U.; Spiccia, L. Highly Active Nickel Oxide Water Oxidation Catalysts Deposited from Molecular Complexes. *Energy & Environmental Science* **2013**, *6*, 579.

45) Zhao, Q.; Li, D.; Gao, G.; Yuan, W.; Hao, G.; Li, J. Nanostructured Iron(III) Oxide Catalyst Electrodeposited from Fe(II) Triflate for Electrocatalytic Water Oxidation. *International Journal of Hydrogen Energy* **2016**, *41*, 17193.

46) Jiao, F.; Frei, H. Nanostructured Cobalt and Manganese Oxide Clusters as Efficient Water Oxidation Catalysts. *Energy & Environmental Science* **2010**, *3*, 1018.

47) Jiao, F.; Frei, H. Nanostructured Cobalt Oxide Clusters in Mesoporous Silica as Efficient Oxygen-Evolving Catalysts. *Angewandte Chemie-International Edition*

2009, *48*, 1841.

48) Yusuf, S.; Jiao, F. Effect of the Support on the Photocatalytic Water Oxidation Activity of Cobalt Oxide Nanoclusters. *ACS Catalysis* **2012**, *2*, 2753.

49) Grzelczak, M.; Zhang, J.; Pfrommer, J.; Hartmann, J.; Driess, M.; Antonietti, M.; Wang, X. Electro- and Photochemical Water Oxidation on Ligand-Free Co_3O_4 nanoparticles with Tunable Sizes. *ACS Catalysis* **2013**, *3*, 383.

50) Xu, R.; Zeng, H. C. Self-Generation of Tiered Surfactant Superstructures for One-Pot Synthesis of Co_3O_4 Nanocubes and Their Close- and Non-Close-Packed Organizations. *Langmuir : the ACS journal of surfaces and colloids* **2004**, *20*, 9780.

51) Wang, J.; Zhang, N.; Su, J.; Guo, L. α-Fe_2O_3 Quantum Dots: Low-Cost Synthesis and Photocatalytic Oxygen Evolution Capabilities. *RSC Advances* **2016**, *6*, 41060.

52) Zhang, N.; Shi, J.; Mao, S. S.; Guo, L. Co_3O_4 Quantum Dots: Reverse Micelle Synthesis and Visible-Light-Driven Photocatalytic Overall Water Splitting. *Chemical Communications* **2014**, *50*, 2002.

53) Shi, N.; Cheng, W.; Zhou, H.; Fan, T.; Niederberger, M. Facile Synthesis of Monodisperse Co_3O_4 Quantum Dots with Efficient Oxygen Evolution Activity. *Chemical Communications* **2015**, *51*, 1338.

54) Fominykh, K.; Feckl, J. M.; Sicklinger, J.; Döblinger, M.; Böcklein, S.; Ziegler, J.; Peter, L.; Rathousky, J.; Scheidt, E. W.; Bein, T.; Fattakhova-Rohlfing, D. Ultrasmall Dispersible Crystalline Nickel Oxide Nanoparticles as High-Performance Catalysts for Electrochemical Water Splitting. *Advanced Functional Materials* **2014**, *24,* 3123.

55) Chang, C. M.; Orchard, K. L.; Martindale, B. C. M.; Reisner, E. Ligand Removal from CdS Quantum Dots for Enhanced Photocatalytic H_2 Generation in PH Neutral Water. *Journal of Materials Chemistry A* **2016**, *4*, 2856.

56) Blakemore, J. D.; Gray, H. B.; Winkler, J. R.; Müller, A. M. Co_3O_4 Nanoparticle Water-Oxidation Catalysts Made by Pulsed-Laser Ablation in Liquids. *ACS Catalysis* **2013**, *3*, 2497.

57) Liao, L.; Zhang, Q.; Su, Z.; Zhao, Z.; Wang, Y.; Li, Y.; Lu, X.; Wei, D.; Feng, G.; Yu, Q.; Cai, X.; Zhao, J.; Ren, Z.; Fang, H.; Robles-Hernandez, F.; Baldelli, S.; Bao, J. Efficient Solar Water-Splitting Using a Nanocrystalline CoO Photocatalyst. *Nature Nanotechnology* **2014**, *9,* 69.

58) Kwak, I. H.; Im, H. S.; Jang, D. M.; Kim, Y. W.; Park, K.; Lim, Y. R.; Cha, E. H.; Park, J. $CoSe_2$ and $NiSe_2$ Nanocrystals as Superior Bifunctional Catalysts for Electrochemical and Photoelectrochemical Water Splitting. *ACS Applied Materials & Interfaces* **2016**, *8*, 5327.

59) Townsend, T. K.; Sabio, E. M.; Browning, N. D.; Osterloh, F. E. Photocatalytic Water Oxidation with Suspended Alpha-Fe_2O_3 Particles-Effects of Nanoscaling. *Energy & Environmental Science* **2011**, *4*, 4270.

60) Yehezkeli, O.; Harguindey, A.; Domaille, D. W.; He, L.; Cha, J. N. Synthesis and Phase Transfer of Well-Defined $BiVO_4$ Nanocrystals for Photocatalytic Water Splitting. *RSC Advances* **2015**, *5*, 58755.

61) Lijima, S. Helical Microtubules of Graphitic Carbon. *Nature* **1991**, *354*, 56.

62) Sun, Y.; Xie, Y.; Wu, C.; Zhang, S.; Jiang, S. Aqueous Synthesis of Mesostructured $BiVO_4$ Quantum Tubes with Excellent Dual Response to Visible Light and Temperature. *Nano Research* **2010**, *3*, 620.

63) Wu, X.; Zhao, J.; Guo, S.; Wang, L.; Shi, W.; Huang, H.; Liu, Y.; Kang, Z. Carbon Dot and $BiVO_4$ Quantum Dot Composites for Overall Water Splitting via a Two-Electron Pathway. *Nanoscale* **2016**, *8*, 17314.

64) Sun, S.; Wang, W.; Li, D.; Zhang, L.; Jiang, D. Solar Light Driven Pure Water Splitting on Quantum Sized $BiVO_4$ without Any Cocatalyst. *ACS Catalysis* **2014**, *4*, 3498.

65) Mor, G. K.; Shankar, K.; Paulose, M.; Varghese, O. K.; Grimes, C. A. Enhanced Photocleavage of Water Using Titania Nanotube Arrays. *Nano Letters* **2005**, *5*, 191.

66) Grimes, C. A. Synthesis and Application of Highly Ordered Arrays of TiO_2 Nanotubes. *Journal of Materials Chemistry* **2007**, *17*, 1451.

67) Cho, I. S.; Chen, Z.; Forman, A. J.; Kim, D. R.; Rao, P. M.; Jaramillo, T. F.; Zheng, X. Branched TiO_2 Nanorods for Photoelectrochemical Hydrogen Production. *Nano Letters* **2011**, *11*, 4978.

68) Vayssieres, B. L.; Sathe, C.; Butorin, S. M.; Shuh, D. K.; Nordgren, J.; Guo, J. One-Dimensional Quantum-Confinement Effect in α-Fe_2O_3 Ultrafine Nanorod Arrays. *Advanced Materials* **2005**, *17*, 2320.

69) Serpone, N.; Lawless, D.; Khairutdinov, R. Size Effects on the Photophysical Properties of Colloidal Anatase TiO_2 Particles: Size Quantization Versus Direct

Transitions in This Indirect Semiconductor *The Journal of Physical Chemistry* **1995**, *99*, 16646.

70) Iacomino, A.; Cantele, G.; Trani, F.; Ninno, D. DFT Study on Anatase TiO_2 Nanowires: Structure and Electronic Properties as Functions of Size, Surface Termination, and Morphology. *Journal of Physical Chemistry C* **2010**, *114*, 12389.

71) Liu, C.; Sun, H.; Yang, S. From Nanorods to Atomically Thin Wires of Anatase TiO_2: Nonhydrolytic Synthesis and Characterization. *Chemistry - A European Journal* **2010**, *16*, 4381.

72) Hoang, S.; Guo, S.; Hahn, N. T.; Bard, A. J.; Mullins, C. B. Visible Light Driven Photoelectrochemical Water Oxidation on Nitrogen-Modified TiO_2 Nanowires. *Nano Letters* **2012**, *12*, 26.

73) Hoang, S.; Guo, S.; Hahn, N. T.; Bard, A. J.; Mullins, C. B. Visible Light Driven Photoelectrochemical Water Oxidation on Nitrogen-Modified TiO_2 Nanowires. *Nano Letters* **2012**, *12*, 26.

74) Rao, P. M.; Cai, L.; Liu, C.; Cho, I. S.; Lee, C. H.; Weisse, J. M.; Yang, P.; Zheng, X. Simultaneously Efficient Light Absorption and Charge Separation in $WO_3/BiVO_4$ Core/Shell Nanowire Photoanode for Photoelectrochemical Water Oxidation. *Nano Letters* **2014**, *14*, 1099.

75) Liu, Y.; Zhou, W.; Umezawa, N. Electronic and Optical Properties of TiO_2 Solid-Solution Nanosheets for Bandgap Engineering: A Hybrid Functional Study. *The Journal of Physical Chemistry C* **2017**, *121*, 18683.

76) Sasaki, T.; Watanabe, M. Semiconductor Nanosheet Crystallites of Quasi-TiO_2 and Their Optical Properties. *Journal of Physical Chemistry B* **1997**, *5647*, 10159.

77) Osada, M.; Sasaki, T. Exfoliated Oxide Nanosheets : New Solution to Nanoelectronics. *Journal of Materials Chemistry* **2009**, *19*, 2503.

78) Sakai, N.; Ebina, Y.; Takada, K.; Sasaki, T. Photocurrent Generation from Semiconducting Manganese Oxide Nanosheets in Response to Visible Light. *Journal of Physical Chemistry B* **2005**, *109*, 9651.

79) Waller, M. R.; Townsend, T. K.; Zhao, J.; Sabio, E. M.; Chamousis, R. L.; Browning, N. D.; Osterloh, F. E. Single-Crystal Tungsten Oxide Nanosheets: Photochemical Water Oxidation in the Quantum Confinement Regime. *Chemistry of Materials* **2012**,

24, 698.

80) Ge, M.; Li, Q.; Cao, C.; Huang, J.; Li, S.; Zhang, S.; Chen, Z.; Zhang, K.; Al-deyab, S. S.; Lai, Y. One-Dimensional TiO_2 Nanotube Photocatalysts for Solar Water Splitting. *Advanced Science* **2017**, *4*, 1600152.

81) Zhao, Y.; Chang, C.; Teng, F.; Zhao, Y.; Chen, G.; Shi, R.; Waterhouse, G. I. N.; Huang, W.; Zhang, T. Defect-Engineered Ultrathin δ-MnO_2 Nanosheet Arrays as Bifunctional Electrodes for Efficient Overall Water Splitting. *Advanced Energy Materials* **2017**, *7*, 1700005.

82) Gao, S.; Sun, Y.; Lei, F.; Liu, J.; Liang, L.; Li, T.; Pan, B.; Zhou, J.; Xie, Y. Freestanding Atomically-Thin Cuprous Oxide Sheets for Improved Visible-Light Photoelectrochemical Water Splitting. *Nano Energy* **2014**, *8*, 205.

83) Gomes Silva, C.; Gomes Silva, C.; Bouizi, Y.; Bouizi, Y.; Fornés, V.; Fornés, V.; García, H.; García, H. Layered Double Hydroxides as Highly Efficient Photocatalysts for Visible Light Oxygen Generation from Water. *Journal of the American Chemical Society* **2009**, *131*, 13833.

84) Online, V. A.; Kim, S. J.; Lee, Y.; Lee, D. K.; Lee, J. W.; Kang, J. K. Efficient Co-Fe Layered Double Hydroxide Photocatalysts for Water Oxidation under Visible Light. *Journal of Materials Chemistry A* **2014**, *2*, 4136.

85) Environ, E. Titanium-Embedded Layered Double Hydroxides as Highly Efficient Water Oxidation Photocatalysts under Visible Light. *Energy & Environmental Science* **2011**, *4*, 914.

86) Zhao, Y.; Li, B.; Wang, Q.; Gao, W.; Wang, C. J.; Wei, M.; Evans, D. G.; Duan, X.; O'Hare, D. LDH NiTi-Layered Double Hydroxides Nanosheets as Efficient Photocatalysts for Oxygen Evolution from Water Using Visible Light. *Chemical Science* **2014**, *5*, 951.

87) Li, B.; Zhao, Y.; Zhang, S.; Gao, W.; Wei, M. Visible-Light-Responsive Photocatalysts toward Water Oxidation Based on NiTi-Layered Double Hydroxide/Reduced Graphene Oxide Composite Materials. *ACS Applied Materials & Interfaces* **2013**, *5*, 10233.

88) Zhao, Y.; Jia, X.; Waterhouse, G. I. N.; Wu, L.-Z.; Tung, C.-H.; O'Hare, D.; Zhang, T. Layered Double Hydroxide Nanostructured Photocatalysts for Renewable Energy

Production. *Advanced Energy Materials* **2016**, *6*, 1501974.

89) Article, E. NiTi-Layered Double Hydroxides Nanosheets as Efficient Photocatalysts for Oxygen Evolution from Water Using Visible Light. *Chemical Science* **2014**, *5*, 951.

90) Liu, Y.; Cheng, H.; Lyu, M.; Fan, S.; Liu, Q.; Zhang, W.; Zhi, Y.; Wang, C.; Xiao, C.; Wei, S.; Ye, B.; Xie, Y. Low Overpotential in Vacancy-Rich Ultrathin $CoSe_2$ nanosheets for Water Oxidation. *Journal of the American Chemical Society* **2014**, *136*, 15670.

91) Sun, Y.; Cheng, H.; Gao, S.; Sun, Z.; Liu, Q.; Leu, Q.; Lei, F.; Yao, T.; He, J.; Wei, S.; Xie, Y. Freestanding Tin Disulfide Single-Layers Realizing Efficient Visible-Light Water Splitting. *Angewandte Chemie - International Edition* **2012**, *51*, 8727.

92) Sun, Y.; Sun, Z.; Gao, S.; Cheng, H.; Liu, Q.; Piao, J.; Yao, T.; Wu, C.; Hu, S.; Wei, S.; Xie, Y. Fabrication of Flexible and Freestanding Zinc Chalcogenide Single Layers. *Nature Communications* **2012**, *3*, 1057.

93) Di, J.; Chen, C.; Yang, S.-Z.; Ji, M.; Yan, C.; Gu, K.; Xia, J.; Li, H.; Li, S.; Liu, Z. Defect Engineering in Atomically-Thin Bismuth Oxychloride towards Photocatalytic Oxygen Evolution. *Journal of Materials Chemistry A* **2017**, *5*, 14144.

94) Rodenas, P.; Song, T.; Sudhagar, P.; Marzari, G.; Han, H.; Badia-Bou, L.; Gimenez, S.; Fabregat-Santiago, F.; Mora-Sero, I.; Bisquert, J.; Paik, U.; Kang, Y. S. Quantum Dot Based Heterostructures for Unassisted Photoelectrochemical Hydrogen Generation. *Advanced Energy Materials* **2013**, *3*, 176.

95) Sun, W.-T.; Yu, Y.; Pan, H.-Y.; Gao, X.-F.; Chen, Q.; Peng, L.-M. CdS Quantum Dots Sensitized TiO_2 Nanotube-Array Photoelectrodes. *Journal of the American Chemical Society* **2008**, *130*, 1124.

96) Maeda, K.; Ishimaki, K.; Tokunaga, Y.; Lu, D.; Eguchi, M. Modification of Wide-Band-Gap Oxide Semiconductors with Cobalt Hydroxide Nanoclusters for Visible-Light Water Oxidation. *Angewandte Chemie - International Edition* **2016**, *55*, 8309.

97) Chaguetmi, S.; Mammeri, F.; Nowak, S.; Decorse, P.; Lecoq, H.; Gaceur, M.; Ben Naceur, J.; Achour, S.; Chtourou, R.; Ammar, S. Photocatalytic Activity of TiO_2 Nanofibers Sensitized with ZnS Quantum Dots. *RSC Advances* **2013**, *3*, 2572.

98) Gao, X.; Li, H.; Sun, W.; Chen, Q.; Tang, F.; Peng, L. CdTe Quantum Dots-Sensitized TiO_2 Nanotube Array Photoelectrodes. *Journal of Physical Chemistry C* **2009**, *113*,

7531.

99) Ning, F.; Shao, M.; Xu, S.; Fu, Y.; Zhang, R.; Wei, M.; Evans, D. G.; Duan, X. TiO_2/Graphene/NiFe-Layered Double Hydroxide Nanorod Array Photoanodes for Efficient Photoelectrochemical Water Splitting. *Energy & Environmental Science* **2016**, *9*, 2633.

100) Nie, Q.; Yang, L.; Cao, C.; Zeng, Y.; Wang, G.; Wang, C.; Lin, S. Interface Optimization of ZnO Nanorod/CdS Quantum Dots Heterostructure by a Facile Two-Step Low-Temperature Thermal Treatment for Improved Photoelectrochemical Water Splitting. *Chemical Engineering Journal* **2017**, *325*, 151.

101) Zhan, F.; Yang, Y.; Liu, W.; Wang, K.; Li, W.; Li, J. Facile Synthesis of FeOOH Quantum Dots Modified ZnO Nanorods Films via a Metal-Solating Process. *ACS Sustainable Chemistry & Engineering* **2018**, **DOI:** 10.1021/acssuschemeng.8b00776.

102) Cao, S.; Yan, X.; Kang, Z.; Liang, Q.; Liao, X.; Zhang, Y. Band Alignment Engineering for Improved Performance and Stability of $ZnFe_2O_4$ modified CdS/ZnO Nanostructured Photoanode for PEC Water Splitting. *Nano Energy* **2016**, *24*, 25.

103) Shao, M.; Ning, F.; Wei, M.; Evans, D. G.; Duan, X. Hierarchical Nanowire Arrays Based on ZnO Core-Layered Double Hydroxide Shell for Largely Enhanced Photoelectrochemical Water Splitting. *Advanced Functional Materials* **2014**, *24*, 580.

104) Huang, J.; Zhang, Y.; Ding, Y. Rationally Designed/Constructed CoOx/WO_3 Anode for Efficient Photoelectrochemical Water Oxidation. *ACS Catalysis* **2017**, *7*, 1841.

105) Tang, Y.; Wang, R.; Yang, Y.; Yan, D.; Xiang, X. Highly Enhanced Photoelectrochemical Water Oxidation Efficiency Based on Triadic Quantum Dot/Layered Double Hydroxide/$BiVO_4$ Photoanodes. *ACS Applied Materials & Interfaces* **2016**, *8*, 19446.

106) Zhang, H.; Tian, W.; Li, Y.; Sun, H.; Tadé, M. O.; Wang, S. Heterostructured WO_3@$CoWO_4$ bilayer Nanosheets for Enhanced Visible-Light Photo, Electro and Photoelectro-Chemical Oxidation of Water. *Journal of Materials Chemistry A* **2018**, *6*, 6265.

107) Liu, J.; Liu, Y.; Liu, N.; Han, Y.; Zhang, X.; Huang, H.; Lifshitz, Y.; Lee, S. T.; Zhong, J.; Kang, Z. Metal-Free Efficient Photocatalyst for Stable Visible Water Splitting via a Two-Electron Pathway. *Science* **2015**, *347*, 970.

108) Maeda K.; Wang X.; Nishihara Y.; Lu D.; Antonietti M.; Domen K. Photocatalytic Activities of Graphitic Carbon Nitride Powder for Water Reduction andOxidation under Visible Light. *Journal of Physical Chemistry C* **2009**, *113*, 4940.

109) Huang, D.; Li, M.; Wang, M. Significant Enhancement of the Photoelectrochemical Activity of WO_3 Nano Flakes by Carbon Quantum Dots Decoration. *Carbon* **2016**, *105*, 387.

110) Su, T.; Shao, Q.; Qin, Z.; Guo, Z.; Wu, Z. Role of Interfaces in Two-Dimensional Photocatalyst for Water Splitting. *ACS Catalysis* **2018**, *8*, 2253.

111) Zhang, J.; Grzelczak, M.; Hou, Y.; Maeda, K.; Domen, K.; Fu, X.; Antonietti, M.; Wang, X. Photocatalytic Oxidation of Water by Polymeric Carbon Nitride Nanohybrids Made of Sustainable Elements. *Chemical Science* **2012**, *3*, 443.

112) Zhang, G.; Zang, S.; Wang, X. Layered $Co(OH)_2$ Deposited Polymeric Carbon Nitrides for Photocatalytic Water Oxidation. *ACS Catalysis* **2015**, *5*, 941.

113) Zhou, L.; Zhang, H.; Sun, H.; Liu, S.; Tade, M. O.; Wang, S.; Jin, W. Recent Advances in Non-Metal Modification of Graphitic Carbon Nitride for Photocatalysis: A Historic Review. *Catalysis Science & Technology* **2016**, *6*, 7002.

114) Ma, T. Y.; Dai, S.; Jaroniec, M.; Qiao, S. Z. Graphitic Carbon Nitride Nanosheet-Carbon Nanotube Three-Dimensional Porous Composites as High-Performance Oxygen Evolution Electrocatalysts. *Angewandte Chemie - International Edition* **2014**, *53*, 7281.

Every reasonable effort has been made to acknowledge the owners of copyright material. I would be pleased to hear from any copyright owner who has been omitted or incorrectly acknowledged.

Chapter 3. Flower-Like Cobalt Hydroxide/Oxide on Graphitic Carbon Nitride for Visible-Light-Driven Water Oxidation

Abstract

Direct water oxidation via photocatalysis is a four-electron and multiple-proton process which requires a high extra energy input to produce free dioxygen gas, making it exacting especially under visible light irradiations. In this chapter, 2D nanosheet-constructed flower-like cobalt hydroxide/oxide (Fw-Co(OH)$_2$/Fw-Co$_3$O$_4$) cocatalysts for improving OER kinetics, are loaded onto 2D graphitic carbon nitride (g-C$_3$N$_4$) nanosheets that serve as visible light absorber towards enhanced visible-light-driven oxygen evolution reaction (OER) efficiencies. The synthesized Fw-Co(OH)$_2$ or Fw-Co$_3$O$_4$/g-C$_3$N$_4$ hybrids reveal favorable combination and synergism, reflected by the modified photoelectric activities and the improved OER performances. Attributed by its prominent hydrotalcite structure, Fw-Co(OH)$_2$ shows a better cocatalytic activity for g-C$_3$N$_4$ modification compared with Fw-Co$_3$O$_4$. Specifically, 7 wt.% Fw-Co(OH)$_2$/g-C$_3$N$_4$ photocatalyst exhibits 4 times higher photocurrent density and 5 times better OER performance than pristine g-C$_3$N$_4$. This work unambiguously promotes the application of the green photocatalyst of g-C$_3$N$_4$ in water oxidation.

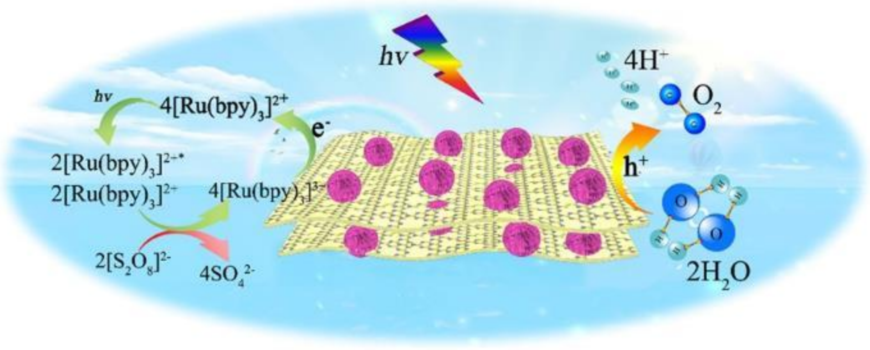

3.1 Introduction

Using renewable energy sources to split water into oxygen and hydrogen for replacing fossil fuels could be a boon to earthlings. Especially, the generation of oxygen by water oxidation is regarded as a much tougher step in water splitting, because it relates to a four-electron and multiple-proton procedure. Over the years, gratifying achievements have been made and high quantum efficiency has been achieved by employing semiconductor catalysts in the area of water splitting under UV irradiations.[1-4] However, the activity of water oxidation under visible light, which occupies the majority of solar spectrum energy, is still far from satisfactory when merely using traditional semiconductor catalysts such as TiO_2.[5] Interestingly, g-C_3N_4 which is a newly developed photocatalyst has demonstrated a great potential in visible-light-driven photocatalysis.[6-10] Compared with other wide band-gap semiconductor materials, the unique band structure enables g-C_3N_4 to absorb more visible light.[11] In addition, the metal-free nature and facile synthesis endow g-C_3N_4 with the advantages of sustainability and environmental geniality, making it promising for a large-scale application. From chemical thermodynamics, the valence band position of g-C_3N_4 is more positive than oxygen evolution potential, yet the activity is not satisfactory due to imperfect charge separation ability.[12-13] For this reason, modification of g-C_3N_4 to make it a more competitive light-harvesting platform for water oxidation has attracted much attention.[14-16] Various modification strategies on g-C_3N_4 have been performed, such as textural engineering, co-polymerization, doping, cocatalyst deposition, heterostructure design, and thin-film fabrication.[11, 17-23] Among them, deposition of efficient cocatalysts onto g-C_3N_4 has been proved to be a feasible and effective measure to finally obtain a better water oxidation performance. These cocatalysts can provide effective catalytic sites with lower overpotentials for water oxidation, and can also serve as selective trapping sites for photogenerated electrons, and thus restraining recombination of charge carriers.[24-26]

Various cocatalysts including transition-metal-based materials (such as MnO_x, NiO, Fe_2O_3, Co_3O_4),[27-32] organometallic complexes, bimetallic and polyoxometalate-based oxides (such as $NiFe_2O_4$, $NiCo_2O_4$) have been studied at the frontier of this field.[33-36] Among various cocatalysts, interest in earth-abundant cobalt has been stimulated along with a surge towards solar energy utilization. Moreover, it was found that the selectivity to oxygen evolution using cobalt hydroxides was more competitive than other metallic hydroxides (like $Fe(OH)_3$, $Ni(OH)_2$).[37] Therefore, we aim to develop an effective cobalt-based cocatalysts for g-C_3N_4 in this work.

Impregnating, adsorbing, or coating the cocatalysts onto the framework of semiconductor photocatalysts are the common methods for the contact and robust loading.[5, 15-16, 34, 38-39] For example, Maeda et al.[5] recently reported that after hybridizing $Co(OH)_2$ with TiO_2 using the impregnation method, an improved water oxidation effect was observed. Inspired by them, herein we report a facile coating approach to load shape-controlled cobalt hydroxides/oxides onto 2D g-C_3N_4 nanosheets to achieve water catalytic oxidation on g-C_3N_4. The synthesized cobalt hydroxide and oxide showed 2D-nanosheet built three-dimensional flower-like morphologies and well-defined combination with g-C_3N_4. The composites displayed an improved catalytic activity for OER under visible light irradiations.

3.2 Experimental Section

3.2.1 Chemical Reagents

Cobalt (II) nitrate hexahydrate, cobalt (II) acetate tetrahydrate, urea, methanol, polyvinylpyrrolidone (PVP, K30), 5,5-dimethyl-1-pyrroline N-oxide (DMPO; ≥97.0%) were purchased from Sigma-Aldrich. All the chemicals were of analytical grade and employed as received without further purification.

3.2.2 Materials Preparation

g-C_3N_4 photocatalyst was prepared by a thermal polymerization method. In a typical route, 5 g of urea was annealed at 550 °C for 2 h in air. The final light yellow powder was then gathered and denoted as g-C_3N_4.

Flower-like $Co(OH)_2$ was synthesized by a modified hydrothermal method firstly.[40] Typically, 0.498 g of $Co(CH_3COO)_2 \cdot 4H_2O$, 0.24 g of urea and 0.5 g of polyvinylpyrrolidone (PVP, K30) were firstly dissolved in methanol before ultrasonication and mixing. Then 40 mL of the aqueous solutions were infused into a 120 mL Teflon-liner with a stainless steel autoclave and subsequently sealed for heating at 200 °C for 6 h in an oven. After centrifugation and washing the possible residual urea and PVP with water and ethanol for several times, the resulting product was obtained as Fw-$Co(OH)_2$. As shown in Scheme 3.1, Fw-$Co(OH)_2$/g-C_3N_4 composites were prepared by a facile coating method. The synthesized $Co(OH)_2$ particles were first dispersed in ethanol with a desired concentration, which was then subjected to ultrasonic treatment for 30 min to promote the dispersion of $Co(OH)_2$ in the solution. Carbon nitride powders were dispersed in 20 mL ethanol and then a certain amount of $Co(OH)_2$ suspension was added to the mixture. The mixture was then dried in an oil bath, transferred to a vacuum oven and kept at 80 °C overnight to remove ethanol. After that, the uniform powders were annealed at 120 °C for 2 h to strengthen the adhesion between g-C_3N_4 and the cocatalysts and denoted as Fw-$Co(OH)_2$/g-C_3N_4, or annealed at 300 °C for 2 h to get Fw-Co_3O_4/g-C_3N_4 composites. The loading amounts of Fw-$Co(OH)_2$ and Fw-Co_3O_4 were designed at 3 wt.% for comparison. Also, OER efficiencies of g-C_3N_4 loaded with various Fw-$Co(OH)_2$ ratios (3 wt.%, 7 wt.% and 15 wt.%) were conducted to estimate the influence of the loading amount of cobalt hydroxide. Additionally, a physical mixture of Fw-$Co(OH)_2$ and g-C_3N_4 was obtained by mixing them together in ethanol and drying at room temperature.

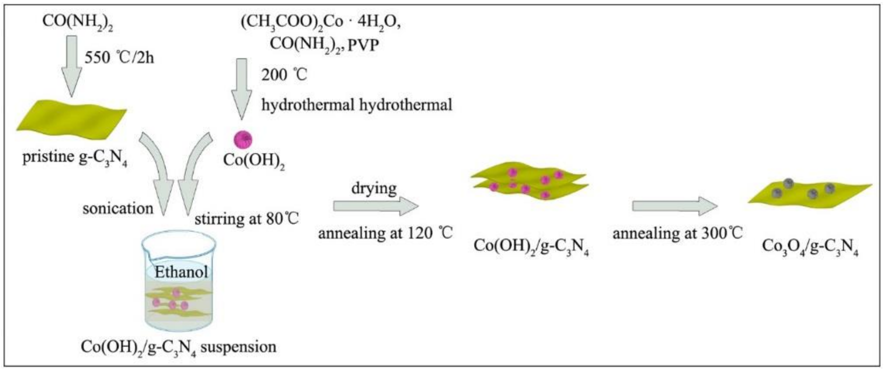

Scheme 3.1 Synthesis of $Co(OH)_2$/g-C_3N_4 and Co_3O_4/g-C_3N_4.

3.2.3 Characterization Techniques

Powder X-ray diffraction (XRD) patterns were obtained on an Empyrean multi-purpose research diffractometer (Panalytical Empyrean XRD) utilizing Copper Kα radiation (λ =

1.5418 Å) with a current of 40 mA and an voltage of 40 kV. Scanning electron microscopy (SEM) with EDS mapping images were catched on a FEI Verios XHR SEM microscope. TEM and SAED images were received with a JEOL 2100 TEM microscope. High angle annular dark field scanning transmission electron microscopy images (HAADF-STEM) with corresponding energy-dispersive X-ray spectroscopy (EDX) elemental mapping images were observed under an FEI TITAN G2 (200 kV). The Brunauer-Emmett-Teller (BET) specific surface area and pore size dispersion of the materials were assessed by N_2 adsorption/desorption utilizing a Micromeritics Tristar 3000. Beforehand, the materials were degassed at 100 ^{o}C overnight under vacuum condition. X-ray photoelectron spectroscopy (XPS) was tested under ultra-high vacuum (UHV) condition on a Kratos Axis Ultra DLD system. All spectra were calibrated based on a primary C 1s component at 284.6 eV. Electron Paramagnetic Resonance (EPR) mensuration were accomplished using a Bruker EMXplus spectrometer under the condition of modulation amplitude (8 G); modulation frequency (100 kHz); microwave frequency (9.48 GHz); and non-saturating microwave power (1.02 Mw).

3.2.4 Photoelectrochemical Measurements

Photoelectrochemical tests were accomplished on a Zennium workstation with the CIMPS system (Zahner, Germany) through a three electrode framework, applying a saturated calomel electrode (SCE) as the reference electrode and a Pt wire as the counter electrode. F-doped tin oxide (FTO) glasses were cleaned by sonication in ethanol for 30 min and dried at 80 °C to act as the working electrode. Na_2SO_4 solution (0.2 M, pH = 6.8) was served as the neutral electrolyte during the measurements. Loading of samples on the FTO was performed as below: suspensions containing 8 mg of catalyst, 50 μL 5 wt% Nafion 117 solutions and 500 μL ethanol were obtained by ultrasonic mixing for about 15 min. The resulted suspension (40 μL) was then dropped onto the working electrode through a spin coating method and dried in air (catalyst loading∼0.60 mg cm^{-2}). Photocurrent and EIS measurements were carried out utilizing a Oriel Solar Simulator with a 450 W Xenon arc lamp. Prior to test, the internal light was filtered using a neutral density filters and an AM 1.5G filter into an optical fiber. The output power was calibrated to 100 mW/cm^2 utilizing a thermopile detector.

3.2.5 Oxygen Evolution Reaction

For each reaction, designed amount of catalyst (50 mg) was dispersed in a 50 mL buffered solution (Na_2SiF_6-$NaHCO_3$, 0.022 M) which was prepared, adjusted the pH to 5.8 and aged for 2 days. Then 0.4875 g of Na_2SO_4, 0.1785 g of $Na_2S_2O_8$, and 30 mg of $[Ru(bpy)_3]Cl_2 \cdot 6H_2O$ were added to the reaction solution.

Oxygen was probed quantitatively utilizing an oxygen sensor (Ocean Optics, Neofox, FOSPOR-R 1/16).[28, 31] The water oxidation reactor was a customized airtight stainless steel cell covered by a quartz window (the volume of the headspace was 350 mL, excluding the space occupied by the septum, oxygen sensor, and the solution). The needle probe was inserted into the 1/16" threaded holes through a rubber septum and conducted uninterrupted O_2 readings at 1 s intervals throughout the test. Ahead of the detecting, the probe was calibrated through 2 points method (air, 20.9% O_2 and Nitrogen, 0% O_2), with a reading error of 1%. The test started with 30 min of baseline O_2 reading followed by 120 min of irradiation via a 300 W Xeon lamp (Newport) thread an light filter ($\lambda > 420$ nm) and aligned to 200 mW/cm^2 (2 suns). Before irradiation, the reactor was purged with nitrogen for 30 mins to exclude air and guarantee anaerobic circumstances in the reaction system. The probe measures the O_2 exponent in the headspace and records as mole %. This was converted to μmol after first adjusting for the O_2 dissolved in solution by Henry's Law. The proposed mechanism for the water oxidation systems catalyzed by buffered Tris(2, 2'-bipyridyl) ruthenium system can be deduced in the following reaction sequence:[41]

$$Ru(bpy)_3^{2+} + hv \rightarrow Ru(bpy)_3^{2+^*} \qquad (3.1)$$

$$Ru(bpy)_3^{2+^*} + S_2O_8^{2-} \rightarrow Ru(bpy)_3^{3+} + SO_4^{2-} + SO_4^{-} \qquad (3.2)$$

$$Ru(bpy)_3^{2+} + SO_4^{-} \rightarrow Ru(bpy)_3^{3+} + SO_4^{2-} \qquad (3.3)$$

$$4Ru(bpy)_3^{3+} + 2H_2O \rightarrow 4Ru(bpy)_3^{2+} + 4H^{+} + O_2 \qquad (3.4)$$

Apparent quantum efficiency (AQE) for photocatalytic oxygen evolution reaction was detected at the same experimental condition through a band-pass filter ($\lambda = 450$ nm). The photo flux of incident light was determined using a spectroradiometer (DeltaOHM, LP471

PAR / LP471 RAD, resolution, 0.01 μmol m^{-2} s^{-1} / 0.1*10^{-3} W m^{-2}). AQE was calculated by the following formula:

$$\text{AQE}=\frac{4\times \text{ evolved } O_2 \text{ molecule number}}{\text{Indicent photon number}}\times 100\% \tag{3.5}$$

3.3 Results and Discussion

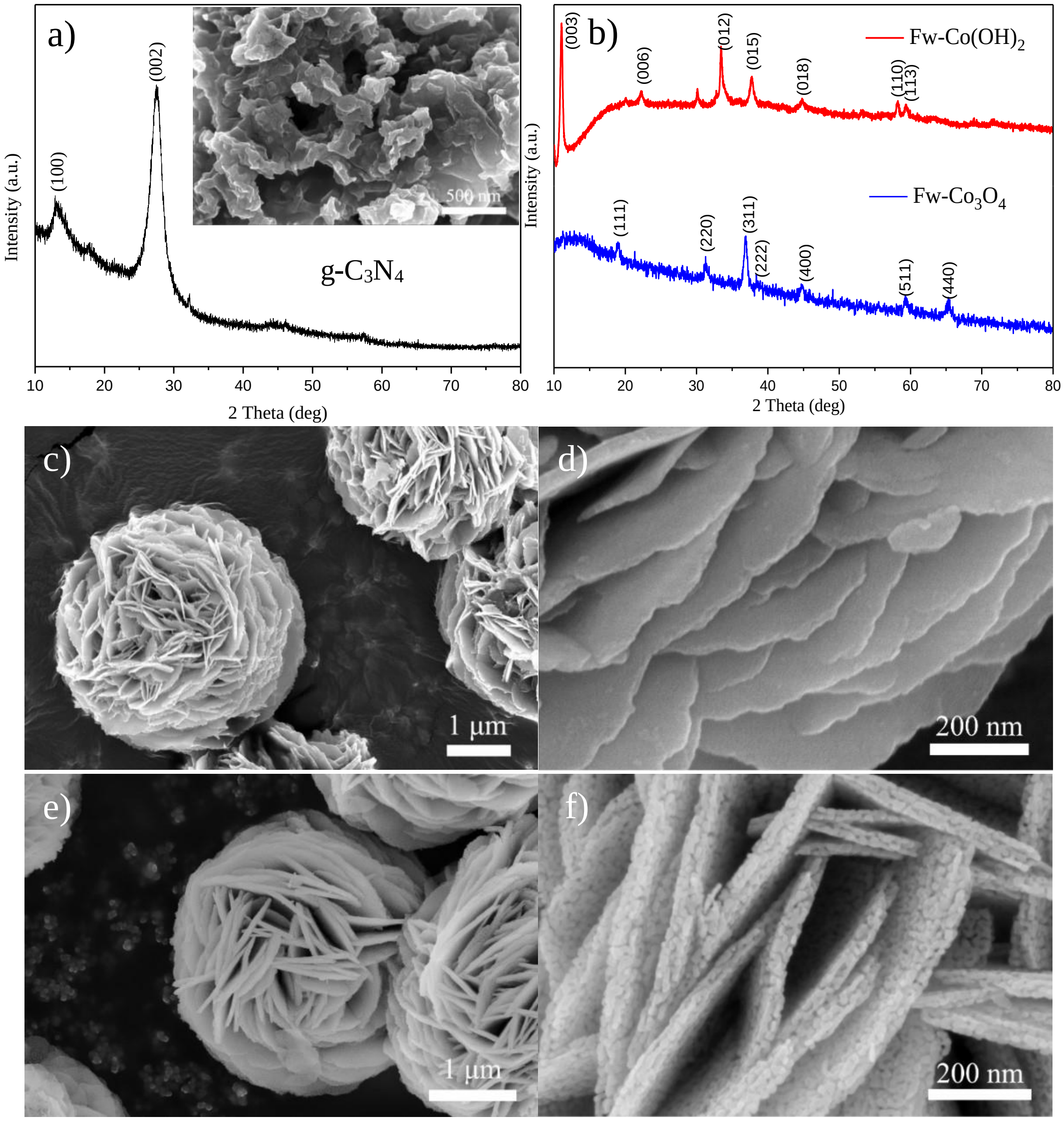

Figure 3.1 XRD patterns of (a) g-C_3N_4, (b) $Co(OH)_2$ and Co_3O_4; SEM images of g-C_3N_4 (inserted in Figure 3.1a), (c, d) $Co(OH)_2$ and (e, f) Co_3O_4.

According to the powder XRD data (Figure 3.1a), a sharp characteristic peak is observed at

27.8°, which corresponds to (002) lattice plane of g-C_3N_4, and reflects the typical interlayer stacking in a conjugated polymers system.[42] As can be seen from the inserted SEM image, morphology feature of g-C_3N_4 also well illustrates a sheet stacking structure. XRD pattern of cobalt hydroxide (Figure 3.1b) displays a prominent diffraction peak of (003) plane, suggesting it grew along the preferred c-axis during crystal growth with a type of α-$Co(OH)_2$ (JCPDS card, No. 46-0605).[43] Furthermore, diffraction peaks of the sample obtained from the calcination of cobalt hydroxide demonstrate a crystal pattern of Co_3O_4 with a spinel structure (JCPDS card, No. 76-1802), indicating its sufficient oxidation during the annealing process. SEM images of $Co(OH)_2$ and Co_3O_4 are displayed in Figures 3.1c-f. As shown, cobalt hydroxide and oxide particles exhibit well-defined floriform morphologies, which are virtually composed of stacked flat slices. The formation of such morphologies is described in Scheme 3.2. The hydrolysis reaction of urea with crystallized water in cobaltous acetate generates OH^- anions, which then react with Co^{2+} to form $Co(OH)_2$. With the assistance of PVP, the hydroxides were assembled into the rod and then flake precipitates, which stacked and formed floriform morphology.[44-45] Interestingly, numerous mesopores are observed on the magnified surface of Co_3O_4 (Figure 3.1f), which is obviously different from $Co(OH)_2$ (Figure 3.1d). Such a mesoporous structure can also be observed in other references which involved urea during synthesis.[46] To assess the textural properties of g-C_3N_4 and its composites with Fw-$Co(OH)_2$ and Fw-Co_3O_4, N_2 adsorption-desorption isotherms were acquired (Figure 3.2). The BET surface area of g-C_3N_4 (54.5 $cm^3\ g^{-1}$) and 3% Fw-$Co(OH)_2/C_3N_4$ (56.2 $cm^3\ g^{-1}$) are similar, while 3% Fw-Co_3O_4/C_3N_4 exhibits a higher value of 68.3 (Figure 3.2a). Pore size distribution (Figure 3.2b) illustrates that there is an increase in the pore volume of Fw-Co_3O_4/C_3N_4, especially in the mesopore-size range, in accordance with SEM observation.[46]

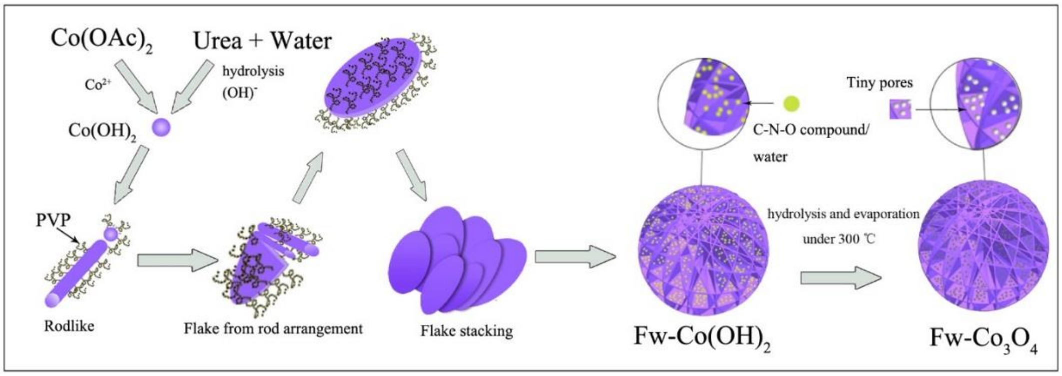

Scheme 3.2 Evolutionary process of surface morphology from Fw-$Co(OH)_2$ to Fw-Co_3O_4 during annealing.

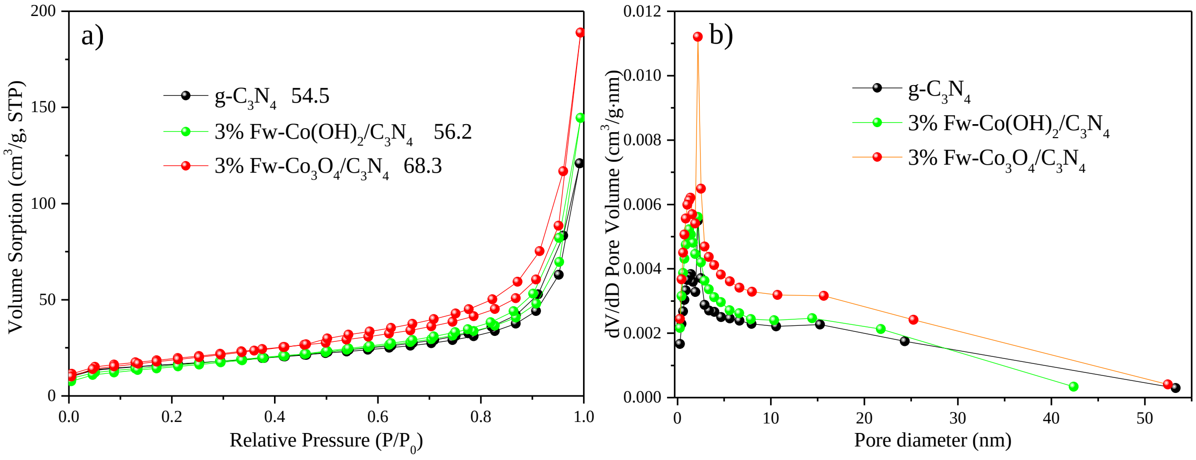

Figure 3.2 a) N_2 adsorption-desorption isotherms, b) Pore size distributions calculated by BJH desorption of g-C_3N_4 and its composites with Co compounds.

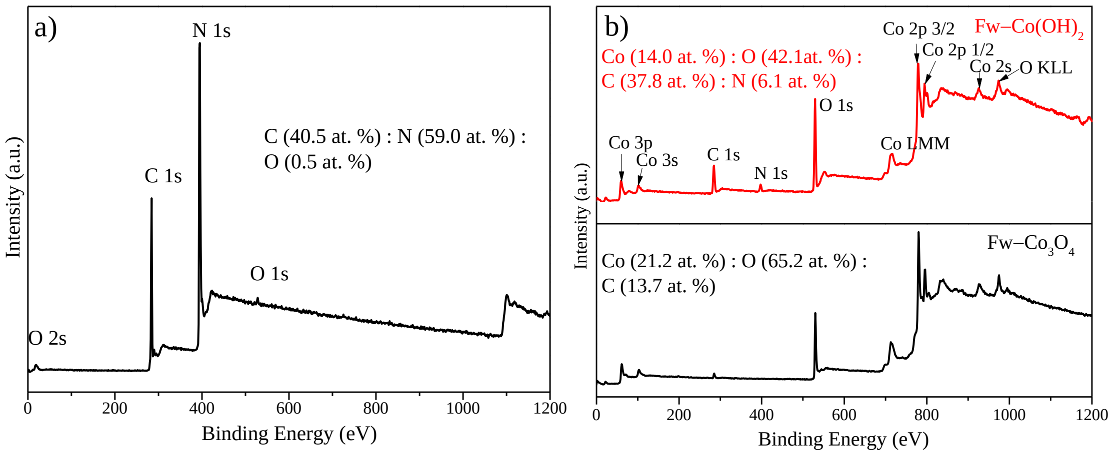

Figure 3.3 XPS survey of (a) C_3N_4, (b) Fw-$Co(OH)_2$ and Fw-Co_3O_4.

Based on XPS analysis (Figure 3.3a), an atomic C/N proportion of 0.69 was measured in g-C_3N_4, and on account of the adsorbed water, slight amount of oxygen was detected (0.5 at.%).[47] High-resolution C 1s and N 1s were shown in Figure 3.4a. The peak at 284.6 eV is a characteristic signal for sp^2-hybridized carbon bonded to nitrogen in g-C_3N_4,[14] while the tale at 290.1 eV is a typical energy loss "shake-up" feature.[48-49] In N 1s (Figure 3.4b), four peaks at 398.7, 399.9, 401.0, and 404.5 eV can be deconvoluted, corresponding to C-N=C, N-$(C)_3$, C-N-H and a shake-up satellite feature, respectively.[14, 49]

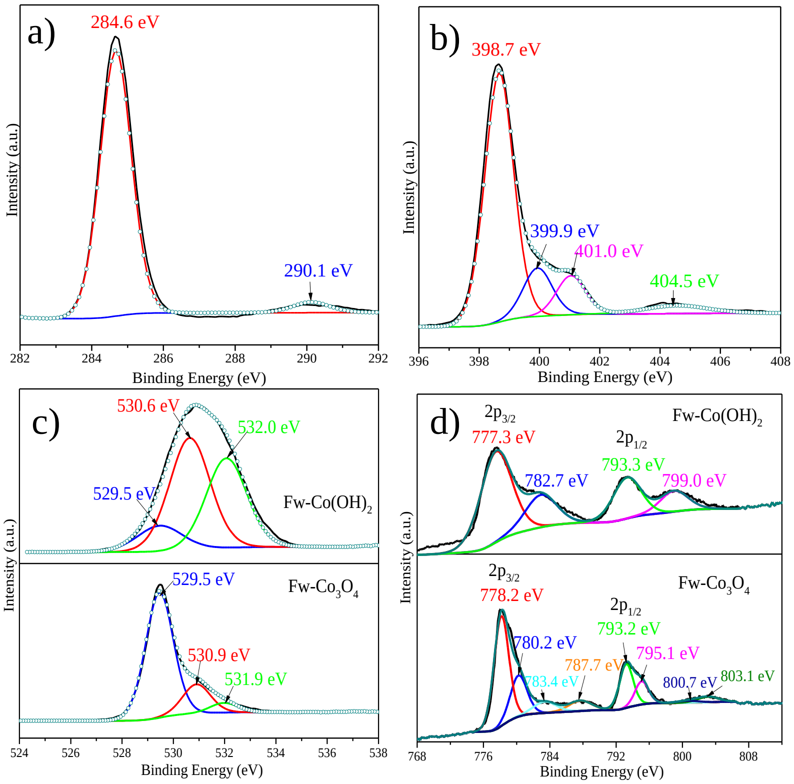

Figure 3.4 (a) C1s and (b) N1s XPS signals for g-C_3N_4, (c) O 1s and (d) Co 2p spectra of Fw-Co(OH)$_2$ and Fw-Co_3O_4.

Full spectrum of Fw-Co(OH)$_2$ (Figure 3.3b) indicates the existence of Co (14.0 at.%), O (42.1 at.%), C (37.8 at.%), and N (6.1 at.%) in the prepared samples, while the surface element contents in Fw-Co_3O_4 were detected to be Co (21.2 at.%), O (65.2 at.%) and C (13.7 at.%). The high contents of C and N in Fw-Co(OH)$_2$ were deduced to be C-N-O by-products of urea during hydrothermal treatment, which are embroiled in lamellas of Fw-Co(OH)$_2$ during its growth process. It is thus reasonable to conclude that the mesopores in the lamellas of Fw-Co_3O_4 are resulted from the decomposition of both hydroxide and numerous C-N-O by-products, as described in Scheme 3.2. Three peaks at 530.6, 532.0 and 529.5 eV fitted in O 1s of Fw-Co(OH)$_2$ are considered to be O from C-O groups, hydroxide, and oxide ions (O^{2-}), respectively.[49-50] In O 1s of Fw-Co_3O_4 (Figure 3.4c), 529.5, 530.9 and 531.9 eV can be ascribed to the lattice oxygen, oxygen species in H_2O and C-O groups, respectively.[50-51] Co 2p analysis of Fw-Co(OH)$_2$ (Figure 3.4d) indicates two pairs of individual peaks at 777.3 and 793.3 eV, corresponding to the Co 2$p_{3/2}$ and Co 2$p_{1/2}$, which are identified as the major binding energies of Co^{2+} in $Co(OH)_2$.[50] Furthermore, the best deconvolution of the Co 2p profile was attained with the assumption of eight species, including two pairs of spin-orbit doublets and their four shakeup satellites (783.4, 787.7, 800.7, and 803.1 eV), indicating the coexistence of Co^{2+} and Co^{3+}.[52]

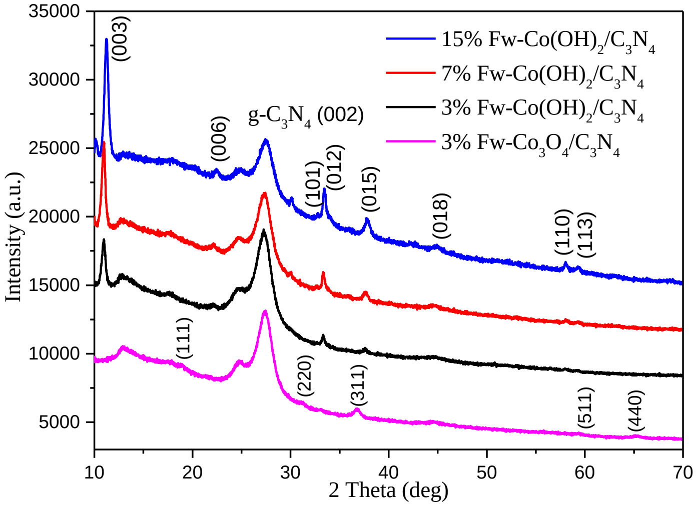

Figure 3.5 Powder X-ray diffraction patterns (XRD) of 3% Fw-Co_3O_4/C_3N_4 and 3%-15% Fw-$Co(OH)_2/C_3N_4$.

When it comes to the hybrid materials, XRD data prove the structure stability of α-$Co(OH)_2$ during the annealing process for recombination with g-C_3N_4, which is highly desirable as α-$Co(OH)_2$ possesses a higher conductivity than β-$Co(OH)_2$. As shown in Figure 3.5, Fw-$Co(OH)_2$/g-C_3N_4 displays the gradual rising diffraction peaks of α-$Co(OH)_2$ with increasing loading amount, meaning no crystal structure transformation with the low-temperature treatment. Besides, the graphite-like structure of g-C_3N_4 does not show obvious changes after annealing with Fw-$Co(OH)_2$. Typical morphologies of the hybridized materials can be well illustrated from SEM images (Figures 3.6-3.8), in which Fw-$Co(OH)_2$ or Fw-Co_3O_4 are well wrapped and infiltrated with g-C_3N_4, proving that they coordinate well in the conjugated system. The 2D-nanosheet-built flower-like interlayers of Fw-$Co(OH)_2$ or Fw-Co_3O_4 can serve as a well-defined support for g-C_3N_4 to disperse, which is optimal for light-harvesting and electron conduction. Further, as we can see from Figures 3.7a and 3.8a, which were captured under a relative lower magnification, Fw-$Co(OH)_2$ and Fw-Co_3O_4 particles were immersed well into a broader g-C_3N_4 matrix. The coordination and interfaces between these units were tested by EDS mapping of 3% Fw-$Co(OH)_2/C_3N_4$ (Figure 3.6c) and HAADF-

STEM mapping of 3% Co_3O_4/g-C_3N_4 (Figure 3.8c).

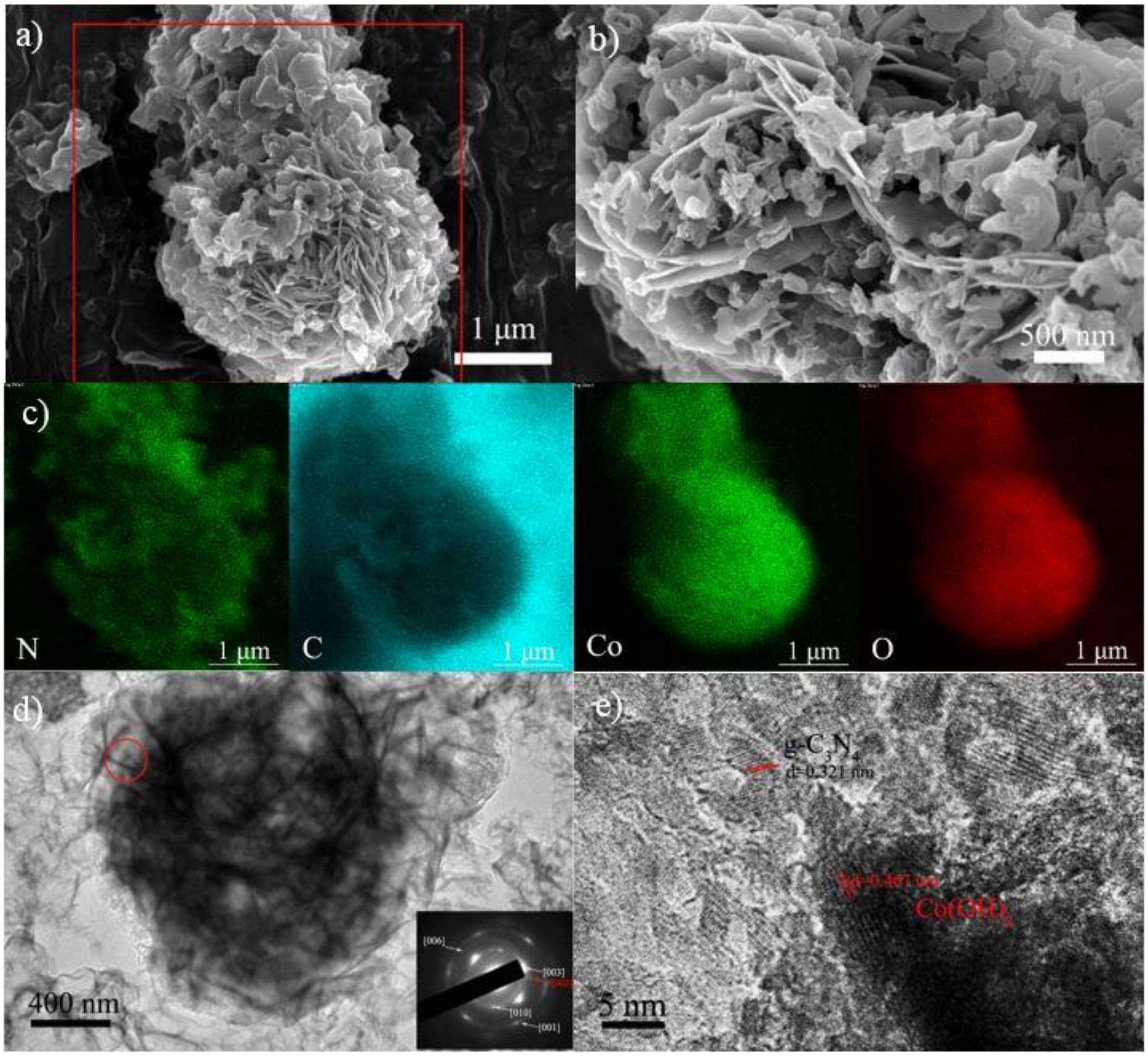

Figure 3.6 (a, b) SEM images, (c) EDS mapping of the marked area in a, (d) TEM and (e) HRTEM images of 3% Fw-$Co(OH)_2$/C_3N_4.

The graphite-like nanosheet-structure of g-C_3N_4 can be well illustrated in TEM image (Figure 3.9a). TEM characterization of the hybrids (Figures 3.6d, 3.9b) clearly shows that g-C_3N_4 can be successfully attached to the interlayers and surfaces of Fw-$Co(OH)_2$ and Fw-Co_3O_4. HRTEM images (Figures 3.6e and 3.9c) display a lattice interval of 0.32 nm, corresponding to (002) plane of g-C_3N_4.[53] Meanwhile, an interlayer spacing of 0.47 nm can be identified to (001) plane of $Co(OH)_2$ (Figure 3.6e), whereas 0.24 nm lattice fringe can be assigned to (311) plane of Co_3O_4 (Figure 3.9c). Inserted selective area electron diffraction (SAED) graph shows a classifiable ring structure characteristic for polycrystalline materials of $Co(OH)_2$ and g-C_3N_4 (Figure 3.6d). In addition, HRTEM with Fast Fourier Transform (FFT) in Figure 3.9c characterizes the interfaces region between spinel Co_3O_4 and g-C_3N_4.

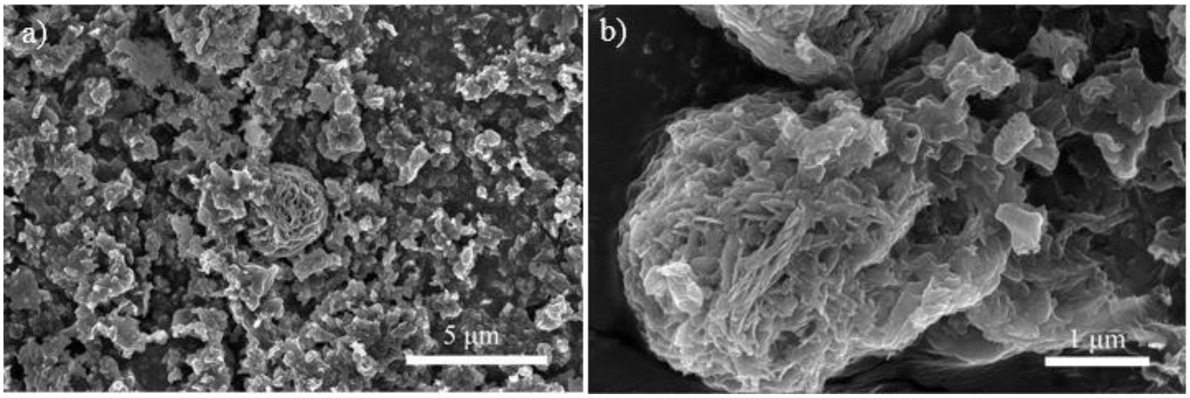

Figure 3.7 SEM images of (a) 3% Fw-$Co(OH)_2/C_3N_4$ under wide field and (b) 7% Fw-$Co(OH)_2/C_3N_4$ composites.

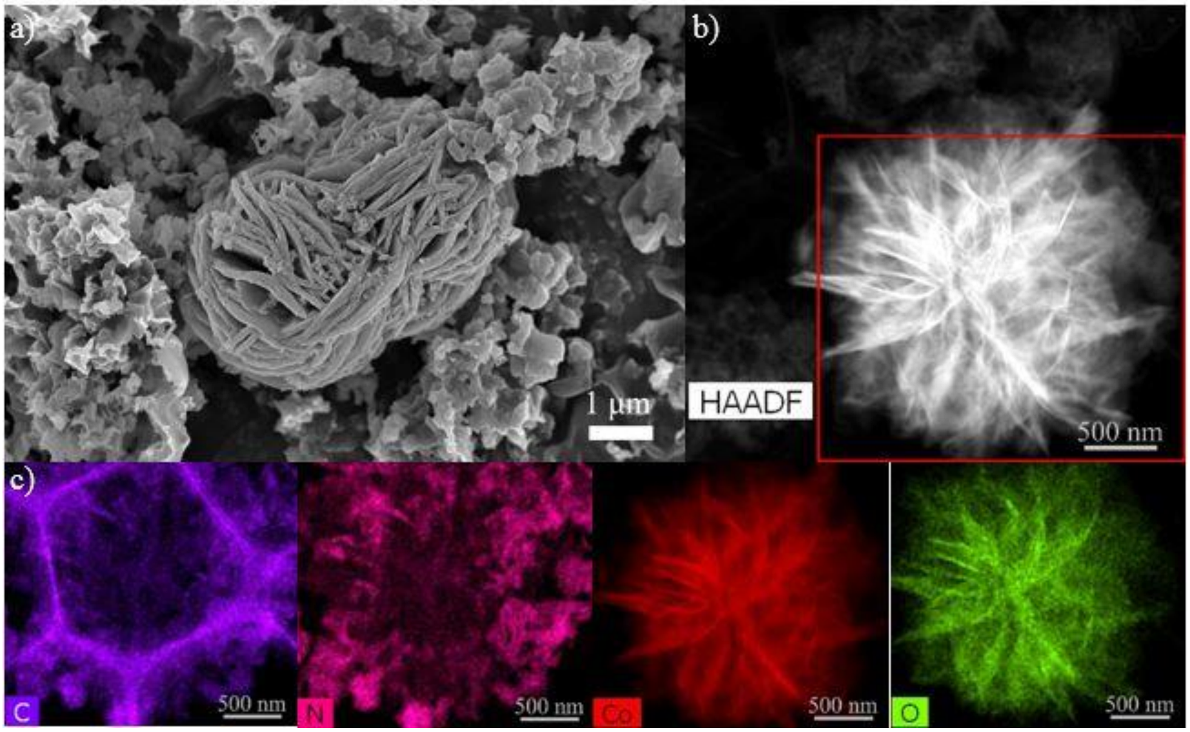

Figure 3.8 (a) SEM and (b) HAADF-STEM images of 3% Fw-Co_3O_4/C_3N_4; (c) the corresponding STEM mapping (C, N, Co, O) of the marked region in b.

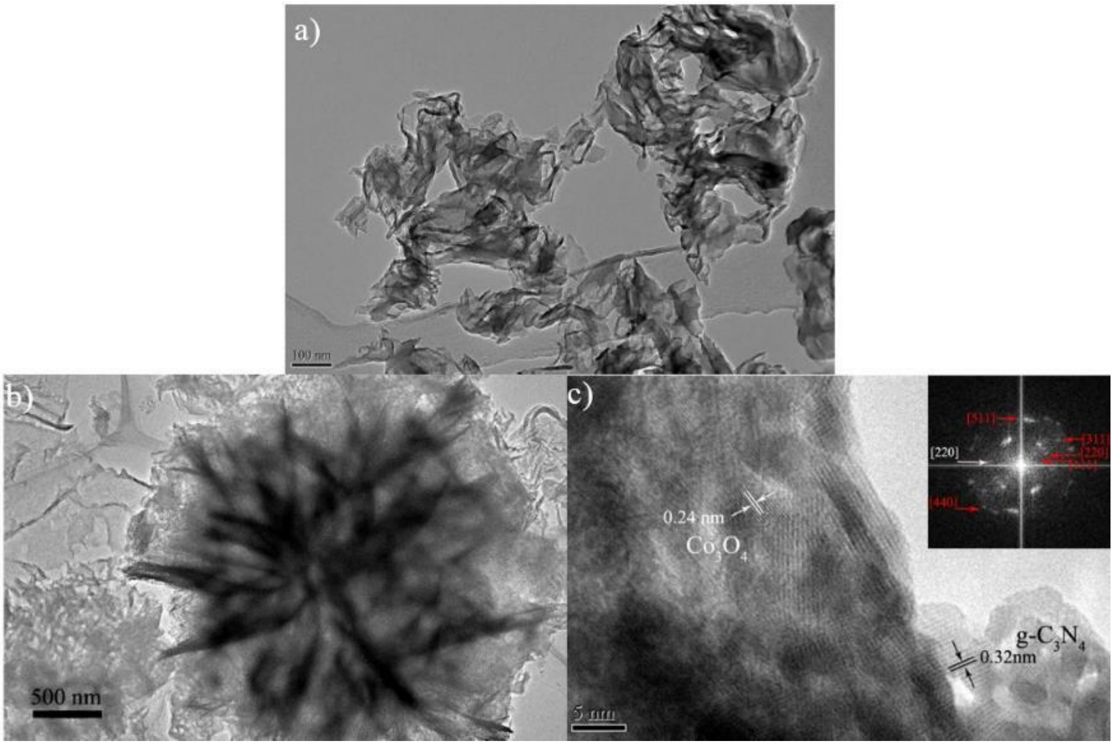

Figure 3.9 (a) TEM image of pure g-C_3N_4, (b) TEM and (c) HRTEM of Fw-Co_3O_4/C_3N_4.

UV-Vis diffuse reflectance spectra (DRS) were acquired (Figure 3.10a) and converted into absorbance via the Kubelka-Munk function $F(R) = (1-R)^2/2R = K/S$, where R is the diffuse reflectance, K is the absorption and S is the scattering coefficient. Obviously, all the absorption spectra exhibit steep edges at the wavelength of around 450 nm, which can be attributed to the band gap transition. It is noted that there is an increase of optical absorption in wavelengths ranging from 430 to 750 nm, after loading Fw-$Co(OH)_2$ or Fw-Co_3O_4 onto g-C_3N_4. In other words, better absorption occurred in the visible spectrum region on the composites. The accelerated charge carrier transfer was investigated through room temperature photoluminescence (PL) spectra (inset picture in Figure 3.10a). As shown, when the exciting light irradiates on the composites, the quenching is more remarkable compared with pristine g-C_3N_4.

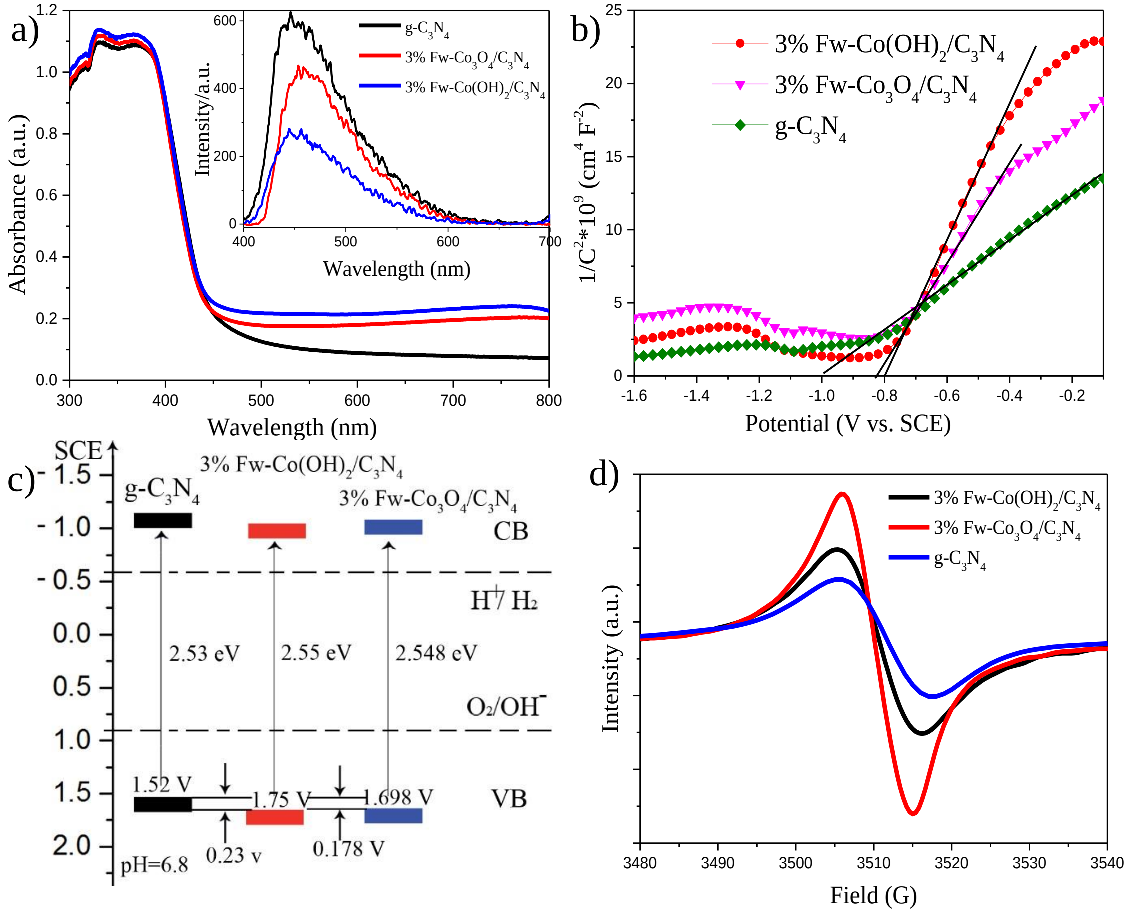

Figure 3.10 (a) UV-vis absorption spectra, and PL (inserted graph), (b) Electrochemical Mott-Schottky plots, (c) Band structure diagram of g-C_3N_4 and corresponding composites, (d) Room temperature EPR spectra of g-C_3N_4, 3% Fw-$Co(OH)_2/C_3N_4$ and 3% Fw-Co_3O_4/C_3N_4.

Mott-Schottky relationship ($1/C^2$ vs E, (MS)) for g-C_3N_4, 3% Fw-$Co(OH)_2/C_3N_4$ and 3% Fw-Co_3O_4/C_3N_4 were investigated and combined with UV-Vis DRS to determine the changes of band structure of g-C_3N_4, 3% Fw-$Co(OH)_2/C_3N_4$ and 3% Fw-Co_3O_4/C_3N_4. Figure 3.10b features a typical n-type semiconductor for all the three materials. The flat band potential values (E_{fb}) of g-C_3N_4, 3% Fw-$Co(OH)_2/C_3N_4$ and 3% Fw-Co_3O_4/C_3N_4 were calculated to be -1.01, -0.80, and -0.85 V, respectively, versus the saturated calomel electrode (SCE). Relatively positive flat band potential of the composites reflects the weaker upward band bending of g-C_3N_4, originating from its n-type semiconductor properties.[39, 54] Further, a positive shift of the flat band potential demonstrates that a heterojunction forms at the interface between g-C_3N_4 and Fw-$Co(OH)_2$. As a result, the valence band position of 3% Fw-$Co(OH)_2/C_3N_4$ and 3% Fw-Co_3O_4/C_3N_4 will be more positive, which will be further confirmed by the extrapolation method (Figure 3.11) and band structure diagram (Figure 3.10c).[54]

The bandgap energy of the sample was determined using the following equation: $(\alpha h\nu)^n = k(h\nu - Eg)$.[15] α is the absorption factor, $h\nu$ is the energy quantum, k is a material determined constant and n equals 0.5. As shown in Figure 3.11, the plots of $(\eta h\nu)^{1/2}$ versus hν (Kubelka-Munk) were transformed from UV-vis DRS spectra according to the above equation. The intercepts were obtained at 2.53, 2.55, and 2.48 eV for g-C_3N_4, 3% Fw-$Co(OH)_2$ and 3% Fw-Co_3O_4, respectively, which correspond to their bandgap energies. Combined with the Mott-Schottky plots and the band gap, values of the valence band (VB) are +1.52, +1.75, +1.70 V for g-C_3N_4, Fw-$Co(OH)_2$/g-C_3N_4 and Fw-Co_3O_4/g-C_3N_4, respectively. Values of the conduction band (CB) can be estimated based on the E_{fb} values, to be -1.01, -0.80, and -0.85 V. Based on these values, a band structure diagram was plotted (Figure 3.10c). The formed heterojunction and positively shifted band alignment can elevate the separation efficiency of the photogenerated holes and electrons, favorable for more efficient photocatalytic water oxidation.

Figure 3.10d shows the spectra of room-temperature electron paramagnetic resonance (EPR) of g-C_3N_4, 3% Fw-$Co(OH)_2/C_3N_4$ and 3% Fw-Co_3O_4/C_3N_4. All the compounds including g-C_3N_4 presented one single Lorentzian line with a g value of 2.003, derived from the delocalized π-bonded system of carbon nitride.[55] Interestingly, the signals of 3% Fw-$Co(OH)_2$/g-C_3N_4 has some degrees of fluctuation compared with pure g-C_3N_4. This further exemplified that the essential band structure and texture of g-C_3N_4 are influenced slightly after being coated with Fw-$Co(OH)_2$. Fw-Co_3O_4/g-C_3N_4 exhibits the highest peak, suggesting the extended π-bonding caused by the repolymerization of the redundant s-triazine units during annealing progress at higher temperature.

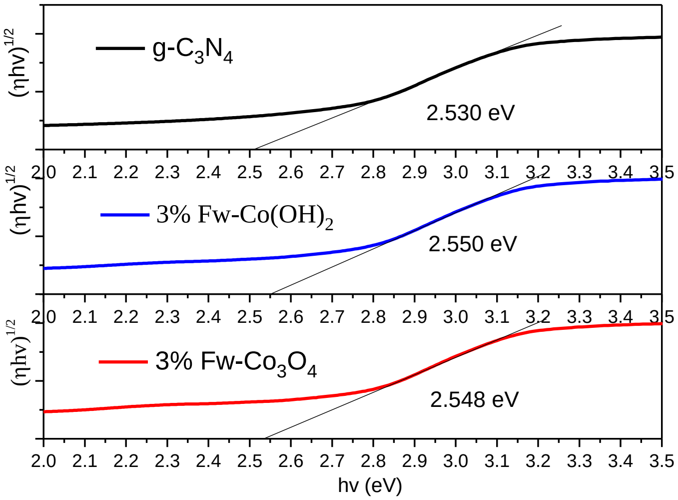

Figure 3.11 The lines of transformed Kubelka-Munk functions versus the light energy.

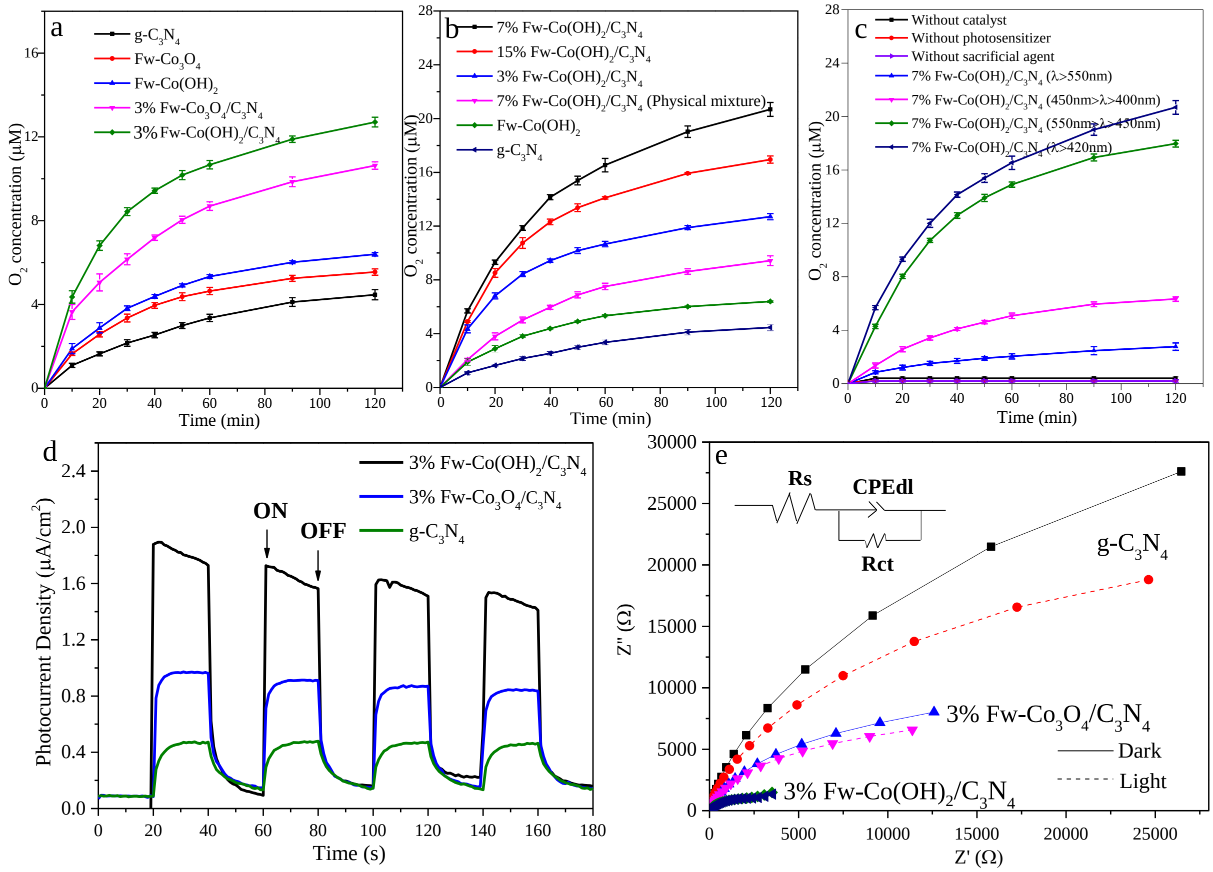

Figure 3.12 Heterogeneous water oxidation of (a), (b) on different samples, (c) in different conditions (Error bar: standard deviation), (d) Photo-electric properties of g-C_3N_4, 3% Fw-Co(OH)$_2$/C_3N_4 and 3% Fw-Co_3O_4/C_3N_4, and (e) Electrochemical impedance spectroscopy under dark and light condition.

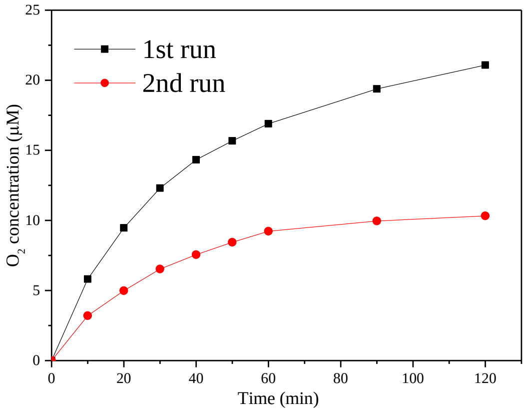

Figure 3.13 Recycling water oxidation performance of 7% Fw-$Co(OH)_2$/g-C_3N_4.

Photocatalytic water oxidation of the as-prepared samples were conducted under visible light irradiations ($\lambda > 420$ nm), using persulfate ($S_2O_8^{2-}$) as a sacrifice oxidant for the reduction reaction, whereas tris (2,2'-bipyridine) ruthenium(II) ($Ru(bpy)_3^{2+}$) as a one-electron oxidant photosensitizer to promote multiple-electron water oxidation kinetics and avoid excessive driving potentials.[41, 56] Figure 3.12a describes the time dependence of oxygen concentration over the synthesized catalysts, among which 3% Fw-$Co(OH)_2$/C_3N_4 displayed the best performance, followed by 3% Fw-Co_3O_4/C_3N_4, Fw-$Co(OH)_2$, Fw-Co_3O_4 and g-C_3N_4. It is also observed that the reaction rates show an inevitable slowdown trend for all the catalysts with longer reaction time. This can be explained by two possible reasons, e.g. the consumption of sacrificial agents $[S_2O_8]^{2-}$, and the quenching and decomposition of photosensitizers.[41, 56] Actually, $Co(OH)_2$ and Co_3O_4 are also semiconductor materials. The observable O_2 evolution by pure $Co(OH)_2$ indicates that it can work alone for photocatalytic water oxidation. Even though the activity is low, the results suggest that electrons can be transferred from $Co(OH)_2$ to $[Ru(bpy)_3]^{3+}$ molecules and oxidize water upon photo-irradiation.[5] Fw-Co_3O_4 exhibited an inferior but observable catalytic oxygen evolution performance compared with Fw-$Co(OH)_2$. For optimization of the oxygen production efficiency, different ratios of Fw-$Co(OH)_2$ (3 wt.%, 7 wt.%, and 15 wt.%) were loaded onto g-C_3N_4. Figure 3.12b displays that, as the weight ratio of Fw-$Co(OH)_2$ increased to 7 wt.%, oxygen production concentration significantly increased. When the ratio was further elevated to 15 wt.%, the rate slightly decreased, as extravagant loading of Fw-$Co(OH)_2$ might block the optical absorption of g-C_3N_4. The water oxidation performance of physically mixed 7%

Fw-Co(OH)$_2$/g-C$_3$N$_4$ was also conducted. It is worth noting that the sample exhibited a higher rate of O$_2$ evolution than both g-C$_3$N$_4$ and Fw-Co(OH)$_2$, however, the activity was still much lower than that of the annealed hybrid material.(Figure 3.12b) Recycling experiments were conducted using the collected sample of 7% Fw-Co(OH)$_2$/C$_3$N$_4$ after the first-run. The performance of the catalyst in the second run is presented in Figure 3.13, achieving about 50% retention. A similar pattern was reported in Ref. [5]. These results suggest that the synergistic and heterojunction interaction between Fw-Co(OH)$_2$ and g-C$_3$N$_4$ are crucial for the visible-light water oxidation activity. The apparent quantum efficiency (AQE) under a irradiation at λ=450 nm for 7% Fw-Co(OH)$_2$/g-C$_3$N$_4$ was calculated to be approximately 0.16 %. Furthermore, the OER activity of 7% Fw-Co(OH)$_2$/g-C$_3$N$_4$ is among the best cocatalyst/g-C$_3$N$_4$ composites under visible light irridation in comparision to recent studies (Table 3.1).

Table 3.1 Photocatalytic activities of modified g-C$_3$N$_4$ catalysts for O$_2$ evolution.

Catalyst	**Catalyst addition amount (g)**	**Irradiation wavelength (nm)**	**Oxygen evolution (μmol h^{-1})**	**Reactant solution Volume (mL)**	**Reference**
RuO$_2$ (3.0wt%)/g-C$_3$N$_4$	0.1	>420 nm	1.2	100	[13]
3.0 wt% RuO$_2$/g-C$_3$N$_4$	0.1	>420 nm	0.9	100	[57]
RuO$_2$ coated g-C$_3$N$_4$	-	UV+visible	9	32	[11]
PMDA incorporated g-C$_3$N$_4$	0.2	>420 nm	3.5	400	[12]
3 wt% Co$_3$O$_4$/HR-CN	0.02	>300 nm	3.0	100	[7]
mpg-C$_3$N$_4$	0.05	>420 nm	3.8	100	[54]
CoSe$_2$/g-C$_3$N$_4$	0.05	> 420 nm	9.0	100	[34]
S-Co-g-C$_3$N$_4$	0.05	> 420 nm	12.5 / 1st hour	100	[58]
3wt% FwCo$_3$O$_4$/g-C$_3$N$_4$	0.05	>420 nm	1.9 (± 0.4%)	50	This work
7wt% Fw-Co(OH)$_2$/g-C$_3$N$_4$	0.05	>420 nm	3.7 (± 1%)	50	This work

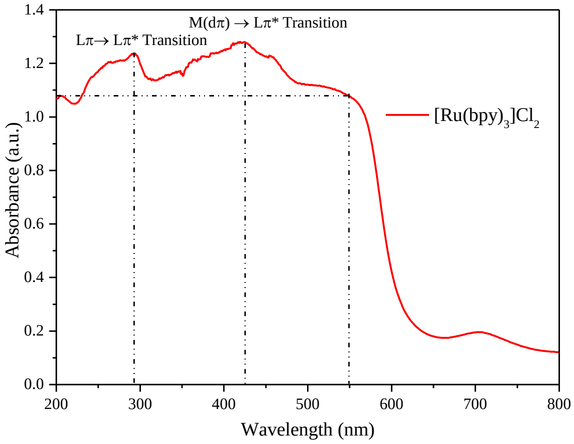

Figure 3.14 UV-vis absorption spectra of photosensitizer $[Ru(bpy)_3]Cl_2$. (There is a typical inter ligand π→π* transition at 290 nm (UV-range), while another obvious peak centering at around 430 nm and extending to 550 nm (visible-light range) could be distinguished due to the metal-to-ligand dπ ⟶ π* charge transition.)

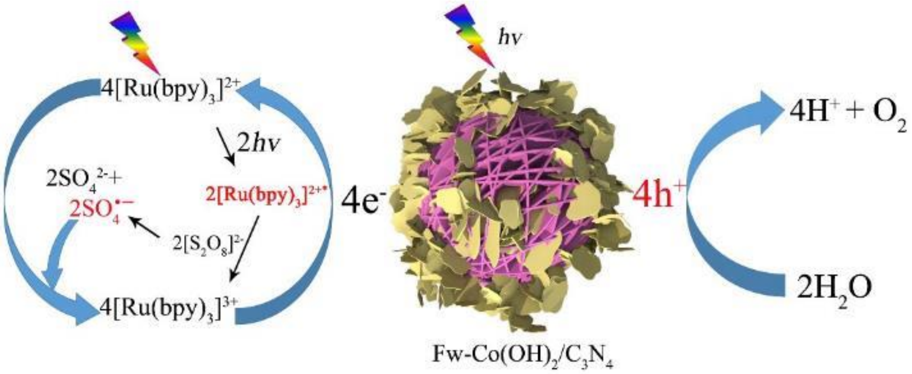

Scheme 3.3 Heterogeneous water oxidation system catalyzed by Fw-$Co(OH)_2$/Fw-Co_3O_4 deposited g-C_3N_4.

For the mechanistic studies, experiments without a photosensitizer, a catalyst or a sacrificial agent were performed (Figure 3.12c). Almost no activity was observed, indicating that Fw-$Co(OH)_2/C_3N_4$, $[Ru(bpy)_3]^{2+}$ and $Na_2S_2O_8$ are critical for the whole oxygen evolution processes. Since both 7% Fw-$Co(OH)_2/C_3N_4$ and $[Ru(bpy)_3]^{2+}$ can absorb visible light, band-pass filters were employed to differentiate their individual photo-absorption wavelength for oxygen evolution reaction. 7% Fw-$Co(OH)_2/C_3N_4$ indicates strong absorption mainly in the range of 400 to 450 nm (Figure 3.10a), while $[Ru(bpy)_3]Cl_2{\bullet}6H_2O$ (Figure 3.14) displays wide and strong visible light absorption in 400-550 nm. Therefore, three wavelength ranges were selected at 400-450, 450-550 and > 550 nm, respectively. O_2 evolution rates using 7% Fw-$Co(OH)_2/C_3N_4$ under the three ranges are depicted in Figure 3.12c. Under a wide range irradiation of 450 to 550 nm, in which 7% Fw-$Co(OH)_2/C_3N_4$ shows weak absorption, and the O_2 evolution rate only displayed a slight decay compared with that performed under the full visible light range. However, in 400-450 nm, which is the strongest absorption range for 7% Fw-$Co(OH)_2/C_3N_4$ and a relatively narrow range for $[Ru(bpy)_3]Cl_2{\bullet}6H_2O$, the activity was significantly weakened. For wavelength longer than 550 nm, the performance was further lowered. Therefore, we can conclude that $[Ru(bpy)_3]^{2+}$ acted as a photon acquisition agent. The complete diagram of the reaction mechanism during water oxidation is illustrated in Scheme 3.3. As shown, $[Ru(bpy)_3]^{2+}$ could trap the same equivalent of photons from the incident light and be activated to the metal-to-ligand charge-transfer (MLCT) excited state $[Ru(bpy)_3]^{2+*}$. $[Ru(bpy)_3]^{2+*}$ can be quenched by $S_2O_8^{2-}$, resulting in SO_4^{2-}, $SO_4^{\bullet-}$ (sulfate radical) and $[Ru(bpy)_3]^{3+}$. $SO_4^{\bullet-}$ can then oxidize other $[Ru(bpy)_3]^{2+}$ to $[Ru(bpy)_3]^{3+}$. Upon irradiation, electrons and holes are activated and separated from Fw-$Co(OH)_2/C_3N_4$, and then the photogenerated electrons transfer to $[Ru(bpy)_3]^{3+}$ regenerating $[Ru(bpy)_3]^{2+}$, leading to O_2 evolution via water oxidation. The redox process can be verified by the room temperature EPR under in-situ irradiation (Figure 3.15). When the reaction solution was irradiated for 30 s, distinct signal of $SO_4^{\bullet-}$ can be observed. Meanwhile, the $OH^{\bullet-}$ (hydroxyl radical) oxidized from water molecules during the catalytic half-reaction can be also detected. Due to the small capacity limitation of EPR capillary and the consumption for $[Ru(bpy)_3]^{2+}$ oxidation, the produced signals of $SO_4^{\bullet-}$ and $OH^{\bullet-}$ were quenched under longer time irradiations.

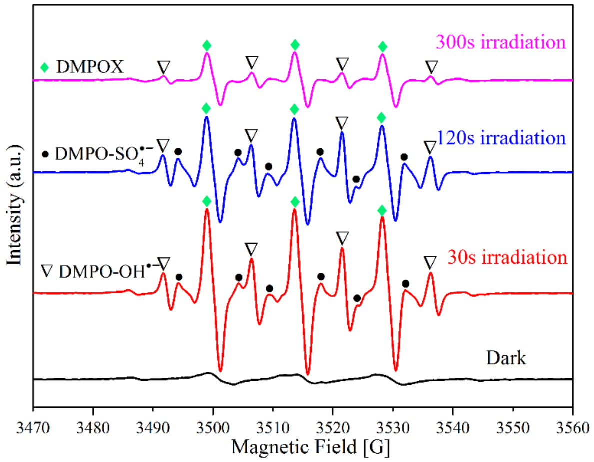

Figure 3.15 Room temperature EPR signals of DMPO-$OH^{\bullet-}$ and DMPO-$SO4^{\bullet-}$ adducts produced by water oxidation system under visible light irradiation (DMPO was adopted as a

spin-trapping agent to capture the free radicals. DMPOX was denoted as the oxidized DMPO; microwave power, 1 mW; field modulation, 0.02 mT; DMPO, 0.16 M)

To explain the catalytic performance of the acquired catalysts, photoelectrochemical tests were performed under dark or visible light irradiations ($\lambda > 420$ nm). As shown in Figure 3.12d, the photocurrent intensity of 3% Fw-$Co(OH)_2/C_3N_4$ is about 4 times as high as that of pristine g-C_3N_4 in the first cycle. Fw-Co_3O_4/C_3N_4 is inferior, yet still stronger than pure g-C_3N_4, consistent with their OER performance. It is thought that Fw-$Co(OH)_2$/Fw-Co_3O_4 can promote the separation and transfer efficiency of the charge carrier of g-C_3N_4, resulting in more intense photocurrent response of the hybrids and better OER effect, as described in Scheme 3.3. This can be further supported by the electrochemical Nyquist program tests (Figure 3.12e), which are commonly adopted to evaluate electron transfer abilities. In electrochemical impedance spectra (EIS), the high frequency zone corresponds to a charge transfer limiting process and can be related to the charge transfer resistance (Rct) in the contacting interface with double-layer capacitance (CPEdl) (As shown in the inset equivalent circuit, Rs is the solution resistance).[14, 59] The arc radius of 3% Fw-$Co(OH)_2$/ C_3N_4 is the smallest, followed by 3% Fw-Co_3O_4/C_3N_4, implying their better charge transfer ability than pure g-C_3N_4.

The more excellent modification on g-C_3N_4 by Fw-$Co(OH)_2$ than Fw-Co_3O_4 can be virtually ascribed to the prominent hydrotalcite-like structure of α-$Co(OH)_2$, whose layered double hydroxyl (LDH) groups provide a more effective layered channel for transfer of photogenerated holes in g-C_3N_4 to $Co(OH)_2$, as illustrated in Scheme 3.4.[60-62] However, due to spinel structure of Co_3O_4, the excited holes are transmitted saltatorily between Co^{2+} (tetrahedral interstice) and Co^{3+} (octahedral interstices), resulting in its relatively inefficient rate of charge transfer comparing with Fw-$Co(OH)_2$.[63] Further, the active sites in Co_3O_4 are limited to an exclusive octahedral Co^{3+} because Co^{2+} is ineffective in the spinel crystal structure.[26] However, the flexible oxidoreduction transformation of dissimilar valence states (Co^{2+}, Co^{3+}) are able to happen in Fw-$Co(OH)_2$ with hydrotalcite-like LDH.[64] Apart from the inefficiency of assistant separation of photogenerated electrons and holes, the darker color of the cobalt oxide results in the higher photoelectron absorption ability with a relatively lower release rate.[14]

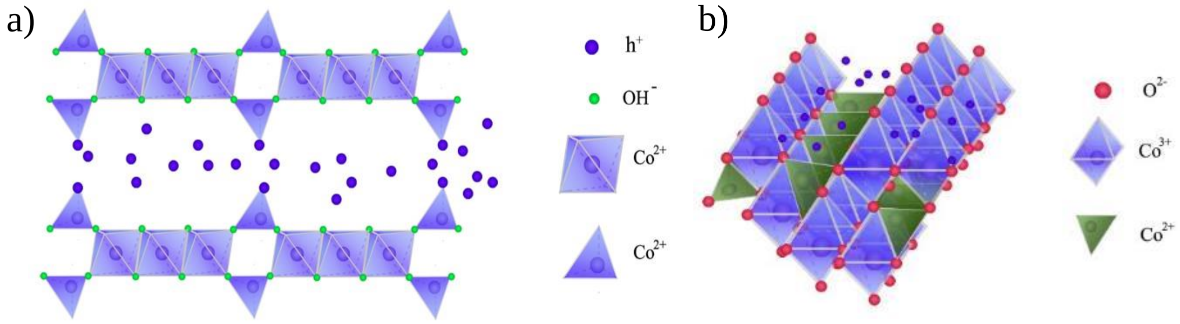

Scheme 3.4 (a) Schematic drawings of α-$Co(OH)_2$ with hydrotalcite structure with layered double hydroxyl (LDH) groups, (b) Co_3O_4 with a spinel structure.

3.4 Conclusions

In summary, we have shown that 2D pristine g-C_3N_4 closely decorated with flower-like cobalt hydroxide/oxide composites, developed by a simple coating route, are effective catalysts for water oxidation under visible-light irradiations. Slight amount of Co specie introduction and heterojunction construction have a positive effect on electron-hole separation, charge carriers transfer rate and electronic conductivity of g-C_3N_4, which result in more active photocatalytic OER activities. Owing to superior electron transfter ability of hydrotalcite structure in α-$Co(OH)_2$, Fw-$Co(OH)_2$/g-C_3N_4 possesses a more excellent OER activity than Fw-Co_3O_4/g-C_3N_4. 7 wt.% loading amount of Fw-$Co(OH)_2$ onto g-C_3N_4 displayed the best photocatalytic capability. This study provides a fresh insight into the use of non-noble OER cocatalysts decorated g-C_3N_4 for water oxidation in aqueous phase.

References

1) Kim, T. W.; Ping, Y.; Galli, G. A.; Choi, K. S., Simultaneous Enhancements in Photon Absorption and Charge Transport of Bismuth Vanadate Photoanodes for Solar Water Splitting. *Nature Communications* **2015,** *6*, 8769.

2) Carroll, G. M.; Zhong, D. K.; Gamelin, D. R., Mechanistic Insights into Solar Water Oxidation by Cobalt-Phosphate-Modified Alpha-Fe_2O_3 Photoanodes. Energy & Environmental Science **2015,** *8*, 577.

3) Sharma, P. P.; Wu, J. J.; Yadav, R. M.; Liu, M. J.; Wright, C. J.; Tiwary, C. S.; Yakobson, B. I.; Lou, J.; Ajayan, P. M.; Zhou, X. D., Nitrogen-Doped Carbon Nanotube Arrays for High-Efficiency Electrochemical Reduction of CO_2: On the Understanding of Defects, Defect Density, and Selectivity. *Angewandte Chemie-International Edition* **2015,** *54*, 13701.

4) Yang, Y.; Fei, H.; Ruan, G.; Tour, J. M., Porous Cobalt-Based Thin Film as a Bifunctional Catalyst for Hydrogen Generation and Oxygen Generation. *Advanced Materials* **2015,** *27*, 3175.

5) Maeda, K.; Ishimaki, K.; Tokunaga, Y.; Lu, D.; Eguchi, M., Modification of Wide-Band-Gap Oxide Semiconductors with Cobalt Hydroxide Nanoclusters for Visible-Light Water Oxidation. *Angewandte Chemie International Edition* **2016**, *55*, 8309.

6) Zhang, J.; Zhang, G.; Chen, X.; Lin, S.; Mohlmann, L.; Dolega, G.; Lipner, G.; Antonietti, M.; Blechert, S.; Wang, X., Co-Monomer Control of Carbon Nitride Semiconductors to Optimize Hydrogen Evolution with Visible Light. *Angewandte Chemie International Edition* **2012,** *51*, 3183.

7) Zheng, Y.; Lin, L.; Ye, X.; Guo, F.; Wang, X., Helical Graphitic Carbon Nitrides with Photocatalytic and Optical Activities. *Angewandte Chemie International Edition* **2014,** *53*, 11926.

8) Dong, X. P.; Cheng, F. X., Recent Development in Exfoliated Two-Dimensional g-C_3N_4 Nanosheets for Photocatalytic Applications. *Journal of Materials Chemistry A* **2015,** *3*, 23642.

9) Cao, S.; Low, J.; Yu, J.; Jaroniec, M., Polymeric Photocatalysts Based on Graphitic Carbon Nitride. *Advanced Materials* **2015,** *27*, 2150.

10) Niu, P.; Zhang, L.; Liu, G.; Cheng, H.-M., Graphene-Like Carbon Nitride Nanosheets for Improved Photocatalytic Activities. *Advanced Functional Materials* **2012,** *22*, 4763.

11) Jorge, A. B.; Martin, D. J.; Dhanoa, M. T. S.; Rahman, A. S.; Makwana, N.; Tang, J.; Sella, A.; Corà, F.; Firth, S.; Darr, J. A.; McMillan, P. F., H_2 and O_2 Evolution from Water Half-Splitting Reactions by Graphitic Carbon Nitride Materials. *The Journal of Physical Chemistry C* **2013,** *117*, 7178.

12) Chu, S.; Wang, Y.; Guo, Y.; Feng, J.; Wang, C.; Luo, W.; Fan, X.; Zou, Z., Band Structure Engineering of Carbon Nitride: In Search of a Polymer Photocatalyst with High Photooxidation Property. *ACS Catalysis* **2013,** *3*, 912.

13) Maeda, K.; Wang, X. C.; Nishihara, Y.; Lu, D. L.; Antonietti, M.; Domen, K., Photocatalytic Activities of Graphitic Carbon Nitride Powder for Water Reduction and Oxidation under Visible Light. *The Journal of Physical Chemistry C* **2009,** *113*, 4940.

14) Zhang, G. G.; Zang, S. H.; Wang, X. C., Layered $Co(OH)_2$ Deposited Polymeric Carbon Nitrides for Photocatalytic Water Oxidation. *ACS Catalysis* **2015,** *5*, 941.

15) Tian, N.; Huang, H.; Liu, C.; Dong, F.; Zhang, T.; Du, X.; Yu, S.; Zhang, Y., In Situ Co-Pyrolysis Fabrication of CeO_2/g-C_3N_4 n–n Type Heterojunction for Synchronously Promoting Photo-Induced Oxidation and Reduction Properties. *Journal of Materials Chemistry A* **2015,** *3*, 17120.

16) Zhang, S.; Pan, N., Supercapacitors Performance Evaluation. *Advanced Energy Materials* **2015,** *5*, 1401401.

17) Algara-Siller, G.; Severin, N.; Chong, S. Y.; Bjorkman, T.; Palgrave, R. G.; Laybourn, A.; Antonietti, M.; Khimyak, Y. Z.; Krasheninnikov, A. V.; Rabe, J. P.; Kaiser, U.; Cooper, A. I.; Thomas, A.; Bojdys, M. J., Triazine-Based Graphitic Carbon Nitride: A Two-Dimensional Semiconductor. *Angewandte Chemie International Edition* **2014,** *53*, 7450.

18) Bojdys, M. J.; Muller, J. O.; Antonietti, M.; Thomas, A., Ionothermal Synthesis of Crystalline, Condensed, Graphitic Carbon Nitride. *Chemistry-A European Journal* **2008,** *14*, 8177.

19) Zhang, G.; Lan, Z.-A.; Lin, L.; Lin, S.; Wang, X., Overall Water Splitting by Pt/g-C_3N_4 Photocatalysts without Using Sacrificial Agents. *Chemical Science* **2016,** *7*, 3062.

20) Cui, Y.; Ding, Z.; Fu, X.; Wang, X., Construction of Conjugated Carbon Nitride Nanoarchitectures in Solution at Low Temperatures for Photoredox Catalysis. *Angewandte Chemie International Edition* **2012,** *51*, 11814.

21) He, M. S.; Zhou, S.; Zhang, J.; Liu, Z. F.; Robinson, C., CVD Growth of N-Doped Carbon Nanotubes on Silicon Substrates and its Mechanism. *Journal of Physical Chemistry B* **2005,** *109*, 9275.

22) Zhang, J.; Zhang, M.; Lin, L.; Wang, X., Sol Processing of Conjugated Carbon Nitride Powders for Thin-Film Fabrication. *Angewandte Chemie International Edition* **2015,** *54*, 6297.

23) Zheng, D.; Cao, X. N.; Wang, X., Precise Formation of a Hollow Carbon Nitride Structure with a Janus Surface To Promote Water Splitting by Photoredox Catalysis. *Angewandte Chemie International Edition* **2016,** *55*, 11512.

24) Zhang, F.; Yamakata, A.; Maeda, K.; Moriya, Y.; Takata, T.; Kubota, J.; Teshima, K.; Oishi, S.; Domen, K., Cobalt-Modified Porous Single-Crystalline $LaTiO_2N$ for Highly Efficient Water Oxidation under Visible Light. *Journal of the American Chemical Society* **2012,** *134*, 8348.

25) Higashi, M.; Domen, K.; Abe, R., Highly Stable Water Splitting on Oxynitride TaON Photoanode System under Visible Light Irradiation. *Journal of the American Chemical Society* **2012,** *134*, 6968.

26) Hutchings, G. S.; Zhang, Y.; Li, J.; Yonemoto, B. T.; Zhou, X. G.; Zhu, K. K.; Jiao, F., In Situ Formation of Cobalt Oxide Nanocubanes as Efficient Oxygen Evolution Catalysts. *Journal of the American Chemical Society* **2015,** *137*, 4223.

27) Xiang, Q. J.; Chen, G.; Lau, T. C., Effects of Morphology and Exposed Facets of Alpha-Fe_2O_3 Nanocrystals on Photocatalytic Water Oxidation. *RSC Advances* **2015,** *5*, 52210.

28) Ahn, H. S.; Yano, J.; Tilley, T. D., Photocatalytic Water Oxidation by Very Small Cobalt Domains on a Silica sSurface. Energy & Environmental Science **2013,** *6*, 3080.

29) Zidki, T.; Zhang, L. H.; Shafirovich, V.; Lymar, S. V., Water Oxidation Catalyzed by Cobalt(II) Adsorbed on Silica Nanoparticles. *Journal of the American Chemical Society* **2012,** *134*, 14275.

30) Huynh, M.; Shi, C. Y.; Billinge, S. J. L.; Nocera, D. G., Nature of Activated Manganese Oxide for Oxygen Evolution. *Journal of the American Chemical Society* **2015,** *137*, 14887.

31) Wee, T. L.; Sherman, B. D.; Gust, D.; Moore, A. L.; Moore, T. A.; Liu, Y.; Scaiano, J. C., Photochemical Synthesis of a Water Oxidation Catalyst Based on Cobalt Nanostructures. *Journal of the American Chemical Society* **2011,** *133*, 16742.

32) Seabold, J. A.; Choi, K. S., Efficient and Stable Photo-Oxidation of Water by a Bismuth Vanadate Photoanode Coupled with An Iron Oxyhydroxide Oxygen Evolution Catalyst. *Journal of the American Chemical Society* **2012,** *134*, 2186.

33) Jiao, F.; Frei, H., Nanostructured Cobalt Oxide Clusters in Mesoporous Silica as Efficient Oxygen-Evolving Catalysts. *Angewandte Chemie International Edition* **2009,** *48*, 1841.

34) Ge, L.; Han, C.; Xiao, X.; Guo, L., In Situ Synthesis of Cobalt–Phosphate (Co–Pi) Modified g-C_3N_4 Photocatalysts with Enhanced Photocatalytic Activities. *Applied Catalysis B: Environmental* **2013,** *142-143*, 414.

35) Han, X. B.; Zhang, Z. M.; Zhang, T.; Li, Y. G.; Lin, W. B.; You, W. S.; Su, Z. M.; Wang, E. B., Polyoxometalate-Based Cobalt-Phosphate Molecular Catalysts for Visible Light-Driven Water Oxidation. *Journal of the American Chemical Society* **2014,** *136*, 5359.

36) Han, X. B.; Li, Y. G.; Zhang, Z. M.; Tan, H. Q.; Lu, Y.; Wang, E. B., Polyoxometalate-Based Nickel Clusters as Visible Light-Driven Water Oxidation Catalysts. *Journal of the American Chemical Society* **2015,** *137*, 5486.

37) Grzelczak, M.; Zhang, J. S.; Pfrommer, J.; Hartmann, J.; Driess, M.; Antonietti, M.; Wang, X. C., Electro- and Photochemical Water Oxidation on Ligand-free Co_3O_4 Nanoparticles with Tunable Sizes. *ACS Catalysis* **2013,** *3*, 383.

38) Zhang, J. S.; Grzelczak, M.; Hou, Y. D.; Maeda, K.; Domen, K.; Fu, X. Z.; Antonietti, M.; Wang, X. C., Photocatalytic Oxidation of Water by Polymeric Carbon Nitride Nanohybrids Made of Sustainable Elements. *Chemical Science* **2012,** *3*, 443.

39) Bai, X. J.; Wang, L.; Wang, Y. J.; Yao, W. Q.; Zhu, Y. F., Enhanced Oxidation Ability of g-C_3N_4 Photocatalyst via C-60 Modification. *Applied Catalysis B: Environmental* **2014,** *152*, 262.

40) He, C. Z.; Qiu, S.; Wang, X. Z.; Liu, J. R.; Luan, L. Q.; Liu, W.; Itoh, M.; Machida, K., Facile Synthesis of Hollow Porous Cobalt Spheres and Their Enhanced Electromagnetic Properties. *Journal of Materials Chemistry A* **2012,** *22*, 22160.

41) Morris, N. D.; Mallouk, T. E., A High-Throughput Optical Screening Method for the Optimization of Colloidal Water Oxidation Catalysts. *Journal of the American Chemical Society* **2002,** *124*, 11114.

42) Yang, S.; Gong, Y.; Zhang, J.; Zhan, L.; Ma, L.; Fang, Z.; Vajtai, R.; Wang, X.; Ajayan, P. M., Exfoliated Graphitic Carbon Nitride Nanosheets as Efficient Catalysts for Hydrogen Evolution under Visible Light. *Advanced Materials* **2013,** *25*, 2452.

43) Liu, Z. P.; Ma, R. Z.; Osada, M.; Takada, K.; Sasaki, T., Selective and Controlled Synthesis of Alpha- and Beta-Cobalt Hydroxides in Highly Developed Hexagonal Platelets. *Journal of the American Chemical Society* **2005,** *127*, 13869.

44) Koczkur, K. M.; Mourdikoudis, S.; Polavarapu, L.; Skrabalak, S. E., Polyvinylpyrrolidone (PVP) in Nanoparticle Synthesis. *Dalton Transactions* **2015,** *44*, 17883.

45) Wu, S.; Liu, T.; Zeng, W.; He, J.; Yu, W.; Gou, Z., Rose-Like Cu_2O Synthesized by Assisted PVP K30 Hydrothermal Method. *Journal of Materials Science: Materials in Electronics* **2013,** *24*, 2404.

46) Wang, Y.; Zhou, T.; Jiang, K.; Da, P.; Peng, Z.; Tang, J.; Kong, B.; Cai, W.-B.; Yang, Z.; Zheng, G., Reduced Mesoporous Co_3O_4 Nanowires as Efficient Water Oxidation Electrocatalysts and Supercapacitor Electrodes. *Advanced Energy Materials* **2014,** *4*, 1400696.

47) Lyth, S. M.; Nabae, Y.; Moriya, S.; Kuroki, S.; Kakimoto, M.-a.; Ozaki, J.-i.; Miyata, S., Carbon Nitride as a Nonprecious Catalyst for Electrochemical Oxygen Reduction. *The Journal of Physical Chemistry C* **2009,** *113*, 20148.

48) Zhu, Y.; Murali, S.; Stoller, M. D.; Ganesh, K. J.; Cai, W.; Ferreira, P. J.; Pirkle, A.; Wallace, R. M.; Cychosz, K. A.; Thommes, M.; Su, D.; Stach, E. A.; Ruoff, R. S., Carbon-Based Supercapacitors Produced by Activation of Graphene. *Science* **2011,** *332*, 1537.

49) Moulder, J. F.; Chastain, J., *Handbook of X-ray Photoelectron Spectroscopy: A Reference Book of Standard Spectra for Identification and Interpretation of XPS Data*. Physical Electronics Division, Perkin-Elmer Corporation: 1992.

50) Yang, J.; Liu, H.; Martens, W. N.; Frost, R. L., Synthesis and Characterization of Cobalt Hydroxide, Cobalt Oxyhydroxide, and Cobalt Oxide Nanodiscs. *The Journal of Physical Chemistry C* **2010,** *114*, 111.

51) Fukuzumi, S.; Jung, J.; Yamada, Y.; Kojima, T.; Nam, W., Homogeneous and Heterogeneous Photocatalytic Water Oxidation by Persulfate. *Chemistry-An Asian Journal* **2016,** *11*, 1138.

52) Ma, T. Y.; Dai, S.; Jaroniec, M.; Qiao, S. Z., Metal-Organic Framework Derived Hybrid Co_3O_4-Carbon Porous Nanowire Arrays as Reversible Oxygen Evolution Electrodes. *Journal of the American Chemical Society* **2014,** *136*, 13925.

53) Tian, J.; Liu, Q.; Ge, C.; Xing, Z.; Asiri, A. M.; Al-Youbi, A. O.; Sun, X., Ultrathin Graphitic Carbon Nitride Nanosheets: A Low-Cost, Green, and Highly Efficient Electrocatalyst Toward the Reduction of Hydrogen Peroxide and its Glucose Biosensing Application. *Nanoscale* **2013,** *5*, 8921.

54) Zhang, J.; Sun, J.; Maeda, K.; Domen, K.; Liu, P.; Antonietti, M.; Fu, X.; Wang, X., Sulfur-Mediated Synthesis of Carbon Nitride: Band-gap Engineering and Improved Functions for Photocatalysis. Energy & Environmental Science **2011,** *4*, 675.

55) Sun, J.; Zhang, J.; Zhang, M.; Antonietti, M.; Fu, X.; Wang, X., Bioinspired Hollow Semiconductor Nanospheres as Photosynthetic Nanoparticles. *Nature Communications* **2012**, 2152.

56) Hong, D. C.; Yamada, Y.; Nagatomi, T.; Takai, Y.; Fukuzumi, S., Catalysis of Nickel Ferrite for Photocatalytic Water Oxidation Using $[Ru(bpy)_3]^{2+}$ and $S_2O_8^{2-}$. *Journal of the American Chemical Society* **2012,** *134*, 19572.

57) Wang, X.; Maeda, K.; Thomas, A.; Takanabe, K.; Xin, G.; Carlsson, J. M.; Domen, K.; Antonietti, M., A Metal-Fee Polymeric Photocatalyst for Hydrogen Production from Water under Visible Light. *Nature Materials* **2009,** *8*, 76.

58) Zhang, G.; Zang, S.; Lan, Z.-A.; Huang, C.; Li, G.; Wang, X., Cobalt Selenide: A Versatile Cocatalyst for Photocatalytic Water Oxidation with Visible Light. *Journal of Materials Chemistry A* **2015,** *3*, 17946.

59) Dong, G.; Zhao, K.; Zhang, L., Carbon Self-Doping Induced High Electronic Conductivity and Photoreactivity of g-C_3N_4. *Chemical Communications* **2012,** *48*, 6178.

60) Fan, G.; Li, F.; Evans, D. G.; Duan, X., Catalytic Applications of Layered Double Hydroxides: Recent Advances and Perspectives. *Chemical Society Reviews* **2014,** *43*, 7040.

61) Abellan, G.; Coronado, E.; Marti-Gastaldo, C.; Ribera, A.; Jorda, J. L.; Garcia, H., Photo-Switching in a Hybrid Material Made of Magnetic Layered Double Hydroxides Intercalated with Azobenzene Molecules. *Advanced Materials* **2014,** *26*, 4156.

62) Wang, L.; Dong, Z. H.; Wang, Z. G.; Zhang, F. X.; Jin, J., Layered α-$Co(OH)_2$ Nanocones as Electrode Materials for Pseudocapacitors: Understanding the Effect of Interlayer Space on Electrochemical Activity. *Advanced Functional Materials* **2013,** *23*, 2758.

63) Xiao, X.; Liu, X.; Zhao, H.; Chen, D.; Liu, F.; Xiang, J.; Hu, Z.; Li, Y., Facile Shape Control of Co_3O_4 and the Effect of the Crystal Plane on Electrochemical Performance. *Advanced Materials* **2012,** *24*, 5762.

64) Ma, R.; Takada, K.; Fukuda, K.; Iyi, N.; Bando, Y.; Sasaki, T., Topochemical Synthesis of Monometallic (Co^{2+}-Co^{3+}) Layered Double Hydroxide and its Exfoliation into Positively Charged $Co(OH)_2$ Nanosheets. *Angewandte Chemie International Edition* **2008,** *47*, 86.

Every reasonable effort has been made to acknowledge the owners of copyright material. I would be pleased to hear from any copyright owner who has been omitted or incorrectly acknowledged.

Chapter 4. Monodisperse Co_3O_4 Quantum Dots on Porous Carbon Nitride Nanosheets for Enhanced Visible-Light-Driven Water Oxidation

Abstract

In Chapter 3, we reported the facile coating of micron-sized flower-like cobalt hydroxides/oxides onto 2D g-C_3N_4 nanosheets to achieve enhanced water catalytic oxidation. Here we further use a facile annealing process for even-deposition of zero-dimensional (0D) Co_3O_4 quantum dots (Co_3O_4 QDs) onto porous 2D g-C_3N_4 nanosheets. It was discovered that catalyzed pores generation appeared around Co_3O_4 QDs. In the synthesis, the annealing temperature is found to be crucial for the textural property, optical absorption, and the corresponding photocatalytic water oxidation as well as photoelectrochemical performances. The largest specific surface area, pore volume and optimal O_2 production rate as well as the highest photocurrent are obtained on 0.8 wt.% Co_3O_4 QDs decorated g-C_3N_4 nanosheets annealed at 300 °C (0.8% Co_3O_4-C_3N_4-300). These results underline the importance of surface heterojunction and afford us a feasible protocol for the rational design of g-C_3N_4 based photocatalysts for water oxidation.

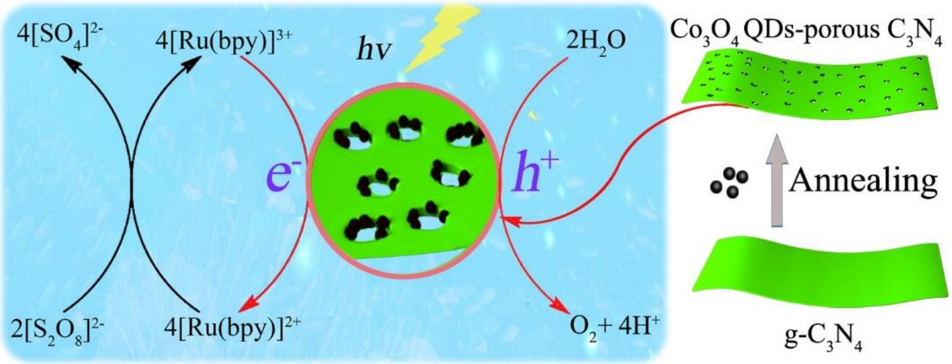

4.1 Introduction

Direct water splitting using hetero/homogeneous photocatalysts is a highly attractive approach for utilization of solar energy, which represents the most universally abundant and renewable energy source.[1-2] This process can be divided into two half reactions, e.g., water reduction and water oxidation, between which much attention has been paid to the more complex water oxidation half reaction.[3-4] In the production of one O_2 molecule, coupling of four electrons and transfer of four protons are involved, making this rate-determining reaction become a kinetically competitive process.[5-6] Therefore, the development of efficient photocatalysts for water oxidation is far more difficult than water reduction.[7]

To date, heterogeneous photocatalytic water oxidation has focused on developing semiconductor materials with sufficiently small band gap energies, suitable band edge positions, and excellent charge-carrier conductivities.[8-9] Compared with traditional metal-based photocatalysts such as $BiVO_4$, TiO_2, and WO_3, the discovery of metal-free graphitic carbon nitride (g-C_3N_4) is expected to provide new opportunities for widespread applications, because of the advantages of visible-light absorption, wide availability of precursors and feasibility of preparation.[8, 10-14] The sp^2 hybridization of C and N atoms in g-C_3N_4 form π-conjugated planar planes, endowing it with intrinsic semiconductive features.[13, 15] With the conduction band level at -1.4 V (versus Ag/AgCl) and the valence band level at 1.3 V, g-C_3N_4 covers the full potential range of thermodynamic water splitting redox.[16-17] It has been observed that g-C_3N_4 could exhibit the ability of photocatalytic H_2/O_2 evolution in the presence of sacrificial reagents under visible light irradiations.[18-21] However, without adding the cocatalysts, g-C_3N_4 alone provides a limited rate for H_2 or O_2 production due to the imperfect charge separation and the rapid recombination of electron-hole (e^--h^-) pairs.[6, 20] Thus, integrating cocatalysts have attracted considerable interests to achieve enhanced photocatalytic water oxidation activity.[4, 22-23] Suitable cocatalysts would provide sufficient surface active sites with lower overpotentials, which could also act as selective trapping sites for the photogenerated electrons from g-C_3N_4, and thus suppress the recombination of charge carriers.[4, 16] Currently, the most efficient cocatalysts are based on noble metals such as Ru or Pd, which are of a high cost and scarcity.[24]

Among the various candidates, Co_3O_4 with a bandgap of about 2.1 eV has been extensively employed as a cocatalyst for photocatalytic water oxidation, because of its excellent oxidation ability and robust stability.[25-28] Also, the cobalt-based compounds are cost-effective and earth-abundant. Recently, 0D quantum dots of cobalt oxides have attracted growing interest because they can offer enhanced catalytic properties by providing higher specific surface areas, shorter charger transport paths and quantum confinement effects.[29-30] Besides, Co_3O_4 quantum dots can be homogeneously dispersed in H_2O or ethanol, making it readily for being loaded onto g-C_3N_4 through a temperature-dependent deposition process. Compared with other reported methods, such as in-situ growth method and electrochemical deposition, the formation of nanocrystals in a separate process allows for a much better control of the properties such as size, shape and chemical composition.[26]

In this chapter, we prepared monodisperse Co_3O_4 QDs with a size of 4.5 nm based on a reported method.[29] The quantum dots can be easily dispersed in ethanol and homogeneously loaded onto the surface of g-C_3N_4 by a feasible evaporation process. To enhance the combination strength, further annealing treatments of the composites are conducted at different temperatures. Interestingly, it is observed that pores are generated on the surface of g-C_3N_4 where Co_3O_4 quantum dots appear, which are especially evident at higher temperature treatments. With Co_3O_4 QDs decoration, g-C_3N_4 displays an obvious enhancement in water oxidation reactions.

4.2 Experimental Section

4.2.1 Chemical Reagents

Urea ($\geq$ 99.5%), ethanol ($\geq$ 99.8%), Nafion® 117 solution (5wt. %, Aldrich), sodium sulfate (Na_2SO_4, $\geq$ 99.0%), sodium persulfate ($Na_2S_2O_8$, $\geq$ 99%), sodium hexafluorosilicate (Na_2SiF_6, $\geq$99.0%), sodium bicarbonate ($NaHCO_3$, $\geq$ 99.7%) and tris(2,2′-bipyridyl) dichlororuthenium (II) hexahydrate ($[Ru(bpy)_3]Cl_2{\cdot}6H_2O$, 99.95%). All chemical reagents employed in this work were purchased from Sigma-Aldrich and used as received without further purifications.

4.2.2 Preparation of g-C_3N_4

Traditional thermal polymerization method was utilized to prepare g-C_3N_4. Typically, 10 g of urea was heated to 550 °C with a heating rate of 5 ºC/min and kept at this temperature for 2 h in a muffle furnace. Finally, the light yellow powder was obtained and denoted as g-C_3N_4.

4.2.3 Synthesis of Co_3O_4 QDs/g-C_3N_4 Samples

Monodisperse Co_3O_4 quantum dots with a size about 4.5 nm were synthesized according to a recent report.[31] The synthesized Co_3O_4 QDs were dispersed in absolute ethanol with a concentration of 0.8 g/L. The designed Co_3O_4 QDs/g-C_3N_4 composite were then prepared as follows. Firstly, 0.2 g of g-C_3N_4 was weighed and added into 20 mL absolute ethanol. The suspension was further ultra-sonicated for 1 h and then put on a hotplate for vigorous stirring, during which 2 mL suspension containing 1.6 mg Co_3O_4 were added dropwisely. Accordingly, the weight ratio of Co_3O_4 QDs in the composite was 0.8 wt. %. After that, the solution was evaporated at 100 ºC under constant stirring. The dried mixture was collected, followed by annealing at 180, 250 and 300 ºC, respectively, for 2 h with a heating rate of 5 ºC/min. The obtained samples were denoted as 0.8% Co_3O_4-C_3N_4-180, 0.8% Co_3O_4-C_3N_4-250, and 0.8% Co_3O_4-C_3N_4-300, respectively. For comparison, the pristine g-C_3N_4 was also annealed under the same process and denoted as C_3N_4-180, C_3N_4-250 and C_3N_4-300, respectively. 0.4% Co_3O_4-C_3N_4-300 and 1.2% Co_3O_4-C_3N_4-300 containing 0.4 wt. % and 1.2 wt. % Co_3O_4 QDs were also prepared using the same method annealing at 300 ºC.

4.2.4 Photoelectrochemical and Oxygen Evolution Reaction

Photocurrent and electrochemical impedance spectroscopy (EIS) were accomplished on a Zennium workstation with the CIMPS system (Zahner, Germany) in a three-electrode framework, applying a Pt wire as the counter electrode and a saturated calomel electrode (SCE) as the reference electrode. F-doped tin oxide (FTO) glasses were cleaned by sonication in ethanol for 30 min and dried at 80 ºC to act as the working electrode. 0.2 M Na_2SO_4 solution (pH = 6.8) was adopted as the neutral electrolyte during the measurements. The loading of the materials on the working electrode was performed as below: suspensions containing 8 mg of catalyst, 30 μL Nafion® 117 solution and 500 μL ethanol were obtained by ultrasonic mixing for about 15 min. 50 μL of the above slurry was then dropped onto the FTO glass electrode through a spin coating method and left to dry in air (catalyst loading ~0.60 mg cm^{-2}). Photocurrents were obtained by passing light from a 300 W Xe arc lamp through neutral density filters and an AM 1.5G filter into an optical fiber and calibrating the output to 100 mW/cm^2 using a thermopile detector from International Light.

For each oxygen evolution reaction (OER), the designed amount of catalyst (50 mg) was dispersed in a 100 mL buffered solution (the mixture of 0.022 M Na_2SiF_6 and 0.028 M $NaHCO_3$) which was prepared and aged for 2 days and the pH was adjusted to 5.8. Then 0.975 g of Na_2SO_4, 0.357 g of $Na_2S_2O_8$, and 50 mg of $[Ru(bpy)_3]Cl_2 \cdot 6H_2O$ were added to the reaction solution.

The water oxidation reactor was a customized airtight stainless steel cell covered by a quartz window (the volume of the headspace, excluding the space occupied by the septum, oxygen sensor, and the solution, was 800 mL). Before irradiation, the 300 W Xeon lamp (Newport) was installed with a light filter ($\lambda > 420$ nm) and the central light intensity aligned to 200 mW/cm^2 (2 suns). Prior to testing, the reactor was purged with nitrogen for 30 min to exclude air and guarantee the anaerobic circumstance in the reaction system. After stabilization for another 10 min, the GC started testing with a baseline O_2 reading followed by timing sampling during 120 min of irradiation. The proposed mechanism for the water oxidation systems catalyzed by buffered Tris(2, 2'-bipyridyl) ruthenium system can be deduced according to equation 3.1-3.4 in Chapter 3.[32]

4.2.5 Characterizations

Details on XRD, XPS TEM, HRTEM, HAADF-STEM with EDX mapping and N_2 adsorption/desorption measurements can be referred to Chapter 3. Thermal gravity analysis was carried out by a thermogravimetric analysis instrument (TGA/DSC1 STAR^e system, Mettler-Toledo). Diffused reflectance spectra and photoluminescence spectra were collected on a Cary 100 UV-Visible Spectrophotometer and a Cary Eclipse Fluorescence Spectrophotometer (Agilent, US), respectively. Oxygen evolution reaction was probed quantitatively utilizing a Gas Chromatograph (Agilent 490 Micro GC) with a thermal conductivity detector.

4.3 Results and Discussion

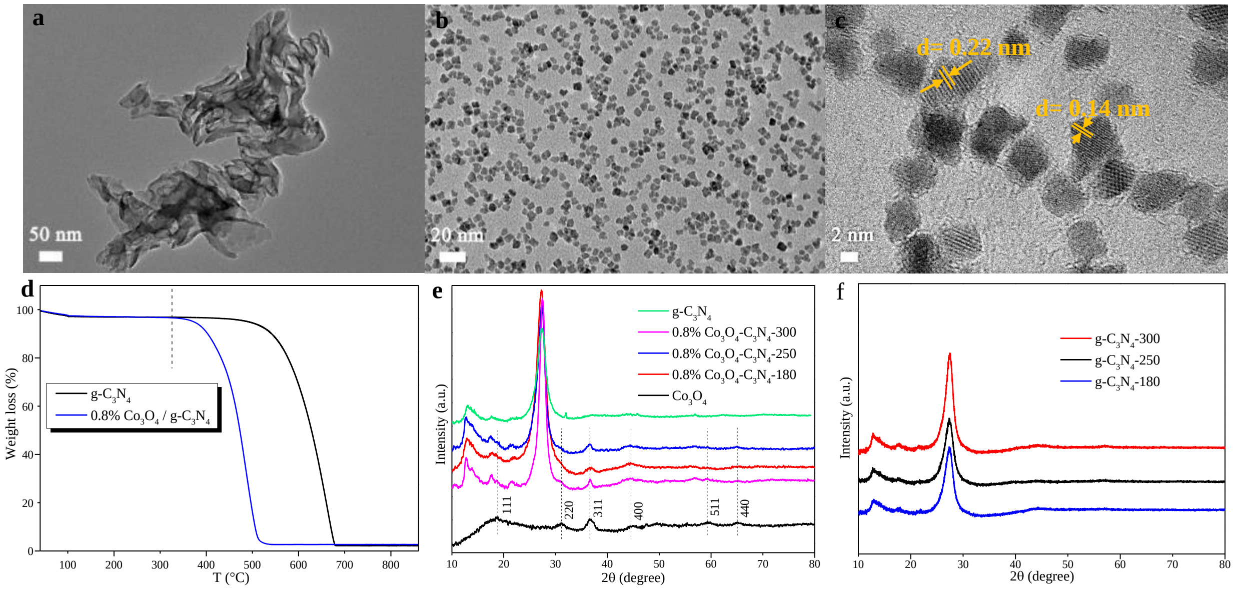

Figure 4.1 a) TEM image of g-C_3N_4, b) TEM and c) HRTEM images of Co_3O_4 quantum dots, d) TGA curves of g-C_3N_4 and the mixture of 0.8% Co_3O_4 QDs with g-C_3N_4, e) and f) XRD patterns of the samples.

Figure 4.1a shows TEM image of typical g-C_3N_4 nanosheets obtained from thermal polymerization of urea. In good agreement with Ref. [29], the produced Co_3O_4 QDs displayed in Figure1b indicate that they are uniform in size (about 4.5 nm) without aggregation. The HRTEM image (Figure 4.1c) further illustrates the crystalline structure with clear lattice spacing of 0.23 nm and 0.14 nm, corresponding to (311) and (440) lattice planes of Co_3O_4, respectively. TGA was conducted on the 0.8 wt. % Co_3O_4/g-C_3N_4 mixture to determine a suitable annealing craft (Figure 4.1d). Interestingly, g-C_3N_4 remains stable until 450 °C, whereas 0.8 wt. % Co_3O_4/g-C_3N_4 mixture starts to display an obvious weight loss at the temperatures higher than 320 °C. To avoid destruction to the structure of g-C_3N_4, the treatment temperatures were set at 180, 250 and 300 °C, respectively. XRD pattern of g-C_3N_4 displays two distinct peaks, which accord with (001) and (002) planes of the typical graphitic layer (Figure 4.1e).[33-34] Powder XRD patterns show broad peaks of Co_3O_4 QDs, and can be assigned to cubic phase (JCPDS No. 42-1467). Some small peaks of Co_3O_4 could be observed in XRD patterns of the Co_3O_4/g-C_3N_4 composites. There are no noticeable changes in the crystal structure for g-C_3N_4 before and after being modified with Co_3O_4 quantum dots at different temperatures (Figure 4.1e and f).

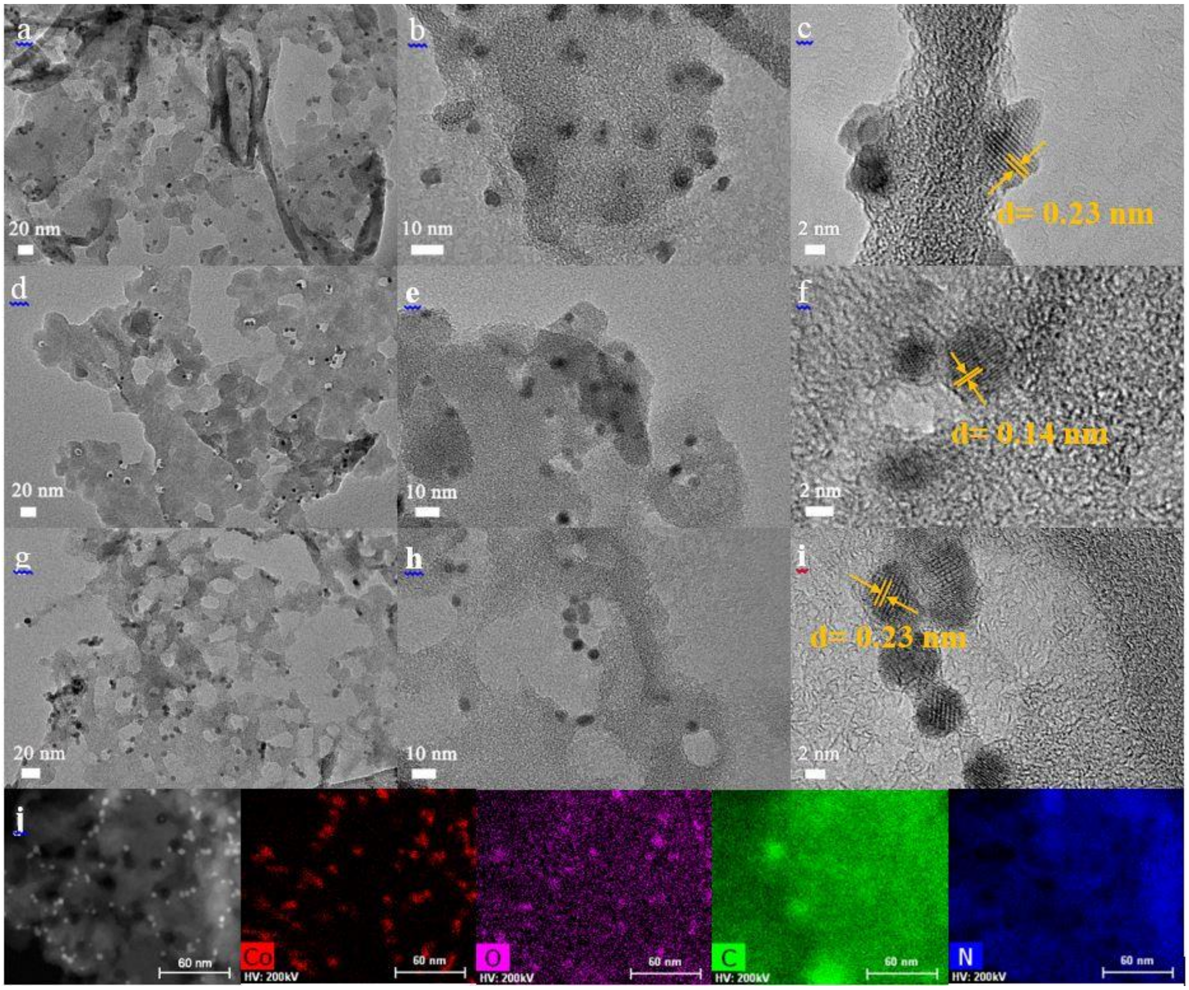

Figure 4.2 TEM and HRTEM images of a-c) 0.8% Co_3O_4-C_3N_4-180, d-f) 0.8% Co_3O_4-C_3N_4-250, g-i) 0.8% Co_3O_4-C_3N_4-300, and j) High angle annular dark field scanning TEM image and corresponding EDX elemental mapping images of 0.8% Co_3O_4-C_3N_4-300.

TEM images were also performed to reveal the local morphology of Co_3O_4 decorated g-C_3N_4 (Figure 4.2). Characterization on 0.8% Co_3O_4-C_3N_4-180 proves that Co_3O_4 QDs are well-dispersed on the thin g-C_3N_4 layers (Figure 4.2a and b). HRTEM image suggests a well-defined adaptive contact between them (Figure 4.2c). Interestingly, small pores are in-situ generated around Co_3O_4 QDs on g-C_3N_4 nanosheet in 0.8% Co_3O_4-C_3N_4-250, indicating the strong interactions between them (Figures 4.2 d and e). It is worth noting that the pores continue to increase and enlarge with a higher treatment temperature at 300 ºC (Figure 4.2g, h), but the crystal structure of Co_3O_4 remains stable (Figure 4.2i). In addition, the HAADF-STEM with EDX elemental mapping images of 0.8 % Co_3O_4-C_3N_4-300 further proves the porosity and relatively uniform distribution of Co_3O_4 QDs on g-C_3N_4 nanosheets. Further, unmodified C_3N_4-300 was characterized in Figure 4.3, displaying a nanosheet-like morphology without pores on the surface, and the thickness might be thinner compared with pristine g-C_3N_4 due to potential thermal exfoliation at 300 ºC.[35]

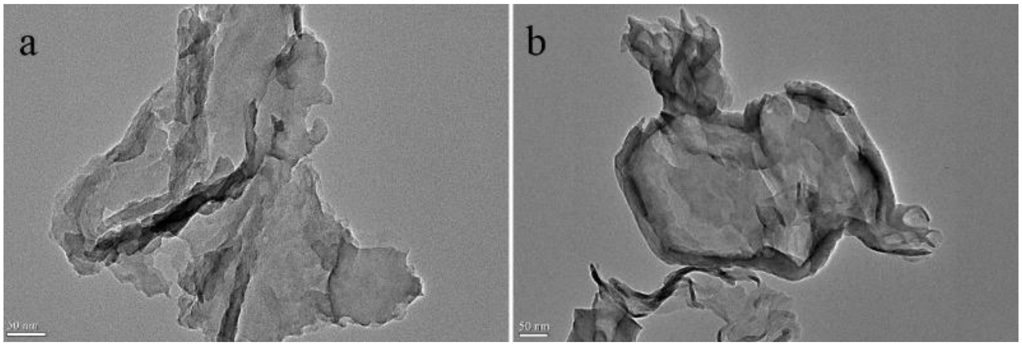

Figure 4.3 TEM images of C_3N_4-300.

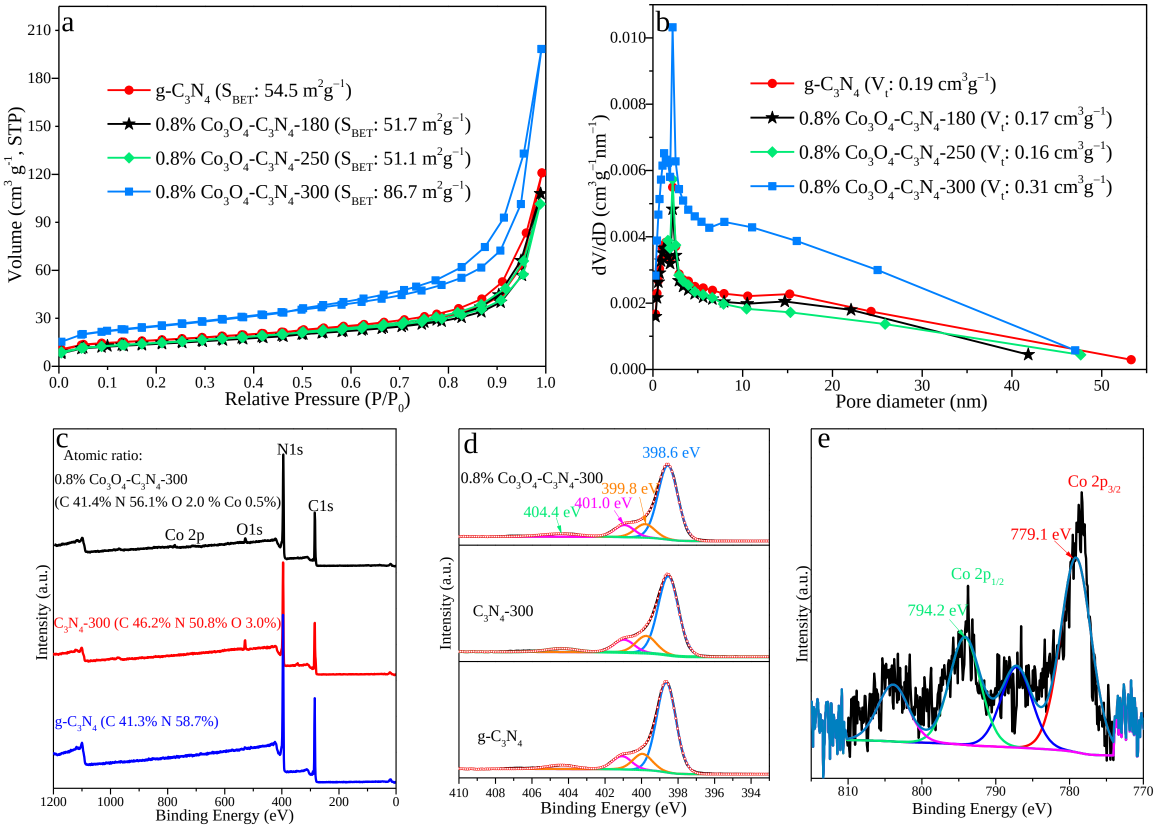

Figure 4.4 a) N_2 adsorption-desorption isotherms, b) Pore size distributions calculated by BJH desorption, c) full XPS survey, d) high-resolution N 1s spectra and e) high-resolution Co 2p spectrum of 0.8% Co_3O_4-C_3N_4-300.

To determine the textural properties of the samples, N_2 adsorption-desorption isotherms were performed and summarized in Figures 4.4a and b, which reveal the porous property of the pristine g-C_3N_4. 0.8% Co_3O_4-C_3N_4-180 and 0.8% Co_3O_4-C_3N_4-250 show similar specific BET surface areas (S_{BET}) as well as total pore volume (V_t) with g-C_3N_4. Notably, there is a significant increase of S_{BET} on 0.8% Co_3O_4-C_3N_4-300, accompanying by an increased pore volume in the full range of 0.28-47.0 nm.

To view changes of annealing at 300 ºC, XPS was performed on g-C_3N_4, C_3N_4-300 and 0.8% Co_3O_4-C_3N_4-300 and the results are shown in Figures 4.4c-e. Full spectrum of g-C_3N_4 indicates a C/N ratio of 0.7. After annealing at 300 ºC, 3.22 at. % of oxygen was detected in C_3N_4-300 with a C/N ratio of 0.91, while the ratio turns to 0.74 on 0.8% Co_3O_4-C_3N_4-300. However, high resolution N1s of the three samples does not show noticeable differences. Four peaks at around 398.6, 399.8, 401.0 and 404.4 eV can be fitted in N1s, which are related to C−N=C sp^2-hybridized N atoms, N−$(C)_3$ groups,[23] C−N−H functional groups,[23, 36] and a typical shake-up satellite or oxidized N species.[37] Figure 4.4e indicates that two pairs of individual peaks at 779.1 and 794.2 eV can be deconvoluted in Co 2p spectrum of 0.8% Co_3O_4-C_3N_4-300, corresponding to Co $2p_{3/2}$ and Co $2p_{1/2}$, proving the structure stability of Co_3O_4 QDs.

The optical properties and band structure of g-C_3N_4, 0.8% Co_3O_4 decorated g-C_3N_4 (180, 250, 300) were analyzed through UV-Vis diffuse reflectance spectroscopy (DRS), photoluminescence spectrum (PL) and Mott-Schottky analysis. As shown in Figure 4.5a, absorption spectra of g-C_3N_4 exhibited steep edges at wavelength of around 380 nm, which can be attributed to the band gap transition of g-C_3N_4. As shown in the inset graph, due to the $O^{2-} \rightarrow Co^{3+}$ and $O^{2-} \rightarrow Co^{2+}$ transitions of Co_3O_4, the composites showed another band edges located at around 730 nm besides the common edges at 380 nm.[38] The increased absorbance in visible light region, i.e. wavelengths ranging from 380 to 750 nm, further illustrates the existence of these transition bands in Co_3O_4-C_3N_4 composites.

The charge carrier transfer and separation were investigated through room temperature PL spectra. As can be seen in Figure 4.5b, when the 370 nm exciting light irradiates on the composites, the intensity of single luminescence peak located between 400 and 550 nm decreases more obviously than pristine g-C_3N_4. It is clear that the quantum-sized Co_3O_4 and its heterojunction with g-C_3N_4 can induce synergistic effect for separation and capture efficiency of the holes photoexcited from valance band of g-C_3N_4, thereby inhibiting direct luminescent charge recombination.[39] Meanwhile, with increasing annealing temperature, the interfacial heterojunction between Co_3O_4 and g-C_3N_4 was strengthened, as verified by the weakest luminescence peak in 0.8% Co_3O_4-C_3N_4-300. The scattering effect in 0.8% Co_3O_4-C_3N_4-300 was also enhanced contributed by the enlarged pore volume, which could provide more surface terminal sites for transfer and separation of photoinduced holes.[21, 40] As a result, 0.8% Co_3O_4-C_3N_4-300 displays the most effective charge separation ability.

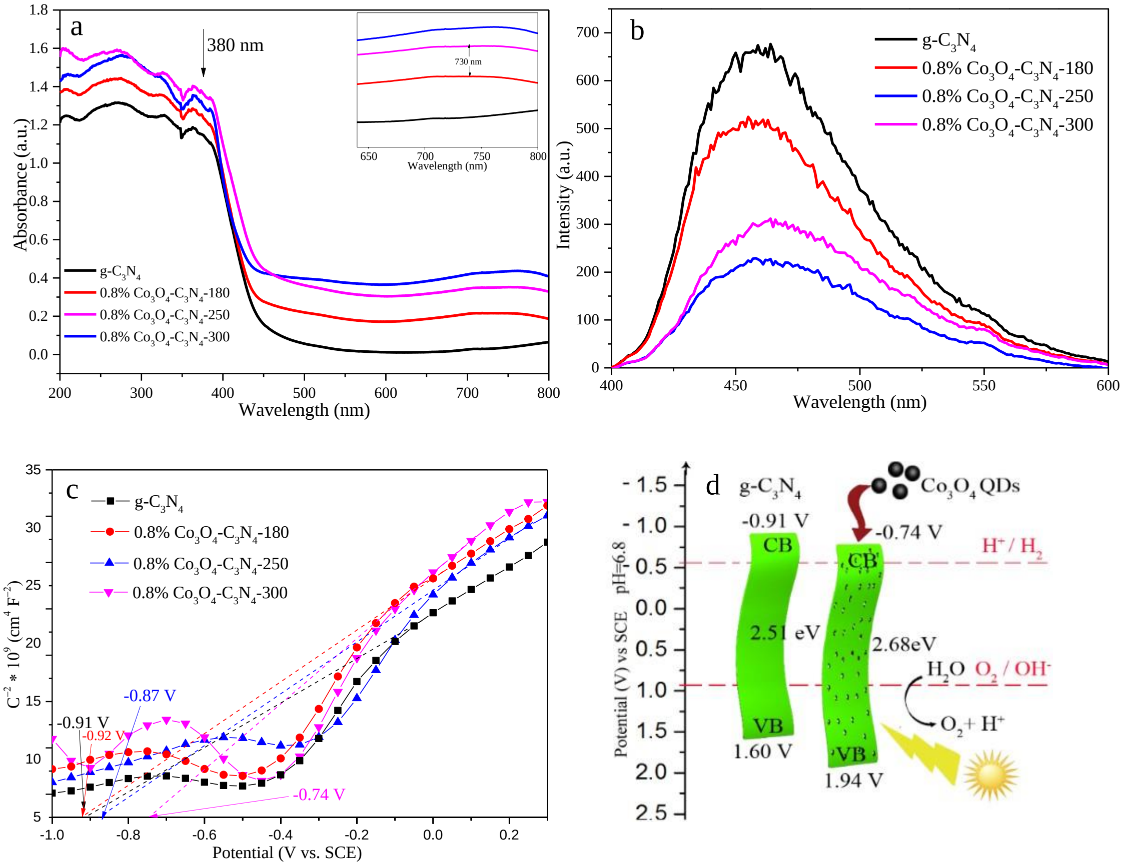

Figure 4.5 a) UV-vis DRS absorption spectra, amplification of partial visible light region (inset graph), b) PL spectrum and c) Electrochemical Mott-Schottky plots of g-C_3N_4 and 0.8% Co_3O_4-C_3N_4 (180, 250, 300). d) Band structure diagram of g-C_3N_4 and 0.8% Co_3O_4-C_3N_4-300.

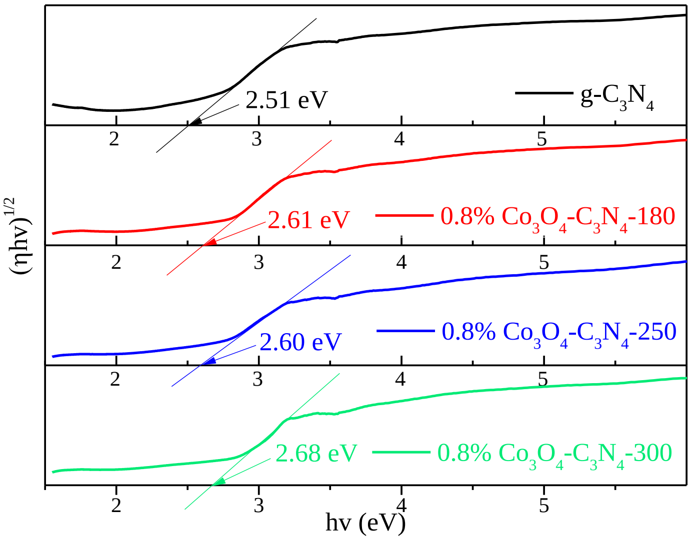

Figure 4.6 The curves of transformed Kubelka-Munk functions versus the light energy.

Mott-Schottky relationship was investigated to illustrate the electronic band structure changes and the flat band potential shifts of the samples. The typical n-type semiconductor properties for all the materials are presented in Figure 4.5c. The flat band potential values (E_{fb}) of g-C_3N_4, and 0.8% Co_3O_4-C_3N_4 (180, 250, 300) were calculated to be -0.91, -0.92, -0.87 and -0.74 V (vs SCE), respectively, showing the weakest upward band alignment of g-C_3N_4. Furthermore, the weak shift demonstrates that an electric field formed at the interface between g-C_3N_4 and Co_3O_4, which can elevate the efficiency of hole transport from g-C_3N_4 to Co_3O_4.

In addition, based on the extrapolation method (Figure 4.6), the calculated energy gaps of the samples proved that the semiconductor properties of g-C_3N_4 are indeed changed with Co_3O_4 decoration and the valance band position shift positively. The band-gap energy of the sample was determined using the following equation: $(\alpha h\nu)^n = k(h\nu\text{-Eg})$.[41] Wherein α is the absorption factor, *hν* is the energy quantum, *k* is a material determined constant and n equals 0.5. The plots of $(\eta h\nu)^{1/2}$ versus hν (Kubelka-Munk) were transformed from UV-vis DRS absorption spectra according to the above equation (Figure 4.6). The intercepts were obtained at 2.51, 2.61, 2.60 and 2.68 eV for g-C_3N_4, 0.8% Co_3O_4-C_3N_4-180, 0.8% Co_3O_4-C_3N_4-250, and 0.8% Co_3O_4-C_3N_4-300 respectively, which correspond to their band-gap energies. Values of the conduction band (CB) can be estimated based on the E_{fb} values. Combined with the Mott-Schottky plots and the band gap, values of the valence band (VB) are +1.60, +1.69, +1.73, 1.94 V for g-C_3N_4, 0.8% Co_3O_4-C_3N_4-180, -250, and -300, respectively. Based on these values, Figure 4.5d was plotted, which presents the representative comparison of band structure between g-C_3N_4 and 0.8% Co_3O_4-C_3N_4-300. Apparently, Co_3O_4-C_3N_4-300 provides a more positive potential for photocatalytic oxidation of water thermodynamically.

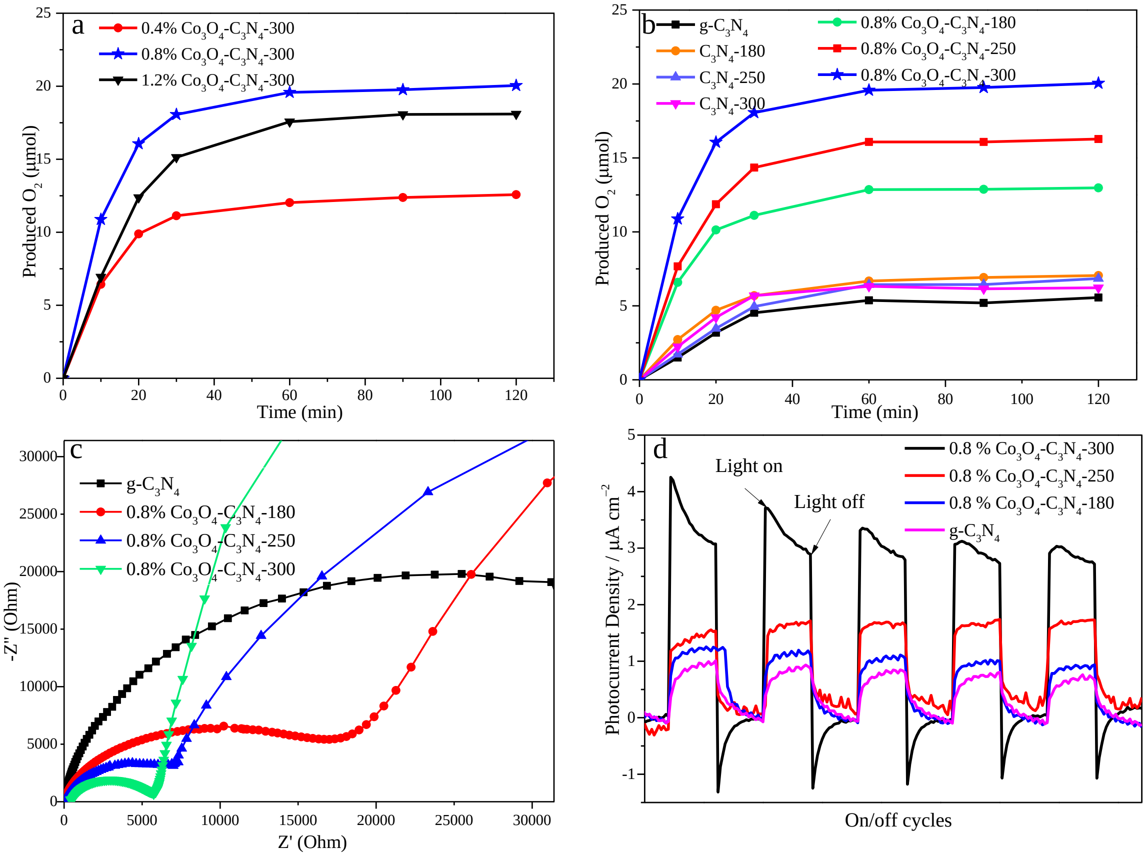

Figure 4.7 Amount of O_2 evolution for a) g-C_3N_4 modified with different ratios of Co_3O_4 QDs treated at 300 ºC, b) samples annealed at different temperatures, c) EIS plots and d) periodic on/off photocurrent response under visible-light irradiations.

The photocatalytic water oxidation using different ratios of Co_3O_4 decorated C_3N_4 at 300 ºC were performed and compared in Figure 4.7a. The performance of 0.4% Co_3O_4-C_3N_4-300 and

1.2% Co_3O_4-C_3N_4-300 are all inferior to 0.8% Co_3O_4-C_3N_4-300, which is consistent to a previous report.[23] It is reported that trace amounts of cocatalyst loading cannot provide sufficient capacity to change the inherent band structure of g-C_3N_4, while excessive loading may be unfavourable for photoredox catalysis. Water oxidation activities of the as-prepared g-C_3N_4 and 0.8 wt. % Co_3O_4/g-C_3N_4 annealed at different temperatures are summarized in Figure 4.7b. It is observed that g-C_3N_4 as well as 180, 250 and 300 ºC treated g-C_3N_4 exhibit comparable O_2 production performances. This proved that the impact of annealing treatment on water oxidation ability of g-C_3N_4 is negligible. Compared to them, the activity was enhanced significantly after modification with Co_3O_4 QDs. Interestingly, the activity of the composites show an enhancing trend with increasing annealing temperatures from 180 to 300 ºC. The produced O_2 amount by 0.8% Co_3O_4-C_3N_4-300 was elevated approximately 4 times compared to pristine g-C_3N_4. The improved performance can be explained by the restrained recombination rate of photoinduced charge carrier, contributed by the establishment of heterojunction between g-C_3N_4 and Co_3O_4 QDs. Specifically, during photocatalytic reactions under visible-light irradiations, the electrons and holes are photogenerated from g-C_3N_4, which can migrate to the interface and then to Co_3O_4 QDs, and thereby facilitating the heterogeneous photocatalysis.[42]

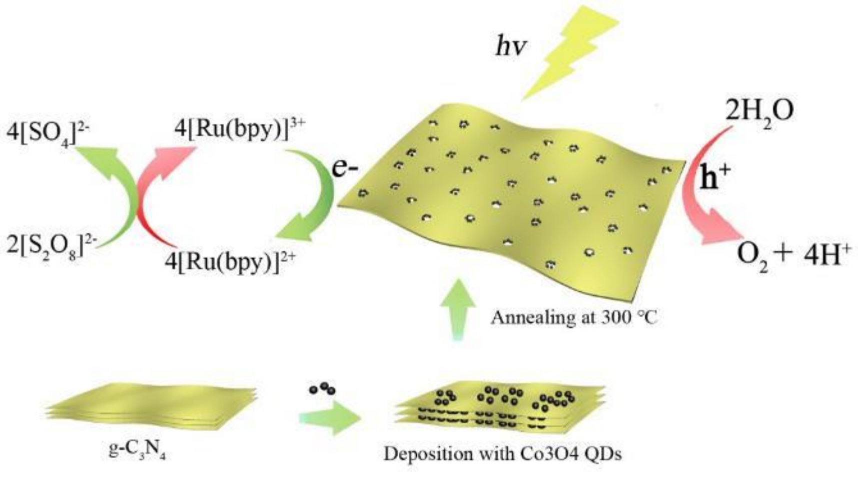

Scheme 4.1 Heterogeneous water oxidation system catalyzed by Co_3O_4 QDs deposited g-C_3N_4.

The photoelectrochemical measurements were further conducted to help explain the performance of the hybrids. As shown in the EIS curves (Figure 4.7c), dramatically decreased semicircles were obtained for the composites compared with pure g-C_3N_4, demonstrating the reduced resistance of the electrodes. In other words, after modification with Co_3O_4, the interfacial charge transfer/migration of g-C_3N_4 was accelerated. It is also worth noting that with increasing annealing temperature, a remarkably declined radius of semicircle was observed, implying a better coupling between them. After annealing process, the resulting interaction and synergistic effect of Co_3O_4 and g-C_3N_4 can provide more active sites for the transfer of charge carrier. Therefore, better conductivity and oxidation ability of the hybrids were obtained, as described in Scheme 4.1. In accordance with this, transient photocurrent enlarged with elevating annealing temperature. The photocurrent activated by 0.8% Co_3O_4-C_3N_4-300 was about 4 four times over that of g-C_3N_4 (Figure 4.7d). The electrochemical results prove the creation of Co_3O_4/g-C_3N_4 junctions, which can act as active sites for heterogeneous photocatalytic water oxidation. It is also speculated that the junction interface turns tighter at higher annealing temperatures, evidenced by the enhanced activity with elevating temperature. Another reason for the well-defined activity of 0.8% Co_3O_4-C_3N_4-300 lies in its larger S_{BET} and V_t, which also promote the transfer of photogenerated electrons.

4.4 Conclusions

Co_3O_4 quantum dots were dispersively loaded onto porous g-C_3N_4 nanosheets as cocatalyst via an annealing deposition process at 180, 250 and 300 ºC, without destroying the major structure of g-C_3N_4 and Co_3O_4. Numerous pores are in-situ produced and tight heterojunctions are created during this process due to the strong interaction between Co_3O_4 and g-C_3N_4. The water oxidation performance shows an increasing trend with elevated treatment temperature. Compared with pure g-C_3N_4, O_2 production amount and photocurrent are improved by a factor of nearly 4 times on 0.8% Co_3O_4-C_3N_4-300 under visible light irradiations, associated with an obviously decreased charge transfer resistance. This work demonstrates the importance of a tight heterojunction to realize the modification of g-C_3N_4 with cocatalysts, providing novel strategies for designing hybrid materials.

References

1) Maeda, K.; Teramura, K.; Lu, D. L.; Takata, T.; Saito, N.; Inoue, Y.; Domen, K., Photocatalyst Releasing Hydrogen from Water - Enhancing Catalytic Performance Holds Promise for Hydrogen Production by Water Splitting in Sunlight. *Nature* **2006,** *440*, 295.
2) Hisatomi, T.; Kubota, J.; Domen, K., Recent Advances in Semiconductors for Photocatalytic and Photoelectrochemical Water Splitting. *Chemical Society Reviews* **2014,** *43*, 7520.
3) Blakemore, J. D.; Crabtree, R. H.; Brudvig, G. W., Molecular Catalysts for Water Oxidation. *Chemical Reviews* **2015,** *115*, 12974.
4) Zhang, P.; Wang, T.; Chang, X.; Zhang, L.; Gong, J., Synergistic Cocatalytic Effect of Carbon Nanodots and Co_3O_4 Nanoclusters for the Photoelectrochemical Water Oxidation on Hematite. *Angewandte Chemie International Edition* **2016,** *55*, 5851.
5) Hurst, J. K., In Pursuit of Water Oxidation Catalysts for Solar Fuel Production. *Science* **2010,** *328*, 315.
6) Zhang, K.; Wang, L.; Sheng, X.; Ma, M.; Jung, M. S.; Kim, W.; Lee, H.; Park, J. H., Tunable Bandgap Energy and Promotion of H_2O_2 Oxidation for Overall Water Splitting from Carbon Nitride Nanowire Bundles. *Advanced Energy Materials* **2016,** *6*, 1502352.
7) Zou, X.; Su, J.; Silva, R.; Goswami, A.; Sathe, B. R.; Asefa, T., Efficient Oxygen Evolution Reaction Catalyzed by Low-Density Ni-Doped Co_3O_4 Nanomaterials Derived from Metal-Embedded Graphitic C_3N_4. *Chemical Communications* **2013,** *49*, 7522.
8) Maeda, K.; Wang, X. C.; Nishihara, Y.; Lu, D. L.; Antonietti, M.; Domen, K., Photocatalytic Activities of Graphitic Carbon Nitride Powder for Water Reduction and Oxidation under Visible Light. *Journal of Physical Chemistry C* **2009,** *113*, 4940.
9) Ke, J.; Liu, J.; Sun, H.; Zhang, H.; Duan, X.; Liang, P.; Li, X.; Tade, M. O.; Liu, S.; Wang, S., Facile Assembly of $Bi_2O_3/Bi_2S_3/MoS_2$ n-p Heterojunction with Layered n-Bi_2O_3 and p-MoS_2 for Enhanced Photocatalytic Water Oxidation and Pollutant Degradation. *Applied Catalysis B: Environmental* **2017,** *200*, 47.
10) Agiral, A.; Soo, H. S.; Frei, H., Visible Light Induced Hole Transport from Sensitizer to Co_3O_4 Water Oxidation Catalyst across Nanoscale Silica Barrier with Embedded Molecular Wires. *Chemistry of Materials* **2013,** *25*, 2264.

11) dos Santos, W. S.; Almeida, L. D.; Afonso, A. S.; Rodriguez, M.; Mesquita, J. P.; Monteiro, D. S.; Oliveira, L. C. A.; Fabris, J. D.; Pereira, M. C., Photoelectrochemical Water Oxidation Over Fibrous and Sponge-like $BiVO_4/\beta\text{-}Bi_4V_2O_{11}$ Photoanodes Fabricated by Spray Pyrolysis. *Applied Catalysis B: Environmental* **2016,** *182*, 247.
12) Li, W.; Bak, T.; Atanacio, A.; Nowotny, J., Photocatalytic Properties of TiO_2: Effect of Niobium and Oxygen Activity on Partial Water Oxidation. *Applied Catalysis B: Environmental* **2016,** *198*, 243.
13) Xiao, J.; Xie, Y.; Nawaz, F.; Wang, Y.; Du, P.; Cao, H., Dramatic Coupling of Visible Light with Ozone on Honeycomb-Like Porous g-C_3N_4 Towards Superior Oxidation of Water Pollutants. *Applied Catalysis B: Environmental* **2016,** *183*, 417.
14) Lan, Z.-A.; Zhang, G.; Wang, X., A Facile Synthesis of Br-Modified g-C_3N_4 Ssemiconductors for Photoredox Water Splitting. *Applied Catalysis B: Environmental* **2016,** *192*, 116.
15) Zheng, Y.; Liu, J.; Liang, J.; Jaroniec, M.; Qiao, S. Z., Graphitic Carbon Nitride Materials: Controllable Synthesis and Applications in Fuel Cells and Photocatalysis. *Energy & Environmental Science* **2012,** *5*, 6717.
16) Zhang, G. G.; Zang, S. H.; Lan, Z. A.; Huang, C. J.; Li, G. S.; Wang, X. C., Cobalt Selenide: a Versatile Cocatalyst for Photocatalytic Water Oxidation with Visible Light. *Journal of Materials Chemistry A* **2015,** *3*, 17946.
17) Yang, S.; Gong, Y.; Zhang, J.; Zhan, L.; Ma, L.; Fang, Z.; Vajtai, R.; Wang, X.; Ajayan, P. M., Exfoliated Graphitic Carbon Nitride Nanosheets as Efficient Catalysts for Hydrogen Evolution under Visible Light. *Advanced Materials* **2013,** *25*, 2452.
18) Wang, X.; Maeda, K.; Chen, X.; Takanabe, K.; Domen, K.; Hou, Y.; Fu, X.; Antonietti, M., Polymer Semiconductors for Artificial Photosynthesis: Hydrogen Evolution by Mesoporous Graphitic Carbon Nitride with Visible Light. *Journal of the American Chemical Society* **2009,** *131*, 1680.
19) Liu, G.; Niu, P.; Sun, C. H.; Smith, S. C.; Chen, Z. G.; Lu, G. Q.; Cheng, H. M., Unique Electronic Structure Induced High Photoreactivity of Sulfur-Doped Graphitic C_3N_4. *Journal of the American Chemical Society* **2010,** *132*, 11642.
20) Jorge, A. B.; Martin, D. J.; Dhanoa, M. T. S.; Rahman, A. S.; Makwana, N.; Tang, J.; Sella, A.; Corà, F.; Firth, S.; Darr, J. A.; McMillan, P. F., H_2 and O_2 Evolution from Water

Half-Splitting Reactions by Graphitic Carbon Nitride Materials. *The Journal of Physical Chemistry C* **2013,** *117*, 7178.

21) Wang, Y.; Zhang, J.; Wang, X.; Antonietti, M.; Li, H., Boron- and Fluorine-Containing Mesoporous Carbon Nitride Polymers: Metal-Free Catalysts for Cyclohexane Oxidation. *Angewandte Chemie International Edition* **2010,** *49*, 3356.
22) Zhang, G. G.; Zang, S. H.; Lin, L. H.; Lan, Z. A.; Li, G. S.; Wang, X. C., Ultrafine Cobalt Catalysts on Covalent Carbon Nitride Frameworks for Oxygenic Photosynthesis. *ACS Applied Materials & Interfaces* **2016,** *8*, 2287.
23) Zhang, G. G.; Zang, S. H.; Wang, X. C., Layered $Co(OH)_2$ Deposited Polymeric Carbon Nitrides for Photocatalytic Water Oxidation. *ACS Catalysis* **2015,** *5*, 941.
24) Duan, L. L.; Bozoglian, F.; Mandal, S.; Stewart, B.; Privalov, T.; Llobet, A.; Sun, L. C., A Molecular Ruthenium Catalyst with Water-Oxidation Activity Comparable to that of Photosystem II. *Nature Chemistry* **2012,** *4*, 418.
25) Bajdich, M.; Garcia-Mota, M.; Vojvodic, A.; Norskov, J. K.; Bell, A. T., Theoretical Investigation of the Activity of Cobalt Oxides for the Electrochemical Oxidation of Water. *Journal of the American Chemical Society* **2013,** *135*, 13521.
26) Feckl, J. M.; Dunn, H. K.; Zehetmaier, P. M.; Muller, A.; Pendlebury, S. R.; Zeller, P.; Fominykh, K.; Kondofersky, I.; Doblinger, M.; Durrant, J. R.; Scheu, C.; Peter, L.; Fattakhova-Rohlfing, D.; Bein, T., Ultrasmall Co_3O_4 Nanocrystals Strongly Enhance Solar Water Splitting on Mesoporous Hematite. *Advanced Materials Interfaces* **2015,** *2*, 1500358.
27) Zhang, Y.; Huang, J.; Ding, Y., Porous Co_3O_4/CuO Hollow Polyhedral Nanocages Derived from Metal-Organic Frameworks with Heterojunctions as Efficient Photocatalytic Water Oxidation Catalysts. *Applied Catalysis B: Environmental* **2016,** *198*, 447.
28) Sun, H.; Ang, H. M.; Tadé, M. O.; Wang, S., Co_3O_4 Nanocrystals with Predominantly Exposed Facets: Synthesis, Environmental and Energy Applications. *Journal of Materials Chemistry A* **2013,** *1*, 14427.
29) Shi, N.; Cheng, W.; Zhou, H.; Fan, T. X.; Niederberger, M., Facile Synthesis of Monodisperse Co_3O_4 Quantum Dots with Efficient Oxygen Evolution Activity. *Chemical Communications* **2015,** *51*, 1338.

30) Nozik, A. J.; Miller, J., Introduction to Solar Photon Conversion. *Chemical Reviews* **2010,** *110*, 6443.

31) Shi, N.; Cheng, W.; Zhou, H.; Fan, T.; Niederberger, M., Facile Synthesis of Monodisperse Co_3O_4 Quantum Dots with Efficient Oxygen Evolution Activity. *Chemical Communications* **2015,** *51*, 1338.

32) Morris, N. D.; Mallouk, T. E., A High-Throughput Optical Screening Method for the Optimization of Colloidal Water Oxidation Catalysts. *Journal of the American Chemical Society* **2002,** *124*, 11114.

33) Lan, Z. A.; Zhang, G. G.; Wang, X. C., A Facile Synthesis of Br-Modified g-C_3N_4 Semiconductors for Photoredox Water Splitting. *Applied Catalysis B-Environmental* **2016,** *192*, 116.

34) Wang, X.; Maeda, K.; Thomas, A.; Takanabe, K.; Xin, G.; Carlsson, J. M.; Domen, K.; Antonietti, M., A Metal-Free Polymeric Photocatalyst for Hydrogen Production from Water under Visible light. *Nature Materials* **2009,** *8*, 76.

35) Niu, P.; Zhang, L.; Liu, G.; Cheng, H.-M., GO/C_3N_4 Graphene-Like Carbon Nitride Nanosheets for Improved Photocatalytic Activities. *Advanced Functional Materials* **2012,** *22*, 4763.

36) Duan, J. J.; Chen, S.; Jaroniec, M.; Qiao, S. Z., Porous C_3N_4 Nanolayers@N-Graphene Films as Catalyst Electrodes for Highly Efficient Hydrogen Evolution. *ACS Nano* **2015,** *9*, 931.

37) Moulder, J. F.; Chastain, J.; King, R. C., Handbook of X-ray Photoelectron Spectroscopy: A Reference Book of Standard Spectra for Identification and Interpretation of XPS data. Perkin-Elmer Eden Prairie, MN: 1992.

38) Pal, J.; Chauhan, P., Study of Physical Properties of Cobalt Oxide (Co_3O_4) Nanocrystals. *Materials Characterization* **2010,** *61*, 575.

39) Feckl, J. M.; Dunn, H. K.; Zehetmaier, P. M.; Müller, A.; Pendlebury, S. R.; Zeller, P.; Fominykh, K.; Kondofersky, I.; Döblinger, M.; Durrant, J. R.; Scheu, C.; Peter, L.; Fattakhova-Rohlfing, D.; Bein, T., Ultrasmall Co_3O_4 Nanocrystals Strongly Enhance Solar Water Splitting on Mesoporous Hematite. *Advanced Materials Interfaces* **2015,** *2*, 1500358.

40) Zhang, Y.; Liu, J.; Wu, G.; Chen, W., Porous Graphitic Carbon Nitride Synthesized via Direct Polymerization of Urea for Efficient Sunlight-Driven Photocatalytic Hydrogen Production. *Nanoscale* **2012,** *4*, 5300.

41) Tian, N.; Huang, H.; Liu, C.; Dong, F.; Zhang, T.; Du, X.; Yu, S.; Zhang, Y., In Situ Co-Pyrolysis Fabrication of CeO_2/g-C_3N_4 n–n Type Heterojunction for Synchronously Promoting Photo-Induced Oxidation and Reduction Properties. *Journal of Materials Chemistry A* **2015,** *3*, 17120.

42) Zhang, X. H.; Yu, L. J.; Zhuang, C. S.; Peng, T. Y.; Li, R. J.; Li, X. G., Highly Asymmetric Phthalocyanine as a Sensitizer of Graphitic Carbon Nitride for Extremely Efficient Photocatalytic H_2 Production under Near-Infrared Light. *ACS Catalysis* **2014,** *4*, 162.

Every reasonable effort has been made to acknowledge the owners of copyright material. I would be pleased to hear from any copyright owner who has been omitted or incorrectly acknowledged.

Chapter 5. Heterostructured WO_3@$CoWO_4$ Bilayer Nanosheets for Enhanced Visible-Light Photo, Electro and Photoelectrochemical Oxidation of Water

Abstract

In Chapters 3 and 4, we focused on metal-free g-C_3N_4 photocatalyst modified by cobalt-based cocatalysts for photocatalytic water oxidation. In this chapter, we further studied metal-based semiconductors. A facile interface-induced synthesis method is first established to newly fabricate two-dimensional (2D) bilayer nanosheets of WO_3@$CoWO_4$ as highly efficient catalysts for enhanced photo, electro and photoelectrochemical oxygen evolution reactions (OERs). The heterostructure and the interfacial oxygen vacancy of WO_3@$CoWO_4$ reduce the energy barriers in OER. Density functional theory (DFT) calculations and material characterizations reveal that WO_3@$CoWO_4$ p-n heterojunction endows the composite with a narrowed band gap for better visible-light harvesting, rapid charge transfer across the interface and lower recombination rate of the photo-excited carriers. The interface O-vacancy vests the active Co site with an enhanced density of state (DOS) at valence band maximum (VBM), which can increase the concentration of the photogenerated holes to improve photocatalytic and photoelectrochemical (PEC) activity. This study presents a proof-of-concept design toward low cost and multi-metal 2D/2D nanosheets for water oxidation applications.

5.1 Introduction

As an emerging technology for solar energy conversion and storage, photocatalytic and photoelectrochemical (PEC) splitting of water into H_2 and O_2 has attracted tremendous attention for sustainable environment and energy development.[1–3] In this course, decomposition of water to dissociative oxygen (known as water oxidation or OER) is kinetically sluggish, due to the multi-step, four-electron and multi-proton transfer processes. Rational design of efficient photocatalytic or PEC water oxidation catalysts (WOCs) is essential for advancing the technologies toward efficient water-splitting into hydrogen.[4,5] Enormous efforts have been devoted to pursuing suitable semiconductor materials that can achieve efficient solar-energy-conversion and propel the complex water oxidation reactions by photo-generated holes.[6,7] Among them, low-cost tungsten oxide (WO_3) has emerged as a promising n-type and visible-light-active semiconductor material, which possesses up to 12% solar spectrum absorption with a bandgap energy of 2.7 eV.[8,9] Nonetheless, the low photon energy conversion efficiency, instability caused by photo-corrosion, and poor kinetics of pristine WO_3 usually result in an unsatisfactory activity in OER.[10,11]

It was revealed that WO_3 in a 2D nanosheet configuration has planar conduction channels, promoting the exposure of catalytically active facets to accelerate fast transport of the photoexcited charge carriers.[12,13] However, the long migration route in WO_3 makes it easy for electron-hole recombination. To solve this problem, construction of a heterojunction composite using two semiconductors is an excellent strategy.[14,15] As a p-type semiconductor with low cost and high stability, cobalt tungstate ($CoWO_4$) has drawn our attention. We project that coupling WO_3 nanosheet with $CoWO_4$ nanosheet in a p-n heterostructure would be a promising WOC candidate. However, specific challenges have to be addressed in the synthesis of WO_3 nanosheet because it is a nonlayered compound and lacks the driving force for 2D anisotropic growth.[16] Therefore, the design and integration of $CoWO_4$-WO_3 bilayered nanosheets are much more difficult. To the best of our knowledge, no such a material has been attempted and reported.

In this chapter, we elaborately propose a hydrothermal method to generate WO_3 nanosheets. Then, a scalable interface-induced strategy for bilayer formation was established by coating

$CoWO_4$ onto WO_3 to obtain 2D WO_3@$CoWO_4$ bilayer hybrids. In this format, $CoWO_4$ produces benefits to photocatalytic or PEC OER with triple functions: i) construction of WO_3@$CoWO_4$ p-n heterojunction; ii) prevention of WO_3 from corrosion; iii) $CoWO_4$ as an active OER electrocatalyst[17–19] to serve as a cocatalyst to promote photocatalytic OER. For the first time, evident enhancement of electrochemical, visible-light photocatalytic and PEC water oxidation performance was verified simultaneously. Moreover, we performed DFT calculations for structural insights to the enhanced electro/photo-chemical and PEC activities of WO_3@$CoWO_4$ nanosheets.

5.2 Experimental Section

5.2.1 Synthesis of WO_3 Nanosheets

WO_3 nanosheets were synthesized via a hydrothermal method. In detail, 0.38 g of tungstic acid was dispersed in 27 mL deionized (DI) water, followed by dissolving 0.5 g thiourea in the solution. The suspension was then transferred into a 50 ml Teflon liner and sealed in an autoclave. The autoclave was heated at 180 ºC for 24 h. The precipitates were separated using a centrifuge and washed with DI water and ethanol for several times. Finally, WO_3 powders were obtained after drying at 60 ºC.

5.2.2 Synthesis of WO_3@$CoWO_4$ Nanosheet Composites

The obtained WO_3 (0.1 g) was dispersed into 10 mL DI water under stirring for 10 min at room temperature. After that, certain amount of $Co(NO_3)_2 \cdot 6H_2O$ was added into the suspension solution and stirred for another 10 min. Then, 2.5 mL ammonium hydroxide solution was added dropwise into the above solution and stirred for 1 h at room temperature before evaporating at 80 ºC. Finally, the residual powders were collected and heated at 300 ºC for 2 h under air with a heating rate of 5 ºC min^{-1}. The synthesized catalysts were designated as WO_3@$CoWO_4$-1, WO_3@$CoWO_4$-2, WO_3@$CoWO_4$-3, and WO_3@$CoWO_4$-4, and WO_3@$CoWO_4$-5 according to the different additive amount of $Co(NO_3)_2 \cdot 6H_2O$ at 3.2, 6.4, 9.6, 64 and 128 mg, respectively.

5.2.3. Electrochemical Measurements

Electrocatalytic tests were conducted in N_2-saturated 0.1 M KOH in a three-electrode electrochemical system using a rotating disk electrode (RDE) configuration (Pine Instrument Company, USA), which is controlled by a Gamry electrochemical workstation (Reference 3000). Ag/AgCl (KCl sat.) and Pt wire were adopted as the reference electrode and the counter electrode, respectively.

Preparation of working electrode is described as follows: 7 mg catalyst was added into a solution containing 25 µL Nafion® 117 solution and 500 µL ethanol to generate a suspension by sonication. Then, 10 µL of the catalyst ink was dripped onto a glassy carbon electrode (5.0 mm in diameter) and dried in air. All potentials were converted into reversible hydrogen electrode (RHE) values based on equation (5.1):

$$\boldsymbol{E_{RHE} = E_{Ag/AgCl} + 0.059\mathrm{pH} + 0.197\ \mathrm{V}} \quad (\mathbf{5.1})$$

The electrodes were activated by running cyclic voltammetry (CV) cycles from 1.2 to 1.8 V (vs RHE) for at least 10 times till stable and reproducible curves were obtained. Then, polarization curves using linear sweep voltammetry (LSV) were recorded with a rotation speed of 1600 rpm at a scan rate of 5 mV s^{-1}. The overpotential (η) was calculated according to the following formula:

$$\eta = E_{RHE} - 1.23\ \mathrm{V} \qquad (5.2)$$

All polarization plots were recorded after iR-correction. The accelerated durability tests (ADT) for WO_3@$CoWO_4$-4 were conducted by measuring CV cycles in potentials from 1.164 to 1.764 V (vs RHE) at a scan rate of 200 mV s^{-1}. LSV of ADT after 1000 and 10000 CV cycles were recorded. To probe changes in double-layer capacitance (C_{dl}) during ADT, CV cycles were tested from 1.25 - 1.30 V at scan rates of 10, 20, 30, 40, and 60 mV s^{-1} before and after 1000 and 10000 cycles. The corresponding capacitive current densities at 1.275 V were plotted as a function of scan rate. The slope of the fitted line equals twice the value of C_{dl} and represents electrochemically active surface area (EASA). The EASAs of the other samples were evaluated using the same method for comparison. Further, chronoamperometric response (i-t) of WO_3@$CoWO_4$-4 was estimated at 1.614 V (vs. RHE) in 0.1 M KOH at 1600 rpm.

5.2.4 Photocatalytic Oxygen Evolution Reaction Tests

For each reaction, 50 mg catalyst was dispersed in 50 mL phosphate buffer solution and the pH value was adjusted to around 6.8, followed by adding 0.49 g Na_2SO_4, 0.18 g $Na_2S_2O_8$ and 0.03 g $[Ru(bpy)_3]Cl_2 \cdot 6H_2O$. After that, the solution was transferred to a sealed double jacketed reactor (800 mL) with a quartz window, which was connected to an on-line gas chromatograph (Agilent 490 Micro GC) with a thermal conductivity detector. To remove air in the reactor completely, N_2 was pumped in for at least 30 min. Then, the solution was stabilized in the dark for 10 min, which was probed as the baseline. The solution was irradiated via a 300 W Xeon lamp (Newport) through a light filter ($\lambda > 420$ nm) and aligned to 200 mW/cm^2 (2 suns) to start the reaction. The reaction temperature was maintained at 25 ºC by a flow of cooling water, controlled by a thermostatic water bath.

5.2.5 Photoelectrochemical Measurement

Photoelectrochemical tests were carried out on a Zennium workstation (Zahner, Germany) in a three-electrode framework, with Ag/AgCl electrode as the reference electrode and Pt plate (1.5×1.5 cm^2) as the counter electrode. F-doped tin oxide (FTO) glasses were adopted as the photoanode substrates, which were cleaned before use under sonication by acetone, ethanol, and distilled water successively. Samples were loaded onto the FTO as below: 8 mg catalyst, 25 μL Nafion 117 solutions and 500 μL ethanol were mixed by ultrasonication and 40 μL of the resulted suspension was loaded onto the 1×1 cm2 FTO each time via a spin coating method. The photoanodes were obtained by annealing the FTO glasses at 300 ℃ for 30 min under air atmosphere. The PEC properties were measured via the linear sweep voltammetry (LSV) method under irradiation of AM 1.5G simulated solar light (light intensity: 1 sun or 100 mW cm^{-2}) from 0.6 to 1.8 V (vs RHE) at a sweep rate of 10 mV s^{-1}.

Electrochemical impedance spectra (EIS) measurements were carried out under dark and irradiation, respectively, in a frequency range of 100k Hz to 100m Hz. Potentiostatic response was measured at 1.23 V (vs RHE) under irradiation for 1 h. The Na_2SO_4 solution (0.5 M, pH 6.8) as the electrolyte was purged with N_2 for 30 min prior to the measurement. Mott-Schottky analysis was carried out at a frequency of 1 kHz.

5.2.6 Materials Characterizations

Details on XRD, XPS, TEM, HAADF-STEM with EDX mapping analysis, UV-Visible diffuse reflectance spectra and photoluminescence spectra tests can refer to Chapters 3 and 4.

Electron paramagnetic resonance (EPR) signals of radicals were trapped by 5, 5-dimethyl-1-pyrroline N-oxide (DMPO) and recorded on a Bruker EMXplus spectrometer. A sample of 40 μL solution containing 0.5 mg/mL catalysts (WO_3 or WO_3@$CoWO_4$-3), 0.05 M Na_2SO_4, 0.01 M $Na_2S_2O_8$ and 0.8 μM $Ru(bpy)_3Cl_2$ was mixed with 40 μL 0.08 M DMPO. After that, the home-made quartz tube with the samples was illuminated under a 100 W Hg lamp. The settings for the EPR spectrometer were as follows: center field (3514.70 G); sweep width (100 G); microwave frequency (9.82 GHz); modulation frequency (200 kHz); power (10.00 mW).

5.2.7 Density Functional Theory (DFT) calculations

Spin-polarized DFT calculations were performed using the Vienna *Ab initio* Simulations Package (VASP)[20,21] and projected augmented wave (PAW)[22–24] method (with 5*p*, 6*s* and 5*d* treated as valence electrons for W, 3*d* and 4*s* for Co, and 2*s* and 2*p* for O). Generalized gradient approximation (GGA) in the Perdew, Burke and Ernzerhof (PBE)[25] parameterization was used to account for exchange-correlation interaction. The Hubbard U parameters (GGA+U) with U=4.5 eV [26] and 6.0 eV [27] for Co and W, respectively, were used to describe the on-site *d*-electron correlations in $CoWO_4$ (space group *P2/c*, No. 13) and WO_3 (space group *P6/mmm*, No. 191).

For relaxations of bulk WO_3 and $CoWO_4$, the cut-off energy of plane-wave basis was set to 520 eV, and integrations over the first Brillouin zone were made using Gamma-centred k-point sets of 4×4×8 for WO_3 and 4×2×4 for $CoWO_4$. With these settings, the total energy was able to converge within 1 meV/atom. Atomic positions were fully relaxed with the energy converged within 10^{-6} eV/cell and the force converged to less than 10^{-4} eV/Å. Surface calculations used the same cutoff energy and k-point grids as dense as in the bulk calculations (in the case of vacuum direction, only Gamma point was used).

Gibbs free energy changes for the four elementary steps of OER were calculated using following equations:[28,29]

$$\begin{aligned}\Delta G_1 &= G(*\,\mathrm{OH}) - G(*) - G(\mathrm{OH}) \\ &= E(*\,\mathrm{OH}) + 0.5E(\mathrm{H_2}) - E(*) - E(\mathrm{H_2O}) - e\mathrm{U} + k_B T\ln(a_{\mathrm{H^+}}) + \Delta\mathrm{ZPE} \\ &\quad - T\Delta S \qquad (5.3)\end{aligned}$$

$$\begin{aligned}\Delta G_2 &= G(*\,\mathrm{O}) + G(\mathrm{H}) - G(*\,\mathrm{OH}) \\ &= E(*\,\mathrm{O}) + 0.5E(\mathrm{H_2}) - E(*\,\mathrm{OH}) - e\mathrm{U} + k_B T\ln(a_{\mathrm{H^+}}) + \Delta\mathrm{ZPE} - T\Delta S \qquad (5.4)\end{aligned}$$

$$\begin{aligned}\Delta G_3 &= G(*\,\mathrm{OOH}) - G(\mathrm{OH}) - G(*\,\mathrm{O}) \\ &= E(*\,\mathrm{OOH}) - E(*\,\mathrm{O}) + 0.5E(\mathrm{H_2}) - E(\mathrm{H_2O}) - e\mathrm{U} + k_B T\ln(a_{\mathrm{H^+}}) + \Delta\mathrm{ZPE} \\ &\quad - T\Delta S \qquad (5.5)\end{aligned}$$

$$\Delta G_4 = 4 \times [1.23\ eV - e\mathrm{U} + k_B T\ln(a_{\mathrm{H^+}})] - (\Delta G_1 + \Delta G_2 + \Delta G_3) \qquad (5.6)$$

Table 5.1 Entropy and zero-point energy contributions to Gibbs free energy of gaseous and adsorbed OER species.[30]

Species	ZPE (eV)	TS (eV)
H_2O	0.56	0.67
H_2	0.27	0.41
*OH	0.35	0.0
*O	0.05	0.0
*OOH	0.41	0.0

where $E(\mathrm{H_2O})$, $E(*)$, $E(*\,\mathrm{OH})$, $E(*\,\mathrm{O})$, and $E(*\,\mathrm{OOH})$ are DFT total energies on catalytic surfaces without and with *OH, *O and *OOH, respectively. $G(*)$, $G(*\,\mathrm{O})$, $G(*\,\mathrm{OH})$, and $G(*\,\mathrm{OOH})$ are the Gibbs free energies of the surfaces without and with *O, *OH and *OOH groups, respectively. k_B is the Boltzmann constant and T is temperature (300 K). ZPE is the abbreviation of zero-point energy. S denotes entropy. The entropy and ZPE contributions to the Gibbs free energy change are included in the term of $(\Delta\text{ZPE} - T\Delta S)$. The used ZPE and entropy values of gaseous and adsorbed OER species are listed in Table 5.1.

5.3 Results and Discussion

5.3.1 Synthesis and Structure Analysis

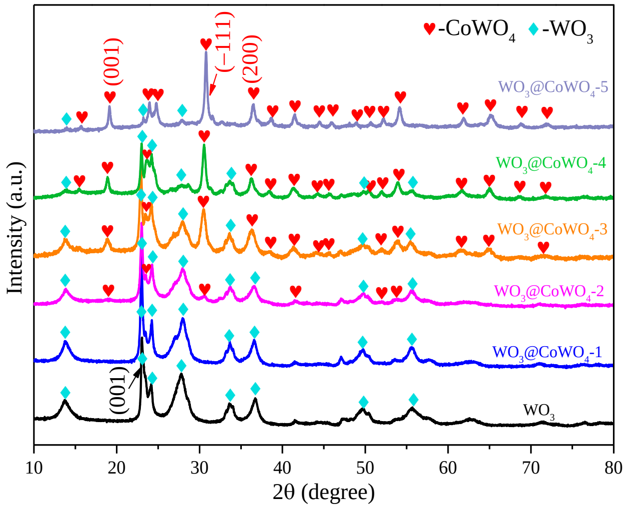

Figure 5.1 XRD patterns of WO_3 and WO_3@$CoWO_4$ composites.

X-ray diffraction (XRD) patterns (Figure 5.1) indicate that WO_3 nanosheets have a hexagonal crystalline structure (h-WO_3, JCPDS # 33-1387). Different WO_3/$CoWO_4$ molar ratios of 1:0.026, 1:0.055, 1:0.083, 1:1 and 0.023:1 were prepared from WO_3@$CoWO_4$-1, -2, -3, -4 to -5, respectively. Accordingly, the diffraction peaks of monoclinic $CoWO_4$ (JCPDC 15-0867) enhance gradually in the five samples with $CoWO_4$ being as the main phase in WO_3@$CoWO_4$-5.

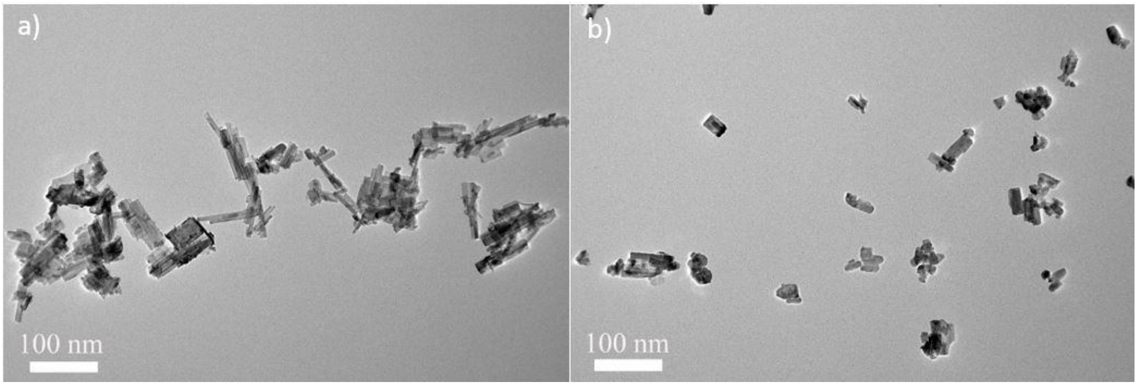

Figure 5.2 Low magnitude TEM images of a) WO_3, and b) WO_3@$CoWO_4$-3.

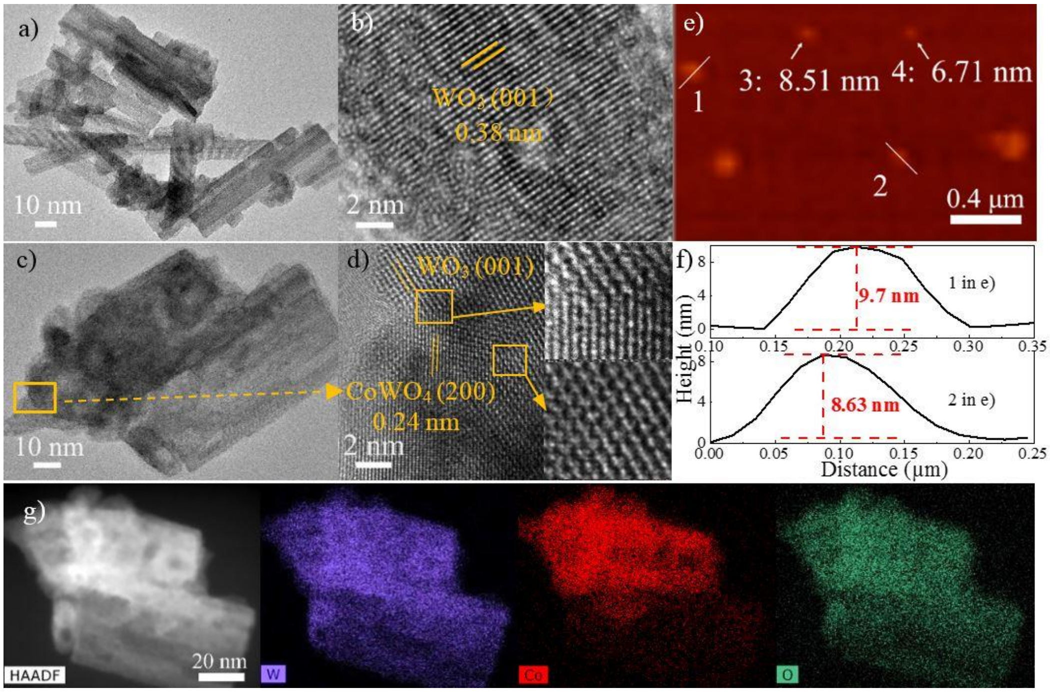

Figure 5.3 TEM and HRTEM images of a, b) WO_3 and c, d) WO_3@$CoWO_4$-3. e) 3D AFM image of WO_3@$CoWO_4$-3 and f) thickness data of 1, 2 in e). g) HAADF-STEM image of WO_3@$CoWO_4$-3 and its EDX elemental mapping analysis.

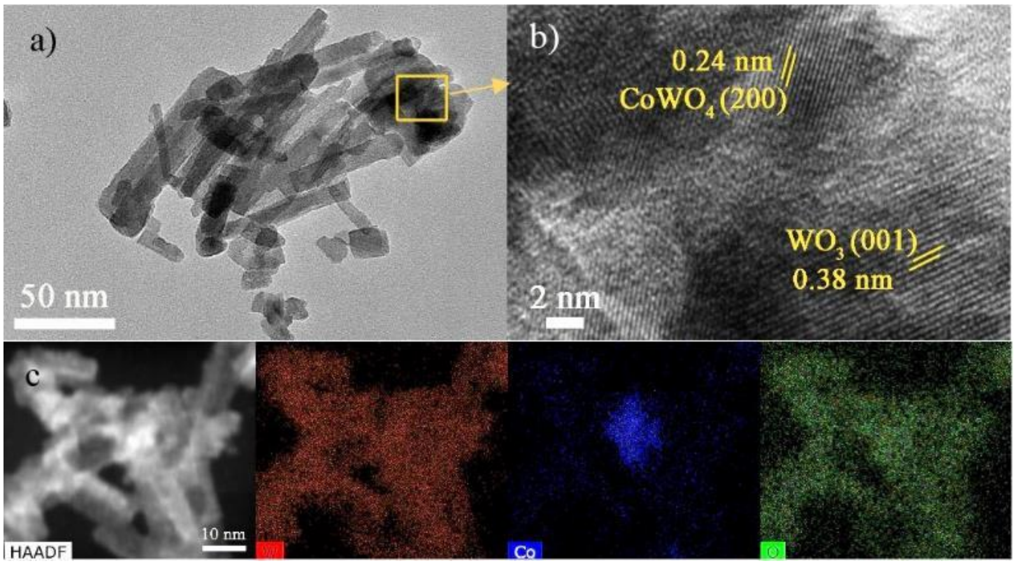

Figure 5.4 a) TEM, b) HRTEM, c) HAADF-STEM and the corresponding EDX elemental mapping images of WO_3@$CoWO_4$-1.

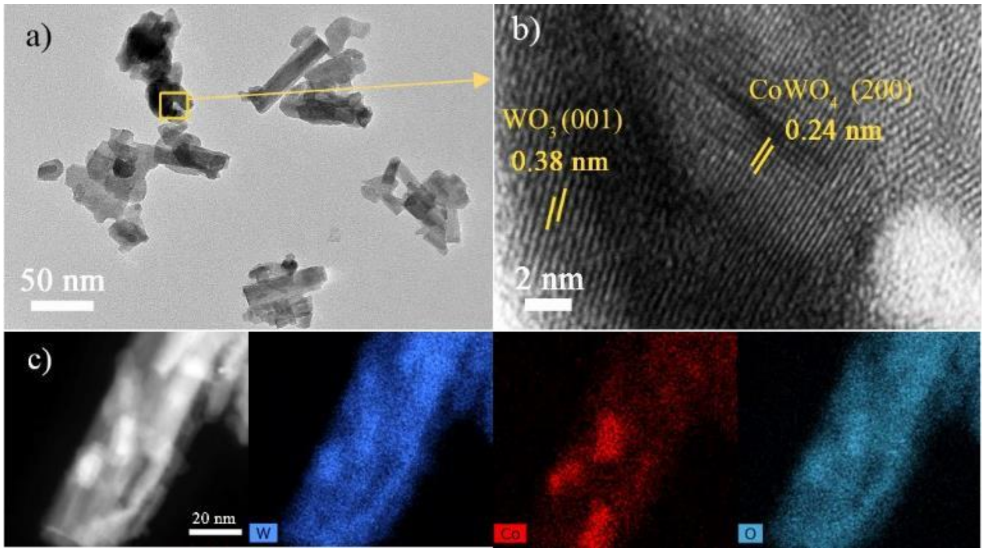

Figure 5.5 a) TEM, b) HRTEM, c) HAADF-STEM and the corresponding EDX elemental mapping images of WO_3@$CoWO_4$-2.

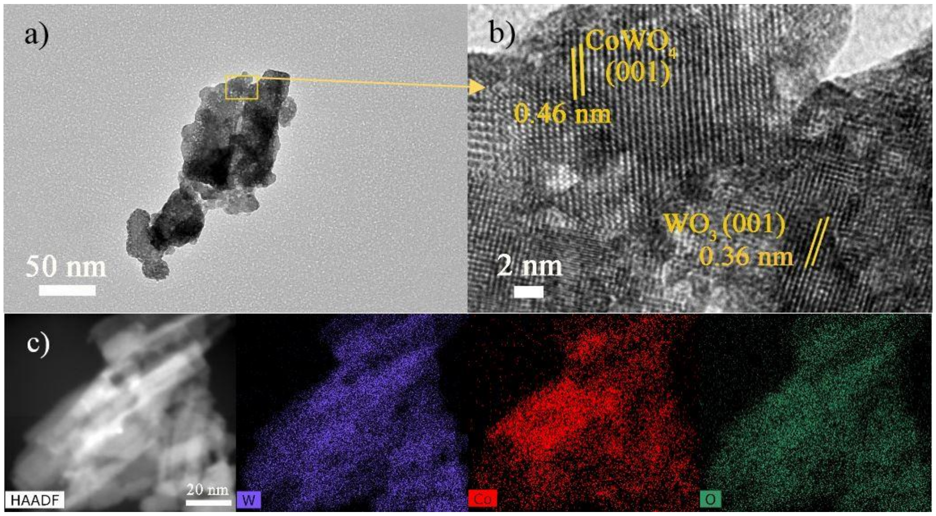

Figure 5.6 a) TEM, b) HRTEM, c) HAADF-STEM and the corresponding EDX elemental mapping images of $WO_3@CoWO_4$-4.

Transmission electron microscopy (TEM) images in Figures 5.2a and 5.3a reveal the nanosheet morphology of WO_3. The high-resolution TEM (HRTEM) analysis indicates that (001) planes are exposed planes of WO_3 (Figure 5.3b). $WO_3@CoWO_4$ composites display very similar nanosheet morphologies (Figures 5.2-5.7). Figure 5.3d ($WO_3@CoWO_4$-3) depicts the close atomic bonding between the (200) planes of $CoWO_4$ and the (001) planes of WO_3 with interface defects and vacancies caused by lattice mismatches. These defects or vacancies are also observed in other composites (Figure 5.4-5.7). The presence of O vacancies in the composites can also be verified by the signal of W^{5+} (g=1.96) in representative solid-state EPR test on $WO_3@CoWO_4$-3 (Figure 5.8).[31]

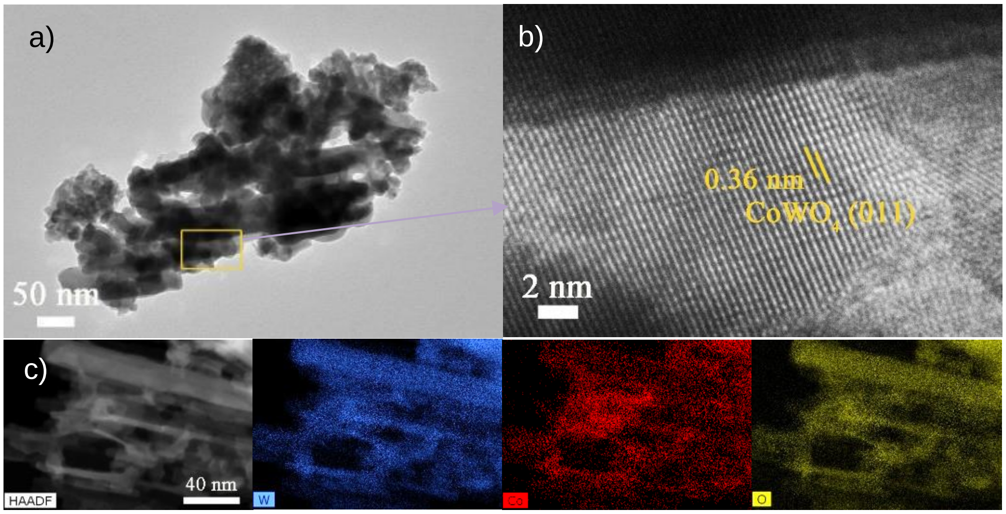

Figure 5.7 a) TEM, b) HRTEM, c) HAADF-STEM and the corresponding EDX elemental mapping images of WO_3@$CoWO_4$-5.

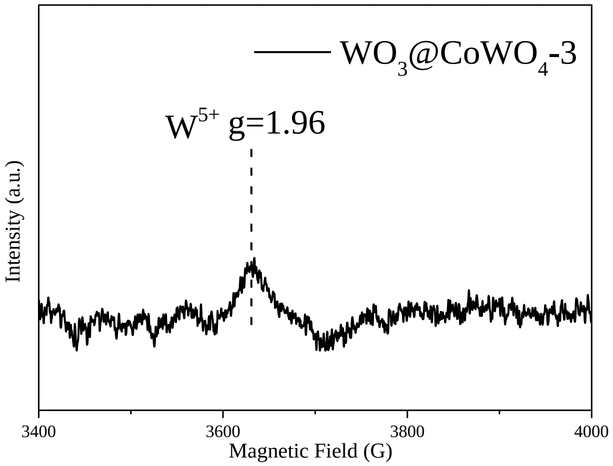

Figure 5.8 Solid-state EPR signals of W^{5+} tested on WO_3@$CoWO_4$-3.

Representative three-dimensional (3D) atomic force microscopy (AFM) measurements (Figures 5.3e and f) on WO_3@$CoWO_4$-3 show that the nanosheets might be thinner than 10 nm. HAADF-STEM) and corresponding energy-dispersive X-ray spectroscopy (EDX) elemental mapping images of the composites (in Figures 5.3-5.7) implicate the different coverage levels of $CoWO_4$ on WO_3. The full-scan X-ray photoelectron spectroscopy (XPS) spectra of WO_3 and WO_3@$CoWO_4$-3 are provided in Figure 5.9. The peaks in W 4f spectra centering at 35.6, and 37.8 eV are ascribed to the spin-orbit splitting of W $4f_{7/2}$ and W $4f_{5/2}$, illustrating W^{6+} as the dominant valence state in both samples.[32,33] In the O1s spectra (Figure 5.9c), the peak at 530.4 eV can be associated with oxygen bonded to metal species, whereas the one centred at 531.6 eV is typical of the low coordination oxygen ions on the surface.[34,35] Co 2p spectrum featured the main peaks of Co $2p_{3/2}$ at 781.4 and Co $2p_{1/2}$ at 796.7 eV with separate satellite shake-up lines and spin energy separation of 15.3 eV, indicating the typical oxidation state of Co^{2+} (Figure 5.9d).[33,34]

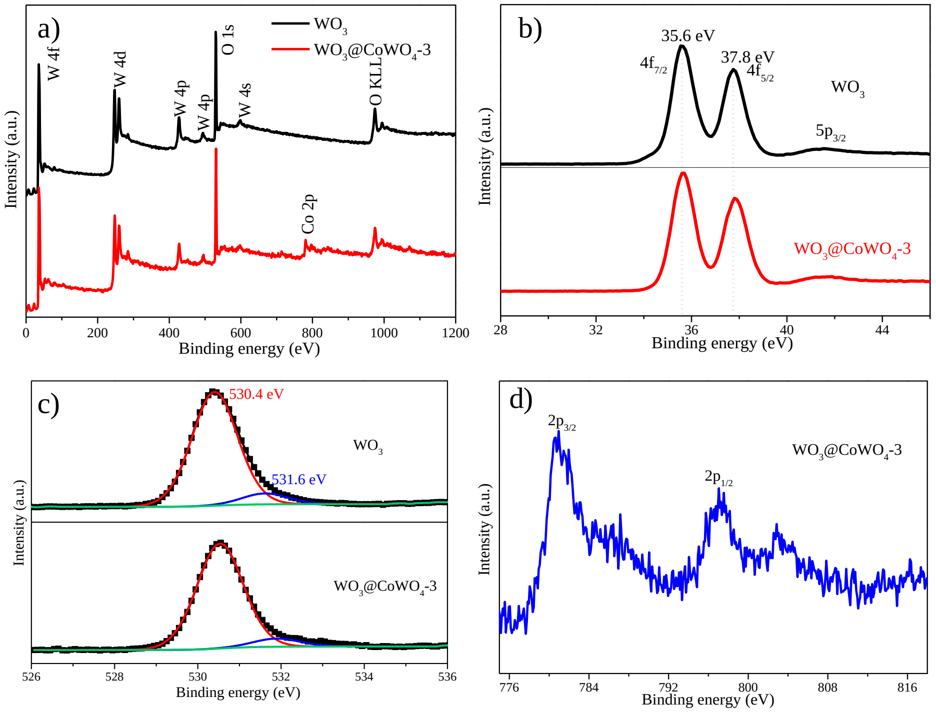

Figure 5.9 XPS survey of WO_3 and $WO_3@CoWO_4$-3. a) Full spectra and high-resolution XPS spectra of b) W 4f, c) O 1s and d) Co 2p.

The formation mechanism of the bilayer nanosheet composite is briefly proposed in Figure 5.10. During the dropwise addition of $NH_3{\cdot}H_2O$ into a $Co(NO_3)_2$ solution with dispersed WO_3, $Co(OH)_2$ formed initially, but it was dissolved by excess $NH_3{\cdot}H_2O$ to generate a $[Co(NH_3)_6]^{2+}$ complex.[36] Meanwhile, partial WO_3 can be transformed into $(NH_4)_2WO_4$ by $NH_3{\cdot}H_2O$,[37] which will interact with the $[Co(NH_3)_6]^{2+}$ to form $[Co(NH_3)_6]WO_4$ or $CoWO_4$ sediments on the surface of residual WO_3. After annealing in air, stable $WO_3@CoWO_4$ nanosheets were obtained. It is a simultaneous process of continuous WO_3 exfoliation and in-situ $CoWO_4$ coating, which results in thinner layers of WO_3 and $CoWO_4$ in the composites.

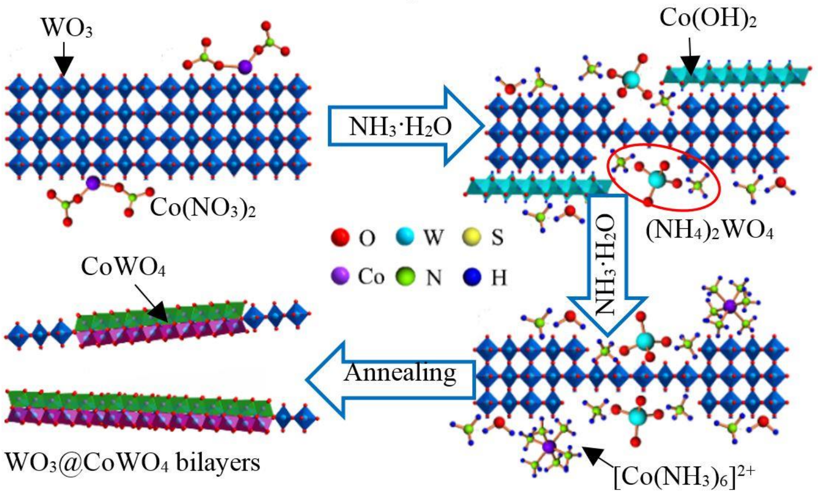

Figure 5.10 Schematic showing of the formation process of $WO_3@CoWO_4$ bilayer nanosheets.

5.3.2 Evaluation of the Electrochemical OER Performance

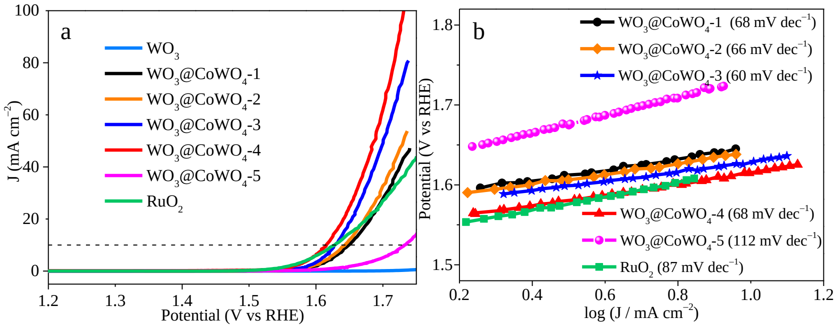

Figure 5.11 a) Polarization curves tested in 0.1M KOH and b) the corresponding Tafel plots.

The electrocatalytic OER activity of the samples was evaluated by polarization curves (Figure 5.11a). The overpotential at a current density (J) of 10 mA cm^{-2} is a criterion for assessing OER properties. WO_3 was almost inactive in the electrocatalytic OER. With higher $CoWO_4$ loading in the composites, the electrocatalytic activity increased dramatically and then declined. $WO_3@CoWO_4$-4 gave the smallest overpotential of 0.38 V, which is lower than commercial RuO_2 (0.40 V). $WO_3@CoWO_4$-5 displayed an enlarged overpotential, attributable to fewer interface defects from low WO_3 content. These defects can serve as catalytically active sites in OER, proved by the DFT calculations shown later. The Tafel plots (Figure 5.11b) indicated smaller Tafel slopes of $WO_3@CoWO_4$-1, -2, -3 and -4 than RuO_2, suggesting their more favorable OER kinetics.[38] WO_3@$CoWO_4$-5 showed a much higher Tafel slope. As the best OER catalyst, WO_3@$CoWO_4$-4 displayed excellent durability, as provided in Figure 5.12.

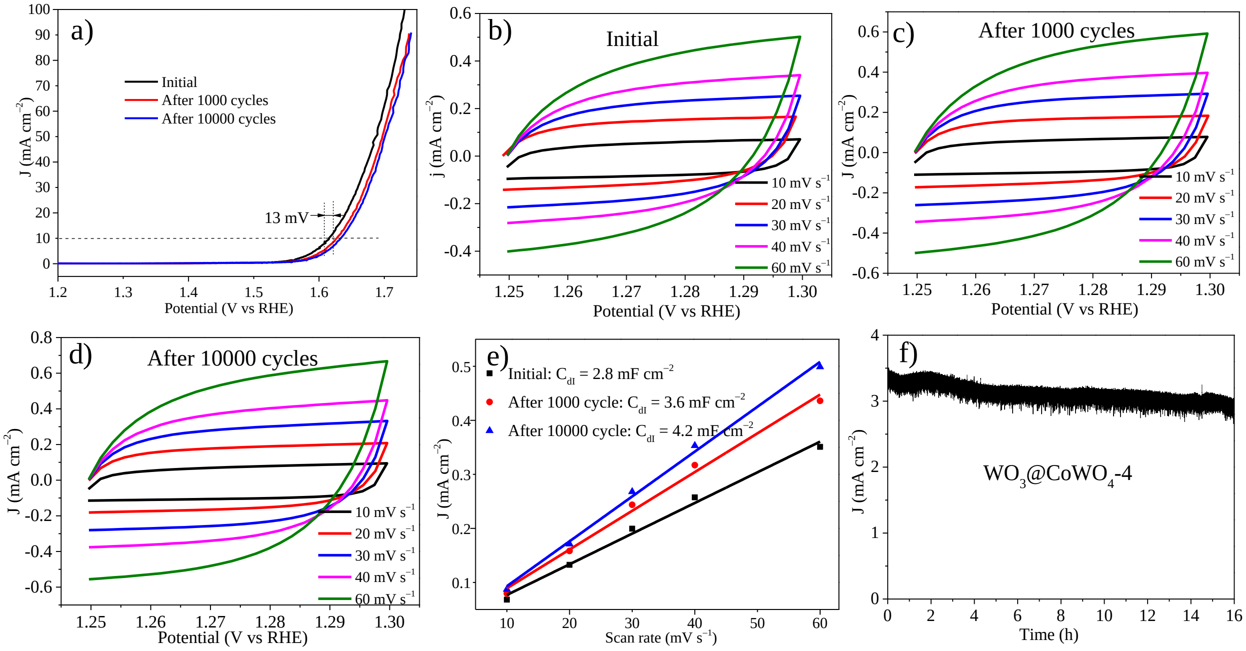

Figure 5.12 Durability test on WO_3@$CoWO_4$-4 in 0.1M KOH. a) ADT tests; b-d) CV tests at different scan rates before and after ADT tests of 1000 and 10000 cycles; e) current density as a function of the scan rate before and after ADT tests; f) chronoamperometric response (i-t) of WO_3@$CoWO_4$-4 estimated at 1.614 V (vs. RHE) and 1600 rpm.

As shown in Figure 5.12a, after accelerated durability test (ADT) of 1000 cycles, the overpotential of WO_3@$CoWO_4$-4 increased by about 13 mV. Notably, negligible difference was observed after another 9000 cycles, revealing its fairly excellent durability performance. The electrochemical double-layer capacitances (C_{dl}) before and after ADT tests were calculated by measuring CV curves (Figure 5.12b-d) to estimate the electrochemical active surface area (EASA). As shown in Figure 5.12e, C_{d1} increased from the initial 5.67 to 7.17 and 8.3 mF cm^{-2} after 1000 and 10000 cycles, respectively. The results indicated the stability of the active sites, which is beneficial to the catalytic performance. The slight enhancement in ECSA might arise from the changes in the valence states of Co (Co^{2+}/Co^{3+}) and W (W^{5+}/W^{6+}) on the catalyst surface during the ADT tests.[39] The stability of WO_3@$CoWO_4$-4 was also evaluated by measuring Chronoamperometric response (i-t), which showed a little decay (17%) of J over 16 h (Figure 5.12f).

In addition, WO_3@$CoWO_4$ composites all displayed much higher electrochemically active surface area (EASA) than WO_3, with WO_3@$CoWO_4$-4 to be the highest. (Figure 5.13). This result indicates that abundant active sites were introduced to WO_3 by loading of $CoWO_4$.

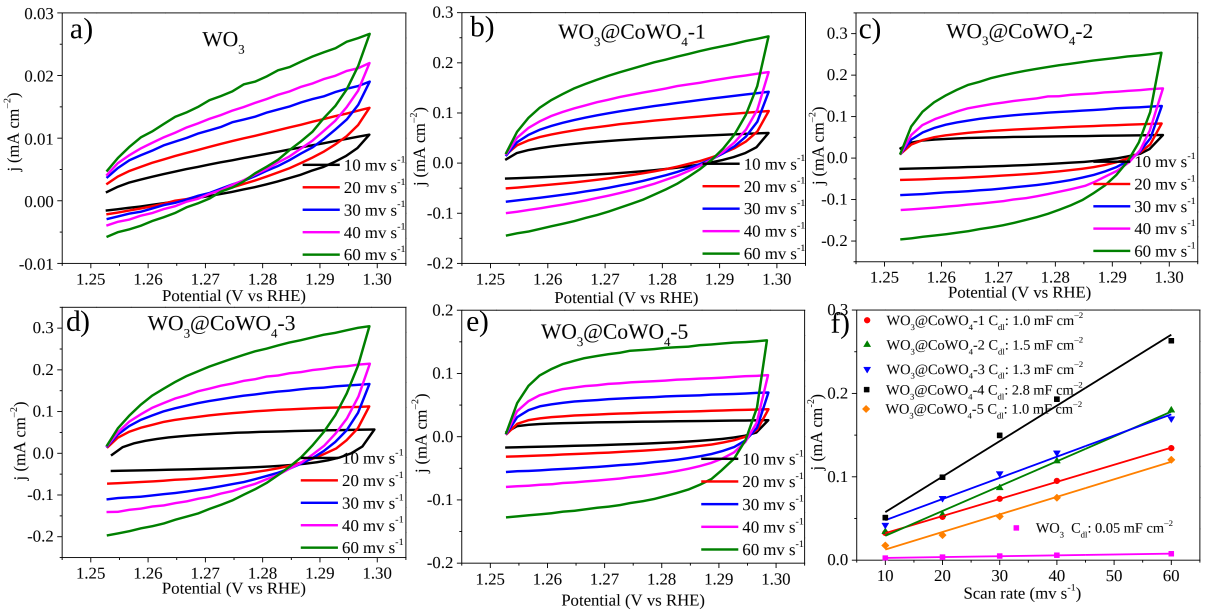

Figure 5.13 a-e) CV tests at different scan rates and f) current density as a function of scan rate.

5.3.3 Visible-Light Photocatalytic OER Performance

Figure 5.14a displays photocatalytic OER activities of the samples. Elevated performance was observed on WO_3@$CoWO_4$ composites compared with WO_3. With rising $CoWO_4/WO_3$ ratios, the OER activity increased first and then decreased. WO_3@$CoWO_4$-3 presented the highest O_2 evolution rate (1.6 mmol g^{-1} O_2 in 1 h), which is over 9 times higher than WO_3. This rate is among the highest values reported for nonprecious metallic OER catalysts, as compared in Table 5.2.

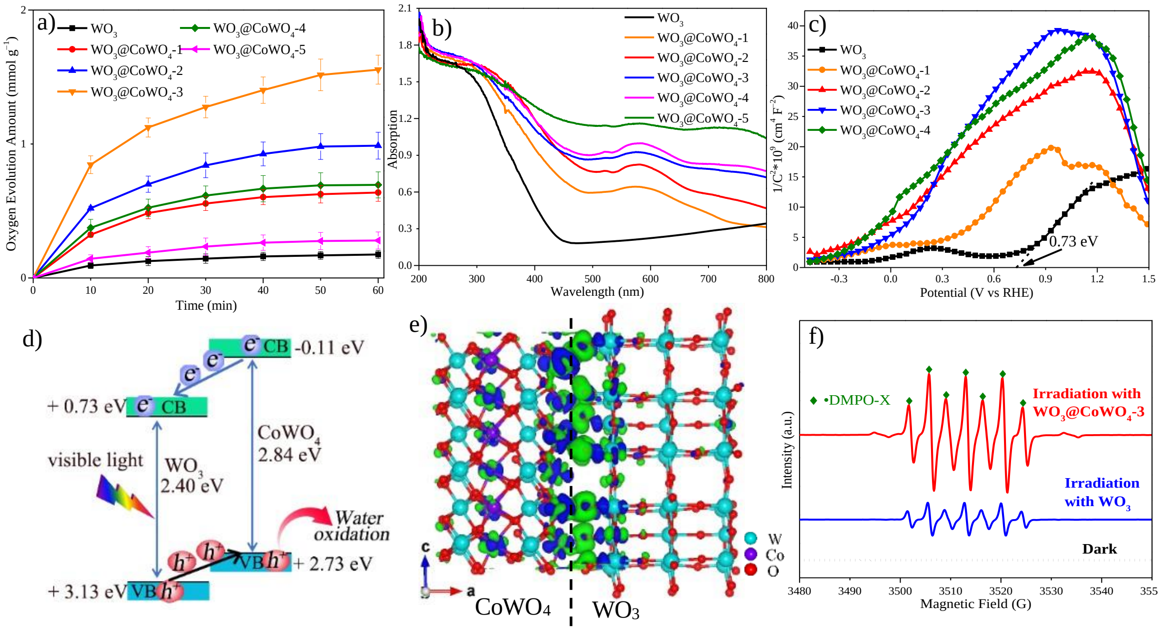

Figure 5.14 a) Visible-light photocatalytic OER activity. b) UV-Vis DRS and c) M-S plots. d) Band structure diagram (CB: Conduction band; VB: valence band; vs. NHE, pH=7). e) Charge density distribution for WO_3@$CoWO_4$ (M-3): The green region indicates charge accumulation, while the blue area represents charge depletion; the isosurface value is 0.0038 e per Å^3. f) Room temperature EPR signals tested in water oxidation system.

Table 5.2 Photocatalytic activities of metallic OER catalysts for O_2 evolution.

Catalyst	Catalyst addition amount (mg)	Irradiation wavelength (nm)	Oxygen evolution (mmol/g)	Irradiation time (h)	Reference
WO_3–RGO	50	>420 nm	0.23	5	40
0.001 wt% RuO_2/WO_3	100	>420 nm	1.4	4	41
3 wt% $Co(OH)_2$-TiO_2	100	> 500nm	0.4	10	42
$PtOx/WO_3$	100	>350 nm	0.279	3	43
Pt(0.5)/Au(3.0)/WO_3	50	Blue LED	0.036	1	44
Bulk WO_3	50	>400 nm	0.796	1	45
$WO_{3\text{-}X}$-HT	100	>400 nm	0.75	1	46
RuO_2/Bi_4TaO_8X (X = Cl, Br)	100	>420 nm	0.375	1	47
(0.1%) RuO_2/α-Fe_2O_3/2D g-C_3N_4/Pt (3%)	50	>400 nm	0.19	5	48
CoS	50	>420 nm	1.866	0.2	49
MoO_2 -HTCC	30	>420 nm	0.7	25	50
mWO_3/AuNP	2.5	>400 nm	0.065	0.067	51
WO_3@$CoWO_4$–3	**50**	**>420 nm**	**1.6**	**1**	**This work**

A series of photo-dependent tests were carried out on the synthesized samples. As shown in UV-visible diffuse reflectance spectra (UV-Vis DRS, Figure 5.14b), the visible light absorption intensity of the composites gradually improved with increasing $CoWO_4$ loadings. In addition, a red shift occurred in the absorption band-edge of the composites, reflecting better absorption at longer wavelengths. WO_3 presented a positive slope, typical for n-type semiconductors in the Mott-Schottky (M-S) plot (Figure 5.14c). Since $CoWO_4$ is a p-type semiconductor with a negative slope, inverted “V-shapes” were then observed on WO_3@$CoWO_4$ composites, reflecting a well-matched p-n heterostructure.[52–54] Figure 5.14d shows a band structure diagram for WO_3@$CoWO_4$ system. The conduction band minimum (CBM) of WO_3 (0.73 eV) was evaluated from the flat band potential of the M-S plot (Figure 5.14c). The band gap of WO_3 (2.40 eV) was obtained from the Tauc’s plot (Figure 5.15). VBM was acquired by the sum of CBM and band gap. Since we did not prepare pure $CoWO_4$, the band structure data of $CoWO_4$ were obtained by DFT calculations using the monoclinic $CoWO_4$ slab (M-1, Figure 5.16a). The band gap (2.84 eV), CBM (-0.11 eV) and VBM (2.73 eV) of $CoWO_4$ were obtained via the corresponding DOS (Figure 5.16b), which are close to those values reported in the literature.[55] The band gap of the WO_3@$CoWO_4$ system can be narrowed with $CoWO_4$ as the VBM, and WO_3 as the CBM, which helps explain their better light-harvesting ability than WO_3. Since the CBM of $CoWO_4$ is more negative than WO_3, it is thermodynamically favorable for the photo-excited electrons to move from $CoWO_4$ to WO_3. Meanwhile, the holes generated in the valence bands of the two semiconductors can transfer from WO_3 to $CoWO_4$ due to their potential difference in VBM. Due to effective electron-hole separation by WO_3@$CoWO_4$ heterojunction, their recombination rates would be largely reduced, inducing the enhanced photoactivity.[56] A large number of activated and migrated holes on the surface of $CoWO_4$ can efficiently oxidize the adsorbed H_2O molecules into O_2. Although WO_3@$CoWO_4$-4 exhibited the best electrochemical OER performance, its photocatalytic OER activity was much lower than WO_3@$CoWO_4$-3. It is conjectured that the excessive coverage of $CoWO_4$ on WO_3 in WO_3@$CoWO_4$-4 might block the photon absorption of WO_3, which impairs the function of WO_3 in the heterostructure and leads to the deteriorated photocatalytic efficiency. As OER tends to occur at the side of $CoWO_4$ and WO_3 is physically coated by $CoWO_4$, the corrosion of WO_3 by peroxo species generated during the OER process can be prevented. The stability of WO_3 can be improved.

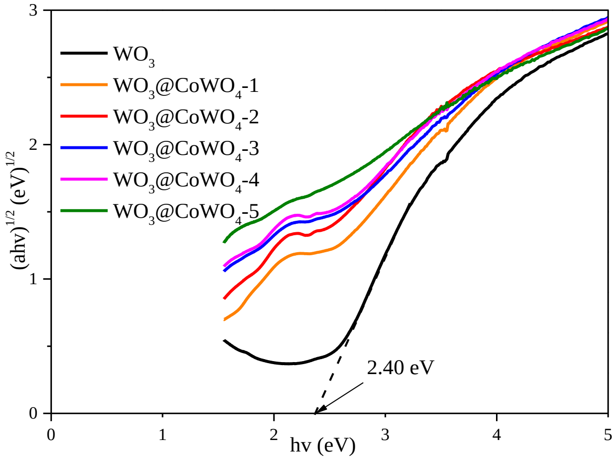

Figure 5.15 Tauc's plots of the samples acquired from the adsorption spectra (Figure 5.14b) based on Kubelka-Munk equation: (αhν)n = k(hν-Eg) (n=1/2).

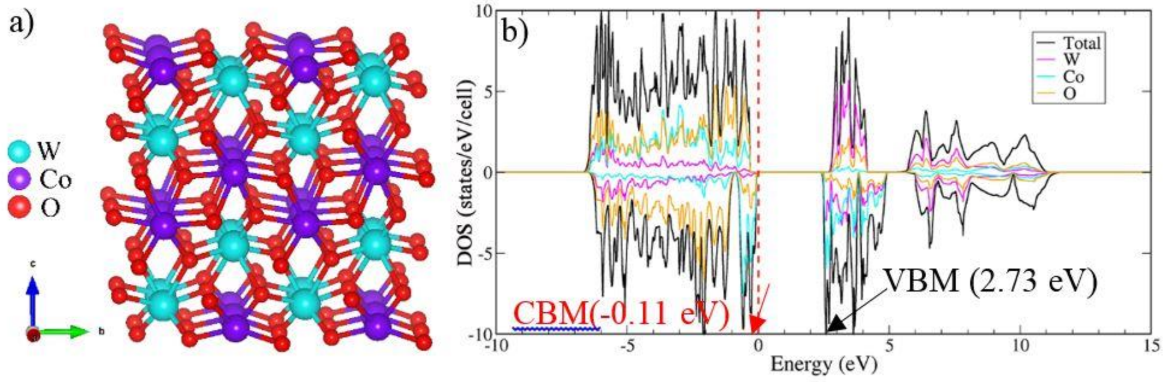

Figure 5.16 a) Molecular models of monoclinic $CoWO_4$ (M-1) and b) its corresponding density of states (DOS).

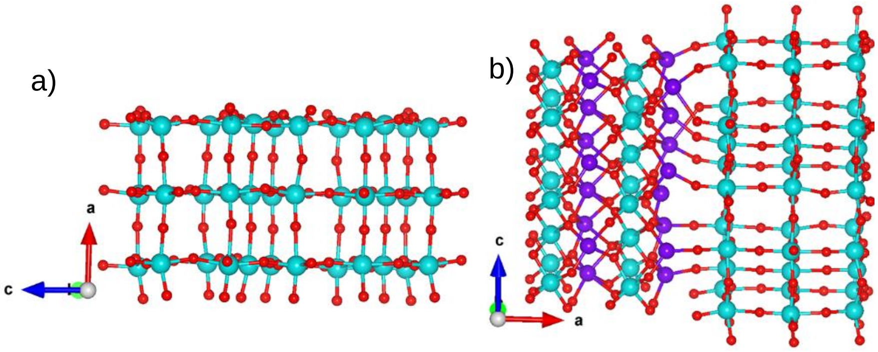

Figure 5.17 Molecular models of a) hexagonal WO_3 slab (M-2) and b) $WO_3@CoWO_4$ slab (M-3).

To explore the charge redistribution across the WO_3@$CoWO_4$ interface, molecular models including a hexagonal WO_3 slab (M-2) and a WO_3@$CoWO_4$ slab (M-3) were constructed (as given in Figure 5.17). The (200) planes of $CoWO_4$ and the (001) planes of WO_3 were selected to construct the interface in M-3, as TEM images (Figures 5.3d, 5.4b and 5.5b) have revealed the close atomic bonding between the two planes and they possess a small planar mismatch (~0.8%) while there is a remarkable lattice mismatch in other combinations. The general oxidation states of Co and W in $CoWO_4$ are +2 and +6, respectively, suggesting that the bonding between W and O is much stronger than that between Co and O.[26] In this regard, it requires more energy to break up the W-O bond than the cleavage of Co-O bond. Therefore, compared with W (200) surface, Co (200) surface of $CoWO_4$ is more likely to bond with WO_3. The stoichiometric WO_3@$CoWO_4$ heterogeneous structure was built in Figure 5.17 with Co-terminated (200) surface of $CoWO_4$ connected with O-terminated (001) surface of WO_3, containing 228 atoms. The M-3 has a composition close to WO_3@$CoWO_4$-3.

The charge redistribution across the interface (Figure 5.14e) was explored by subtracting the electronic charge of M-3 from those of the M-1 and M-2. Specifically, charge accumulation mainly occurs at the side of WO_3 while charge depletion focuses on $CoWO_4$ near the interface. Therefore, interface electric dipole forms at the interface, which enables electrons to transfer from $CoWO_4$ to WO_3 while the holes transfer from WO_3 to $CoWO_4$.[57] This makes it easier for electron-hole transport and separation across the interface under light irradiation, which can also be experimentally demonstrated by photoluminescence (PL) spectra (Figure 5.18). As shown, the lower luminescence intensity of the composites than WO_3 suggests the reduced charge recombination.

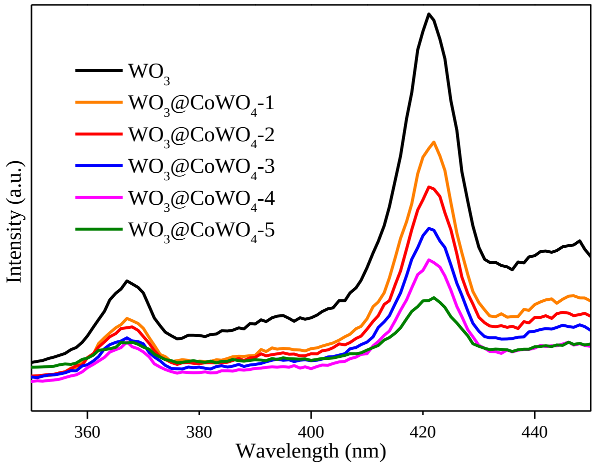

Figure 5.18 Photoluminescence (PL) spectra of pure WO_3 and the composites.

Room temperature in-situ electron paramagnetic resonance (EPR) was performed in the water oxidation system with 5, 5-dimethyl-1-pyrroline N-oxide (DMPO) as the trapping agent (Figure 5.14f). No visible signal was obtained under dark. Interestingly, active seven-line paramagnetic signals were captured as $^{\bullet}$DMPO-X under irradiation after adding WO_3 or WO_3@$CoWO_4$-3, which might arise from the excessive oxidation of DMPO by peroxide generated during OER.[58–60]

In general, water oxidation reaction proceeds via four-electron-transfer steps based on the following mechanism:[38]

$$*+H_2O \rightarrow *OH+H^++e^- \qquad \text{(step 1)}$$

$$*OH \rightarrow *O+H^++e^- \qquad \text{(step 2)}$$

$$*O+H_2O \rightarrow *OOH+H^++e^- \qquad \text{(step 3)}$$

$$*OOH \rightarrow O_2+H^++e^- \qquad \text{(step 4)}$$

where * denotes the surface site.

Peroxo species (*OOH) serve as the intermediates in the third step and can be readily decomposed into O_2. The system with WO_3@$CoWO_4$-3 displayed much stronger peak signals of $^{\bullet}$DMPO-X than that with WO_3, indicating the higher concentration of peroxo species and the more active OER performance.

5.3.4 Photoelectrochemical (PEC) OER Performance

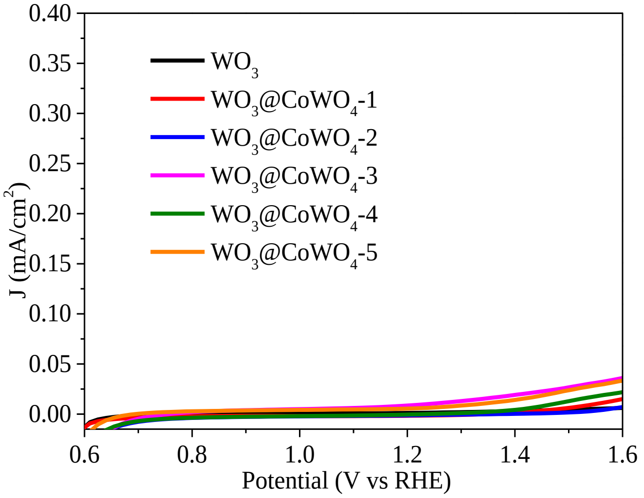

Figure 5.19 Current-voltage curves of the composites in the dark.

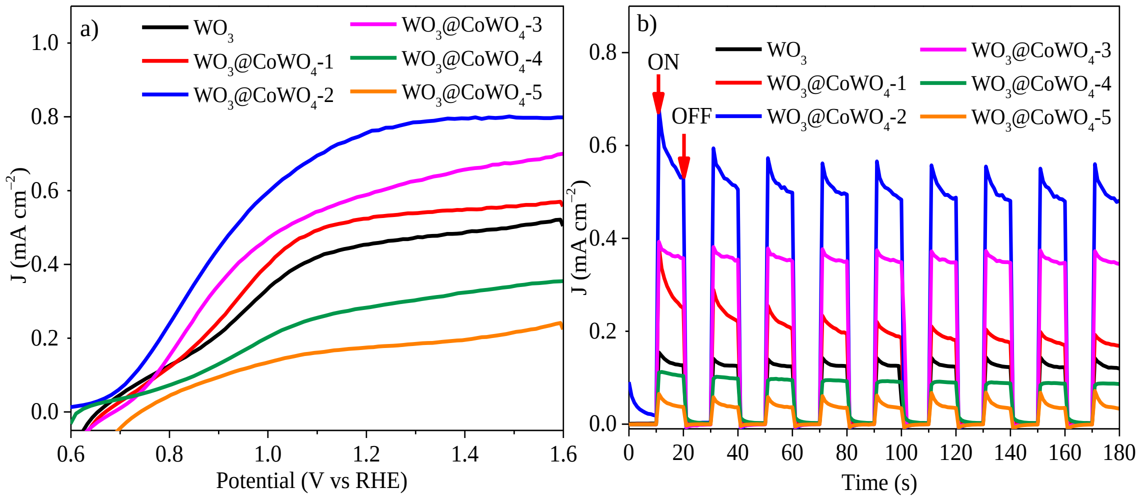

Figure 5.20 a) Current-voltage curves of the composites under illumination; b) i-t curves at a potential of 1.0 V (vs RHE) under light ON-OFF cycling.

Based on the enhanced electro and photocatalytic OER performances of $WO_3@CoWO_4$ composites, their PEC properties were further evaluated. Current-voltage curves were first recorded under dark (Figure 5.19). By comparison, all the photoanodes presented deeply enhanced anodic photocurrent densities upon illumination (Figure 5.20a). Compared to WO_3, the photocurrent density of the composites firstly improved significantly along with the increased loading of $CoWO_4$ on WO_3 with WO_3@$CoWO_4$-2 reaching a maximum. The photocurrent density of WO_3@$CoWO_4$-2 is about 2 times larger than that of WO_3 at 1.3 V. However, the anodic photocurrent densities decreased dramatically on WO_3@$CoWO_4$-3, -4 and -5 with further higher ratios of $CoWO_4$. Similar to the above discussion on photocatalytic OER tests, this phenomenon can be explained by the destruction of the optimum synergistic function of heterostructure for PEC activity. The transient photoresponse of the composites were assessed by measuring i-t curves at 1.0 V (Figure 5.20b). Prompt and steady photocurrent responses can be captured on the photoanodes during on and off cycles of illumination, which had the same trend with Figure 5.20a. It is noted that an applied bias is imposed on the photoanode during PEC OER, which promotes the output of the photogenerated electrons in WO_3 through FTO-glass. The electron-hole recombination rate is reduced and thus the OER activity of WO_3 is largely elevated in PEC test compared with that in photocatalysis. Due to the different mechanisms, WO_3 exhibited the worst performance in photocatalysis but it was not the worst in PEC OER and the optimal $CoWO_4$/WO_3 ratio was also various in the two systems.

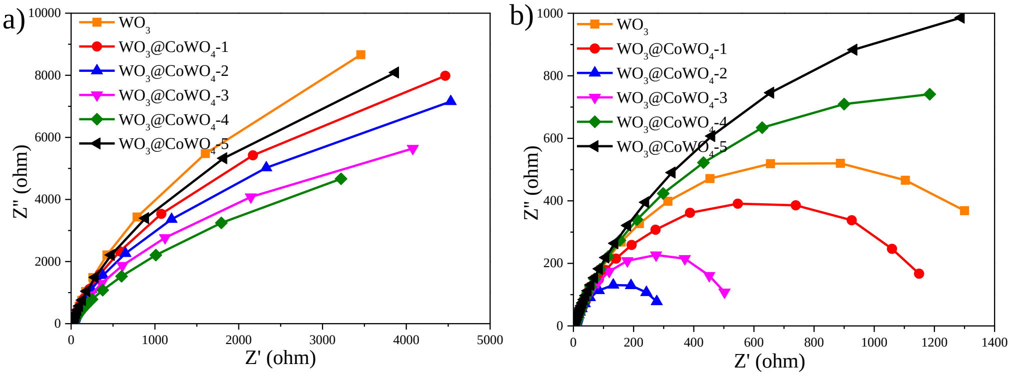

Figure 5.21 Electrochemical impedance spectra collected under a) dark and b) irradiation condition.

EIS measurements were conducted on the photoanodes under dark and irradiation, respectively (Figure 5.21). Compared to those collected under dark, all the semicircles in EIS were largely minished under irradiation, proving the lowered charge transfer resistance by photo-induced charge carries. Especially, WO_3@$CoWO_4$-2 exhibited the smallest resistance diameter, which helps explain its highest photocurrent response in PEC test. Therefore, an appropriate construction of WO_3/$CoWO_4$ heterostructure could effectively boost the conductivity and PEC activity of WO_3.

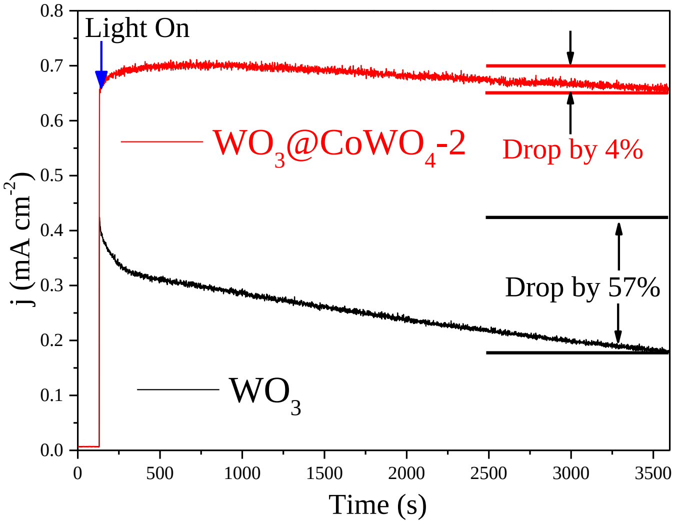

Figure 5.22 Potentiostatic measurement of WO_3 and WO_3@$CoWO_4$-2 at 1.23 V (vs RHE) under irradiation for 1 h.

Besides, the instability of WO_3 caused by photo-corrosion was largely improved. As provided in Figure 5.22, WO_3@$CoWO_4$-2 (decayed by 4%) exhibited a much better long-term PEC stability than WO_3 (decayed by 57%) tested by the potentiostatic method.

5.3.5 DFT Calculations for OER

To study the effect of interface oxygen vacancies or defects on OER, M-4 (Figure 5.23a) was built by removing an interface O in M-3. We probed adsorbates of *OH, *O and *OOH on the surfaces terminated with Co (200) of $CoWO_4$ in M-1 (Figure 5.24) and (001) surface planes of WO_3 in M-2 (Figure 5.25). For M-3 and M-4, the adsorbates on the selected Co site of Co (200) interface were monitored, as provided in Figure 5.26 and the inset images in Figure 5.23b. This is because OER prefers to occur on the side of $CoWO_4$ in the composites due to the migration of holes as analyzed in Figures 5.14d and e. Moreover, Co sites are believed to be more active centres for OER in $CoWO_4$.[61,62]

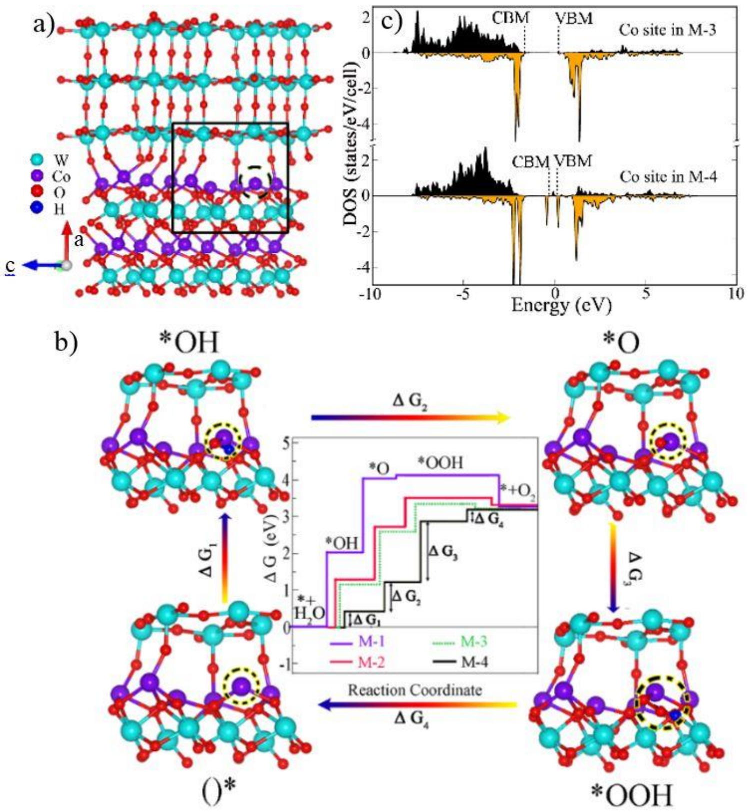

Figure 5.23 a) Molecular model of M-4; b) illustration of the Gibbs free energy changes for the four elementary steps of OER at pH = 7 and U = 0 in M-1, M-2, M-3 and M-4. Insets are close-up atomic structures of the selected area in M-4 which interpret the adsorption of intermediate species on active Co site. c) DOS of the selected Co site with and without O vacancy in M-3 and M-4.

Table 5.3 Gibbs free energy changes during the four elementary steps of OER (U = 0 and pH= 7).

Model	Δ G_1	Δ G_2	Δ G_3	Δ G_4
M-1	2.02	2.00	0.11	-0.82
M-2	1.27	1.51	0.80	-0.27
M-3	1.23	1.42	0.77	-0.11
M-4	0.47	0.83	1.51	0.48

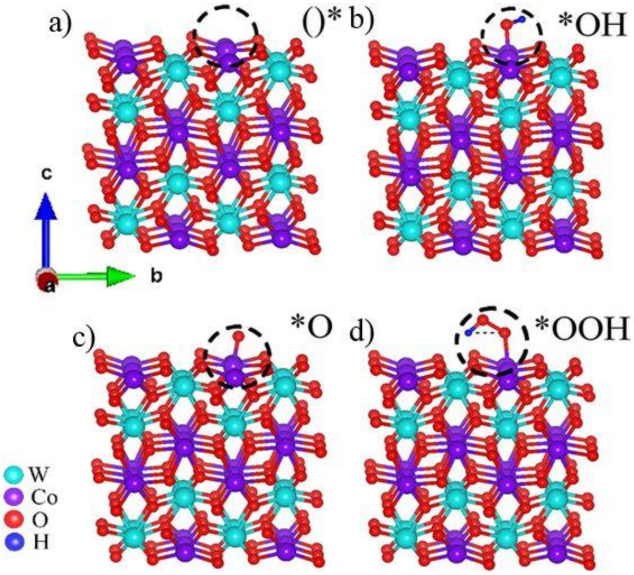

Figure 5.24 $CoWO_4$ slab (M-1) with the adsorbed species generated in OER.

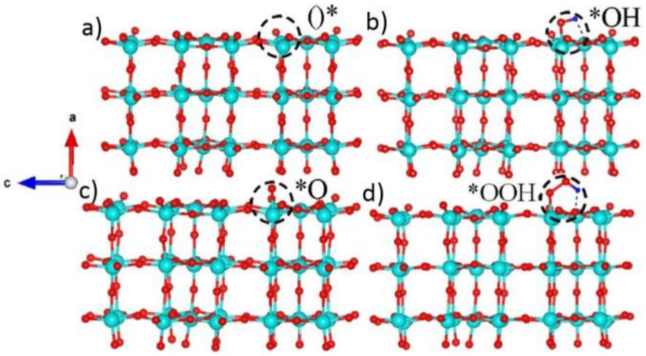

Figure 5.25 WO_3 slab (M-2) with the adsorbed species generated in OER.

The specific Gibbs free energy changes during the four elementary steps are shown in Figure 5.23b and Table 5.3. All adsorption scenarios in the four models shared uphill/endothermic energy profiles from *OH (step 1), *O (step 2) to *OOH (step 3), suggesting that an external driving force (light irradiation or electrical potential) is required to initiate the OER reaction. Once the reaction got to *OOH, the diagrams became downhill/exothermic in M-1, M-2 and M-3, indicating that step 4 is apt to happen and *OOH will convert to O_2 (step 4) automatically. The step with the highest free energy barrier is referred as the overpotential-determining step.[63] It was noted that steps 1 and 2 were the potential-determining steps of WO_3, while these energy barriers were lower in $CoWO_4$ with step 2 being the hardest one. $CoWO_4$ was catalytically more active than WO_3 in OER. Compared with $CoWO_4$, the energy barriers in steps 1, 2 and 3 were reduced in M-3, indicating the lowered OER overpotential on WO_3@$CoWO_4$ interface. This can be associated with the hole accumulation at the side of $CoWO_4$ across the interface (Figure 5.23e). Interestingly, after an O was removed in the interface, the barriers in steps 1 and 2 were significantly lowered (M-4), implying a simpler adsorption of water molecules onto the active Co site (step 1) and easier formation of OH* (step 2). As these two initial steps were the hardest in M-1, M-2 and M-3, their easier proceedings promoted by interface-O-vacancy were considered to contribute considerably to the overall OER activity in WO_3@$CoWO_4$ composites. Therefore, the WO_3@$CoWO_4$ interface and especially interface-O-vacancies can serve as active sites for both electro, photo-catalytic and PEC oxidation of water.

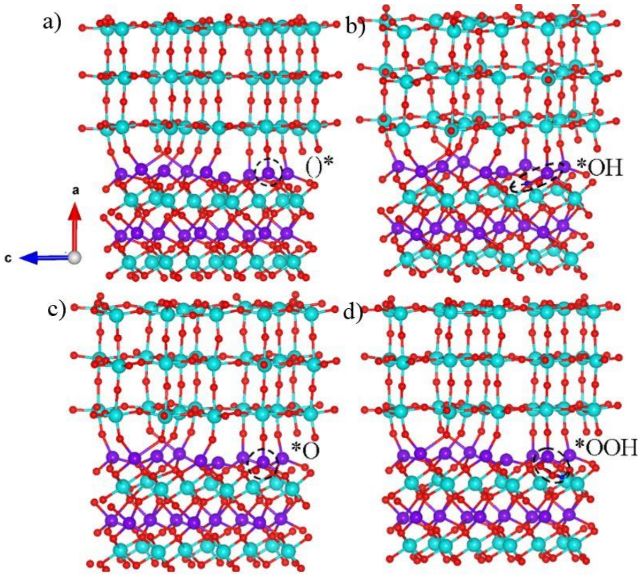

Figure 5.26 WO_3@$CoWO_4$ slab (M-3) with the adsorbed species generated in OER.

DOS of the designated Co site in M-3 and M-4 are projected in Figure 5.23c. Especially, the interface-O-vacancy induced dramatically increased DOS of Co site at both VBM and CBM, which can accelerate the transport of photon-generated carriers under light irradiation.[16,64] Faster diffusion kinetics, higher photo-conversion efficiency and higher concentration of the photogenerated holes to react with H_2O can be achieved. Thus, interface-O-vacancies can not only reduce OER energy barriers but also induce enhanced photo-responsive behavior.

5.4 Conclusions

In summary, a versatile method was proposed for the synthesis of WO_3@$CoWO_4$ bilayer nanosheets as excellent WOCs for enhanced visible-light-driven photo, electro-catalytic and PEC OER processes. Due to the theoretically reduced OER barriers by WO_3@$CoWO_4$ interface and the interface-O-vacancies, WO_3@$CoWO_4$-4 displayed a low overpotential of 0.38 V in 0.1 M KOH for electrocatalysis. The creation of p-n heterojunctions and interface-O-vacancies can increase the photo-energy conversion efficiency and the water oxidation ability, enabling WO_3@$CoWO_4$-3 to present over 9-time-higher O_2 evolution rate than WO_3. A larger photocurrent with a high stability was also observed on WO_3@$CoWO_4$-2 for PEC OER. The paradigm we presented in this work could provide a refreshing perspective for pursuing and designing more efficient low-dimensional photocatalytic, electrocatalytic and PEC OER catalysts.

References

1) Reece, S. Y.; Hamel, J. A.; Sung, S.; Jarvi, T. D.; Esswein, A. J.; Pijpers, J. J. H.; Nocera, D. G. Wireless Solar Water Splitting Using Silicon-Based Semiconductors and Earth-Abundant Catalysts. *Science* **2011**, *1*, 3.
2) Hisatomi, T.; Kubota, J.; Domen, K. Recent Advances in Semiconductors for Photocatalytic and Photoelectrochemical Water Splitting. *Chemical Society Reviews* **2014**, *43*, 7520.
3) Zong, X.; Yan, H.; Wu, G.; Ma, G.; Wen, F.; Wang, L.; Li, C. Enhancement of Photocatalytic H_2 Evolution on CdS by Loading MoS_2 as Cocatalyst under Visible Light Irradiation. *Journal of The American Chemical Society* **2008**, *130,* 7176.
4) Faunce, T.; Styring, S.; Wasielewski, M. R.; Brudvig, G. W.; Rutherford, A. W.; Messinger, J.; Lee, A. F.; Hill, C. L.; deGroot, H.; Fontecave, M.; MacFarlane, D. R.; Hankamer, B.; Nocera, D. G.; Tiede, D. M.; Dau, H.; Hillier, W.; Wang, L.; Amal, R. Artificial Photosynthesis as a Frontier Technology for Energy Sustainability. *Energy & Environmental Science* **2013**, *6*, 1074.
5) Parent, A. R.; Crabtree, R. H.; Brudvig, G. W. Comparison of Primary Oxidants for Water-Oxidation Catalysis. *Chemical Society Review* **2013**, *42,* 2247.

6) Kirner, J. T.; Finke, R. G. Water-Oxidation Photoanodes Using Organic Light-Harvesting Materials: A Review. *Journal of Material Chemistry A* **2017**, *5*, 19560.

7) Li, X.; Yu, J.; Low, J.; Fang, Y.; Xiao, J.; Chen, X. Engineering Heterogeneous Semiconductors for Solar Water Splitting. *Journal of Material Chemistry A* **2015**, *3*, 2485.

8) Zhang, N.; Li, X.; Ye, H.; Chen, S.; Ju, H.; Liu, D.; Lin, Y.; Ye, W.; Wang, C.; Xu, Q.; Zhu, J.; Song, L.; Jiang, J.; Xiong, Y. Oxide Defect Engineering Enables to Couple Solar Energy into Oxygen Activation. *Journal of the American Chemical Society* **2016**, *138*, 8928.

9) Huang, J.; Zhang, Y.; Ding, Y. Rationally Designed/Constructed CoO_x/WO_3 Anode for Efficient Photoelectrochemical Water Oxidation. *ACS Catalysis* **2017**, *7*, 1841.

10) Martínez-García, A.; Vendra, V. K.; Sunkara, S.; Haldankar, P.; Jasinski, J.; Sunkara, M. K. Tungsten Oxide-Coated Copper Oxide Nanowire Arrays for Enhanced Activity and Durability with Photoelectrochemical Water Splitting. *Journal of Materials Chemistry A* **2013**, *1*, 15235.

11) Zhang, B.; Zheng, X. L.; Voznyy, O.; Comin, R.; Bajdich, M.; Garcia-Melchor, M.; Han, L. L.; Xu, J. X.; Liu, M.; Zheng, L. R.; de Arquer, F. P. G.; Dinh, C. T.; Fan, F. J.; Yuan, M. J.; Yassitepe, E.; Chen, N.; Regier, T.; Liu, P. F.; Li, Y. H.; De Luna, P.; Janmohamed, A.; Xin, H. L. L.; Yang, H. G.; Vojvodic, A.; Sargent, E. H. Homogeneously Dispersed Multimetal Oxygen-Evolving Catalysts. *Science* **2016**, *352*, 333.

12) Zhang, J.; Zhang, P.; Wang, T.; Gong, J. Monoclinic WO_3 Nanomultilayers with Preferentially Exposed (002) Facets for Photoelectrochemical Water Splitting. *Nano Energy* **2015**, *11*, 189.

13) Yan, J.; Wang, T.; Wu, G.; Dai, W.; Guan, N.; Li, L.; Gong, J. Tungsten Oxide Single Crystal Nanosheets for Enhanced Multichannel Solar Light Harvesting. *Advanced Materials* **2015**, *27*, 1580.

14) Kalanur, S. S.; Yoo, I.-H.; Park, J.; Seo, H. Insights into the Electronic Bands of $WO_3/BiVO_4/TiO_2$, Revealing High Solar Water Splitting Efficiency. *Journal of Material Chemistry A* **2017**, *5*, 1455.

15) Yu, C.; Zhou, W.; Zhu, L.; Li, G.; Yang, K.; Jin, R. Integrating Plasmonic Au Nanorods with Dendritic like α-$Bi_2O_3/Bi_2O_2CO_3$ Heterostructures for Superior Visible-Light-Driven Photocatalysis. *Applied Catalysis B: Environmental* **2016**, *184*, 1.

16) Li, J.-S.; Wang, Y.; Liu, C.-H.; Li, S.-L.; Wang, Y.-G.; Dong, L.-Z.; Dai, Z.-H.; Li, Y.-F.; Lan, Y.-Q. Coupled Molybdenum Carbide and Reduced Graphene Oxide Electrocatalysts for Efficient Hydrogen Evolution. *Nature Communications* **2016**, *7*, 11204.

17) Tian, T.; Jiang, J.; Ai, L. H. In Situ Electrochemically Generated Composite-Type CoO_x/WO_x in Self-Activated Cobalt Tungstate Nanostructures: Implication for Highly Enhanced Electrocatalytic Oxygen Evolution. *Electrochimica Acta* **2017**, *224*, 551.

18) Jia, H.; Stark, J.; Zhou, L. Q.; Ling, C.; Sekito, T.; Markin, Z. Different Catalytic Behavior of Amorphous and Crystalline Cobalt Tungstate for Electrochemical Water Oxidation. *RSC Advances* **2012**, *2*, 10874.

19) Ahmed, M. I.; Adam, A.; Khan, A.; Rehman, A. U.; Qamaruddin, M.; Siddiqui, M. N.; Qamar, M. Improved Photoelectrochemical Water Oxidation under Visible Light with Mesoporous $CoWO_4$. *Materials Letters* **2016**, *183*, 281.

20) Kresse, G.; Joubert, D. From Ultrasoft Pseudopotentials to the Projector Augmented-Wave Method. *Physical Review B* **1999**, *59*, 1758.

21) Blöchl, P. E. Projector Augmented-Wave Method. *Physical Review B* **1994**, *50*, 17953.

22) Kresse, G.; Furthmüller, J. Efficiency of Ab-Initio Total Energy Calculations for Metals and Semiconductors Using a Plane-Wave Basis Set. *Computational Materials Sciince* **1996**, *6*, 15.

23) Kresse, G.; Furthmüller, J. Efficient Iterative Schemes for Ab Initio Total-Energy Calculations Using a Plane-Wave Basis Set. *Physical Review B* **1996**, *54*, 11169.

24) Kresse, G.; Hafner, J. Ab Initio Molecular Dynamics for Open-Shell Transition Metals. *Physical Review B* **1993**, *48*, 13115.

25) Perdew, J. P.; Burke, K.; Ernzerhof, M. Generalized Gradient Approximation Made Simple. *Physical Review Letter* **1996**, *77*, 3865.

26) Ling, C.; Zhou, L. Q.; Jia, H. First-Principles Study of Crystalline $CoWO_4$ as Oxygen Evolution Reaction Catalyst. *RSC Advances* **2014**, *4*, 24692.

27) Bondarenko, N.; Eriksson, O.; Skorodumova, N. V. Polaron Mobility in Oxygen-Deficient and Lithium-Doped Tungsten Trioxide. *Physical Review B* **2015**, *92*, 165119.

28) Man, I. C.; Su, H.-Y.; Calle-Vallejo, F.; Hansen, H. A.; Martínez, J. I.; Inoglu, N. G.; Kitchin, J.; Jaramillo, T. F.; Nørskov, J. K.; Rossmeisl, J. Universality in Oxygen

Evolution Electrocatalysis on Oxide Surfaces. *ChemCatChem* **2011**, *3*, 1159.

29) Li, Y.; Li, Y.-L.; Sa, B.; Ahuja, R. Review of Two-Dimensional Materials for Photocatalytic Water Splitting from a Theoretical Perspective. *Catalysis Science & Technology* **2017**, *7*, 545.

30) Valdés, Á.; Qu, Z. W.; Kroes, G. J.; Rossmeisl, J.; Nørskov, J. K. Oxidation and Photo-Oxidation of Water on TiO_2 Surface. *Journal of Physical Chemistry C* **2008**, *112*, 9872.

31) Lou, Z.; Zhu, M.; Yang, X.; Zhang, Y.; Whangbo, M.-H.; Li, B.; Huang, B. Continual Injection of Photoinduced Electrons Stabilizing Surface Plasmon Resonance of Non-Elemental-Metal Plasmonic Photocatalyst CdS/WO_{3-x} for Efficient Hydrogen Generation. *Applied Catalysis B: Environmental* **2018**, *226* (December 2017), 10–15.

32) Zhang, J.; Ma, Y.; Du, Y.; Jiang, H.; Zhou, D.; Dong, S. Carbon Nanodots/WO_3 Nanorods Z-Scheme Composites: Remarkably Enhanced Photocatalytic Performance under Broad Spectrum. *Applied Catalysis B: Environmental* **2017**, *209,* 253.

33) Moulder, J. F.; Stickle, W. F.; Sobol, P. E.; Bomben, K. D. Handbook of X-Ray Photoelectron Spectroscopy. *Physical Electronics, Inc.*, **1995**, 261.

34) Chen, S.; Yang, G.; Jia, Y.; Zheng, H. Facile Synthesis of $CoWO_4$ Nanosheet Arrays Grown on Nickel Foam Substrates for Asymmetric Supercapacitors. *ChemElectroChem* **2016**, *3,* 1490.

35) Zhang, H.; Tian, W.; Zhou, L.; Sun, H.; Tade, M.; Wang, S. Monodisperse Co_3O_4 Quantum Dots on Porous Carbon Nitride Nanosheets for Enhanced Visible-Light-Driven Water Oxidation. *Applied Catalysis B: Environmental* **2018**, *223,* 2.

36) Sultan, R. F. Propagating Fronts in Periodic Precipitation Systems with Redissolution. *Physical Chemistry Chemical Physics* **2002**, *4*, 1253.

37) Yourey, J. E.; Kurtz, J. B.; Bartlett, B. M. Water Oxidation on a $CuWO_4$-WO_3 Composite Electrode in the Presence of $[Fe(CN)_6]^{3-}$: Toward Solar Z-Scheme Water Splitting at Zero Bias. *Journal of Physical Chemistry C* **2012**, *116,* 3200.

38) Wang, H. Y.; Hung, S. F.; Chen, H. Y.; Chan, T. S.; Chen, H. M.; Liu, B. In Operando Identification of Geometrical-Site-Dependent Water Oxidation Activity of Spinel Co_3O_4. *Journal of the American Chemical Society* **2016**, *138*, 36.

39) Zhu, Y. L.; Zhou, W.; Sunarso, J.; Zhong, Y. J.; Shao, Z. P. Phosphorus-Doped Perovskite Oxide as Highly Efficient Water Oxidation Electrocatalyst in Alkaline Solution.

Advanced Functional Materials **2016**, *26*, 5862.

40) Huang, H.; Yue, Z.; Li, G.; Wang, X.; Huang, J.; Du, Y.; Yang, P. Ultraviolet-Assisted Preparation of Mesoporous WO_3/Reduced Graphene Oxide Composites: Superior Interfacial Contacts and Enhanced Photocatalysis. *Journal of Materials Chemistry A* **2013**, *1*, 15110.
41) Ma, S. S. K.; Maeda, K.; Abe, R.; Domen, K. Visible-Light-Driven Nonsacrificial Water Oxidation over Tungsten Trioxide Powder Modified with Two Different Cocatalysts. *Energy & Environmental Science* **2012**, *5,* 8390.
42) Maeda, K.; Ishimaki, K.; Tokunaga, Y.; Lu, D.; Eguchi, M. Modification of Wide-Band-Gap Oxide Semiconductors with Cobalt Hydroxide Nanoclusters for Visible-Light Water Oxidation. *Angewandte Chemie International Edition* **2016,** *55,* 8309.
43) Maeda, K.; Lu, D.; Domen, K. Solar-Driven Z-Scheme Water Splitting Using Modified $BaZrO_3$–$BaTaO_2N$ Solid Solutions as Photocatalysts. *ACS Catalysis* **2013**, *3*, 1026.
44) Tanaka, A.; Hashimoto, K.; Kominami, H. Visible-Light-Induced Hydrogen and Oxygen Formation over Pt/Au/WO_3 Photocatalyst Utilizing Two Types of Photoabsorption Due to Surface Plasmon Resonance and Band-Gap Excitation. *Journal of the American Chemical Society* **2014**, *136*, 586.
45) Waller, M. R.; Townsend, T. K.; Zhao, J.; Sabio, E. M.; Chamousis, R. L.; Browning, N. D.; Osterloh, F. E. Single-Crystal Tungsten Oxide Nanosheets: Photochemical Water Oxidation in the Quantum Confinement Regime. *Chemistry of Materials* **2012**, *24*, 698.
46) Yan, J.; Wang, T.; Wu, G.; Dai, W.; Guan, N.; Li, L.; Gong, J. Tungsten Oxide Single Crystal Nanosheets for Enhanced Multichannel Solar Light Harvesting. *Advanced Materials* **2015**, *27,* 1580.
47) Tao, X.; Zhao, Y.; Mu, L.; Wang, S.; Li, R.; Li, C. Bismuth Tantalum Oxyhalogen: A Promising Candidate Photocatalyst for Solar Water Splitting. *Advanced Energy Materials* **2018,** *8*, 1701392.
48) She, X.; Wu, J.; Xu, H.; Zhong, J.; Wang, Y.; Song, Y.; Nie, K.; Liu, Y.; Yang, Y.; Rodrigues, M.-T. F.; Vajtai, R.; Lou, J.; Du, D.; Li, H.; Ajayan, P. M. High Efficiency Photocatalytic Water Splitting Using 2D α-Fe_2O_3/g-C_3N_4 Z-Scheme Catalysts. *Advanced Energy Materials* **2017**, *7,* 1700025.
49) Zheng, M.; Ding, Y.; Yu, L.; Du, X.; Zhao, Y. In Situ Grown Pristine Cobalt Sulfide as

Bifunctional Photocatalyst for Hydrogen and Oxygen Evolution. *Advanced Functional Materials* **2017**, *27* (11), 1605846.

50) Hu, Z.; Liu, G.; Chen, X.; Shen, Z.; Yu, J. C. Enhancing Charge Separation in Metallic Photocatalysts: A Case Study of the Conducting Molybdenum Dioxide. *Advanced Functional Materials* **2016**, *26*, 4445.

51) Liu, B.; Kuo, C. H.; Chen, J.; Luo, Z.; Thanneeru, S.; Li, W.; Song, W.; Biswas, S.; Suib, S. L.; He, J. Ligand-Assisted Co-Assembly Approach toward Mesoporous Hybrid Catalysts of Transition-Metal Oxides and Noble Metals: Photochemical Water Splitting. *Angewandte Chemie International Edition* **2015**, *54*, 9061.

52) Ke, J.; Liu, J.; Sun, H.; Zhang, H.; Duan, X.; Liang, P.; Li, X.; Tade, M. O.; Liu, S.; Wang, S. Facile Assembly of Bi_2O_3 /Bi_2S_3 /MoS_2 n-p Heterojunction with Layered n -Bi_2O_3 and p -MoS_2 for Enhanced Photocatalytic Water Oxidation and Pollutant Degradation. *Applied Catalysis B: Environmental* **2017**, *200*, 47.

53) Liu, Z.; Tian, J.; Zeng, D.; Yu, C.; Zhu, L.; Huang, W.; Yang, K.; Li, D. A Facile Microwave-Hydrothermal Method to Fabricate B Doped $ZnWO_4$ nanorods with High Crystalline and Highly Efficient Photocatalytic Activity. *Materials Research Bulletin* **2017**, *94*, 298.

54) Yan, X.; Wu, Z.; Huang, C.; Liu, K.; Shi, W. Hydrothermal Synthesis of CdS/$CoWO_4$ heterojunctions with Enhanced Visible Light Properties toward Organic Pollutants Degradation. *Ceramics International* **2017**, *43*, 5388.

55) Montini, T.; Gombac, V.; Hameed, A.; Felisari, L.; Adami, G.; Fornasiero, P. Synthesis, Characterization and Photocatalytic Performance of Transition Metal Tungstates. *Chemical Physics Letters* **2010**, *498*, 113.

56) Yu, C.; Li, G.; Kumar, S.; Yang, K.; Jin, R. Phase Transformation Synthesis of Novel Ag_2 O/Ag_2CO_3 Heterostructures with High Visible Light Efficiency in Photocatalytic Degradation of Pollutants. *Advanced Materials* **2014**, *26*, 892.

57) Fan, W.; Li, C.; Bai, H.; Zhao, Y.; Luo, B.; Li, Y.; Ge, Y.; Shi, W.; Li, H. An In Situ Photoelectroreduction Approach to Fabricate Bi/BiOCl Heterostructure Photocathodes: Understanding the Role of Bi Metal for Solar Water Splitting. *Journal of Materials Chemistry A* **2017**, *5*, 4894.

58) Li, R. G.; Weng, Y. X.; Zhou, X.; Wang, X. L.; Mi, Y.; Chong, R. F.; Han, H. X.; Li, C.

Achieving Overall Water Splitting Using Titanium Dioxide-Based Photocatalysts of Different Phases. *Energy & Environmental Science* **2015**, *8*, 2377.

59) Tian, J.; Wu, Z.; Liu, Z.; Yu, C.; Yang, K.; Zhu, L.; Huang, W.; Zhou, Y. Low-Cost and Efficient Visible-Light-Driven $CaMg(CO_3)_2@Ag_2CO_3$ Microspheres Fabricated via an Ion Exchange Route. *Chinese Journal of Catalysis* **2017**, *38*, 1899.
60) Zhang, H.; Tian, W.; Guo, X.; Zhou, L.; Sun, H.; Tadé, M. O.; Wang, S. Flower-like Cobalt Hydroxide/Oxide on Graphitic Carbon Nitride for Visible-Light-Driven Water Oxidation. *ACS Applied Materials and Interfaces* **2016**, *8*, 35203.
61) Suntivich, J.; May, K. J.; Gasteiger, H. a; Goodenough, J. B.; Shao-horn, Y. A Perovskite Oxide Optimized for Molecular Orbital Principles. *Science* **2011**, *334*, 2010.
62) Ling, C.; Zhou, L. Q.; Jia, H. First-Principles Study of Crystalline $CoWO_4$ as Oxygen Evolution Reaction Catalyst. *RSC Advances* **2014**, *4*, 24692.
63) Zhao, B. T.; Zhang, L.; Zhen, D. X.; Yoo, S.; Ding, Y.; Chen, D. C.; Chen, Y.; Zhang, Q. B.; Doyle, B.; Xiong, X. H.; Liu, M. L. A Tailored Double Perovskite Nanofiber Catalyst Enables Ultrafast Oxygen Evolution. *Nature Communications* **2017**, *8*, 14586.
64) Lei, F. C.; Sun, Y. F.; Liu, K. T.; Gao, S.; Liang, L.; Pan, B. C.; Xie, Y. Oxygen Vacancies Confined in Ultrathin Indium Oxide Porous Sheets for Promoted Visible-Light Water Splitting. *Journal of the American Chemical Society* **2014**, *136*, 6826.

Every reasonable effort has been made to acknowledge the owners of copyright material. I would be pleased to hear from any copyright owner who has been omitted or incorrectly acknowledged.

Chapter 6. Photochemical Deposition of M-Bi (M = Ni, Co, Mn) Layers onto rGO/ZnO Nanorod Arrays for Solar Water Splitting

Abstract

Chapter 5 focuses on developing metal oxides for enhanced photo, electro and photoelectrochemical reactions. In this chapter, we continued to study metal-based materials for photoelectrochemical (PEC) water splitting. Economical and efficient PEC water splitting demands a good integration of solar absorbers with active electrocatalysts. Despite extensive works have focused on the amorphous metal-borate (M-Bi) as ideal electrocatalysts for PEC devices, the catalytic ability of different metal-based systems still remains elusive. Herein we choose three most common M-Bi (M = Ni, Co, Mn) catalysts, as platforms to better comprehend and compare their catalytic activities in OER by a combined computational and experimental method. Density functional theory (DFT) calculations suggest that the zigzag edges serve as active sites in MO_6 structures of M-Bi with NiO_6 possessing the lowest overall energy barriers in OER. Utilizing a photodeposition method, M-Bi thin layers were self-assembled onto ZnO nanorod arrays (NAs) and reduced graphene oxide (rGO/ZnO) as a ternary electrocatalyst/light-harvester PEC system, which has not been studied before. rGO boosts fast charge separation in light-adsorbing ZnO NAs while M-Bi improves the OER kinetics. In accordance with DFT results, Ni-Bi serves as the most active catalyst, followed by Co-Bi and Mn-Bi. Compared to ZnO, the photoelectron-conversion efficiency is elevated by approximately 4 times on Ni-Bi/rGO/ZnO, with its onset potential migrated by 0.17 V in the cathodic direction under 1 sun illumination.

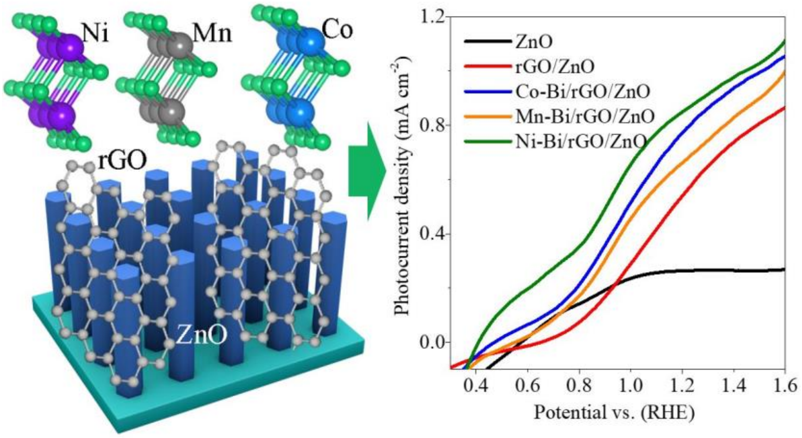

6.1 Introduction

Sunlight provides the earth with plentiful power and has been by far the largest renewable source of energy. There are substantial interests in exploring this energy, especially when fossil fuels are increasingly depleted. Regarding the harvest and storage of solar energy, splitting water into hydrogen and oxygen seems to be an attractive option, whereby solar energy is captured and stored in the produced hydrogen, which can be readily combusted to regenerate water and release energy.[1] In recent years, artificial photosynthesis via a photoelectrochemical (PEC) solar-to-hydrogen process has received particular attention, which is an efficient coupling of sunlight irradiation to electrochemical profiles (by applying an external bias).[2] In this case, considerable studies have been targeting the appropriate electrocatalyst/light-harvester electrode system,[3] where semiconductors with a competing stability and light absorption serve as a light-harvester, while electrocatalysts are generally deposited on the top of the semiconductor to reduce overpotentials in hydrogen evolution reaction (HER) and oxygen evolution reaction (OER).

Compared to HER, OER half-reaction (also known as water oxidation) is the rate-limiting step for water splitting as it is kinetically more-demanding by conducting the $4e^{-} - 4H^{+}$ proton-coupled electron transfer (PCET) process, imposing higher OER overpotentials.[4,5] Therefore, efficient OER electrocatalysts are critical for achieving overall excellent PEC water splitting performance. Despite of superior OER activities, noble metal oxides (e.g. RuO_2 or IrO_2) as electrocatalysts are economically unviable, due to the high cost. Driven by wide availability and low cost, the earth-abundant transition metals as well as their compounds have attracted special attention.[6] The majority of OER electrocatalysts work best in basic media (pH 13-14), in which the charge carrier concentration is the greatest. However, neutral or milder pH electrolytes are desired because most known semiconductors degrade rapidly in extreme pH regimes. In addition, the mild pH environment is beneficial for a long-term performance of the device with a slow degradation rate and possible leakage.[7] In this regard, amorphous thin-film OER catalysts have been self-assembled by photo- or electro-deposition from transition-metal solutions (e.g. aqueous Co^{2+} and Ni^{2+}) in the presence of a buffering electrolyte, like phosphate (Pi), borate (Bi), or methylphosphonate (MePi), and they show a high OER activity at pH 7-9.[8–11] Attributed to the borate or phosphate atoms, these oxygen evolution catalysts (OECs) have superior self-healing capability to reverse catalyst corrosion and operate steadily with high activities.[12,13] Moreover, they can be in-situ interfaced with light absorbers to construct novel artificial-leaf-like architectures for enhanced PEC water splitting.[14–17] Some studies have been reported in such OER catalyst films using Co-Bi, Ni-Bi, Co-Pi, Ni-Pi, and Mn-Pi layers.[13,14,17] However, no systemic investigation has been reported in Ni-, Co-, Mn-based OECs in the same configuration. Herein we perform DFT calculations to reveal the active sites in atomic-level understanding of different OER functions of Ni-Bi, Co-Bi and Mn-Bi electrocatalysts, which were subsequently verified experimentally.

For the construction of electrocatalyst/light-harvest electrode system, ZnO at a low cost and high electron mobility was selected as the target photoabsorber. It is believed that a well-aligned one-dimensional (1D) configuration endows the semiconductor with high surface-to-volume ratios and provides an axial length transport pathway for carriers to reduce their recombination rate. Accordingly, vertically aligned 1D ZnO nanorod arrays (NAs) were grown onto fluorine-doped tin oxide (FTO) glass by a modified hydrothermal method.[18] rGO was further loaded to the ZnO NAs to enhance conductivity, inhibiting electron-hole recombination and promoting charge separation in ZnO, as proved by DFT calculations.[19] Finally, amorphous thin films of M-Bi (M = Ni, Co, Mn) were photo-deposited onto the rGO/ZnO NAs, respectively. It is noted that Mn-Bi is originally proposed. Interestingly, the photochemical deposition has its advantage over electrodeposition for the photo-related applications, because OECs tend to deposite on the locations with high photohole concentrations.[8] This ensures the most efficient use of OECs, resulting in enhanced O_2 evolution.[20] Ni-Bi/rGO/ZnO, Co-Bi/rGO/ZnO and Mn-Bi/rGO/ZnO photoanodes were thus fabricated and to the best of our knowledge, such a ternary system has not been reported elsewhere. We then compared the OER activities of Ni-Bi, Co-Bi and Mn-Bi by DFT calculations and PEC experiments in M-Bi/rGO/ZnO configurations. This endeavor will provide instructive design principles for rational construction of artificial photosynthesis systems.

6.2 Experimental Section

6.2.1 Chemical Reagents

Zinc acetate (99.99%), zinc nitrate hexahydrate (≥ 99%), hexamethylenetetramine (≥ 99%), boric acid (≥ 99.5%), potassium hydroxide (≥ 85%), nickel nitrate hexahydrate (≥ 98.5%), manganese nitrate tetrahydrate (≥ 97%), and cobalt chloride (≥ 98%) were received from Sigma-Aldrich and used without purification.

6.2.2 Preparation of ZnO and rGO/ZnO

ZnO was successfully grown on F-doped SnO_2 (FTO) glass (1×1.5 cm^2) by a modified seed assisted method.[18] Briefly, 100 mL of 0.06 M zinc acetate solution (dissolved in ethanol) was spin-coated onto the pretreated FTO substrate, and annealed at 350 °C in air for 30 min to form ZnO seeds. Then, the FTO substrate was immersed in a mixed 60 mL solution of zinc nitrate hexahydrate (30 mM) and hexamethylenetetramine (HMT, 30 mM), which was transferred into a Teflon-lined autoclave and heated at 110 °C for 12 h. Finally, the resulting ZnO arrays grown on FTO were washed by distilled water and dried. For preparation of rGO/ZnO composite, graphite oxide (GO) prepared via a modified Hummers method was used.[21] The GO aqueous solution (0.2 mg mL^{-1}) was spin-coated onto the prepared ZnO NAs for 5 times, followed by an annealing process at 450 °C for 2 h in N_2 atmosphere, where GO was thermally reduced to rGO.

6.2.3 Preparation of M-Bi/rGO/ZnO

A potassium-borate (K-Bi, 0.2 M) buffer solution was prepared from boric acid and the pH value was adjusted to 9.2 using a KOH solution. Nickel nitrate hexahydrate/or manganese nitrate tetrahydrate/or cobalt chloride (1.0 mM) was prepared in the buffer solutions. Then, the solution was filtrated through a cellulose folded filter (Rotilabo, Typ 600P, 150 mm) and transferred to a quartz cell as the electrolyte. The prepared ZnO/rGO on FTO glass (1×1.5 cm^2) acted as the working photoelectrode, which was connected to a platinum (Pt) plate counter electrode (1.5×1.5 cm^2) to generate a short-circuited (SC) loop. M-Bi layers (M = Ni, Co, Mn) in similar thicknesses were photo-deposited onto rGO/ZnO to prepare M-Bi/rGO/ZnO, adopting the same deposition time under AM 1.5G simulated solar light with an output voltage of 1.5 $\mu W/cm^2$. For comparison, M-Bi/ZnO was synthesized by a similar method without rGO.

6.2.4 PEC Measurement

Photoelectrochemical tests were carried out on a Zennium workstation (Zahner, Germany) in a three-electrode configuration, with Ag/AgCl electrode as the reference electrode and Pt plate (1.5×1.5 cm^2) as the counter electrode. FTO substrate (1×1 cm^2) deposited with catalysts acted as the working photoanodes. A K-Bi buffer solution (pH = 9.2) was adopted as the electrolyte and it is relatively stable with sufficient proton-accepting capacity for M-Bi. All potentials were converted to RHE (reference hydrogen electrode) potentials. Before the tests, all photoanodes were reconditioned (at 1.5 V) through the potentiostatic method. The current density-voltage (J-V) plots were obtained by the linear sweep voltammetry (LSV) method under irradiation of AM 1.5G simulated solar light (light intensity: 1 sun or 100 mW cm^{-2}) at 10 mV s^{-1}. Stability tests were performed using the photoanode (1×1.5 cm^2) as the working electrode by the potentiostatic measurements holding at 1.23 V for 2 h, during which the produced O_2 was monitored by an oxygen sensor (Ocean Optics, Neofox, FOSPOR-R 1/16).

Specifically, the oxygen sensor was inserted into the photoelectrolytic glass cell to probe the produced O_2 concentration via the fluorescence quenching method during the stability test. The glass cell has a quartz window (the volume of the headspace was 30 mL, excluding the space occupied by the septum, oxygen sensor, and the solution). The needle probe was inserted into the 1/16" threaded holes through a rubber septum and conducted uninterrupted O_2 readings at 5 s intervals throughout the test. Ahead of the detection, the probe was calibrated through 2 point method, with a reading error of 1%. Before irradiation, the reactor was purged with N_2 for 10 min to exclude air in the reaction system. The test started from 10 min baseline reading followed by 100 min irradiation under AM 1.5G simulated solar light (light intensity: 1 sun or 100 mW cm^{-2}) with the potentiostatic method (1.23 V vs. RHE).

Electrochemical impedance spectra (EIS) were examined under dark and light conditions from 100000 to 0.1 Hz. Mott-Schottky measurements were also conducted in 0.2 M K-Bi solution (pH = 9.2) in the dark at a frequency of 1000 Hz and a scanning rate of 10 mV s^{-1}. The charge carrier density (N_d) is calculated from the slopes of the plots using equation (6.1):[22]

$$N_d = (2/\mathrm{e}\varepsilon_0\varepsilon)\left[\frac{\mathrm{d}\left(\frac{1}{C^2}\right)}{\mathrm{dV}}\right]^{-1} \qquad (6.1)$$

where $\varepsilon = 10$ is the dielectric constant for ZnO,[23] $\varepsilon_0 = 8.85\times10^{-14}$ F/cm and $e = 1.6 \times 10^{-19}$ C.

To quantify the relationship between PEC performance and light absorption, incident-photon-to current-conversion efficiencies (IPCE) were measured at 1.23 V under the 1.5G simulated solar light on a Zahner Cimps system. IPCE is derived from equation (6.2):

$$\mathrm{IPCE} = (1240 \times \mathrm{I})/(\lambda \times P_{light}) \qquad (6.2)$$

where I (mA/cm^2) stands for the photocurrent density; λ (nm) is the incident light wavelength; and P_{light} (mW/cm^2) is the measured power density of monochromatic light at a specific wavelength.

6.2.5 Materials Characterizations

Details on XRD, XPS, TEM, HAADF-STEM with EDX elemental mapping measurements can refer to Chapter 3. UV-visible diffuse reflectance spectra were collected on a Cary 100 UV-visible spectrophotometer (Agilent, US).

6.2.6 Simulation Details

We performed spin-polarized DFT calculations in order to elucidate the OER activities of M-Bi (M = Ni, Co, Mn). We used the Vienna *Ab initio* Simulations Package (VASP) [24,25] and projected augmented wave (PAW)[26–28] method for total energy calculations. In the calculations, 3*d* and 4*s* electrons were treated as valence electrons for Ni, Co and Mn, and 2*s* and 2*p* for O. The exchange-correlation interaction was treated with Generalized gradient approximation (GGA) parameterized by Perdew, Burke and Ernzerhof (PBE).[29] For strongly localized *d* electrons, the GGA has systematic and noncancelling errors.[30] So, we adopted GGA+U[31] to correct the self-interaction error and overdelocalized *d* states. The effective U_{eff} introduced by Dudarev et al.[31] was used with 5.25[31], 4.5[32] and 5.5 eV[33] for Ni, Co and Mn, respectively.

We started from relaxing bulk MO_2 (space group $R\bar{3}m$, No. 166) composed of MO_6 octahedra. The cutoff energy of plane-wave basis was set to 520 eV, and integrations over the first Brillouin zone were made using Gamma-centred k-point sets of 8×8×8. With these settings, the total energy was able to converge within 1 meV/atom. Atomic positions were fully relaxed with the energy converged within 10^{-6} eV/cell and the force converged to less than 10^{-4} eV/Å. Then, we relaxed the (100) surface with a single layer of MO_6 octahedra spaced by 17 Å. The zigzag ribbons were also relaxed in slab calculations. The same cutoff energy and similar k-point grids as dense as in the bulk calculations (in the case of vacuum direction, only Gamma point was used) were used for slab calculations. The detailed treatment of OER free energy calculations can be found in Chapter 5.[34]

6.3 Results and Discussion

6.3.1 DFT Calculations

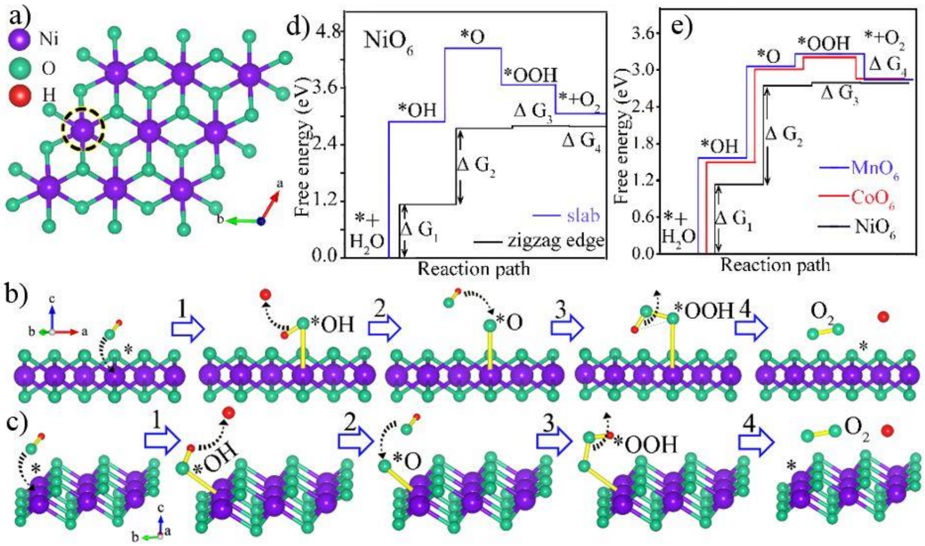

Figure 6.1 a) Model configuration of NiO$_6$. Proposed 4-step OER paths with *OH, *O and *OOH adsorbed on selected Ni sites at b) slab position and c) zigzag edge of NiO$_6$ (pH = 9.2 and U = 5.25 in NiO$_6$).[31] Diagrams of the 4-step Gibbs free energy changes calculated on d) slab and zigzag edges in NiO$_6$ and e) zigzag edges in NiO$_6$, CoO$_6$, MnO$_6$.

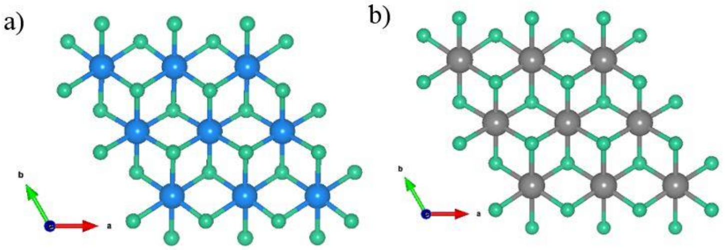

Figure 6.2 Model structures for a) CoO$_6$ and b) MnO$_6$.

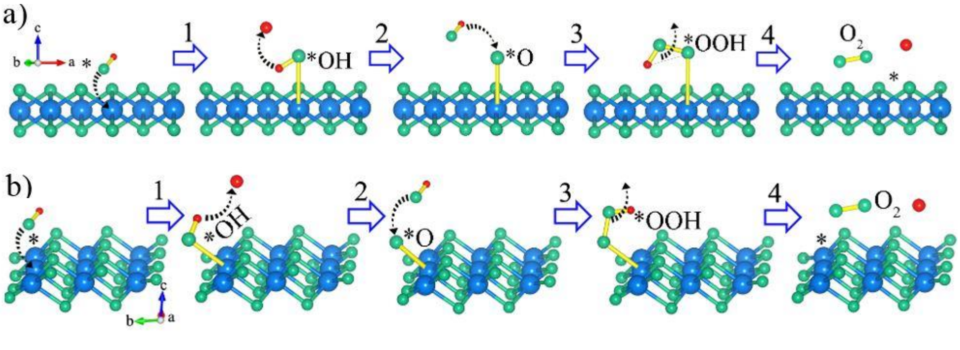

Figure 6.3 Proposed 4-step OER paths with *OH, *O and *OOH adsorbed on selected Co site at a) (001) surface and b) zigzag edge of CoO$_6$ (pH = 9.2 and U = 4.5 in CoO$_6$[32]).

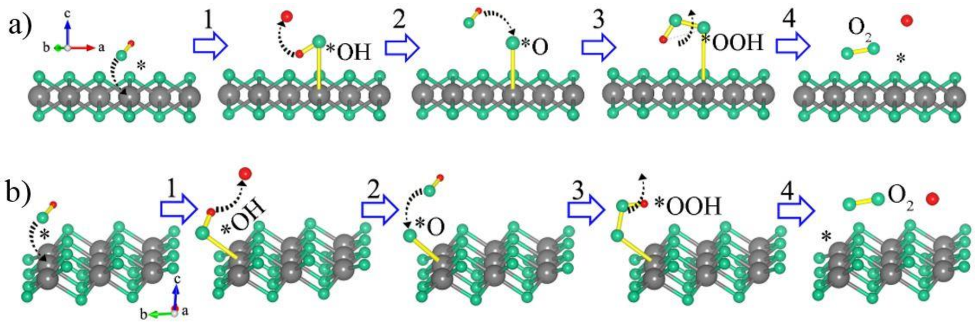

Figure 6.4 Proposed 4-step OER paths with *OH, *O and *OOH adsorbed on selected Co site at a) slab and b) zigzag edge of MnO_6 (pH = 9.2 and U = 5.5 for MnO_6[33]).

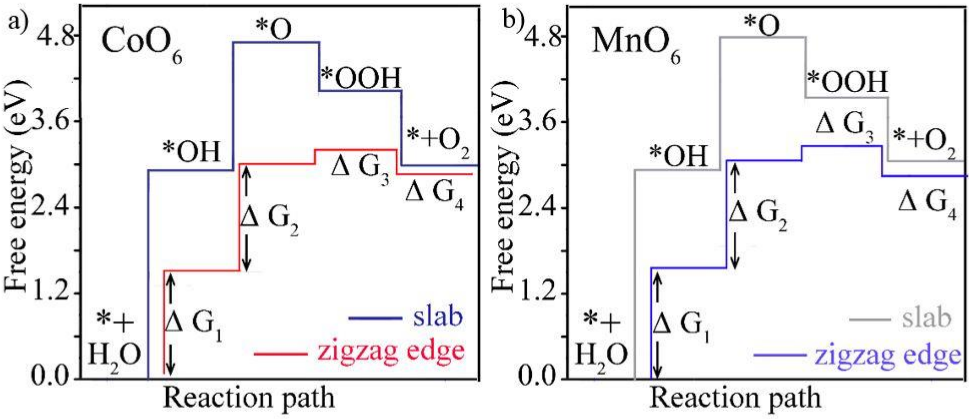

Figure 6.5 Diagrams of the 4-step Gibbs free energy changes calculated on the (001) slab surface and zigzag edge in a) CoO_6 and b) MnO_6.

It is proposed that M-Bi in high metal valence states tend to be obtained by anodized electrodeposition or photo-induced chemical deposition.[4,5] Nocera et al. reported that anodized Ni-Bi films consist of edge-sharing NiO_6 octahedron layers with ordered domain diameters no less than 2 nm (~40 Ni centers).[4] According to X-ray pair distribution function (PDF) analysis, Co-Bi films show coherent ordered domains of 3 - 4 nm with aligned layers of edge-shared CoO_6 octahedron clusters.[5] Based on the above, we built models of NiO_6 (Figure 6.1a) and CoO_6 (Figure 6.2a) for Ni-Bi and Co-Bi, consisting of edge-sharing NiO_6 and CoO_6 octahedron clusters, respectively, which are within the range of their ordered molecular domains. For comparison, MnO_6 (Figure 6.2b) was also constructed with the same structure of edge-sharing MnO_6.[9] Borate species that are not the active sites for water oxidation were not included in the models.

OER can be simulated by four elementary steps, where the intermediates of *OH, *O and *OOH are generated. It is reported that OER usually originates from the most stable (001) surface.[35] For in-depth understanding, the OER energy barriers for adsorption of *OH, *O and *OOH on slab (001) surface and zigzag edge position were investigated, as descried in Figures 6.1b, 6.1c, 6.3, and 6.4. The energy barriers are associated with Gibbs free energy changes in the four steps (ΔG_1-ΔG_4), and the energy diagrams are obtained, as shown in Figures 6.1d, 6.1e and 6.5. Due to the highest uphill/endothermic energy profiles from the deprotonation of H_2O ($*+H_2O \rightarrow *OH+H^++e^-$, step 1) and *OH ($HO* \rightarrow O*+H^++e^-$, step 2), step 1 or 2 is the rate-determining step. Step 3 ($*O+H_2O \rightarrow *OOH+H^++e^-$) requires relatively much lower energy barriers. The diagrams for step 4 ($*OOH \rightarrow O_2+H^++e^-$) are downhill/exothermic, suggesting that it is effortless to proceed. Figures 6.1d and 6.5 show that a much lower Gibbs free energy is needed for OER to occur on the zigzag edges than on slab (001) surfaces of NiO_6, CoO_6 and MnO_6, revealing that the zigzag edges are more active sites for OER. On the zigzag edges of MO_6, the lowest overall uphill Gibbs free energy is observed on NiO_6, meaning the lowest energy barriers for OER in NiO_6. It is indicated that the adsorption of H_2O molecules and their decomposition into *OH in step 1 is highly critical in determining OER activity, since it is the initiation of OER on the surface of catalysts.[36] Especially, NiO_6 possesses a much smaller ΔG_1 value than CoO_6 and MnO_6, suggesting that it is much easier to initiate step 1. Therefore, the DFT calculations reveal the lowest OER kinetics in NiO_6, followed by CoO_6, which is slightly better than MnO_6.

6.3.2 Material Characterization

To verify the DFT results, M-Bi (M = Ni, Co, Mn) electrocatalysts were photodeposited onto rGO/ZnO photo-harvester for further PEC-OER tests. The preparation process of M-Bi/rGO/ZnO photoanodes is schematically described in Figure 6.6a. Scanning electron microscopy (SEM) images (Figures 6.6b and c) indicate that about 2 µm long ZnO NAs with diameters of 100 ~150 nm and smooth surfaces were vertically grown onto an FTO glass. Subsequently, graphene oxide (GO) was spin-coated onto the ZnO NAs, followed by an annealing process in N_2 flow for strong adhesion and reduction of GO to rGO. Figures 6.6d and 6.7 show that gossamer-like rGO nanosheets cover ZnO nanorods from the top or the side flexibly. Finally, M-Bi thin layers in similar thicknesses were uniformly deposited onto rGO/ZnO, turning the surfaces from smooth to rough (Figures 6.6e, 6.7b, and 6.7c). For comparison, M-Bi/ZnO were also prepared without the deposition of rGO (Figure 6.7d-f).

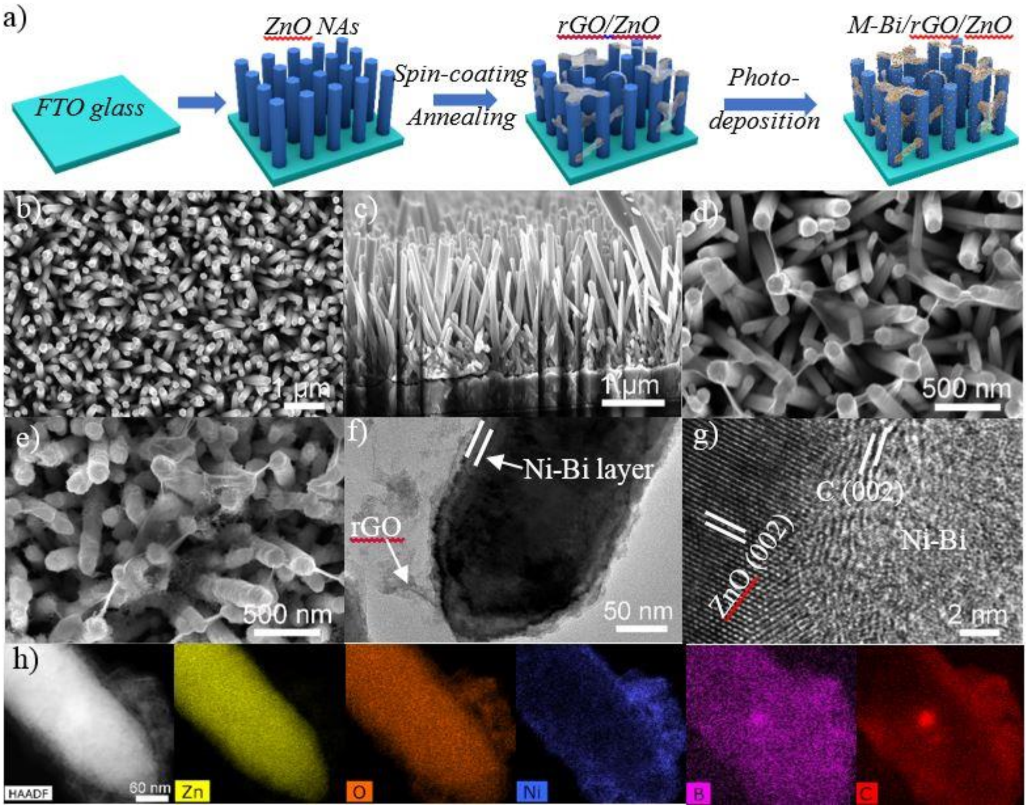

Figure 6.6 a) Schematic fabrication procedure of M-Bi/rGO/ZnO composites. SEM images of b, c) ZnO NAs, d) rGO/ZnO and e) Ni-Bi/rGO/ZnO. f) TEM, g) HRTEM and h) the high angle annular dark field scanning TEM (HAADF-STEM) images with EDX elemental mapping results on Ni-Bi/rGO/ZnO.

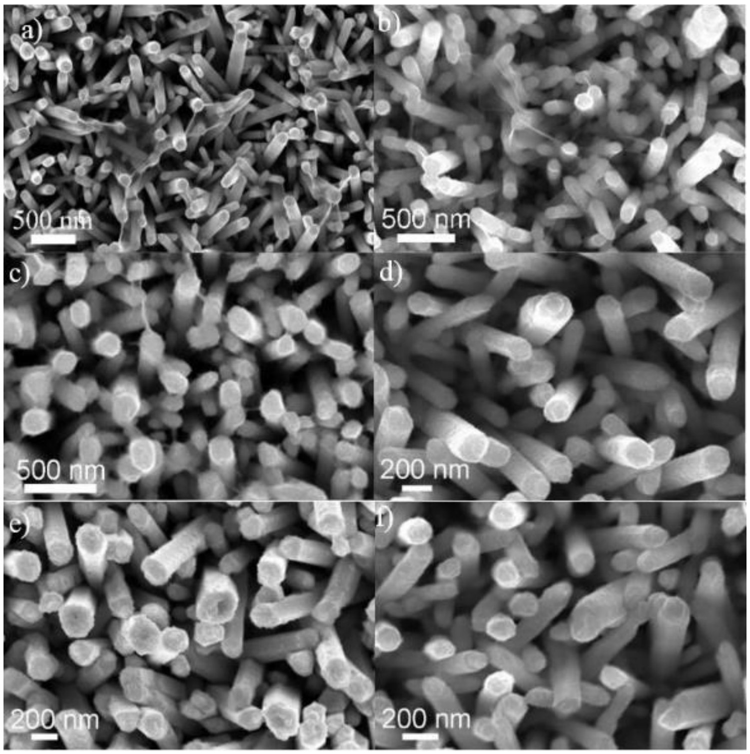

Figure 6.7 SEM images of a) rGO/ZnO, b) Co-Bi/rGO/ZnO, c) Mn-Bi/rGO/ZnO, d) Ni-Bi/ZnO, e) Co-Bi/ZnO and f) Mn-Bi/ZnO.

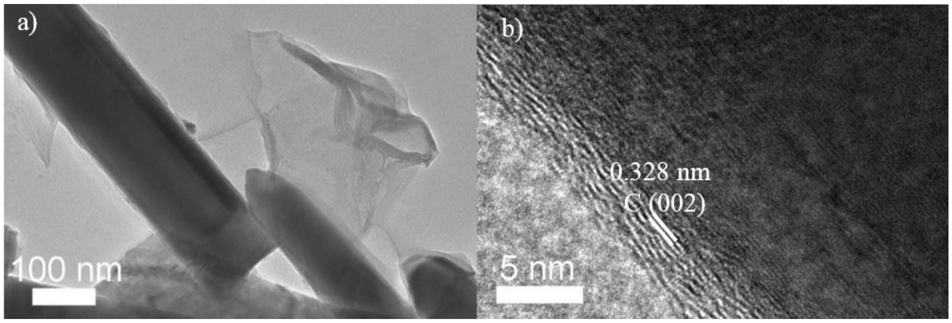

Figure 6.8 a) TEM and b) HRTEM images of rGO/ZnO.

Transmission electron microscopy (TEM) images of rGO/ZnO show their good attachment (Figure 6.8). Further, M-Bi layers (about 8 nm thick) attach tightly onto ZnO or rGO (Figures 6.6f and 6.9-6.11) after photodeposition. Representative high-resolution TEM (HRTEM) images of Ni-Bi/rGO/ZnO (Figure 6.6g) display the amorphous nature of Ni-Bi and clear lattice fringes corresponding to the (002) planes of hexagonal ZnO and the (002) planes of C. The successful coating of Ni-Bi, Co-Bi and Mn-Bi on ZnO or rGO/ZnO can be clearly visualized by energy-dispersive X-ray spectroscopy (EDX) elemental mapping results (in Figures 6.6, 6.9-6.11).

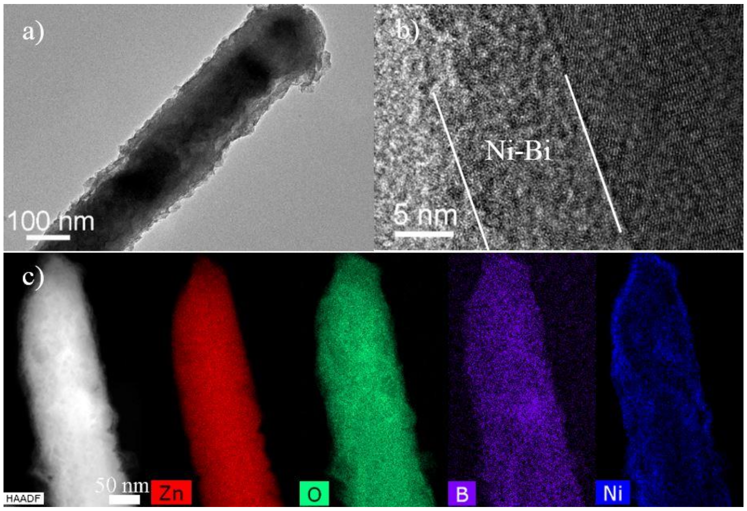

Figure 6.9 a) TEM, b) HRTEM and c) HAADF-STEM with EDX mapping images of Ni-Bi/ZnO.

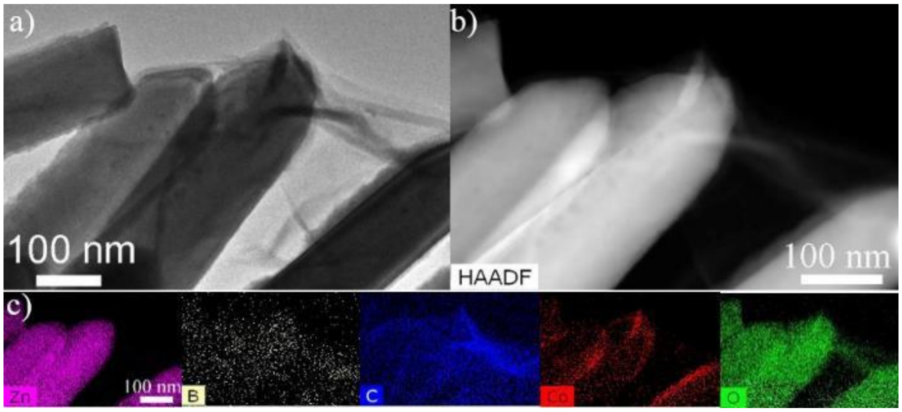

Figure 6.10 a) TEM, b) HAADF-STEM and c) EDX mapping images of Co-Bi/rGO/ZnO.

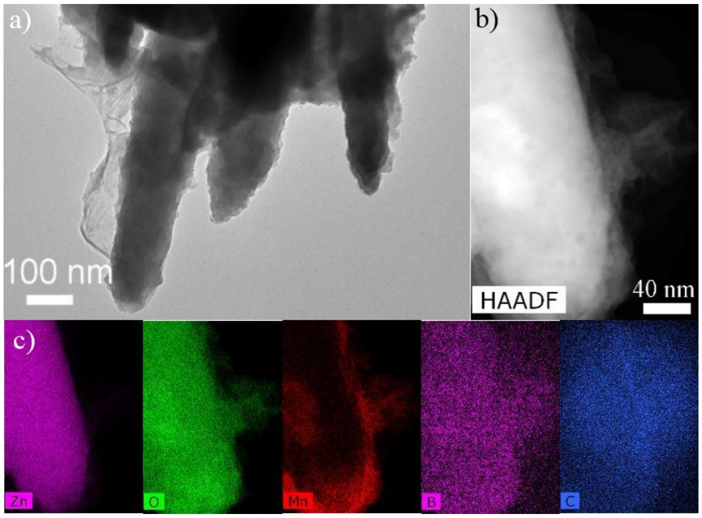

Figure 6.11 a) TEM, b) HAADF-STEM and c) EDX mapping images of Mn-Bi/rGO/ZnO.

Only reflection peaks of ZnO and FTO glass are detected in X-ray diffraction (XRD) patterns of M-Bi/rGO/ZnO composites, mainly due to the low loading amount of rGO and the amorphous nature of M-Bi thin layers (Figure 6.12). X-ray photoelectron spectroscopy (XPS) was further conducted and the full spectra indicate the presence of M (M = Ni, Co, Mn), Zn, B, C, O on M-Bi/rGO/ZnO (Figure 6.13). K arises from the buffer solution, which is intercalated in M-Bi films during the preparation. The high-resolution spectra of Zn 2p, Ni 2p, Co 2p and Mn 2p are provided in Figure 6.13b-e. It is generally difficult for accurate determination of oxidation states of Ni, Co or Mn, due to the diversified binding energies for the same M species.[37] However, it is generally reported that the oxidation states of anodized M-Bi films are predominantly in M^{III} or even higher.[14,17,38]

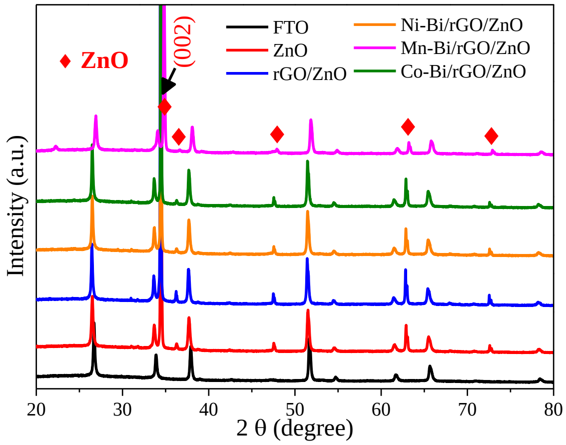

Figure 6.12 XRD patterns of FTO substrate, ZnO, rGO/ZnO and M-Bi/rGO/ZnO.

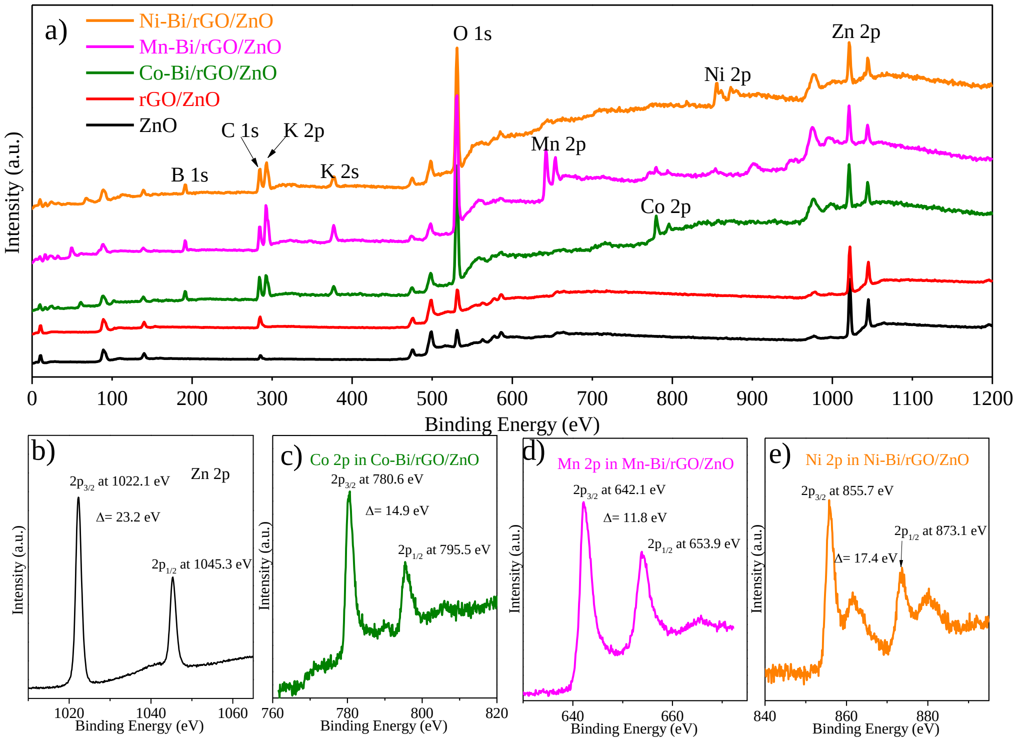

Figure 6.13 a) Full XPS spectra of the samples and high-resolution spectra of b) Zn 2p, c) Co 2p, d) Mn 2p and e) Ni 2p.

6.3.3 PEC Tests

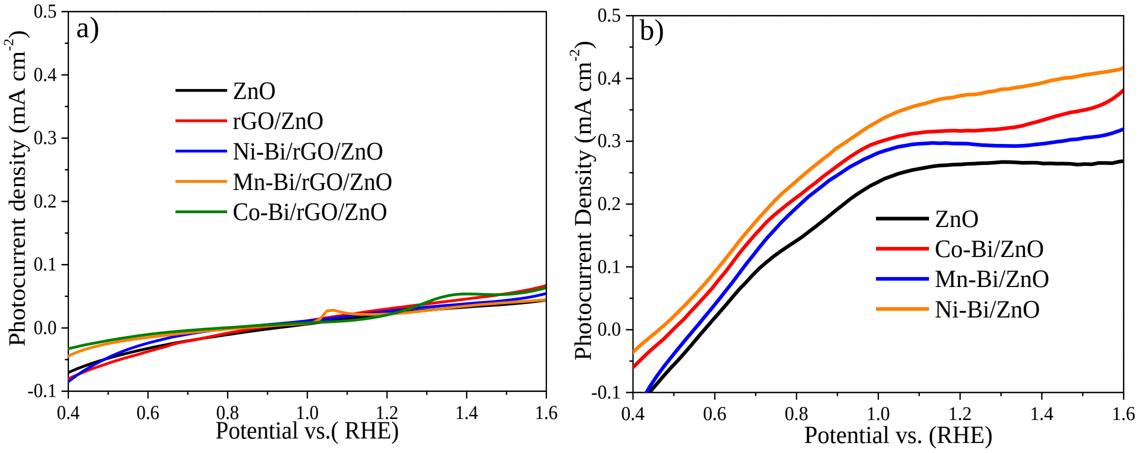

Figure 6.14 a) J-V curves under dark; b) J-V curve comparison of ZnO and M-Bi/ZnO under irradiation.

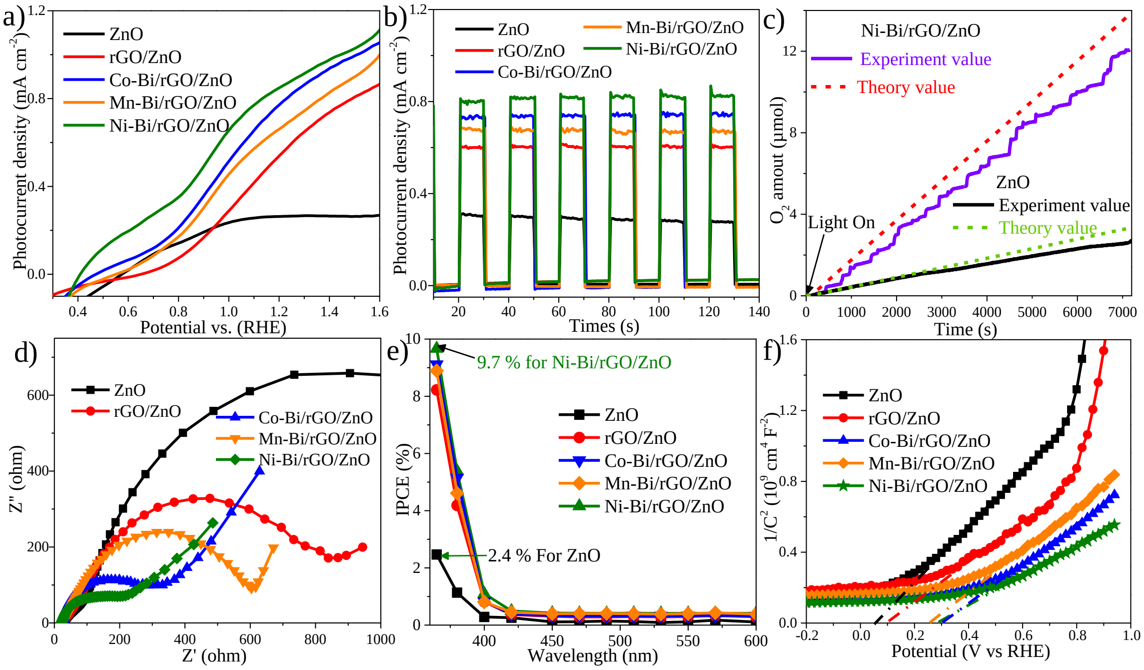

Figure 6.15 a) J-V curves, b) I-t curves tested at 1.23 V under chopped light illumination, c) O_2 amount measured in real-time by an oxygen sensor (the dashed lines are the theoretical O_2 production calculated from the measured photocurrent), d) EIS measured under illumination, e) IPCEs of the photoanodes and f) Mott-Schottky plots.

The PEC measurements were performed under 1 simulated sun illumination, using ZnO, rGO/ZnO, M-Bi/ZnO and M-Bi/rGO/ZnO NAs as the photoanodes. The current density-voltage (J-V) plots of the samples under dark display low current densities (Figure 6.14). Under the irradiation, ZnO displays a limited PEC-OER activity with a current density of 0.26 mA cm^{-2} at 1.23 V (Figure 6.15a). Once rGO is loaded onto ZnO, the photocurrent density (0.58 mA cm^{-2} at 1.23 V) is enlarged by a factor of 2.2, proving that rGO could remarkably inhibit electron-hole recombination and promote charge separation on ZnO. By contrast, when M-Bi overlayers are coated onto ZnO (M-Bi/ZnO), the onset potentials exhibit desirable shifts in the cathodic direction (Figure 6.14b), which confirms the function of M-Bi as efficient electrocatalysts to lower the kinetic barrier of OER. Generally consistent with DFT results, Ni-Bi with the lowest OER energy barrier presents the best catalytic performance and onset potential shifts by 0.12 V in the cathodic direction in Ni-Bi/ZnO, followed by Co-Bi/ZnO (0.08 V) and Mn-Bi/ZnO (0.03 V). In addition, the photocurrent densities are larger than that of ZnO (0.29, 0.32, and 0.38 mA cm^{-2} for Mn-Bi/ZnO, Co-Bi/ZnO and Ni-Bi/ZnO at 1.23 V, respectively). For the ternary M-Bi/rGO/ZnO system, both cathodically shifted onset potentials and largely increased current densities are observed due to the synergistic effect of rGO, M-Bi with ZnO. Distinctly, Ni-Bi/rGO/ZnO represents the best sample. Compared to ZnO, the onset potential migrates by 0.17 V in the cathodic direction (0.58 → 0.41 V) and the water oxidation photocurrent (0.86 mA cm^{-2} at 1.23 V) is enlarged by a factor of 3.3. By contrast, Co-Bi/rGO/ZnO delivers 0.12 V cathodic shift of onset potential and photocurrent density of 0.80 mA cm^{-2} at 1.23 V. Mn-Bi/rGO/ZnO shows an inferior activity with 0.04 V onset potential shift and photocurrent density of 0.69 mA cm^{-2}. The photoresponse behaviors of the photoanodes were further investigated by chronoamperometry (I-t) measurements under chopped light irradiations (Figure 6.15b). Regarding the ON-OFF irradiation cycles, prompt and reproducible current responses were observed toward the light stimulation for all the samples. In high accordance with J-V tests, Ni-Bi/rGO/ZnO shows the highest photocurrent density of 0.8 mA cm^{-2} without attenuation, followed by Co-Bi/rGO/ZnO, Mn-Bi/rGO/ZnO, rGO/ZnO and ZnO. This PEC performance is among the superior values reported for ZnO based photoanodes, as compared in Table 6.1.

Table 6.1 A comparison of the PEC performances of Ni-Bi/rGO/ZnO with previously reported ZnO-based catalysts for water oxidation in a mild medium under light intensity of 100 mW cm^{-2}.

Photoanode	Photocurrent density (potentials vs. RHE)	Testing condition	Reference
C-doped ZnO	1.00 mA cm^{-2} at 1.61 V	0.5 M Na_2SO_4	39
Au NP/$ZnFe_2O_4$/ZnO	1.1 mA cm^{-2} at 1.4 V	0.5 M Na_2SO_4	40
3D ZnO/TiO_2/FeOOH NWs	1.59 mA cm^{-2} at 1.8 V	0.5 M Na_2SO_4	41
$Ni(OH)_2$/ZnO NR	~0.90 mA cm^{-2} at 1.2 V	0.5 M Na_2SO_4	42
Au-ZnO nanopencil	~1.5 mA cm^{-2} at 1.6 V	0.5 M Na_2SO_4	43
ZnO-Au-SnO_2 nanorods	0.08 mA cm^{-2} at 1.4 V	0.5 M Na_2SO_4	44
(N-GQDs)/ZnO nanowire	~0.6 mA cm^{-2} at 1.63 V	0.5 M Na_2SO_4	45
CdS/RGO/ZnO Nanowire	0.8 mA cm^{-2} at 1.63 V	0.1 M phosphate buffer solution	46

Three-dimensional ZnO nanoforests	0.919 mA cm^{-2} at 1.81 V	0.5 M Na_2SO_4	[47]
Au-ZnO Nanowire	1.3 mA cm^{-2} at 1.6 V	0.5 M Na_2SO_4	[48]
ZnO-IrOx nanorod	0.7 mA cm^{-2} at 1.2 V	0.25M Na_2SO_4	[49]
Ni-Bi/rGO/ZnO	1.15 mA cm^{-2} at 1.6 V	0.2 M K-Bi	This work

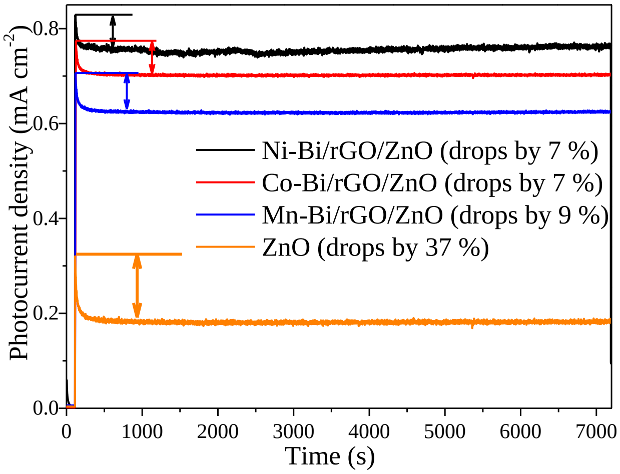

Figure 6.16 Potentiostatic measurements (at 1.23 V vs RHE) of ZnO and M-Bi/rGO/ZnO.

The stabilities of these photoanodes were evaluated by the potentiostatic measurements at 1.23 V (Figure 6.16). Under irradiations, the photocurrent density of ZnO rapidly decays to 0.22 mA cm^{-2} (37% drop), while an enhanced stability is observed on the M-Bi/rGO/ZnO composites (less than 9% recession). This can be ascribed to the more efficient OER in the ternary system, which can restrain the accumulation of photogenerated holes on the electrode surface for photocorrosion. In addition, the amount of O_2 evolution was real-time monitored on ZnO and Ni-Bi/rGO/ZnO during the stability test (Figure 6.15c). Comparing the theoretical O_2 production (calculated from the photocurrent) with the experimental results, the average faradaic efficiencies of ZnO and Ni-Bi/rGO/ZnO were calculated to be around 90%. The high photocurrent-to-oxygen conversion efficiencies highlight the efficient PEC water splitting process. It is proposed that a small portion of the obtained photocurrent in Ni-Bi/rGO/ZnO is created by oxidation of Ni, which is responsible for the gap between the theoretical and experimental O_2 evolution values. For ZnO, the 10% gap mainly originates from its photocorrosion. The amount of O_2 produced by Ni-Bi/rGO/ZnO is approximately 5 times larger than that of ZnO, confirming the largely enhanced OER efficiency of the ternary system.

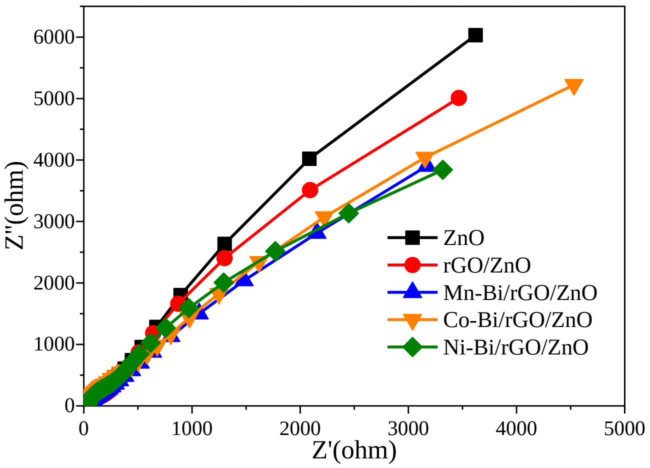

Figure 6.17 Electrochemical impedance spectra (EIS) measured in dark.

Electrochemical impedance spectra (EIS) were examined on the photoanodes under both dark and light conditions, to investigate the charge transport behavior at the electrode/electrolyte interfaces. The large semicircle diameters in the dark (Figure 6.17) for all the photoanodes indicate the high interfacial charge transfer resistances (R_{ct}), which are drastically reduced under light irradiation (Figure 6.15d). Specifically, the R_{ct} of these photoanodes follows an increasing order as: Ni-Bi/rGO/ZnO < Co-Bi/rGO/ZnO < Mn-Bi/rGO/ZnO < rGO/ZnO < ZnO. Therefore, rGO and M-Bi OECs can effectively boost the charge transport from electrode to electrolyte, making PEC water oxidation easier to proceed because of the reduced charge transfer barriers. Among these photoanodes, the Ni-Bi/rGO/ZnO shows the smallest diameter, indicating the fastest charge transfer kinetics.

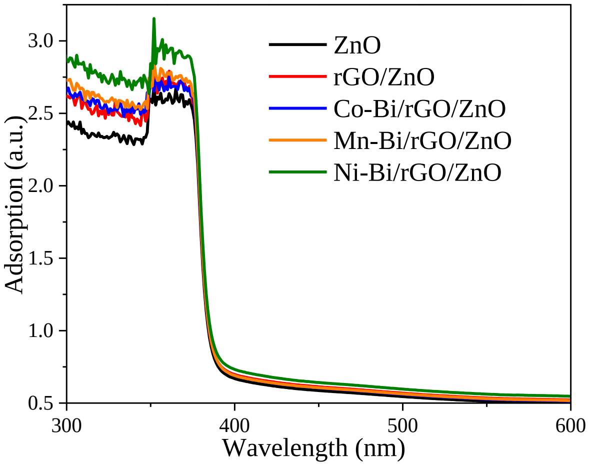

Figure 6.18 UV-vis diffuse reflectance spectra of ZnO, rGO/ZnO and M-Bi/rGO/ZnO.

The optical properties of these samples were investigated by UV-vis diffuse reflectance (Figure 6.18). Strong absorption in UV-light region was observed on ZnO with a steep absorption edge at approximately 380 nm. The band gap was calculated to be 3.2 eV. After coupled with rGO and M-Bi, similar spectra were obtained, indicating that the deposition of rGO and M-Bi will not hinder the light absorption of ZnO. To further quantify the relationship between PEC performance and light absorption, incident-photon-to current-conversion efficiencies (IPCE) were measured on the electrodes. Consistent with the UV-vis spectra, Figure 6.15e exhibits that all these photoanodes possess high photoconversion efficiencies in UV region (below 400 nm), yet little photoresponse in the visible-light region. The maximum IPCEs are obtained at 365 nm, which are 2.4%, 8.2%, 8.9%, 9.1% and 9.7 % for ZnO, rGO/ZnO, Mn-Bi/rGO/ZnO, Co-Bi/rGO/ZnO and Ni-Bi/rGO/ZnO, respectively. Impressively, Ni-Bi/rGO/ZnO delivers an approximately 4 times higher photoelectroconversion efficiency than ZnO. This further confirms the synergistic contributions of rGO, M-Bi and ZnO to the final excellent PEC performance.

Mott-Schottky analysis was performed for further electrochemical characterization (Figure 6.15f). All the samples display positive slopes for n-type ZnO semiconductor as expected. The calculated charge carrier density (N_d) values for ZnO, rGO/ZnO, Co-Bi/rGO/ZnO, Mn-Bi/rGO/ZnO and Ni-Bi/rGO/ZnO are 0.9×10^{22}, 1.23×10^{22}, 1.26×10^{22}, 1.17×10^{22}, and 1.7×10^{22} cm^{-3}, respectively. The very slight change of N_d values indicate that the addition of M-Bi and rGO layers will not affect the doping level or carrier density within the ZnO electrode.[50,51] However, the flat band potentials (E_{fb}) obtained from the X-axis intercept display positive shifts after rGO and M-Bi introduction, suggesting decreased bending degrees of the band edges (as pointed by the red arrows in Figure 6.19a).[50] This means that, although the bandgap of ZnO will not change, the valence band (VB) and conduction band (CB) shift towards positive positions (Figure 6.19a). This change facilitates charge transfer in ZnO and electrode/electrolyte interface and improves OER kinetics in the composites, leading to enhanced OER performance.

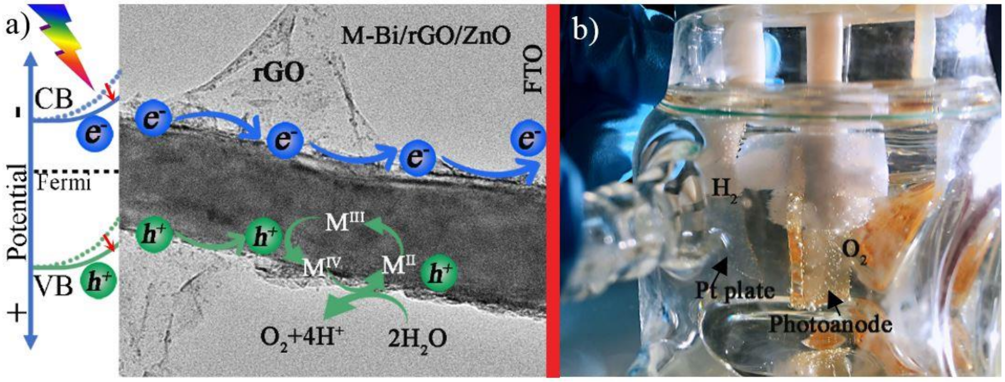

Figure 6.19 a) A schematic illustration of the PEC water oxidation process in the M-Bi/rGO/ZnO photoanodes. b) Image of the photoelectrolytic cell during a PEC test.

The detailed PEC water oxidation process can be illustrated by proton-coupled electron transfer (PCET) process (Figure 6.19a). In brief, electron-holes pairs are excited from ZnO under light radiation. With the assistance of conductive rGO nanosheets, the electrons can be efficiently separated to FTO glass and finally transferred to Pt counter electrode for proton reduction to H_2 via the external circuit, as shown in Figure 6.19b. Meanwhile, the separated photo-induced holes and imposed anodic bias will oxidize M^{III} centres (M = Ni, Co, Mn) to M^{IV} for water oxidation to give O_2 at the electrode/electrolyte interface.[17,52,53] As this occurs, the M^{IV} centres are reduced to M^{II}, which are rapidly re-oxidized and re-deposited as M^{III} oxides by holes and anodic bias (known as the self-healing of M-Bi).[6,12] This redox reaction proceeds circularly for continuous water oxidation. It is worth noting that borate species ensure the long-term stability of M-Bi in water oxidation, by serving as a promulgator catalyst in PCET process and an adsorbate of the active sites.[13]

6.4 Conclusions

In summary, for the first time we explore and compare the OER catalytic abilities of M-Bi (M = Ni, Co, Mn) layers by DFT calculations and experimental investigations. The DFT calculations suggest that zigzag edges act as the active OER sites in MO_6 structures of M-Bi, while NiO_6 exhibits a higher activity than CoO_6 and MnO_6 with the lowest overall OER energy barriers. As beneficial OER catalysts, M-Bi were then successfully photocoated onto rGO/ZnO NAs whereby ZnO acts as a photo-harvester and rGO promotes the efficient charge carrier separation. Consistent with the DFT results, Ni-Bi exhibits the best activity in improving OER kinetics, followed by Co-Bi and Mn-Bi. When the ternary composites (M-Bi/rGO/ZnO) are applied as the photoanodes for PEC water oxidation, significantly enhanced performances are acquired. Distinctly, the onset potential of Ni-Bi/rGO/ZnO is shifted by 0.17 V in the cathodic direction and the photocurrent was enlarged by a factor of 3.3 (at 1.23 V) compared with ZnO. The photoelectroconversion efficiency of ZnO is elevated by about 4 times. This work generates new insight to the different metal-based complex systems for OER and provides an interesting direction in developing more efficient catalysts for economical PEC water splitting.

References

1) Dunn, B.; Kamath, H.; Tarascon, J. Electrical Energy Storage for the Grid: A Battery of Choices. *Science* **2011**, *334,* 928.
2) Armaroli, N.; Balzani, V. Solar Electricity and Solar Fuels : Status and Perspectives in the Context of the Energy Transition**. *Chemistry-A European Journal* **2016**, *22*, 32.
3) Roger, I.; Shipman, M. A.; Symes, M. D. Earth-Abundant Catalysts for Electrochemical and Photoelectrochemical Water Splitting. *Nature Reviews Chemistry* **2017**, *1*, 1.
4) Bediako, D. K.; Lassalle-Kaiser, B.; Surendranath, Y.; Yano, J.; Yachandra, V. K.; Nocera, D. G. Structure-Activity Correlations in a Nickel-Borate Oxygen Evolution Catalyst. *Journal of the American Chemical Society* **2012**, *134*, 6801.
5) (5) Farrow, C. L.; Bediako, D. K.; Surendranath, Y.; Nocera, D. G.; Billinge, S. J. L. Intermediate-Range Structure of Self-Assembled Cobalt-Based Oxygen-Evolving Catalyst. *Journal of the American Chemical Society* **2013**, *135*, 6403.
6) Faber, M. S.; Jin, S. Earth-Abundant Inorganic Electrocatalysts and Their Nanostructures for Energy Conversion Applications. *Energy & Environmental Science* **2014**, *7,* 3519.
7) Esswein, A. J.; Surendranath, Y.; Reece, Y.; Nocera, D. G. Highly Active Cobalt Phosphate and Borate Based Oxygen Evolving Catalysts Operating in Neutral and Natural Waters. Energy & Environmental Science **2011**, *4,* 499.
8) Osterloh, F. E. Inorganic Nanostructures for Photoelectrochemical and Photocatalytic Water Splitting. *Chemical Society Reviews* **2013**, *42*, 2294.

9) Lucht, K. P.; Mendoza-Cortes, J. L. Birnessite: A Layered Manganese Oxide to Capture Sunlight for Water-Splitting Catalysis. *Journal of Physical Chemistry C* **2015**, *119*, 22838.

10) Dinc, M.; Surendranath, Y.; Nocera, D. G. Nickel-Borate Oxygen-Evolving Catalyst That Functions under Benign Conditions. *Proceedings of the National Academy of Sciences* **2010**, *107*, 10337.

11) Surendranath, Y.; Bediako, D. K.; Nocera, D. G. Interplay of Oxygen-Evolution Kinetics and Photovoltaic Power Curves on the Construction of Artificial Leaves. *Proceedings of the National Academy of Sciences* **2012**, *109*, 15617.

12) Lutterman, D. A.; Surendranath, Y.; Nocera, D. G. A Self-Healing Oxygen-Evolving Catalyst. *Journal of the American Chemical Society* **2009**, *131*, 3838.

13) Bediako, D. K.; Surendranath, Y.; Nocera, D. G. Mechanistic Studies of the Oxygen Evolution Reaction Mediated by a Nickel-Borate Thin Film Electrocatalyst. *Journal of the American Chemical Society* **2013**, *135*, 3662.

14) Khnayzer, R. S.; Mara, M. W.; Huang, J.; Shelby, M. L.; Chen, L. X.; Castellano, F. N. edge-Sharing CoO_6 Structure and Activity of Photochemically Deposited “CoPi” Oxygen Evolving Catalyst on Titania. *ACS Catalysis* **2012**, *2*, 2150.

15) Bi, Y.; Zhang, B.; Wang, L.; Zhang, Y.; Ding, Y. Ultrathin FeOOH Nanolayers with Rich Oxygen Vacancies on $BiVO_4$ Photoanodes for Efficient Water Oxidation. *Angewandte Chemie International Edition* **2018**, *57*, 2248.

16) Moniz, S. J. A.; Zhu, J.; Tang, J. 1D Co-Pi Modified $BiVO_4$/ZnO Junction Cascade for Efficient Photoelectrochemical Water Cleavage. *Advanced Energy Materials* **2014**, *4*, 1301590.

17) Xi, L.; Wang, F.; Schwanke, C.; Abdi, F. F.; Golnak, R.; Fiechter, S.; Ellmer, K.; van de Krol, R.; Lange, K. M. Structural Study of MnPi-Modified $BiVO_4$ Photoanodes by Soft X-Ray Absorption Spectroscopy. *The Journal of Physical Chemistry C* **2017**, *121*, 19668.

18) Chen, H. M.; Chen, C. K.; Chang, Y. C.; Tsai, C. W.; Liu, R. S.; Hu, S. F.; Chang, W. S.; Chen, K. H. Quantum Dot Monolayer Sensitized ZnO Nanowire-Array Photoelectrodes: True Efficiency for Water Splitting. *Angewandte Chemie International Edition* **2010**, *122*, 6102.

19) Geng, W.; Zhao, X.; Liu, H.; Yao, X. Influence of Interface Structure on the Properties

of ZnO/Graphene Composites: A Theoretical Study by Density Functional Theory Calculations. *Journal of Physical Chemistry C* **2013**, *117*, 10536.

20) Ellen M. P. Steinmiller and Kyoung-Shin Choi. Photochemical Deposition of Cobalt-Based Oxygen Evolving Catalyst on a Semiconductor Photoanode for Solar Oxygen Production. *Proceedings of the National Academy of Sciences* **2009**, *106*, 20633.
21) Hummers, W. S.; Offeman, R. E. Preparation of Graphitic Oxide. *Journal of the American Chemical Society* **1958**, *80*, 1339.
22) Li, W.; Da, P.; Zhang, Y.; Wang, Y.; Lin, X.; Gong, X.; Zheng, G. WO_3 Nanoflakes for Enhanced Photoelectrochemical Conversion. *ACS Nano* **2014**, *8*, 11770.
23) Mora-Seró, I.; Fabregat-Santiago, F.; Denier, B.; Bisquert, J.; Tena-Zaera, R.; Elias, J.; Lévy-Clément, C. Determination of Carrier Density of ZnO Nanowires by Electrochemical Techniques. *Applied Physics Letters* **2006**, *89*, 1.
24) Kresse, G.; Joubert, D. From Ultrasoft Pseudopotentials to the Projector Augmented-Wave Method. *Physical Review B* **1999**, *59*, 1758.
25) Blöchl, P. E. Projector Augmented-Wave Method. *Physical Review B* **1994**, *50*, 17953.
26) Kresse, G.; Furthmüller, J. Efficiency of Ab-Initio Total Energy Calculations for Metals and Semiconductors Using a Plane-Wave Basis Set. *Computational Materials Science* **1996**, *6*, 15.
27) Kresse, G.; Furthmüller, J. Efficient Iterative Schemes for Ab Initio Total-Energy Calculations Using a Plane-Wave Basis Set. *Physical Review B* **1996**, *54*, 11169.
28) Kresse, G.; Hafner, J. Ab Initio Molecular Dynamics for Open-Shell Transition Metals. *Physical Review B* **1993**, *48*, 13115.
29) Perdew, J. P.; Burke, K.; Ernzerhof, M. Generalized Gradient Approximation Made Simple. *Physical Review Letters* **1996**, *77*, 3865.
30) Li, Y.; Li, Y.-L.; Sa, B.; Ahuja, R. Review of Two-Dimensional Materials for Photocatalytic Water Splitting from a Theoretical Perspective. *Catalysis Science & Technology* **2017**, *7*, 545.
31) Dudarev, S.; Botton, G. Electron-Energy-Loss Spectra and the Structural Stability of Nickel Oxide: An LSDA+U Study. *Physical Review B - Condensed Matter and Materials Physics* **1998**, *57*, 1505.
32) Ling, C.; Zhou, L. Q.; Jia, H. First-Principles Study of Crystalline $CoWO_4$ as Oxygen

Evolution Reaction Catalyst. *RSC Advances* **2014**, *4*, 24692.

33) Tompsett, D. A.; Middlemiss, D. S.; Islam, M. S. Importance of Anisotropic Coulomb Interactions and Exchange to the Band Gap and Antiferromagnetism of β-MnO_2 from DFT+U. *Physical Review B - Condensed Matter and Materials Physics* **2012**, *86*, 1.

34) Zhang, H.; Tian, W.; Li, Y.; Sun, H.; Tade, M. O.; Wang, S. Heterostructured WO_3@$CoWO_4$ Bilayer Nanosheets for Enhanced Visible-Light Photo, Electro and Photoelectro-Chemical Oxidation of Water. *Journal of Materials Chemistry A* **2018**, *6*, 6265.

35) Leng, M.; Huang, X.; Xiao, W.; Ding, J.; Liu, B.; Du, Y.; Xue, J. Enhanced Oxygen Evolution Reaction by Co-O-C Bonds in Rationally Designed Co_3O_4 /Graphene Nanocomposites. *Nano Energy* **2017**, *33*, 445.

36) Sun, Y.; Gao, S.; Lei, F.; Liu, J.; Liang, L.; Xie, Y. Atomically-Thin Non-Layered Cobalt Oxide Porous Sheets for Highly Efficient Oxygen-Evolving Electrocatalysts. *Chemical Science* **2014**, *5*, 3976.

37) Roger, I.; Symes, M. D. First Row Transition Metal Catalysts for Solar-Driven Water Oxidation Produced by Electrodeposition. *Journal of Materials Chemistry A* **2016**, *4*, 6724.

38) Gan, J.; Lu, X.; Rajeeva, B. B.; Menz, R.; Tong, Y.; Zheng, Y. Efficient Photoelectrochemical Water Oxidation over Hydrogen-Reduced Nanoporous $BiVO_4$ with Ni-BiElectrocatalyst. *ChemElectroChem* **2015**, *2*, 1385.

39) Links, D. A. Visible-Light-Driven Photocatalytic Carbon-Doped Porous ZnO Nanoarchitectures for Solar Water-Splitting. *Nanoscale* **2012**, *4*, 6515.

40) Sheikh, A.; Yengantiwar, A.; Deo, M.; Kelkar, S. Near-Field Plasmonic Functionalization of Light Harvesting Oxide–Oxide Heterojunctions for Efficient Solar Photoelectrochemical Water Splitting : The AuNP / $ZnFe_2O_4$ / ZnO System. *Small* **2013**, *9*, 2091.

41) Li, Z.; Feng, S.; Liu, S.; Li, X.; Wang, L.; Lu, W. A Three-Dimensional Interconnected Hierarchical FeOOH/TiO_2/ZnO Nanostructural Photoanode for Enhancing the Performance of Photoelectrochemical Water Oxidation. *Nanoscale* **2015**, *7*, 19178.

42) Mao, Y.; Yang, H.; Chen, J.; Chen, J. Signi Fi Cant Performance Enhancement of ZnO Photoanodes from $Ni(OH)_2$ Electrocatalyst Nanosheets Overcoating. *Nano Energy* **2014**,

6, 10.

43) Gong, J. Au Nanoparticle Sensitized ZnO Nanopencil Arrays for Photoelectrochemical Water Splitting. *Nanoscale* **2014**, *7*, 77.

44) Li, J.; Cheng, H.; Chiu, Y.; Hsu, Y. ZnO–Au–SnO_2 Z-Scheme Photoanodes for Remarkable Photoelectrochemical Water Splitting. *Nanoscale* **2016**, 15720.

45) Zeng, Z.; Xiao, F.; Gui, X.; Wang, R.; Thatt, T.; Tan, Y. Graphene Quantum Dots Monolayer Decorated One- Dimensional Semiconductor Nanoarchitectures for Solar-Driven Water Splitting. *Journal of Materials Chemistry A* **2016**, *4*, 16383.

46) Zhao, K.; Yan, X.; Gu, Y.; Kang, Z.; Bai, Z.; Cao, S.; Liu, Y.; Zhang, X.; Zhang, Y. Self-Powered Photoelectrochemical Biosensor Based on CdS/RGO/ZnO Nanowire Array Heterostructure. *Small* **2016**, *12*, 245.

47) Online, V. A. Morphology-Tunable Synthesis of ZnO Nanoforest and Its Photoelectrochemical Performance. *Nanoscale* **2014**, *6*, 8769.

48) Al, C. E. T. Plasmon Inducing Effects for Enhanced Photoelectrochemical Water Splitting : X -Ray Absorption Approach to Electronic Structures. *ACS Nano* **2012**, *6*, 7362.

49) Shao, D.; Cheng, Y.; He, J.; Feng, D.; Zheng, L.; Zheng, L.; Zhang, X.; Xu, J.; Wang, W.; Wang, W.; Lu, F.; Dong, H.; Li, L.; Liu, H.; Zheng, R.; Liu, H. A Spatially Separated Organic-Inorganic Hybrid Photoelectrochemical Cell for Unassisted Overall Water Splitting. *ACS Catalysis* **2017**, *7*, 5308.

50) Kim, T. W.; Choi, K.-S. Nanoporous $BiVO_4$ Photoanodes with Dual-Layer Oxygen Evolution Catalysts for Solar Water Splitting. *Science* **2014**, *343*, 990.

51) Ning, F.; Shao, M.; Xu, S.; Fu, Y.; Zhang, R.; Wei, M.; Evans, D. G.; Duan, X. TiO_2 /Graphene/NiFe-Layered Double Hydroxide Nanorod Array Photoanodes for Efficient Photoelectrochemical Water Splitting. Energy & Environmental Science **2016**, *9*, 2633.

52) Matthew W. Kanan, Junko Yano, Yogesh Surendranath, Mircea Dinca˘, Vittal K. Yachandra, and D. G. N. Structure and Valency of a Cobalt-Phosphate Water Oxidation Catalyst Determined by in Situ X-Ray Spectroscopy. *Journal of the American Chemical Society* **2010**, *132*, 13692.

53) Ye, K.-H.; Wang, Z.; Gu, J.; Xiao, S.; Yuan, Y.; Zhu, Y.; Zhang, Y.; Mai, W.; Yang, S. Carbon Quantum Dots as a Visible Light Sensitizer to Significantly Increase the Solar

Water Splitting Performance of Bismuth Vanadate Photoanodes. *Energy & Environmental Science* **2017**, *10*, 772.

Chapter 7. Conclusions and Perspectives

7.1 Conclusions

In this thesis, we adopted several methods to synthesize a series of low-dimensional (LD) nanocomposites for photo-related water oxidation applications. In these nanocomposites, low-dimensional semiconductors (e.g. 2D g-C_3N_4 nanosheet, 2D WO_3 nanosheet, 1D ZnO nanorod) that can serve as a solar light harvester, were coupled with a OER cocatalyst or electrocatalyst (e.g. 2D nanosheet-built Fw-$Co(OH)_2$ or Fw-Co_3O_4, 0D Co_3O_4 quantum dots, 2D $CoWO_4$ nanosheet, 2D M-Bi layers) to effectively improve OER kinetics. Under some circumstances where the cocatalyst or electrocatalyst is also a suitable semiconductor, heterojunctions (e.g. g-C_3N_4@$Co(OH)_2$, g-C_3N_4@Co_3O_4, WO_3@$CoWO_4$) can be constructed in the composites to promote photo-induced charge transfer and transport for more efficient photochemical OER. Experimental characterizations including optical and electrochemical measurements were combined with DFT calculations to study the light adsorption and band structure properties of the semiconductors, OER kinetics as well as the active catalytic sites. The primary objectives proposed at the beginning of this thesis have been fully realized. The work conducted in this thesis successfully demonstrate the application of LD-based nanocomposite materials for enhanced photocatalytic or photoelectrochemical (PEC) OERs.

The main conclusions from this PhD study are summarized as follows:

7.1.1 Flower-Like Cobalt Hydroxide/Oxide on Graphitic Carbon Nitride for Visible-Light-Driven Water Oxidation

- Flower-like cobalt hydroxide/oxide (Fw-$Co(OH)_2$/Fw-Co_3O_4) were prepared and loaded onto g-C_3N_4 by a facile coating method.
- The synthesized Fw-$Co(OH)_2$ or Fw-Co_3O_4/g-C_3N_4 hybrids revealed favorable combination and synergism, reflected by the modified photoelectric activities and the improved OER performances.
- Attributed by its prominent hydrotalcite structure, Fw-$Co(OH)_2$ showed a better cocatalytic activity for g-C_3N_4 modification compared with Fw-Co_3O_4.

- 7 wt.% Fw-$Co(OH)_2$/g-C_3N_4 photocatalyst exhibited 4 times higher photocurrent density and 5 times better OER performance than pristine g-C_3N_4.

7.1.2 Monodisperse Co_3O_4 Quantum Dots on Porous Carbon Nitride Nanosheets for Enhanced Visible-Light-Driven Water Oxidation

- Co_3O_4 quantum dots were uniformly deposited onto porous g-C_3N_4 nanosheets by a facile annealing process, where pores were produced around Co_3O_4 via the catalytic effect.
- The largest specific surface area, pore volume and optimal O_2 production rate as well as the highest photocurrent were obtained on 0.8 wt.% Co_3O_4 decorated g-C_3N_4 nanosheets annealed at 300 ºC (0.8% Co_3O_4-C_3N_4-300).
- These results underline the importance of surface heterojunction and afford us a feasible protocol for the rational design of g-C_3N_4 based photocatalysts for visible-light-driven water oxidation.

7.1.3 Heterostructured WO_3@$CoWO_4$ Bilayer Nanosheets for Enhanced Visible-Light Photo, Electro and Photoelectrochemical Oxidation of Water

- A facile interface-induced synthesis method was newly established to fabricate 2D bilayer nanosheets of WO_3@$CoWO_4$ as highly efficient catalysts for the enhanced photo, electro and photoelectron- chemical OERs.
- The heterostructure and the interfacial oxygen vacancy of WO_3@$CoWO_4$ can reduce the energy barriers in OER.
- DFT calculations and material characterizations revealed that the WO_3@$CoWO_4$ p-n heterojunction endowed the composite with a narrowed band gap for higher visible-light harvesting, rapid charge transfer across the interface and lower recombination rate of the photo-excited carriers.
- The interface O-vacancy vested the active Co site with an enhanced density of state (DOS) at the valence band maximum (VBM), which can also increase the concentration of the photogenerated holes to improve photocatalytic and PEC activity.

7.1.4 Photochemical Deposition of M-Bi (M = Ni, Co, Mn) Layers onto rGO/ZnO Nanorod Arrays for Solar Water Splitting

- The OER activity of M-Bi (M = Ni, Co, Mn) catalysts were compared by combining computational and experimental studies.
- DFT calculations suggest that the zigzag edges serve as the active sites in MO_6 structures of M-Bi with NiO_6 possessing the lowest overall energy barrier in OER.
- Utilizing a photodeposition method, M-Bi thin layers were self-assembled onto ZnO nanorod arrays and reduced graphene oxide (rGO/ZnO) as a ternary electrocatalyst/light-harvester PEC system.
- In accordance with the DFT results, Ni-Bi serves as the most active catalyst, followed by Co-Bi and Mn-Bi. Compared to ZnO, the photoelectroconversion efficiency is elevated by approximately 4 times in Ni-Bi/rGO/ZnO, with its onset potential migrated by 0.17 V in the cathodic direction under 1 sun illumination.

7.2 Perspectives and Suggestions for Future Research

In this thesis, we have focused on LD systems for the half-reactions of water splitting, i.e. oxidation of H_2O to O_2. However, the process of photocatalytic water oxidation requires the assistance of expensive photosensitizer and sacrificial electron acceptors, which adds challenges for practical solar-energy-conversion applications. In the future study, water oxidation with fewer or without these chemicals should be explored.

Our attention was mainly given to the photo and photoelectro-chemical water oxidation activities under room temperature and atmosphere pressure. The influences of temperature and pressure on water oxidation or overall water splitting can be investigated in the future as few reports have been concentrated on this topic. As discussed in the studies, the precondition of water splitting is the adsorption of the water molecules onto the surface of catalysts. Foreseeably, certain changes of temperature and/or pressure inevitably affect the dissociation adsorption of water molecules and the chemical intermediates during the reaction. Furthermore, from the viewpoint of the photocatalysts, the effect of elevated temperature or pressure on the surface active sites, defects and the electronic structure of the semiconductors might become an interesting research topic.

Currently, design and fabrication of nanoarray photoelectrodes are mostly based on metal oxides, while little attention has been given to the metal-free based nanoarrays such as carbon nitride. Compared to the stacked state, carbon nitride nanoarrays can make the most of the superiority of carbon nitride such as its outstanding visible-light-harvesting ability. We hypothesize that if the nanoplate or even nanorod arrays of carbon nitride can be in-situ erected on appropriate substrates, their photocatalytic efficiency can be largely enhanced.

The water splitting system or the artificial leaf just imitate the partial function of photosystem II. In the near future, this artificial system can be extended to a broader purpose such as CO_2 reduction and water decomposition. Previous reports already confirmed that the evolution of CO, H_2 and O_2 could be observed simultaneously by ZrO_2 photocatalysts in $NaHCO_3$ solutions. Inspired by this, more low-cost photocatalyst configurations can be developed for the efficiency enhancement.

Appendix

Copyright Permissions

Permissions from the copyright owners have been obtained to reproduce copyright materials in this thesis and the details are shown as follows:

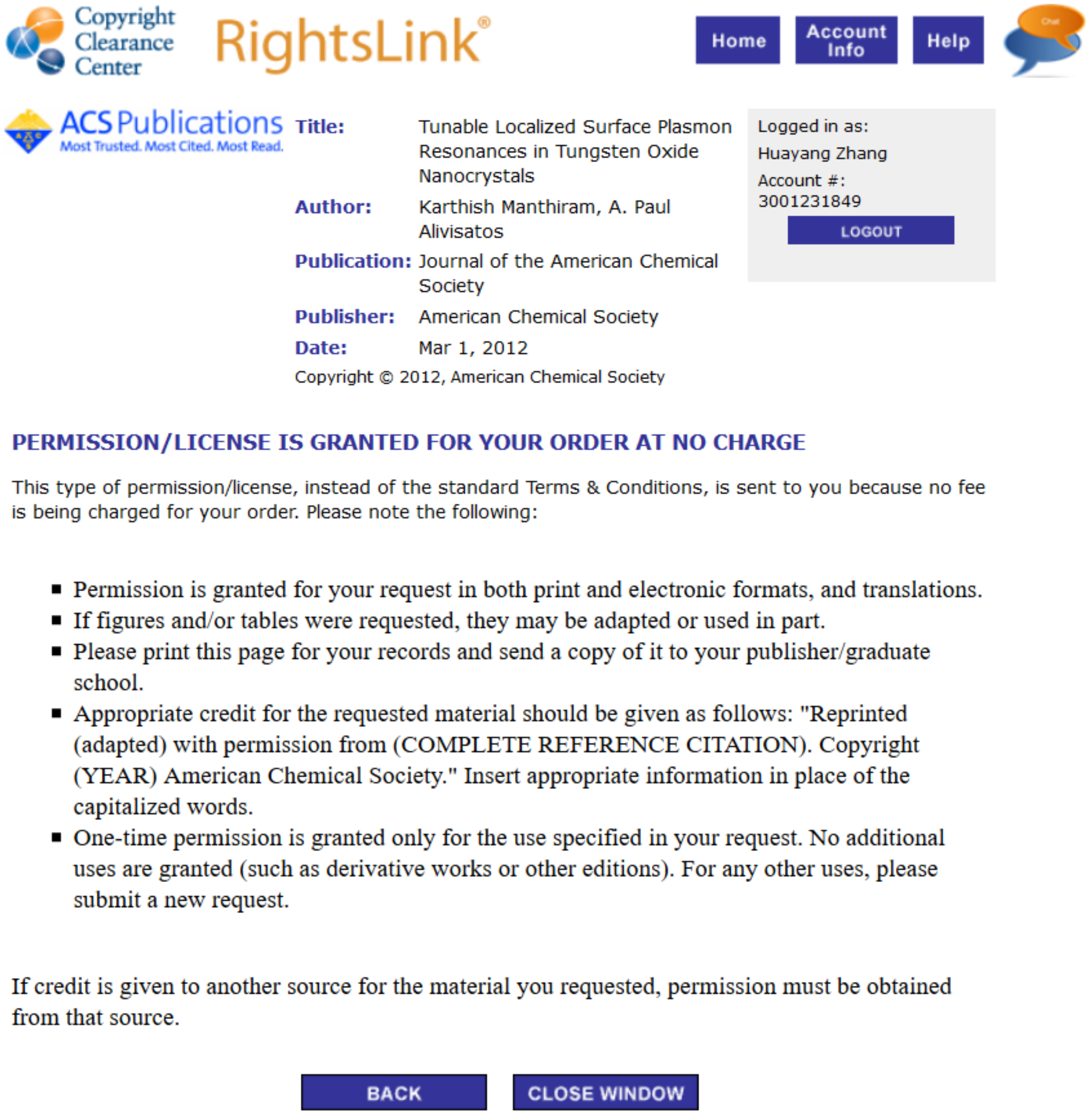

Title: Tunable Localized Surface Plasmon Resonances in Tungsten Oxide Nanocrystals

Author: Karthish Manthiram, A. Paul Alivisatos

Publication: Journal of the American Chemical Society

Publisher: American Chemical Society

Date: Mar 1, 2012

Copyright © 2012, American Chemical Society

Logged in as:
Huayang Zhang
Account #:
3001231849

PERMISSION/LICENSE IS GRANTED FOR YOUR ORDER AT NO CHARGE

This type of permission/license, instead of the standard Terms & Conditions, is sent to you because no fee is being charged for your order. Please note the following:

- Permission is granted for your request in both print and electronic formats, and translations.
- If figures and/or tables were requested, they may be adapted or used in part.
- Please print this page for your records and send a copy of it to your publisher/graduate school.
- Appropriate credit for the requested material should be given as follows: "Reprinted (adapted) with permission from (COMPLETE REFERENCE CITATION). Copyright (YEAR) American Chemical Society." Insert appropriate information in place of the capitalized words.
- One-time permission is granted only for the use specified in your request. No additional uses are granted (such as derivative works or other editions). For any other uses, please submit a new request.

If credit is given to another source for the material you requested, permission must be obtained from that source.

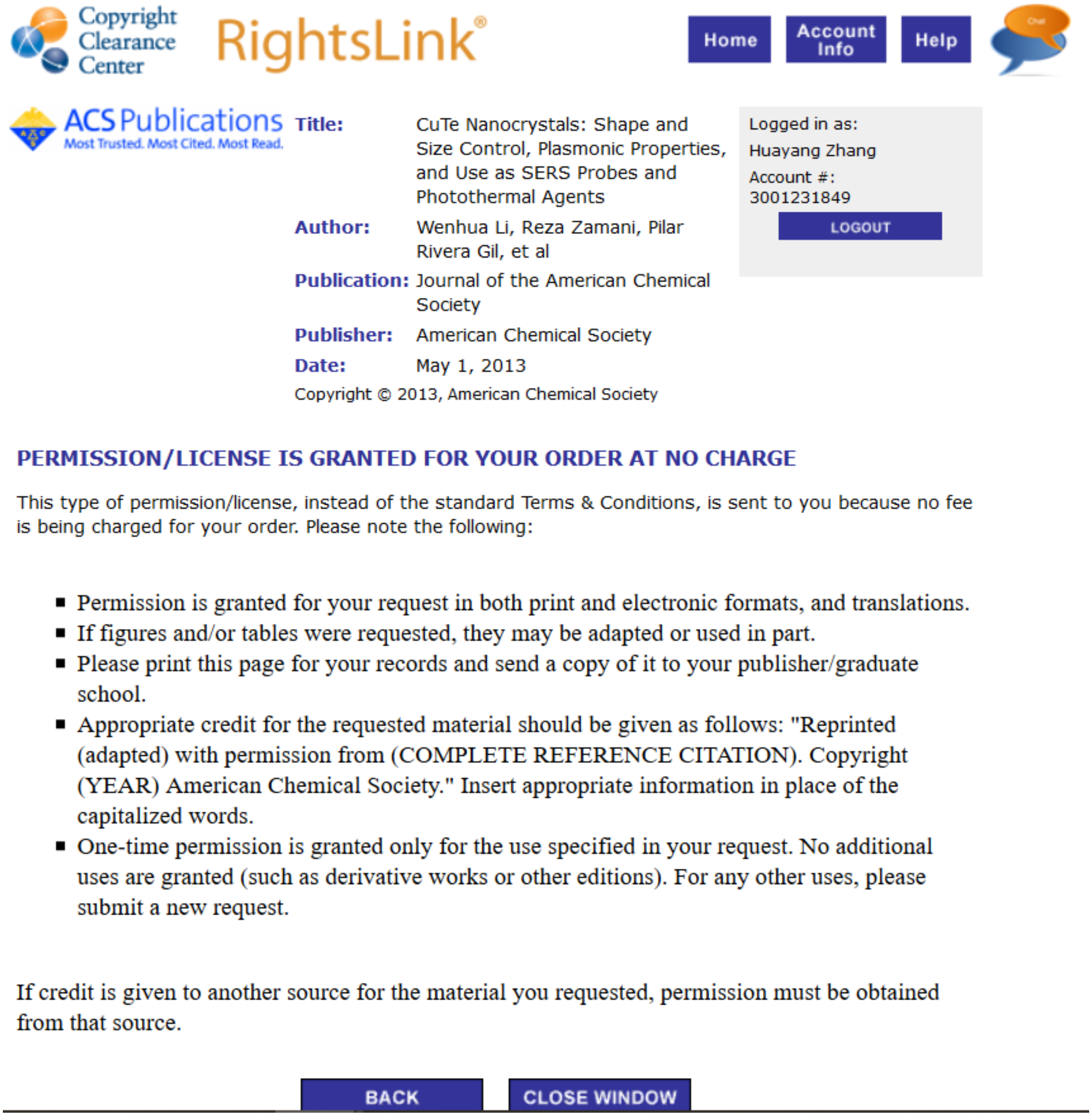

Title:	CuTe Nanocrystals: Shape and Size Control, Plasmonic Properties, and Use as SERS Probes and Photothermal Agents
Author:	Wenhua Li, Reza Zamani, Pilar Rivera Gil, et al
Publication:	Journal of the American Chemical Society
Publisher:	American Chemical Society
Date:	May 1, 2013

Copyright © 2013, American Chemical Society

Logged in as:
Huayang Zhang
Account #:
3001231849

PERMISSION/LICENSE IS GRANTED FOR YOUR ORDER AT NO CHARGE

This type of permission/license, instead of the standard Terms & Conditions, is sent to you because no fee is being charged for your order. Please note the following:

- Permission is granted for your request in both print and electronic formats, and translations.
- If figures and/or tables were requested, they may be adapted or used in part.
- Please print this page for your records and send a copy of it to your publisher/graduate school.
- Appropriate credit for the requested material should be given as follows: "Reprinted (adapted) with permission from (COMPLETE REFERENCE CITATION). Copyright (YEAR) American Chemical Society." Insert appropriate information in place of the capitalized words.
- One-time permission is granted only for the use specified in your request. No additional uses are granted (such as derivative works or other editions). For any other uses, please submit a new request.

If credit is given to another source for the material you requested, permission must be obtained from that source.

Title: Nucleation, Growth, and Repair of a Cobalt-Based Oxygen Evolving Catalyst

Author: Yogesh Surendranath, Daniel A. Lutterman, Yi Liu, et al

Publication: Journal of the American Chemical Society

Publisher: American Chemical Society

Date: Apr 1, 2012

Copyright © 2012, American Chemical Society

Logged in as:
Huayang Zhang
Account #:
3001231849

PERMISSION/LICENSE IS GRANTED FOR YOUR ORDER AT NO CHARGE

This type of permission/license, instead of the standard Terms & Conditions, is sent to you because no fee is being charged for your order. Please note the following:

- Permission is granted for your request in both print and electronic formats, and translations.
- If figures and/or tables were requested, they may be adapted or used in part.
- Please print this page for your records and send a copy of it to your publisher/graduate school.
- Appropriate credit for the requested material should be given as follows: "Reprinted (adapted) with permission from (COMPLETE REFERENCE CITATION). Copyright (YEAR) American Chemical Society." Insert appropriate information in place of the capitalized words.
- One-time permission is granted only for the use specified in your request. No additional uses are granted (such as derivative works or other editions). For any other uses, please submit a new request.

If credit is given to another source for the material you requested, permission must be obtained from that source.

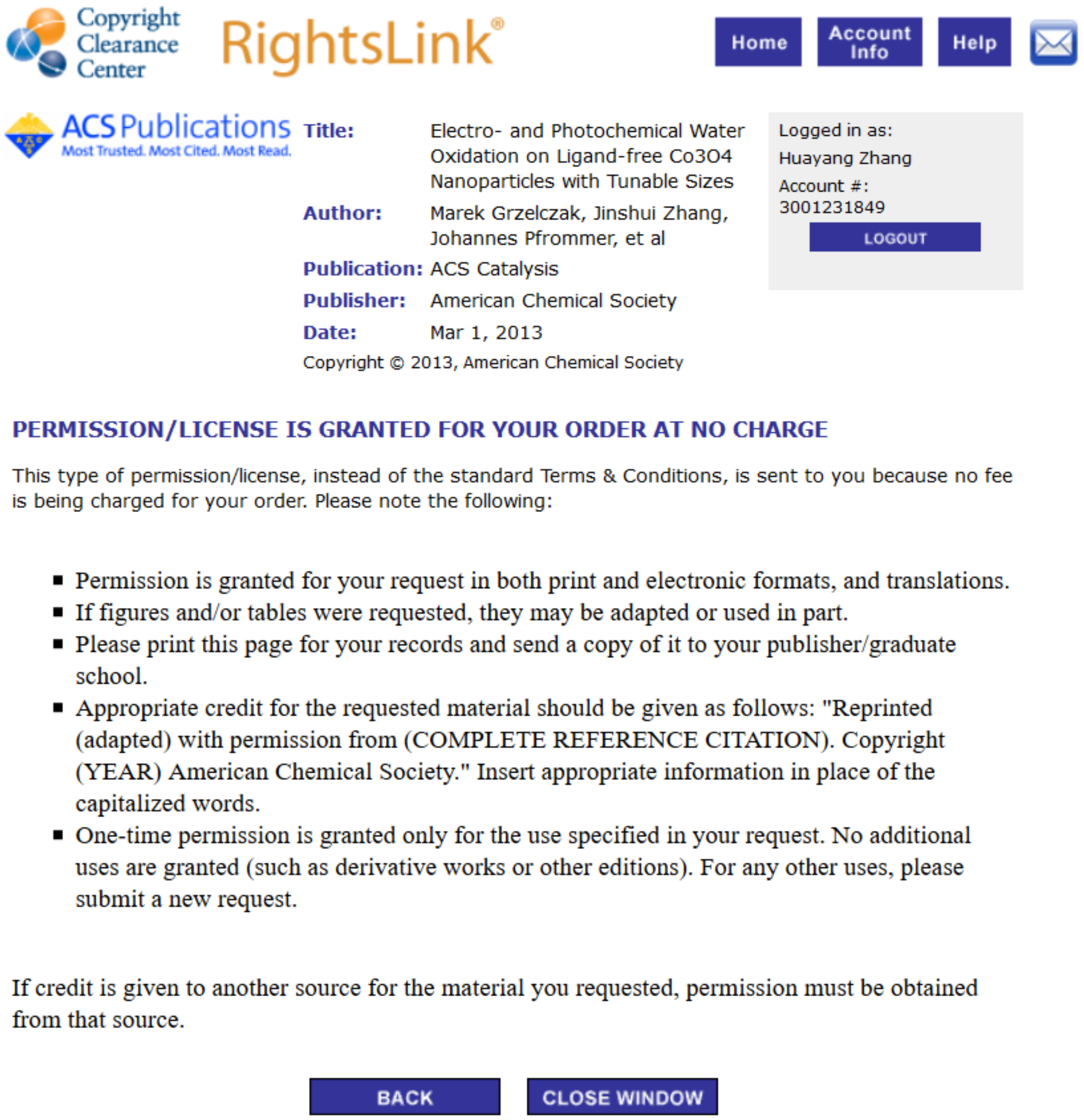

Title: Electro- and Photochemical Water Oxidation on Ligand-free Co3O4 Nanoparticles with Tunable Sizes

Author: Marek Grzelczak, Jinshui Zhang, Johannes Pfrommer, et al

Publication: ACS Catalysis

Publisher: American Chemical Society

Date: Mar 1, 2013

Copyright © 2013, American Chemical Society

Logged in as:
Huayang Zhang
Account #:
3001231849

PERMISSION/LICENSE IS GRANTED FOR YOUR ORDER AT NO CHARGE

This type of permission/license, instead of the standard Terms & Conditions, is sent to you because no fee is being charged for your order. Please note the following:

- Permission is granted for your request in both print and electronic formats, and translations.
- If figures and/or tables were requested, they may be adapted or used in part.
- Please print this page for your records and send a copy of it to your publisher/graduate school.
- Appropriate credit for the requested material should be given as follows: "Reprinted (adapted) with permission from (COMPLETE REFERENCE CITATION). Copyright (YEAR) American Chemical Society." Insert appropriate information in place of the capitalized words.
- One-time permission is granted only for the use specified in your request. No additional uses are granted (such as derivative works or other editions). For any other uses, please submit a new request.

If credit is given to another source for the material you requested, permission must be obtained from that source.

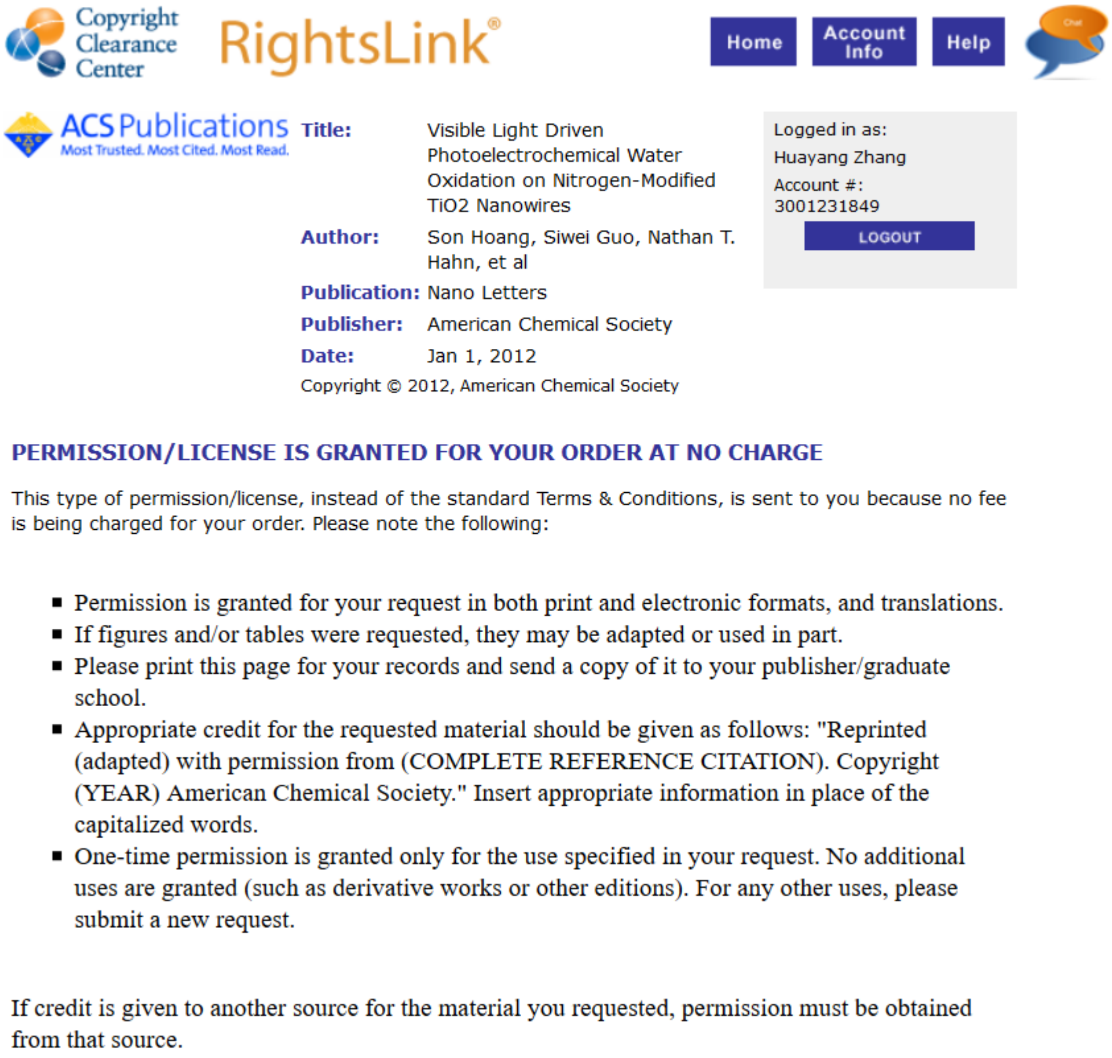

Title: Visible Light Driven Photoelectrochemical Water Oxidation on Nitrogen-Modified TiO2 Nanowires

Author: Son Hoang, Siwei Guo, Nathan T. Hahn, et al

Publication: Nano Letters

Publisher: American Chemical Society

Date: Jan 1, 2012

Copyright © 2012, American Chemical Society

PERMISSION/LICENSE IS GRANTED FOR YOUR ORDER AT NO CHARGE

This type of permission/license, instead of the standard Terms & Conditions, is sent to you because no fee is being charged for your order. Please note the following:

- Permission is granted for your request in both print and electronic formats, and translations.
- If figures and/or tables were requested, they may be adapted or used in part.
- Please print this page for your records and send a copy of it to your publisher/graduate school.
- Appropriate credit for the requested material should be given as follows: "Reprinted (adapted) with permission from (COMPLETE REFERENCE CITATION). Copyright (YEAR) American Chemical Society." Insert appropriate information in place of the capitalized words.
- One-time permission is granted only for the use specified in your request. No additional uses are granted (such as derivative works or other editions). For any other uses, please submit a new request.

If credit is given to another source for the material you requested, permission must be obtained from that source.

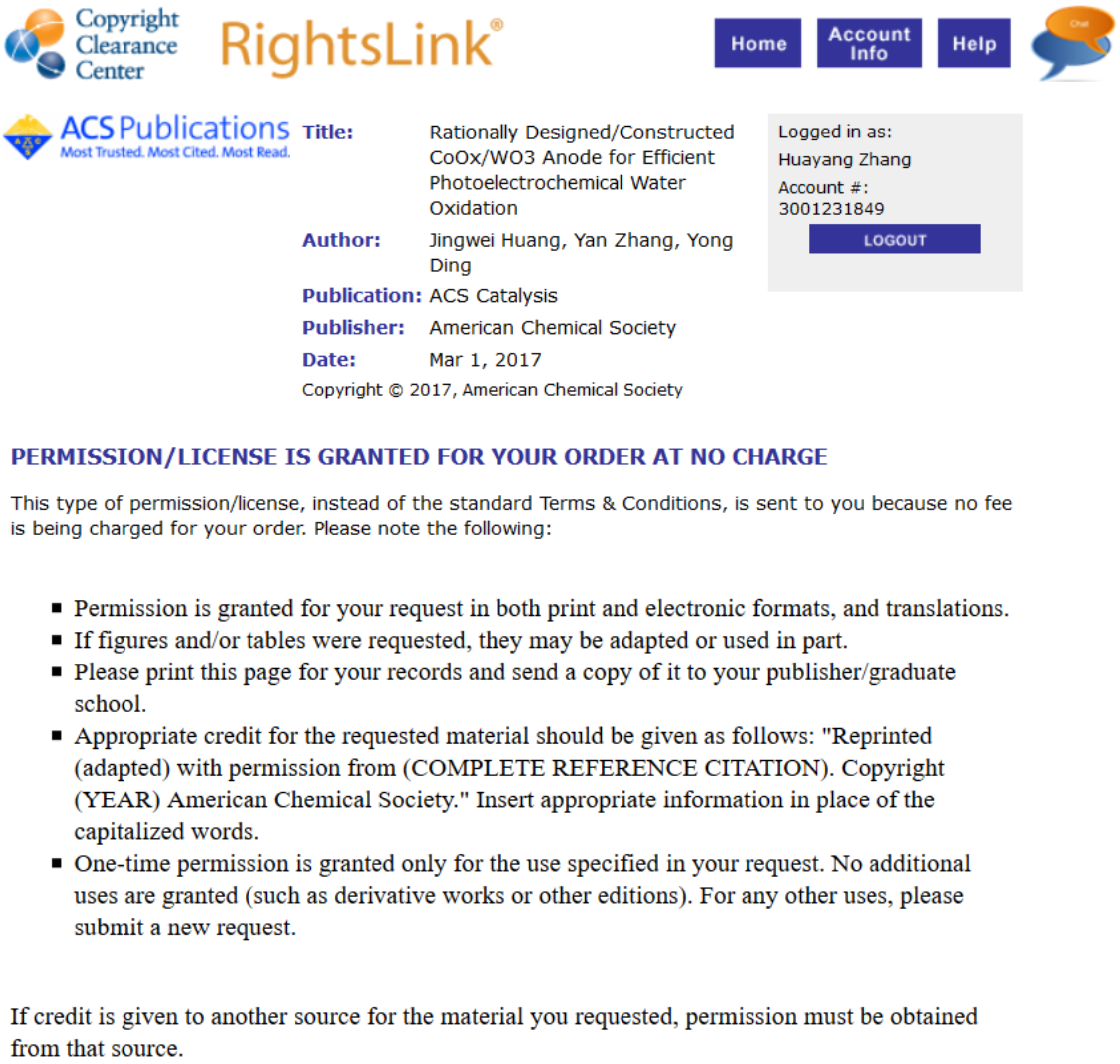

Title: Rationally Designed/Constructed CoOx/WO3 Anode for Efficient Photoelectrochemical Water Oxidation

Author: Jingwei Huang, Yan Zhang, Yong Ding

Publication: ACS Catalysis

Publisher: American Chemical Society

Date: Mar 1, 2017

Logged in as:
Huayang Zhang
Account #:
3001231849

PERMISSION/LICENSE IS GRANTED FOR YOUR ORDER AT NO CHARGE

This type of permission/license, instead of the standard Terms & Conditions, is sent to you because no fee is being charged for your order. Please note the following:

- Permission is granted for your request in both print and electronic formats, and translations.
- If figures and/or tables were requested, they may be adapted or used in part.
- Please print this page for your records and send a copy of it to your publisher/graduate school.
- Appropriate credit for the requested material should be given as follows: "Reprinted (adapted) with permission from (COMPLETE REFERENCE CITATION). Copyright (YEAR) American Chemical Society." Insert appropriate information in place of the capitalized words.
- One-time permission is granted only for the use specified in your request. No additional uses are granted (such as derivative works or other editions). For any other uses, please submit a new request.

If credit is given to another source for the material you requested, permission must be obtained from that source.

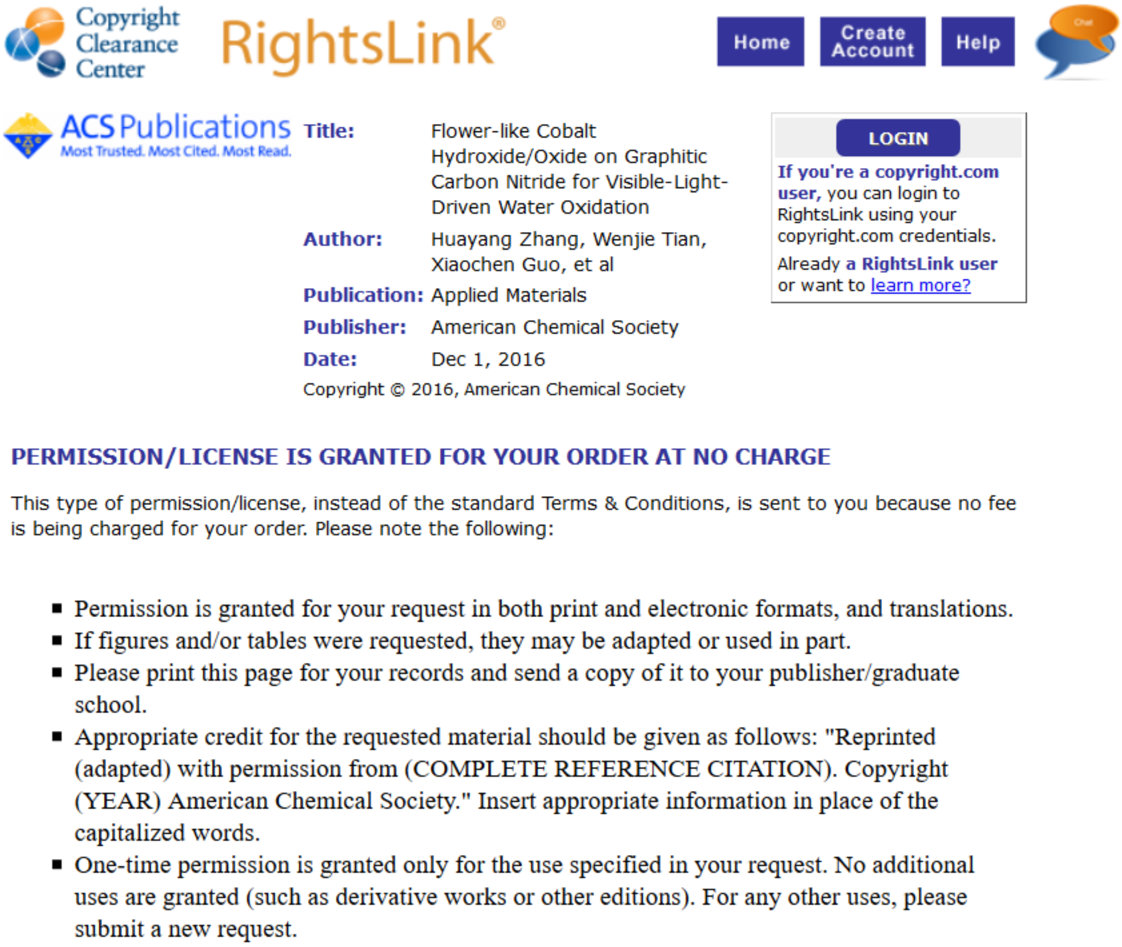

Title: Flower-like Cobalt Hydroxide/Oxide on Graphitic Carbon Nitride for Visible-Light-Driven Water Oxidation

Author: Huayang Zhang, Wenjie Tian, Xiaochen Guo, et al

Publication: Applied Materials

Publisher: American Chemical Society

Date: Dec 1, 2016

Copyright © 2016, American Chemical Society

If you're a copyright.com user, you can login to RightsLink using your copyright.com credentials.

Already **a RightsLink user** or want to learn more?

PERMISSION/LICENSE IS GRANTED FOR YOUR ORDER AT NO CHARGE

This type of permission/license, instead of the standard Terms & Conditions, is sent to you because no fee is being charged for your order. Please note the following:

- Permission is granted for your request in both print and electronic formats, and translations.
- If figures and/or tables were requested, they may be adapted or used in part.
- Please print this page for your records and send a copy of it to your publisher/graduate school.
- Appropriate credit for the requested material should be given as follows: "Reprinted (adapted) with permission from (COMPLETE REFERENCE CITATION). Copyright (YEAR) American Chemical Society." Insert appropriate information in place of the capitalized words.
- One-time permission is granted only for the use specified in your request. No additional uses are granted (such as derivative works or other editions). For any other uses, please submit a new request.

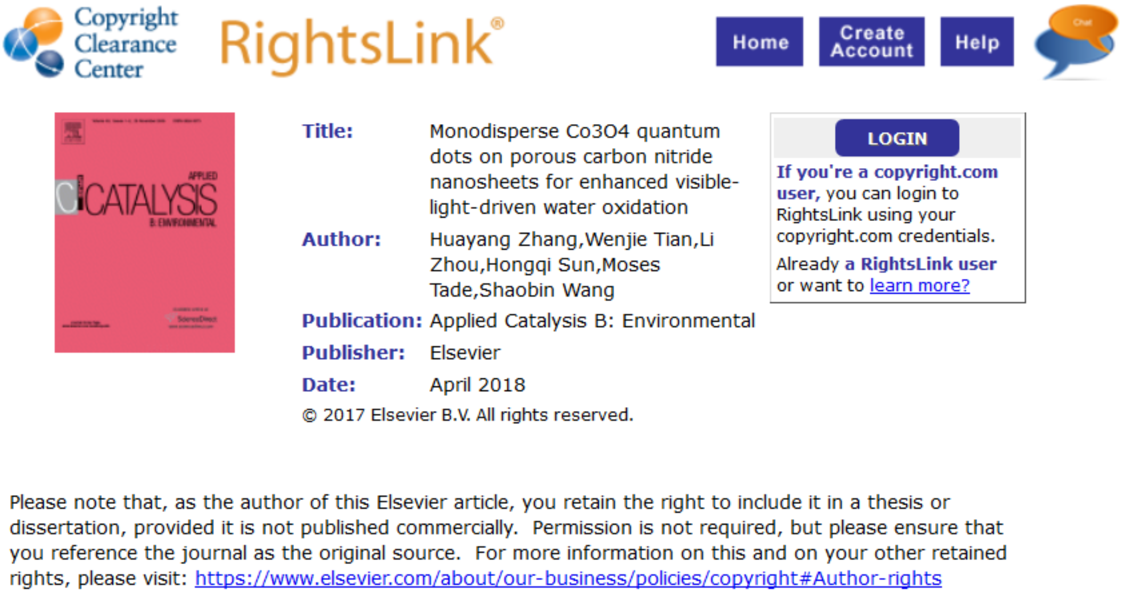

Title: Monodisperse Co3O4 quantum dots on porous carbon nitride nanosheets for enhanced visible-light-driven water oxidation

Author: Huayang Zhang,Wenjie Tian,Li Zhou,Hongqi Sun,Moses Tade,Shaobin Wang

Publication: Applied Catalysis B: Environmental

Publisher: Elsevier

Date: April 2018

© 2017 Elsevier B.V. All rights reserved.

If you're a copyright.com user, you can login to RightsLink using your copyright.com credentials.

Already **a RightsLink user** or want to learn more?

Please note that, as the author of this Elsevier article, you retain the right to include it in a thesis or dissertation, provided it is not published commercially. Permission is not required, but please ensure that you reference the journal as the original source. For more information on this and on your other retained rights, please visit: https://www.elsevier.com/about/our-business/policies/copyright#Author-rights

LICENSE #: 4355350350815
Order Date: 05/24/2018
View printable order
Advanced Functional Materials
Title: Hierarchical Nanowire Arrays Based on ZnO Core−Layered Double Hydroxide

Shell for Largely Enhanced Photoelectrochemical Water Splitting
Type of use: Dissertation/Thesis
Fee: 0.00 USD

LICENSE #: 4355350024826
Order Date: 05/24/2018
View printable order
Angewandte Chemie International Edition
Title: Modification of Wide- Band- Gap Oxide Semiconductors with Cobalt Hydroxide Nanoclusters for Visible- Light Water Oxidation
Type of use: Dissertation/Thesis
Fee: 0.00 USD

LICENSE #: 4355341141397
Order Date: 05/24/2018
View printable order
Journal of Materials Chemistry A
Title: Defect engineering in atomically-thin bismuth oxychloride towards photocatalytic oxygen evolution
Type of use: Thesis/Dissertation
Fee: 0.00 USD

LICENSE #: 4355310955619
Order Date: 05/24/2018
View printable order
Nature Communications
Title: Fabrication of flexible and freestanding zinc chalcogenide single layers
Type of use: Thesis/Dissertation
Fee: 0.00 USD

LICENSE #: 4355310596964
Order Date: 05/24/2018
View printable order
Advanced Energy Materials
Title: Promoting Photogenerated Holes Utilization in Pore- Rich WO_3 Ultrathin Nanosheets for Efficient Oxygen- Evolving Photoanode
Type of use: Dissertation/Thesis
Fee: 0.00 USD

LICENSE #: 4355310159874
Order Date: 05/24/2018
View printable order
Advanced Materials
Title: Tungsten Oxide Single Crystal Nanosheets for Enhanced Multichannel Solar

Light Harvesting
Type of use: Dissertation/Thesis
Fee: 0.00 USD

LICENSE #: 4355301034451
Order Date: 05/24/2018
View printable order
Nature Nanotechnology
Title: Efficient solar water-splitting using a nanocrystalline CoO photocatalyst
Type of use: Thesis/Dissertation
Fee: 0.00 USD

LICENSE #: 4355180251133
Order Date: 05/24/2018
View printable order
Advanced Functional Materials
Title: Size- Controlled Synthesis of Cu$_{2-x}$E (E = S, Se) Nanocrystals with Strong Tunable Near- Infrared Localized Surface Plasmon Resonance and High Conductivity in Thin Films
Type of use: Dissertation/Thesis
Fee: 0.00 USD

Title: HeterostructuredWO$_3$@CoWO$_4$ bilayer nanosheets for enhanced visible-light photo, electro and photoelectro-chemical oxidation of water.
Journal of Materials Chemistry A
http://pubs.rsc.org/en/content/articlelanding/2018/ta/c8ta00555a/unauth#!divAbstract
Type of use: Dissertation/Thesis

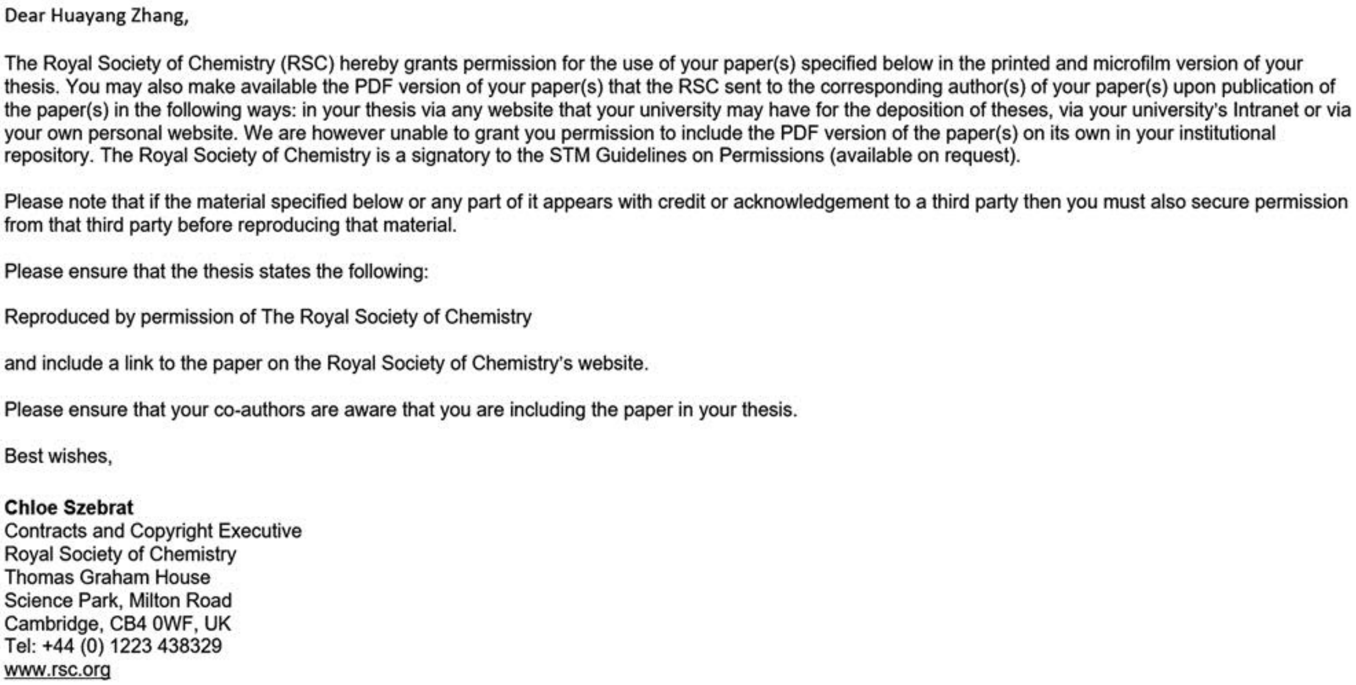

Dear Huayang Zhang,

The Royal Society of Chemistry (RSC) hereby grants permission for the use of your paper(s) specified below in the printed and microfilm version of your thesis. You may also make available the PDF version of your paper(s) that the RSC sent to the corresponding author(s) of your paper(s) upon publication of the paper(s) in the following ways: in your thesis via any website that your university may have for the deposition of theses, via your university's Intranet or via your own personal website. We are however unable to grant you permission to include the PDF version of the paper(s) on its own in your institutional repository. The Royal Society of Chemistry is a signatory to the STM Guidelines on Permissions (available on request).

Please note that if the material specified below or any part of it appears with credit or acknowledgement to a third party then you must also secure permission from that third party before reproducing that material.

Please ensure that the thesis states the following:

Reproduced by permission of The Royal Society of Chemistry

and include a link to the paper on the Royal Society of Chemistry's website.

Please ensure that your co-authors are aware that you are including the paper in your thesis.

Best wishes,

Chloe Szebrat
Contracts and Copyright Executive
Royal Society of Chemistry
Thomas Graham House
Science Park, Milton Road
Cambridge, CB4 0WF, UK
Tel: +44 (0) 1223 438329
www.rsc.org